MOCVD Growth and Characterization of Quantum Dots for Mid-infrared Emission

Yin Zongyou

School of Electrical and Electronic Engineering

A thesis submitted to the Nanyang Technological University
in fulfilment of the requirement for the degree of
Doctor of Philosophy

2008

ACKNOWLEDGEMENTS

First and foremost, I would like to express my sincere gratitude to my supervisor, Assistant Professor Tang Xiaohong, for his constant guidance and encouragement throughout this research work. His vision and insight in this project research have helped me greatly through the critical periods during the study. I am also deep impressed by Dr. Tang’s very conscientious attitude to the research.

Many thanks are expressed to all the research staffs, who give me much help in my project study, in the Photonics Lab, Clean Room and Nanoelectronics lab in school of Electrical & Electronic Engineering, Nanyang Technological University.

Special thanks are due to Mr. Liu Wei, who gives valuable discussion and much help in the theory part of this project.

Thanks are due for Ms. Zhao Jinghua and Deny Sentosa, who give me much help in some experimental measurements for this research work.

I would also thank School of Electrical & Electronic Engineering, Nanyang Technological University, for providing the financial support and inspiring research opportunity for me.

Last but not the least, I would never forget to thank my wife Fu Li for her encouragement and shouldering the heavy family burden.

TABLE OF CONTENTS

SUMMARY

This PhD project mainly covers three themes: development of metal-organic chemical vapor deposition (MOCVD) growths of high density and uniform compound semiconductor quantum dots (QDs); development of mid-infrared (mid-IR) emissive InAs QD structures and study of their properties; and the post-growth energy band gap tuning of QD structures using QD intermixing technology.

High density and uniform semiconductor QDs are very important in developing novel electronic and optoelectronic devices and in physics studies. In this project, MOCVD growth of InAs QDs has been developed under safer growth conditions, i.e. using the low-toxic Tertiarybutylarsine (TBAs) as group-V source to replace the high-toxic AsH_3 and using inertial N_2 as the carrier gas to replace the explosive H_2. Effects of the growth conditions on the InAs QD formations have been investigated. Because of the nucleation process, high dot density and narrow dot size dispersion of the QDs are very difficult to be formed in conventional Stranski-Krastanow (SK) self-assembly growth. In this project, a new two-step growth method has been developed for forming QDs with higher density and more uniformity. In this new QDs growth method, QDs are formed in two steps during the epitaxy growth: a growth rate dependent QDs nucleation in step 1 growth followed by the kinetically self-limited QDs formation in step 2 growth. Compared with InAs QDs formed by the conventional SK self-assembly growth method, morphology of the InAs QDs formed by using this two-step growth method is greatly improved. High density InAs QDs have been formed using this two-step growth method. The QDs surface coverage reaches 60% and the dot-size dispersion is as narrow as ~1 nm. The mechanism of this improvement in two-step growth of QDs has been discussed.

In this project, MOCVD growths of InAs QDs for mid-infrared emissions have been developed. By using an 8 **k·p** theoretical model, transition energies of the InAs/InGaAs/InP QD structure have been calculated under a quantum well approximation. In this calculation, lattice mismatch strain between the InAs and InGaAs barrier layers is considered. Based on the theoretical calculated results, mid-IR emissive InAs/InGaAs/InP QD structures have been designed. By employing the InGaAs barriers in InAs/InP QD structure, emission wavelength of the QD structures has been extended. Emission wavelength of the InAs/InGaAs/InP QD structures reaches >2.2 μm when the indium content of the InGaAs square barrier is >0.72. By using the $In_{0.53\rightarrow(0.53+y)}Ga_{0.47\rightarrow(0.47-y)}As$ graded barriers in the QD structure, the wavelength of the QD structure reaches >2.35 μm at 77 K when the indium gradation y =0.27. This QD structure has been grown by MOCVD using the two-step growth method for growing the QDs layer. The measured emission wavelength from the QD structure matches the calculated transition energy well. This is the longest inter-band transition emission wavelength from the InAs QD structures reported so far.

Finally, post-growth energy band gap tuning of the InAs QD structures has been investigated using argon plasma enhanced QD intermixing technology. Band gap energy of the InAs QD structure has been successfully tuned by as large as 128 meV. Spatial selective intermixing of the InAs QD structure has been investigated by employing a SiO_2 mask on top surface of the sample during the intermixing. By controlling the plasma exposure time or the annealing temperature, multi-wavelengths with 50-nm wavelength separation across one wafer have been achieved for InAs/InGaAs/InP QD structures. This paves a way to realize multi-functional monolithic integration of optoelectronic circuits.

LIST OF FIGURES

LIST OF TABLES

CHAPTER 1. INTRODUCTION

1.1 Motivation

Optoelectronic devices such as semiconductor lasers, light emitting diodes (LED), detectors, etc, working in mid-infrared (IR) region, from 2.0 µm to 5.0 µm, have many important applications:

(i) In mid-IR spectrum range, there are three atmospheric windows where the mid-IR emission can easily penetrate with low absorption. Figure 1.1 shows the mid-infrared transmission spectrum through one meter of air at sea level. The three transmission windows existing in mid-IR region, which includes the wavelength range of 2.0 µm to 2.5 µm, 2.8 µm to 4.2 µm and 4.4 µm to 5.2 µm, produce a unique infrared absorption "fingerprint". The strong absorption bands around 2.7 µm and beyond 5.2 µm are due to vibration and rotational modes of water; and the strong absorption band at 4.2 µm is due to carbon dioxide. Thus, mid-IR radiation in the three low-absorption ranges can transmit a long distance through atmosphere. This

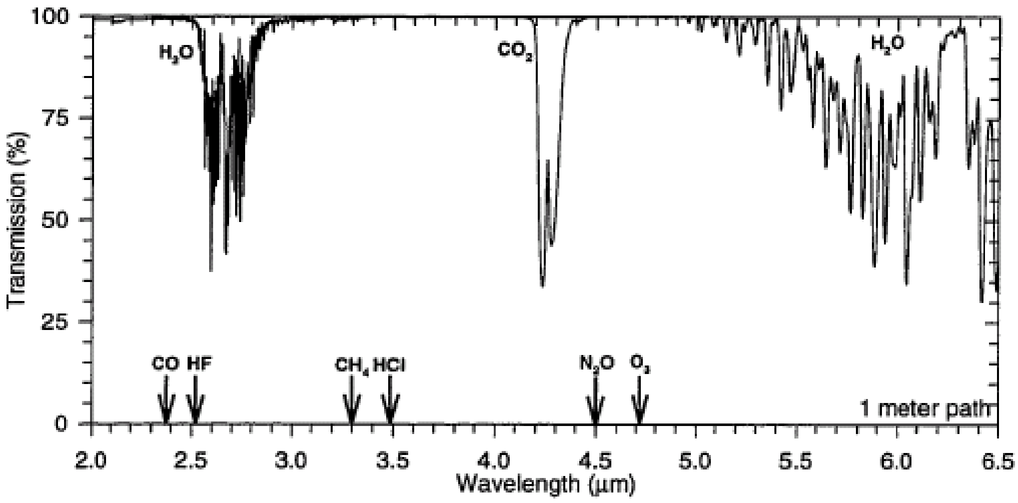

Figure 1.1 Transmission spectrum of electromagnetic wave through one-meter air [1].

allows the mid-infrared radiations in many military applications, such as night vision, remote sensing, range-finding, anti-collision system, long-haul telecommunication and infrared countermeasures [2].

(ii) The frequencies associated with the mid-infrared spectrum span the vibration frequencies of most combustible and atmospheric pollutant gas molecules. The molecules absorb the mid-IR radiation at a particular wavelength determined by the atomic composition and bond structure of adjacent atoms. Thus, as indicated at the bottom of Figure 1.1, the mid-IR spectral range contains the strong fundamental molecular absorption bands of a variety of gases [3], such as the gases of CO (2.4 μm), HF (2.5 μm), CH_4 (3.3 μm), HCl (3.5 μm) and N_2O (4.5 μm). So mid-IR optoelectronic devices have very important applications in air pollution analysis of environmental protection, siren system for natural-disasters of tsunami/earthquake/hurricane, and chemical and biological sensing in anti-terrorism.

(iii) When mid-IR laser beam shines on tissue, it is absorbed by the liquid-water component of tissue. Water has the intense infrared absorption band near 2.8-2.9 μm. So mid-IR lasers emitting near 2.8-2.9 μm are idea for cutting bone and other tissue with minimal thermal damage to adjacent tissue [4]. Also, mid-IR spectrum is very useful in other medical applications such as breath analysis for early detection of ulcers, advancing medical imaging in monitoring the insulin level, cancer cell and blood glucose during therapy, analysis of drugs and laser surgery [5].

With such a variety of applications, intense research on developing high performance mid-IR devices (lasers) has been engaged [6-9]. Different material systems, including Pb-salt based group IV-VI, HgCdTe based group II-VI and Sb-contained III-V semiconductors alloys, have been explored for developing the mid-IR lasers. However the poor mechanical and thermal properties of group IV-VI, II-VI based alloys limits their development for the high power, high reliability and high temperature mid-IR lasers. The strong covalent bonding makes III-V alloys superior mechanical and thermal properties. Compared with conventional gas or solid-state lasers, III-V compound semiconductor lasers are expected to be higher energy efficient, more flexible and compact. The mature growth and device processing technologies make the III-V alloy a favorite in developing low cost mid-IR lasers.

Researchers began to look into developing III-V compound semiconductor mid-IR lasers 20 years ago [10]. GaSb substrate based material systems firstly attracted most researchers' interest for developing mid-IR lasers. This is because the quaternary alloy, InGaAsSb, with lattice matched to GaSb, has a room temperature (RT) direct band gap which is continuously adjustable between 0.29 and 0.73 eV corresponding to a wide spectral range between 1.7 μm and 4.3 μm. But the device fabrication process for GaSb based material system is not as mature as that based on InP substrates. Low band gap mid-IR emissive semiconductors are generally lattice mismatched to InP material. When the low band gap semiconductors are deposited on the InP substrates, the strained thin films or nano-structures will be formed. With the rapid development of epitaxy technologies, such as metal-organic chemical vapor deposition (MOCVD) and molecular beam epitaxy (MBE), growths of the thin films and nano-structures become possible. If the lattice mismatch induced strain between the deposited material and the host substrate is small, e.g. $< 2\%$, the strained thin film so-called quantum well (QW) structure is expected to be formed. However, if the strain is large, e.g. $\geq 2\%$, the formed structure of the low band gap material on InP will be nano-structures, quantum wires (QWR) or quantum dots (QDs). Recently, to develop QW, QWR or QD structures, so-called low dimensional structures, for high-performance optoelectronic devices fabrications has caught intense interest in the worldwide researchers.

Much of the interest in the low dimensional structures for optoelectronic devices lies in the advantages of lower threshold, higher efficiency, better temperature reliability and better emission wavelength control. Quantum confinement occurs when the size of the individual features of a semiconductor structure becomes comparable to the de Broglie wavelength of the electron. In this case, the electron can only occupy certain elevated energy states within the confined region. As the quantum confinement degree increases from one (QW) to two (QWR) to three (QD), the desired confinement effects become more pronounced. The reduced density of states in quantum confined, optoelectronic material means a smaller number of carriers are needed for population inversion, thus leading to the lower thresholds and higher efficiencies. The higher energy quantization promises the better suppression of the carriers' scattering in the momentum space, thus improving the temperature reliability. Also, the elevated states provide the wavelength control. The promise of the improved device performance with increasing the quantum confinement degrees of low dimensional structures provides the motivation for the development and progress of QD growth and characterization. However, QDs are three-dimensional (3-D) structures; dot's height/diameter/shape uniformity, density and crystal quality strongly affect QD structures' electric and optical properties and then QD lasers' performance. In the III-V semiconductors, InAs binary alloy is simple and promising for the mid-IR emissive QDs application since its band gap is as low as 0.36 eV at RT. Presently, difficulty in growing uniform sized/shaped, high density and high crystal-quality mid-IR InAs QDs still remain, which restricts the development of high performance mid-IR QDs devices. Researchers have been devoting their efforts to developing the InAs QDs on InP substrates for the mid-IR applications [11 - 13]. The longest emission wavelength from the InAs/InP QD structures reported so far is only ~ 2.1 μm at RT [12]. For the mid-IR region application, InAs QD structures with the longer emission wavelengths need further exploring.

1.2 Objective

The objectives of this thesis focus on the development of high density and uniform InAs QDs by using MOCVD with safer growth conditions, including the design, growth and characterization of InAs QD structures with mid-IR emission wavelengths.

MOCVD growth of 3-D QDs is very sensitive to the growth conditions including growth time, precursor flux flow, V/III ratio, growth temperature and growth method, etc. In this study, safer precursors and carrier gas, i.e. using low-toxic Tertiarybutylarsine (TBAs) as group-V source to replace high-toxic AsH_3 and using inertial N_2 as the carrier gas to replace the explosive H_2, are employed in QD growths by MOCVD. InAs/GaAs QDs have the most matured epitaxy growth experiences among the III-V semiconductor QD systems. So, as the first research topic of the thesis, we developed high quality, i.e. high dot density and size uniformity, InAs/GaAs QDs growth under the safer MOCVD growth conditions.

In order to realize mid-IR emission from InAs QDs, the QD structures have to be grown on InP, instead of GaAs, substrate due to the properly reduced lattice-mismatch strain of the InAs/InP system compared with that of InAs/GaAs system. Based on InAs/InGaAs/InP QD system, redshift techniques through barrier and strain engineering will be employed to extend the QDs' emission wavelength towards mid-IR region. The second research topic relates to the theoretical design and experimental demonstration of mid-IR InAs/InGaAs/InP QD structures.

Finally, the post-growth QD band gap tuning has been investigated based on the Argon plasma enhanced QD intermixing.

1.3 Major contribution of the thesis

The major contributions of this PhD project include the development of MOCVD growth of high quality InAs QDs on GaAs and InGaAs/InP matrixes under the safer growth conditions, the theoretical design and experimental demonstration of mid-IR emissive QD structures, and the post-growth QD band gap tuning based on the enhanced QD intermixing by Argon plasma exposure. These contributions are summarized below:

(i) High density InAs/GaAs(001) QDs have been grown using conventional Stranski-Krastanow (SK) method by MOCVD in the N_2 ambient with the optimized growth conditions. A growth temperature window of 440-460 ^oC for high density QD formation has been observed.

(ii) A new two-step growth method (fast growth + slow growth) has been developed for growing QDs with higher density and better size uniformity. Under the optimized growth conditions, dot density has reached $2\sim3\times10^{10}$ cm^{-2} and the standard deviation of dot's size can reach several nanometers using the two-step growth process.

(iii) Under a two dimensional QW approximation, transition energy of QD structure has been calculated by using 8 band **k·p** theoretical model. The calculated results agree well with the experimental results.

(iv) Using the 8 band **k·p** theoretical model, mid-IR emission InAs/InP QD structures have been designed. The emission wavelength of the InAs/InP QD structures has been calculated >2.2 μm by using InGaAs as the barrier layers of InAs QDs.

(v) Under the optimization, high density (2.5×10^{10} cm^{-2}) and uniform (~1 nm dot-size dispersion) InAs/InGaAs/InP QDs have been achieved. Graded InGaAs layers as the barriers of InAs QDs for extending the emission wavelength has been proposed. Longer emission wavelength while keeping the strong PL emission intensity of InAs/InGaAs/InP QD structures has been developed. PL emission peaks measured for the grown mid-IR QD structures match well to the designed transition energies. The 77-K emission wavelength of InAs/InGaAs/InP QDs reaches > 2.35 μm. This is the longest inter-band transition emission wavelength from InAs QDs reported so far.

(vi) Argon plasma enhanced QD intermixing for tuning the energy band gap of QD structure has been studied. The QDs' band gap tuning range has been increased greatly by using this QD intermixing technology.

(vii) Selective intermixing with 50-nm separation multi-wavelengths across one wafer has been achieved for InAs/InGaAs/InP QD structures by using plasma exposure and SiO_2 masking techniques.

1.4 Organization of the thesis

This thesis consists of six chapters. An introduction to the thesis is given in Chapter 1, which covers the motivation, objective and major contributions.

In Chapter 2, different material systems for mid-IR emission are discussed with comparison. Subsequently, III-V semiconductor mid-IR lasers with different active region structures are reviewed. Then, the subject to be studied in this project is proposed.

In Chapter 3, technologies for epitaxy growth, characterization and sample process for the QD structures are introduced.

In Chapter 4, the MOCVD growth of InAs/GaAs QDs under the safer growth conditions by using TBA as group-V source and N_2 gas as carrier gas is investigated. The effects of different growth conditions on the QDs formation have been studied in detail. After that, a new two-step growth method is proposed to improve dot's density and size uniformity. The 8 band **k·p** theoretical calculation on the transition energies of InAs/GaAs QD structure is carried out and compared with the experimental results.

In chapter 5, 8 band **k·p** theory model is used to design the mid-IR emissive QD structures based on InAs/InP QDs by embedding InAs QDs between the InGaAs barriers. After that, formation of high density and uniform InAs QDs on InGaAs/InP matrix is developed by optimizing the two-step growth method. Then, the designed mid-IR QD structures are grown, so that the experimental realization of the designed mid-IR QD structures is demonstrated.

Chapter 6 studies the thermal annealing and Argon plasma exposure induced intermixings on QD structures. The thermal annealing effects on the QDs' energy band gap tuning are studied first for the QD structures with different QDs' upper-barrier, top-cap thickness and dot density. Then, the Argon plasma enhanced intermixing is investigated in tuning the QDs' energy band gap. The spatial selective intermixing has been proposed and experimentally demonstrated based on the plasma exposure and SiO_2 masking techniques.

Finally, the last chapter, Chapter 7, concludes the major contributions of this PhD project, and recommends possible works for future research.

CHAPTER 2. BACKGROUND

2.1 Introduction

This chapter presents the background of developing III-V semiconductor QDs for mid-IR emission. In Section 2.2, different material systems for mid-IR emission are discussed. Section 2.3 provides a survey on III-V semiconductor mid-IR lasers, including the mid-IR lasers with double heterostructure (DH), quantum well (QW), quantum cascade (QC), quantum wire (QWR) and QD structures as the active region. Based on the literature survey and current situation, the subject to be studied in this project is proposed and presented.

2.2 Material system for mid-IR emission

Many potential applications of mid-IR devices have attracted intense researches based on the different material systems. Table 2.1 compares different material systems for mid-IR laser applications. It shows that both IV-VI and II-VI alloys can be used for lattice-matched mid-IR laser structures with emission wavelengths from 2 to 5 μm. However, the poor mechanical and thermal properties limit their applications in high power, high reliability and high temperature mid-IR lasers. The strong covalent bonding makes III-V alloys superior mechanical and thermal properties. Compared with conventional gas or solid-state lasers, III-V compound semiconductor lasers are expected to have higher electrical- to optical-power conversion efficiency (higher than 50% by comparison with 1% ~ 2% of conventional lasers), larger wavelength coverage (opposite to the fixed emission wavelengths by the transition levels of atoms or ions), more flexible and compact.

The mature growth and device processing technologies make the III-V alloy a favorite in developing low cost mid-IR lasers. For instance, so far, only Pb-salt lasers based on group IV-VI materials are available with continuous-wave (CW) operation up to 200K emitting at about 4 μm [14, 15]. But Pb-salt lasers have the problems of poor thermal conductance and poor reliability. Their output power is low (<1mW). In the case of group II-VI materials based lasers, HgCdTe lasers emitting between 2.9 and 5.3 μm with pulse operation at 90K have been reported [16]. Because of its poor thermal conductivity and high mobility of Hg due to its weak ionic bonding, practical applications with high output power at high operation temperature of such lasers is not possible.

Table 2.1 Comparison of material systems for mid-IR lasers [17].

Material system	Advantages	Disadvantages
IV-VI	• Availability of low band gap materials • Good carrier confinement • RT operation for λ <6 μm	• Poor mechanical properties • Low thermal conductivity which restricts maximum power to be a few mW at low Temperature
II-VI	• Availability of low gap materials (HgTe has a negative energy gap) • Good lattice matching properties (HgTe and CdTe have very close lattice constants)	• Poor mechanical properties • No high temperature laser operation has yet been reported due to the instability of the materials
III-V	• Availability of mature growth and processing technologies • Strong covalent bonding allows good mechanical and thermal properties	• No lattice matched structures available for good carrier and optical confinement with especially λ >3 μm

In order to develop high power, high reliability and high operating temperature mid-IR lasers, III-V based semiconductors have obvious advantages because of their superior mechanical and thermal properties induced by the strong atoms' covalent bonding. Also, compared with conventional gas or solid-state lasers, III-V compound semiconductor lasers are expected to be more compact and lower cost because of their relatively mature growth and device processing technologies. So, the new III-V-N materials [18,19] are becoming very attractive for mid-IR laser applications because, in principle, they can be used for developing mid-IR lasers' active region based on GaAs and InP substrates.

In addition to the material system, the laser devices' active structures also affect the laser's performance. With the advanced epitaxy technology, growth of III-V semiconductors based low-dimensional structures, from QW to QDs, becomes possible. Intense efforts have been devoted to developing these low dimensional structures for mid-IR applications. In the following Section, evolution of III-V alloys based mid-IR lasers is presented.

2.3 Evolution of III-V semiconductor mid-IR lasers

Researchers began to develop III-V semiconductors based lasers working in mid-IR 2-5 μm region over two decades ago [10]. These semiconductor mid-IR lasers were with DH structure active region. Generally, the DH lasers have high threshold current, low output power and low maximum operating temperature, etc, which restricted their applications [20]. Using QW as the active region of the laser structure enhanced the device's performance [21,22]. Mid-IR emissive QC structures were also proposed [23, 24] for developing long wavelength mid-IR lasers with suppressing Auger nonradiative recombination. Now, QWR [25], quantum dash (QDH) [26] and QDs [27] have attracted much attention due to their applications in high performance mid-IR lasers.

In the following, a survey of different approaches in III-V semiconductor compound active regions for mid-IR laser structures is provided. The performance of mid-IR lasers with different designs of active region has been compared and discussed. The progress in the active region structures for achieving higher performance mid-IR lasers and the recent development of III-V-N based semiconductors for mid-IR applications have been shown.

2.3.1 Double heterostructure to quantum well

The first successful semiconductor mid-IR laser was with InGaAsSb DH active structure grown on GaSb substrate reported by C. Caneau [10]. In the operation of the DH laser, the laser transition is realized through recombination of the injected electron-hole pairs, which are free in all three dimensions in InGaAsSb bulk active region. The reported device structure was grown by liquid phase epitaxy (LPE) and emitted at 2.2 μm. GaSb based material system has attracted most researchers' interest for developing mid-IR DH lasers. This is because InGaAsSb quaternary alloy can be grown lattice-matched to GaSb substrate by controlling its composition, and at the same time, this alloy has a room-temperature (RT) direct band gap covering the wavelength range between 1.7 μm and 4.3 μm. But, because of the very large miscibility gap, composition of $In_xGa_{1-x}As_ySb_{1-y}$ alloy with lattice-matched to GaSb is limited to $x \leq 0.22$ [28] or $x \geq 0.84$ [29]. The longest room-temperature emission wavelength achievable from this quaternary alloy before encountering the immiscible is 2.3 μm. To achieve emission wavelength beyond 2.3 μm, InAs substrate based material system has been investigated. Baranov *et al.* used the InAsSb(P)/InAsSbP/InAs material system to extend the lasers' emission wavelength to 3.9 μm measured at 77 K [30]. But the performance of all these mid-IR lasers is limited with low differential quantum efficiency of 17% and low maximum operating temperature of 180 K.

The reasons for the poor performance of these mid-IR lasers with DH active region structure are mainly because: First, the DH structures are grown by LPE, while for LPE growth technology, it's difficult to grow thermally meta-stable material such as Al or In contained alloys. LPE is also difficult to grow multiple layer structures with sharp interfaces and control the layer thickness precisely [31,32]. However, more sophisticated epitaxy growth technologies, such as MOCVD and MBE, can be used to grow the meta-stable InGaAsSb or AlGaAsSb alloys. In 1991, H.K. Choi *et al* [33] reported the mid-IR laser structure with closely lattice matched GaInAsSb/AlGaAsSb/GaSb DH active region grown by MBE. The laser operated at RT with CW operation, and the threshold current density of the laser achieved J_{th} = 940 A/cm^2. The material quality and hence performance of the lasers have been improved by using advanced MOCVD or MBE epitaxy technologies. Second, DH active region of the mid-IR laser structures limits the device's performance. Using QWs as the active region in mid-IR laser structure improves the laser performance. In a QW laser, electron/hole carriers are confined inside the thin well layer of the QW active region. During the laser operation, the lasing is realized through the recombination of electrons and holes, which are under one-dimensional confinement in the growth direction and free in other two dimensions perpendicular to the growth direction. Compared with DH lasers, QW lasers have lower threshold current density; the temperature performance [34], differential gain [35] and modulation [36] of the mid-IR lasers can also be improved. Since W.T. Tsang at the Bell Telephone Laboratory firstly demonstrated QW lasers with very low threshold current density, ~160 A/cm^2 [37], using QW structures as the active region to improve the mid-IR laser's performance has caught more and more researchers' interests. Following sections review the QW mid-IR lasers.

In QW lasers, QW structure active region is embedded in two spacer layers (or waveguide layers) in QW laser structure. The QW layers have lower band gap energy but higher refractive index as compared with the adjacent cladding layers. So the carriers are confined in the well layers while the emission beam is confined inside the waveguide to prevent it penetrating into the cladding layers [38]. By using different alloys, different QW structures can be constructed based on the energy band edge alignment of the QW hetero-junction in mid-IR laser structures [39, 40], which are presented in the following.

In type I (straddled) QW structure [40], as shown in Figure 2.1-(a), both conduction band edge and valence band edge of the well layer are lower than that of the barrier layers. Electron and hole carriers are confined inside the well layer of the QW structure. Type I QWs based on antimonide material systems have been widely used in mid-IR lasers [20, 21]. Very low loss mid-IR lasers emitting at 2 μm have been reported with the critical temperature T_0 = 140K. Four GaIn(As)Sb QWs were used in the active region of the laser [21]. To extend the emission wavelength beyond 2 μm for GaSb based type I QW mid-IR lasers, GaInAsSb/AlGaAsSb/GaSb QW

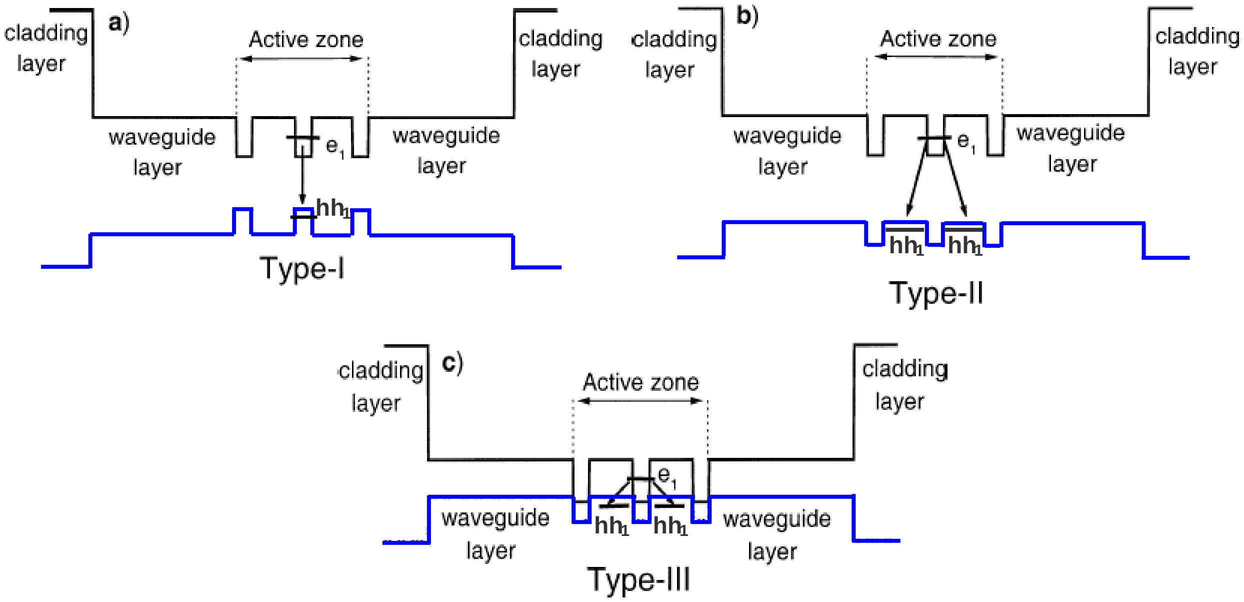

Figure 2.1 Different types of QWs in terms of the band alignment, where the fundamental electron-hole transition e1-hh1 is shown.

structure was used in the laser's active region. Lasers emitting at 2.4 μm with $T_0 = 72$ K was demonstrated by improving hole confinement energy with heavily strained active region [41]. Lasing at wavelength of 2.78 μm with $T_0 = 58$ K has been reported with graded barrier layer structures by varying the waveguide layer from GaSb to $Al_{0.9}Ga_{0.1}As_{0.08}Sb_{0.92}$ [20]. The lasing wavelength based on the quaternary InGaAsSb type I QW structures could be increased in principle; but the laser performance degrades very fast when the emission wavelength is increased due to the solid phase miscibility gap of the GaInAsSb alloy [42]. The longest room temperature emission wavelength from GaInAsSb/AlGaAsSb/GaSb QW laser structures reported so far is only 2.89 μm, and the laser is under pulse operation mode [43]. In Sb-contained alloys, InAsSb is important for long wavelength emission lasers. Lasers with 10 InAsSb/InAlAsSb QWs as the active region were reported lasing at 3.5 μm with $T_0 = 30$ K and maximum CW operation temperature up to 175 K [44]. A laser with 15 InAsSb/InAlAs QWs was reported even lasing at 4.5 μm with $T_0 =26$ K but under pulse operation mode [45]. When the Arsenic content in InAsSb alloys used for laser active region is increased for extending the lasing wavelength, the lasers' performance becomes lower. This is attributed to: inadequate hole carrier confinement in the Sb based QW active structure of the lasers, induced by the reduction of the valence band offset of the QWs; and the increment of Auger recombination in the active region for the lasers emitting at the longer wavelength [46]. So, till now, mid-IR type I QW lasers with impressive performance are fabricated based on GaInAsSb/AlGaAsSb/GaSb material system. The lasers emitting at 2.4 μm have been reported with a room temperature CW output power of 1050 mW. Besides, laser's threshold current density and differential gain have been greatly improved due to the QW compressive strain [41].

On the other hand, III-V-N semiconductors have been becoming more important in type-I QW for mid-IR applications. In principle, InGaAsN and InAsN alloys with the energy band gap in mid-IR emission region can be lattice matched to two commonly used GaAs and InP substrates. For InGaAsN alloy lattice-matched to GaAs or InP substrates, its emission wavelength can cover the full mid-IR region from 2 μm to 5 μm [47]. The calculated band gap energy of $InAs_{1-x}N_x$ alloy covers the wavelength region between 3.4 μm and 5 μm when the nitrogen component x varies from 0 to 0.045 only [48, 49]. The energy band gap reduction of III-V alloys with incorporation of nitrogen improves the electron/hole confinement in III-V-N alloy QW structures. For InGaAsN, the refractive index increases while the band gap energy reduces when the nitrogen content of the alloy is increased. The increase of the refractive index of InGaAsN alloys is much larger than that of GaInAs [50]. This is very important to enhance the optical confinement in InGaAsN based QW active region of the laser structures. M. Maier *et al*. demonstrated the band gap reduction of the lattice matched $In_{0.53}Ga_{0.47}As$ alloy grown on InP substrate by incorporating a few percent of nitrogen in it [51]. Milind R. Gokhale *et al*. also reported growing small band gap (~ 0.6 eV) InGaAsN layers on InP [18]. Strained $InAs_{0.97}N_{0.03}$/InGaAs/InP multiple QWs structure emitting at 2.38 μm at 260K has also been reported [19]. Besides, I. Vurgaftman *et al.* proposed 3 - 6 μm laser structures by combining using the InAsN and GaAsSb material in the type II QW active region based on InP substrate [52]. It shows that III-V-N alloys will be very important in developing high performance mid-IR lasers. However, it is still challenging presently to grow high crystal quality and composition homogeneity III-V-N alloys by using the epitaxy technologies, which needs further research.

Type II QW structure has been proposed in mid-IR laser structure design to reduce Auger nonradiative recombination induced by the resonance between E_g and split-off gap Δ_o in the QW active region of mid-IR lasers [53]. The band edge alignment of typical type II (staggered) QW structure is shown in Figure 2.1-(b). The conduction band (CB) edge of the well layer is placed between the CB and valence band (VB) of the barrier. The electron and hole carriers in the QW structures are spatially separated, and the radiative recombination corresponds to the transitions between the conduction band electrons in QW layer and the valence band holes in the barrier layer. Although, the efficiency of radiative recombination is reduced in type II QWs due to the decreased wave function overlap between the spatially separated electrons and holes, it has been demonstrated [53,22] that, under injection, the localized electrons in the QW can 'pull' the holes from the adjacent barriers due to the Coulomb interaction. Such interaction induces a modification of the band structure near the hetero-interfaces, so that holes in barriers are confined in the nearly triangular potential wells adjacent to the QW interfaces [40, 54]. So, the probability for the holes to be present near the QW is increased, which increases the overlap of electron-hole wave functions. Mid-IR lasers made of type II QW structures have been reported lasing at 2.36 μm [54]. And the laser lasing at 2.35 - 2.65 μm was also reported [53]. In order to extend the emission wavelength beyond 3 μm with suppressing the Auger recombination, InAs-GaSb-AlSb family based type II multiple QW (MQW) and type II superlattice (SL) structures were proposed. For instance, optically pumped four-constituent Type-II (InAs-GaInSb-InAs-AlSb) MQW lasers emitting at 3.9 - 4.1 μm were observed to lase up to 285 K. The stimulated emission at 3.2 μm with T_0 of 36 K has been demonstrated in an optically pumped type II SL mid-IR laser [55], and GaInSb/InAs/AlSb type-II SL pulse operated lasers emitting at 3.3 - 3.9 μm with T_0 of 170 - 84 K have also been reported [8]. However, the performance of type II MQW or SL based mid-IR lasers are still needed to be improved by designing such active region structures with increasing the wavefunction overlap and enhancing the hole confinement in the barrier layers. A particular band alignment of type-II QW as shown in Figure 2.1-(c) with the CB of the well lying below the VB of the barrier is called type-II broken-gap (so called type III) QW. In this type of QW structure, the lowest energy of indirect radiative transitions can be, in principle, reduced to zero by increasing the QW width. So, such QW structure is potential for the longer wavelength applications. RT operation mid-IR lasers based on type III InAs/GaSb multiple QWs structures were reported lasing at 2.32 μm. But the lasers were with low critical temperature, T_0, and low quantum efficiency due to the spatial separation of carriers in the active region [22].

An advanced type II design, i.e. type II "W" laser, was proposed by J. R. Meyer *et al.* [46]. This laser structure has four layers in each period of the active region (e.g. InAs/GaInSb/InAs/GaAlSb) and takes its name from the shape of the conduction band profile. A "W" structure includes a 'hole' QW sandwiched between two 'electron' QWs, which formed a CB profile with a "W" shape. Such "W" arrangement advantages the enhancement of the electron-hole wavefunction overlap, while keeping the advantage of type II QWs i.e. higher electron confinement and reduction of nonradiative Auger recombination rate. Excellent performance lasers with such "W" structure have been reported by W W. Bewley, *et al.* [56]. The active region of the laser structure is composed of five W periods of InAs(15Å)/GaInSb(27Å)/InAs(15Å) separated by an AlGaAsSb (80Å) bi-dimensional spacer layer. This space layer furnishes a two-dimensional dispersion for electrons and holes with strong confinement in each "W" period. These QWs are embedded into a thick AlGaAsSb separate confinement heterostructure (SCH) layer to maximize the optical confinement in the reactive region, while minimizing the free-carrier absorption losses in the doped cladding layers [57]. Besides, a “hole-blocking region”, consisting of a 7-period InAs(15Å)/AlSb(14Å) SL, is inserted between the active QW and electron-injecting SCH layer to prevent hole leakage from the active QW while keeping electrons being able to be injected in. Attributed to such elaborate design of the active structure, mid-IR laser emitting at 3.25 μm has been realized operating in CW mode up to 195 K with a threshold current density of 1.4 kA/cm^2 [56].

In summary, QW, instead of DH, active region can improve laser’s performance greatly. Type I QW reactive region is advantageous for shorter mid-IR wavelength region of 2 μm $\leq \lambda \leq$ 3.5 μm; To achieve higher performance type I QW mid-IR lasers, it is important to design the QWs with: (i) strong electron/hole confinement in the QW to increase the emission efficiency [58]; and (ii) large enough refractive index difference between the active region and cladding layers of the laser structure to increase the optical confinement [40]. Type II, type-II broken-gap (i.e. type III) and type II ‘W’ QW reactive regions are advantageous to extend the emission wavelength with reducing Auger recombination. However, to improve the type II lasers’ performance further, it is important to increase the hole confinement [59] and carrier wave function overlap with minimized internal absorption loss.

2.3.2 Quantum cascade and quantum wire

Semiconductor QC structure opens a new avenue for designing mid-IR lasers in the longer wavelength region. Unlike typical interband semiconductor lasers that rely on the electron-hole radiative recombination across the material band gap, QC lasers generally rely on one type of carrier, electrons or holes, to achieve the radiative emission through intersubband transitions in a repeated stack of semiconductor superlattices. The electron carriers are used due to the large mobility of electrons. The repeated QC structures allow recycling of the electrons to increase the optical gain, which advantages enhancing lasers' quantum efficiency. QC lasers have furnished impressive results in the long wavelength infrared region [24, 60 - 63], and the longest wavelength reported so far reaches 2.1 THz, i.e. 141 μm [63]. Nevertheless, it is challenging to develop the high performance QC lasers for the applications in the relatively shorter wavelength region of 2 ~ 5 μm. This is because the discontinuity, ΔE_c, between the barrier and well layer must be much higher than the inter-subband transition energy in order to avoid electron leakage from the QW [9]. On the other hand, by using the type-II broken-gap heterostructure, a new class of cascade lasers has been proposed: the interband QC laser which is based on electron-hole transition [64]. So, mid-IR QC lasers can be divided into two types: inter-subband and inter-band QC lasers as presented below.

In inter-subband QC lasers, the optical gain is received through electron-electron transitions in CB [65]. By resonant tunneling through a potential barrier, electrons are injected into the upper state of the laser transition region and electrons in the lower energy state tunnel away from the well region to realize the population inversion. The shorter wavelength inter-subband QC lasers are promising with increasing the CB band discontinuity by using GaSb substrate based InAs/AlSb material system [66], InP substrate based InGaAs/AlAsSb material [67], or the strain compensated MQW structures [68, 69]. Till now, to our best knowledge, the shortest wavelength from inter-subband QC structures is 2.5 μm due to the very large CB band discontinuity of 2.1 eV between InAs and AlSb [66]. However, it is only the spontaneous intersubband emission. In terms of the laser emission, the shortest wavelength reported so far is ~ 3 μm which is based on the lattice matched

$In_{0.53}Ga_{0.47}As/AlAs_{0.56}Sb_{0.44}$ grown on InP [67]. The strain compensated MQW engineering has also been used in QC structure design with the lasing emission wavelength reported at 3.4 - 3.6 μm [68, 69]. However, when the lasing wavelength is shortened, the device performance degrades. One reason can be related to the increased influence of interfaces in the structures with reduced thickness of the QW layers, where even very small fluctuation in layer thickness can cause intervalley scattering under device operation conditions thus reducing device performance [66, 67]. On the other hand, inter-subband QC lasers with longer wavelengths of 4 - 5 μm in mid-IR region have been reported largely [70 - 74]. Till now, the maximum CW operation temperature of mid-IR emissive (2 - 5 μm) inter-subband QC lasers has been reported to reach above 333 K with the single-mode emission wavelength of 4.8 μm [72]. This is realized by integrating distributed-feedback technology using buried gratings with the high-power Fabry-Perot QC lasers. However, one common factor limiting the performances of inter-subband mid-IR QC lasers is the fast (with the order of 1 ps) carriers' nonradiative relaxation between the sub-bands via optical phonon scattering, which leads to low radiative efficiency and substantial heating of the devices.

In order to overcome the difficulty of the optical phonon scattering in inter-subband QC laser structures, inter-band QC laser structures were proposed [75]. In inter-band QC laser structures, the optical gain is realized through the resonant inter-band tunneling in a type-II broken-gap QW structure [64]. By using inter-band QC structures, the fast phonon scattering is suppressed due to the opposite dispersion curvatures of the electron and hole states. A strong spatial inter-band coupling and the optical transitions between electrons and light holes have been received. The shortest wavelength from interband QC lasers reported so far is 3.3 μm with CW operation temperature up to 212 K, which is based on Sb-based material system [76]. The longer wavelength from 3.6 to 4.7 µm interband QC lasers has also been reported [77 - 80]. Till now, Very good performance of mid-IR emissive, 4.1 µm, inter-band QC lasers has been reported with the maximum CW operation temperature up to 269 K [78]. To reduce the threshold current density, inter-band QC lasers with "W" QW structures by inserting InAs QWs between the GaInSb and AlSb barrier layers in each active region have been developed. Threshold current density of such QC lasers emitting at around 3.5 µm was reduced to 13.2 A/cm^2 under CW operation at 80 K [81], and that of the 3.6 µm lasers was as low as 9 A/cm^2 under pulse operation at 78 K [82].

In summary, QC mid-IR lasers offer various cascade structures engineering to optimize the laser performance through improving the carrier transport, suppressing nonradiative processes and internal absorption losses. It is advantageous for performance QC mid-IR lasers to achieve long mid-IR, e.g. > 3.5 µm, injection lasers. However, it is a big challenge to develop QC lasers for shorter wavelength, e.g. < 3.5 µm, applications, due to the difficulty in enlarging CB band discontinuity. Although, by combining using conventional high band gap semiconductors (Al(Ga)As) with low band gap nitride-dilute III-V alloys (In(Ga)AsN), CB band discontinuity between these semiconductors could be enlarged when the nitrogen composition is increased. However, it is still difficult presently to grow high crystal quality III-V-N alloys especially with high nitrogen composition [83].

So, in terms of the practical applications in different wavelength regions, lasers with QW active region are promising for relatively shorter mid-IR region (2 - 3.5 µm) applications, and QC structures are promising for relatively longer mid-IR region (3.5 - 5 µm) applications. However, QW and QC active region structures are similarly based on the thin well layers. When the well thickness is thin enough to be comparable with the de Broglie wavelength of an electron in a semiconductor (~ 10 nm), a structure with carriers confined in one-dimension known as a QW is obtained. In such a structure, carriers are confined in the direction perpendicular to the well plane (*z*-direction) by the potential barriers, resulting in a structure having discrete quantized energy levels. Along the well plane (*x*-*y* plane), the crystal is assumed infinite. Generally, density of states (DOS) is used to describe how closely the energy levels are packed in the structures of DHs, QWs, QWRs and QDs. The DOS of carriers in the QW is modified from the conventional $E^{1/2}$-dependence for bulk material to a step-like dependence as shown in Figure 2.2-(a) and -(b) [84, 85]. By increasing the confinement of carriers in the other directions (*x* and *y*), systems with lower dimensions can be obtained: quantum wire (QWR) and quantum dot (QD) with carriers confined in two and three directions, respectively. Especially, when the carriers are confined in three directions as in QD structure, the DOS presents with δ-function-like dependence as shown in Figure 2.2-(d). The main advantages upon

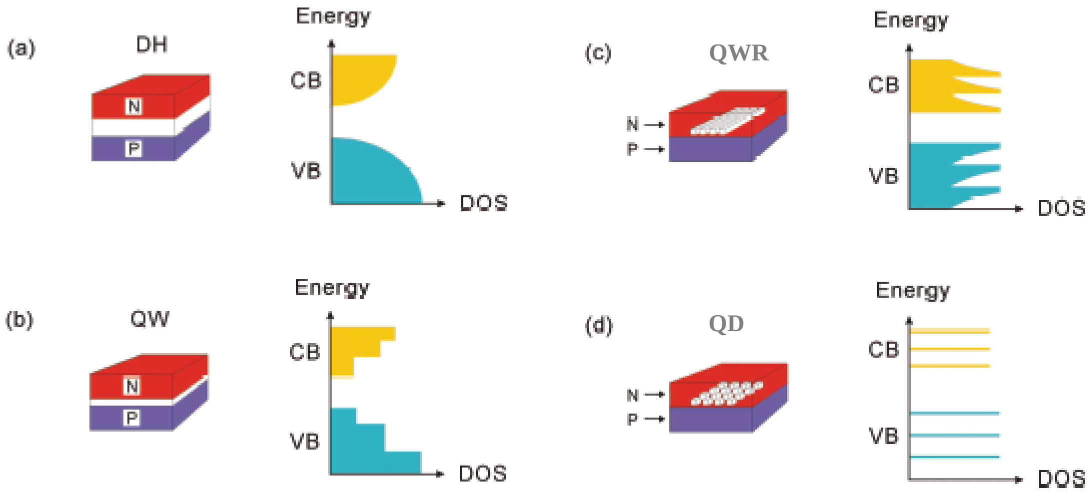

Figure 2.2 Schematic diagrams of the DOS in the CB and VB for (a) DH, (b) QW, (c) QWR, and (d) QD laser.

introducing the lower dimensional QWR and QD as the active medium of a semiconductor laser over conventional QW lasers is the improvement in laser's threshold current density, modulation speed and temperature insensitivity [86 - 88]. In the following, a short survey on QWR structures applied in mid-IR region has been presented before the focus on the topic of QD structures.

QWR, as a low dimensional structure with a wire-like characteristic, needs different growth techniques compared with the QW growth. QWR can be formed in template channels within the porous material [89], or by selective deposition [90]. In general, these approaches yield reasonable control over the diameter of QWRs, but produce unwanted polycrystalline or amorphous material. The second method for preparing high quality QWRs is through thin film and lithography techniques based on the "T-wires" technique [91]. Another commonly used method is based on strain-driven self-assembly. Self-assembled InGaAs [92] and GaAs [25] QWR lasers grown on (775)B-oriented GaAs substrates have been reported. So far, there is no reporting on QWR mid-IR lasers. A theoretical analysis predicated the peak emission wavelength of a GaAs/AlGaAs QWR structure could reach around 5 μm through the transitions between the conduction subbands, i.e. between CB11 and CB21 of the structure [93]. Besides, quantum dash (QDH) is also a low dimensional structure. QDH is an elongated nanostructure, whose cross section is similar to that of a shallow QD, several nanometers × several tens of nanometers, while its length hundreds of nanometers. The InAs/InP QDH structures have been demonstrated to have QWR-like characteristics [94]. There are very few reports on using QDH as reactive region in mid-IR lasers. InP based InAs QDH laser was reported lasing at 2.03 μm with $T_0 = 43$ K, where InAs QDHs were formed by using strain-driven self-assembly method [26]. The internal loss of this laser is as high as 55 cm^{-1}, which is attributed to the local undulations of the refractive index near the QDHs induced by the phase separation during growth. So, lower dimensionality in QWR/QDH active medium instead of QW is advantageous in improving the laser performance, but the difficulty in forming high quality, i.e. uniform in composition/size/interface, QWR/QDH structures restricts the practical improvement in QWR/QDH lasers' performance.

2.3.3 Quantum dots

From the above discussions, we can see that the major improvements in semiconductor laser technology lie in the improvements in carrier confinement and optical mode confinement. For instance, the use of DH to improve both carrier confinement and optical mode confinement in the late 60's and early 70's [95] made the commercialization of diode lasers possible. The employment of a QW gain media started from the mid 70's. It confines carriers by reducing the physical space volume [96]. Today, diode laser technology based on QW or DH active regions are common. However, the use of three-dimensional confinement QDs as laser's active region has introduced many new laser properties.

Compared with QW and DH lasers, QD lasers are expected to present with: **(i)** *Low threshold current density*. The much reduced δ-function-like DOS and smaller physical volume of the active material means that fewer carriers are needed to invert the quantum dots resulting in extremely low threshold current densities [86, 88]. **(ii)** *High speed modulation*. The δ-function-like DOS results in both high material gain and high differential gain. As described in Ref. 97, both these factors contribute to a high modulation bandwidth. **(iii)** *Reduced temperature dependence.* The δ-function-like DOS in QDs suppresses the scattering of carriers in momentum space. The reduced carrier scattering implies that temperature has less effect on laser performance. **(iv)** *Zero linewidth enhancement factor*. The linewidth enhancement factor is the ratio of the change of the real part to the change of the imaginary part in the refraction index with carrier density. The δ-function-like DOS can be modeled as a symmetric Gaussian function. Such a function describes the imaginary part of the refraction index, and through the Kramer-Kronig relation, has a zero linewidth enhancement factor. This implies no chirp of the lasing wavelength upon modulation of the carrier density and no tendency for the formation of filaments in high-power laser diodes.

Due to a great performance improvement expected from QD lasers, using QDs instead of QW as the active region in laser structures has attracted much interesting since the demonstration of first QD laser in 1994 [27]. Moreover, the QD based devices have the advantages in densely packed laser arrays and monolithic integration of lasers with low-power electronics, which has many important applications and attracts strong research interest in optical interconnects, quantum computing, and integrated optoelectronic circuits, etc [98 - 101].

When it comes to the mid-IR semiconductor QD lasers, till now, only one research group reported the QD lasers emitting near 2 μm based on (001) InP substrate [102], where single-layer self-assembled InAsSb QDs were used in the active region. The laser can operate under CW mode up to 25 °C. But the threshold current density is 730 A/cm^2, which is much higher than the 32.5 A/cm^2 achieved from the InAs/GaAs QD laser emitting at 1.25 μm [103]. One of the main reasons for so few reports on mid-IR QD lasers and the limited InAsSb QD laser performance as reported is due to the difficulty in preparing high crystal quality and narrow size dispersive mid-IR emissive dots by MOCVD or MBE. Compared with the relatively matured growth of InAs QDs on GaAs substrate, technology on the growth of mid-IR emissive InAs(Sb) QDs on InP substrate is still not mature. Considerable effort is required to develop InAs(Sb) QDs for the practical applications [104, 105]. Accordingly, most of the mid-IR QDs related research till now is still on the stage of developing the growths of high quality mid-IR QD structures.

Low band gap material such as InAs and InSb binary compounds or InAsSb, InGaAs, InAlAs and InAsP, etc, ternary alloys have been used to form the QDs on the InP substrate for mid-IR emissions. Using InP as the substrate for mid-IR QDs is because the device process technique of InP based material system is mature, the energy band gap of InP is suitable when used as the cladding layer in the mid-IR laser structures, and the lattice mismatch between InAs (or InAs-rich alloys) and InP substrate is suitable for forming QDs with proper size. For example, InAlAs [106], InGaAs [107], InAsP [108], InAsSb [102, 109], InSb [110] and InAs QDs [12, 111, 112] for mid-IR emission have been investigated. But for most of these QDs, the emission wavelength is limited around 2.0 μm. III-V dilute nitride alloys QDs are expected to extend their emission wavelength to mid-IR region because of the bowing effect on the energy band gap of III-V semiconductors by introducing nitrogen in them. However, growing high quality material of these new alloys is still a big challenge as mentioned previously. Another method to develop the QDs for mid-IR emission is to redshift the QDs' emission wavelength by adjusting the strain/barrier in QD structures. Different approaches have been engaged to extend the emission wavelength of InAs/GaAs QD structures for optical communication applications [113,114,115,116,117,118], which include inserting a strained Ga-rich InGaAs layer between InAs QDs and GaAs buffer layer [116], capping an InGaAs layer on InAs QDs [113, 115, 117], and embedding InAs QDs between strained InGaAs or GaAsN barrier layers [114, 118], etc. On the other hand, InAs/InP QD structures are expected to be used for mid-IR, 2 ~ 5 µm, applications by sandwiching InAs QDs between In(Al)GaAs confinement layers. However, InAs QDs grown on In(Al)GaAs/InP matrix are generally with low dot density and large dispersive size distribution [12, 13, 119, 120]. The low dot density is mainly caused by the reduced strain between InP and InAs with comparison to that between GaAs and InAs. Non-uniformity in dot size is mainly due to the nucleation process in the conventional SK QDs self-assembly method. In the conventional SK method, the growth procedures of nucleation, island growth till the final dot formation are generally completed under the same growth conditions. This limits the further optimization in QD formation. All these restrict the mid-IR InAs/InGaAs/InP QDs device development. In addition, the reported longest interband transition based emission wavelength from InAs QDs is only 2.1 µm till now, where the InAs dots are grown on $In_{0.53}Ga_{0.47}As$/InP matrix [12]. The constant band gap of $In_{0.53}Ga_{0.47}As$ barriers used in the InAs QD structures makes it difficult to extend the dots' emission wavelengths further, which restricts InAs QDs' applications in the mid-IR field. In order to develop mid-IR QDs devices, how to grow higher quality and longer wavelength mid-IR QDs becomes urgently needed. Correspondingly, the two challenges of how to grow InAs QDs on InGaAs/InP matrix with high dot density and narrow dot-size dispersion, and how to extend the emission wavelength of InAs/InGaAs/InP QD structures to > 2.1 µm become the main research topics of this PhD project.

2.4 Summary

This chapter first presents why to select III-V semiconductor material for mid-IR device applications. Then, a detailed literature survey is provided on the development of III-V semiconductor mid-IR lasers based on different active region structures, from multiple dimensional DH structures to low dimensional QW/QD structures. Finally, based on the literature review and current situation, the work to develop zero dimensional QD structures for mid-IR emission application is proposed as the main subject for this PhD project.

CHAPTER 3. TECHNOLOGIES FOR QDs STUDY

3.1 Introduction

In this chapter, epitaxy technology of metal-organic chemical vapor deposition (MOCVD), which is used for growing the QD structures in this research project, is introduced. Then, self-assembly growth of QDs is discussed. Four characterization methods of atomic force microscopy (AFM), photoluminescence (PL), Transmission Electron Microscope (TEM) and x-ray diffraction (XRD) are presented. Finally, sample process technologies of inductively coupled plasma (ICP) and rapid thermal annealing (RTA) are also introduced.

3.2 MOCVD epitaxy technology

MOCVD is the most versatile thin film deposition technology for compound semiconductors epitaxy growths. It is also referred to as Metalorganic Vapor Phase Epitaxy (MOVPE). The acronyms OMCVD and OMVPE have also been used with the OM standing for organometallics. Besides, generally used AP-MOCVD stands for atmosphere MOCVD, LP-MOCVD stands for low pressure MOCVD. MOCVD growth technique was developed at the end of the 1960's [121]. It is a variant of vapor phase epitaxy technology where metalorganic compounds are used as precursors. MOCVD is now a widely used deposition process in both research and commercial production activities. It has demonstrated growth capability for state-of-the-art electronic devices such as laser diodes, LEDs, photodetectors, solar cells, field effect transistors (FETs), high-electron-mobility-transistors (HEMTs) and heterojunction-bipolar transistors (HBTs), etc.

In this work, a quartz horizontal reactor of LP-MOCVD system

(AIX200(#1499)) developed by AIXTRON Corporation. It consists of three main parts: precursors and gas handling system, MOCVD reactor with Filmetrics *in-situ* growth monitoring system, and vacuum and exhaust system. In the following, first two parts will be given detailed introduction. The system is fully computer controlled. Figure 3.1 shows the system photo.

Figure 3.1 The MOCVD system under the growth process.

(i) *Precursors and gas handling system*

In order to improve the process safety and cut down the cost at the same time, the inert gas, nitrogen, is used as the carrier gas to replace the hydrogen in our system. The material quality of epitaxial layers/structures by MOCVD using nitrogen as the carrier gas has been proved to be comparable to that of layers/structures grown with hydrogen [122, 123]. Besides, the higher degree ordering in GaInP growth [124] and increased AlGaAs layer homogeneity [125] by using nitrogen carrier gas instead of hydrogen have been demonstrated. The increased layer uniformity in nitrogen is attributed to the enhanced growth rate uniformity due to the larger inertia of nitrogen carrier gas and the reduced diffusion coefficients of chemical species in nitrogen. On the other hand, MOCVD process generally uses high toxic hydrides AsH_3/PH_3 as group V-precursors. For safety reasons, organic-arsines tertiarybutyl-arsine (TBA) and tertiarybutyl-phosphine (TBP), which are less toxic and have higher decomposition efficiency, have been used as replacements for arsine and phosphine in MOCVD growth [126, 127]. Devices made from structures grown with TBA exhibit state-of-the-art performance [128].

The function of gas handling system is mixing and metering of the gases that enter the reactor. Timing and composition of the gas entering the reactor determine the epilayer structure grown. For safety and to achieve growing structures' high properties by preventing oxygen contamination, fully leak-tight stainless steel tubes are used to transfer metalorganics (MO) from the sources to either the reactor chamber or the vent. The ultrahigh purity (99.999% pure) N_2 is passed through a SAES Pure Gas N_2 purifier (PS4-MT3-N-2) to remove any oxygen, water, hydrocarbons, and other impurities. Compressed air controlled valves are used to fast switch on or off the gas flows to ensure the growth for thin film with abrupt interface and QD structures, and the flow rates of the source are controlled by mass flow controllers (MFC) and pressure controllers (PC) to keep growth versatile and stable. Fifteen metalorganic sources are connected to the reactor in our system: five group III sources are two trimethylindium (TMIn), two trimethylgallium (TMGa), one trimethylaluminium (TMAl) sources; six group V sources are two TBAs, one TBP, one trimethylantimony (TMSb), one trimethylbismuth (TMBi) and one DMHy sources; four adulteration sources including one trimethylarsine (TMAs), one dimethylzinc (DMZn), one ferrocene (Cp_2Fe; Cp is not a element, but the shorthand for cyclopentadienyl anion or $C_5H_5^-$) and one SiH_4 are used. For this particular application of our project, TMIn/ TMGa lines for providing group-III sources and TBAs/TBP lines for group-V sources are used to grow the InAs/GaAs and InAs/InGaAs/InP QD structures. All the MO sources are stored inside bubblers and their temperatures are controlled by LAUDA thermostats. The pumps of LAUDA thermostats pump the heat carrier (bath liquid) through the heat exchanger of the through-flow cooler. To lower the source temperatures, the through-flow cooler continuously cools down until to the set source temperatures and then the thermostat maintains the required temperatures by means of controlled counter-heating. The amount of the MO sources transported from the bubblers to the reactor is determined by the source vapor pressure, carrier gas flow rates and the total pressure inside the bubblers, which are controlled by the thermal bath temperature, MFC and PC. If the flow rate is not very high, the equilibrium evaporation condition can be assumed inside the bubblers, thus the source flow rate (κ) is given by:

$$\kappa = \kappa_{Total} \frac{P_{MO}}{P_{Bubbler} - P_{MO}}, \tag{2.1}$$

where P_{MO} is the partial pressure of the MO source inside the bubbler which is the function of source temperature and can be found from charts provided by the MO manufacturer. In the equation (2.1), it is assumed that the MFCs are connected to the inlet of the MO source bubblers.

(ii) *MOCVD chambers*

Shown in Figure 3.2 is a schematic of the MOCVD chamber of the system used in this research. It consists of reactor, glove box, transition box and an attached Filmetric. The reactor is a horizontal quartz tube with 18 mm in height and 25 mm in diameter. Inside the reactor tube a graphite susceptor is used to put wafer for growth. It is 15 mm in height and 20 mm in diameter. The susceptor is connected to a linear sample translator that provides a means of shuttling substrates/samples between the quartz duct and the glove box at the end of the reactor. The glove box is adjacent to but separated from the reactor by a gate valve. Before and after growth, the substrate loading and sample unloading are performed inside the glove box while it is isolated from outside by a transition vacuum box, which is good for the safety of the operator and also prevents contamination of the MOCVD chambers. The substrates are mounted in a molybdenum sample sled, and the sled rests on a longitudinal slot cut into the susceptor. During growth, the sample rotates at a speed of 50 rpm so that epilayers grown are with extremely uniform composition and thickness. An 800 W infrared lamp located below the reactor tube is used to heat the sample to the desired temperatures, which is around 500 ^{o}C for growing the InAs QDs. The top wall of the reactor is cooled by and aluminum heat exchanger supplied with chilled water. The heat exchanger is required to reduce undesired deposition of the MO precursors on the reactor walls. During deposition, nitrogen purge flow enters the reactor at one end of the sample manipulator. The MO compounds are introduced into the reactor at beginning of the quartz tube. In order to avoid the gas phase reaction between sources, the group III and group V/adulteration sources are transferred to the growth chamber separately. At the top flange of the reactor, they are mixed and uniformly pushed through the stainless steel meshes into the growth chamber. The precursors mix with

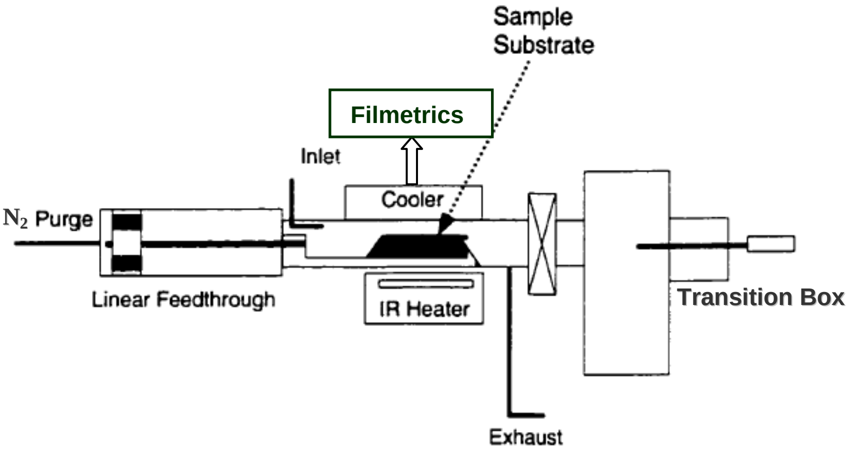

Figure 3.2 Schematic diagram of the MOCVD chamber.

the N_2 purge gas and then flow over the heated substrate. The reactor pressure can be maintained at 20 mbar to 500 mbar during the growth process by a BARATRON gauge and exhaust control valve installed at the end of the quartz tube. The Filmetrics F30 is a spectral reflectance system that *in-situ* measures the thickness and optical constants of thin film layers deposited on substrates. The system is PC-based and integrates measurement and analysis software with a spectrometer and fiber optic measurement hardware.

To take the InAs layer growth as the example, the major processes included in MOCVD growth in the reactor are shown in Figure 3.3. The complicated processes at the growth interface are determined by the growth temperature, growth chamber pressure and the partial pressures of each source, etc. A description of the overall growth process becomes very complicated due to a complex interplay between gas-phase and surface chemistry as well as hydrodynamics. A general categorization into different MOCVD growth regimes can be made [129] based on whether the growth

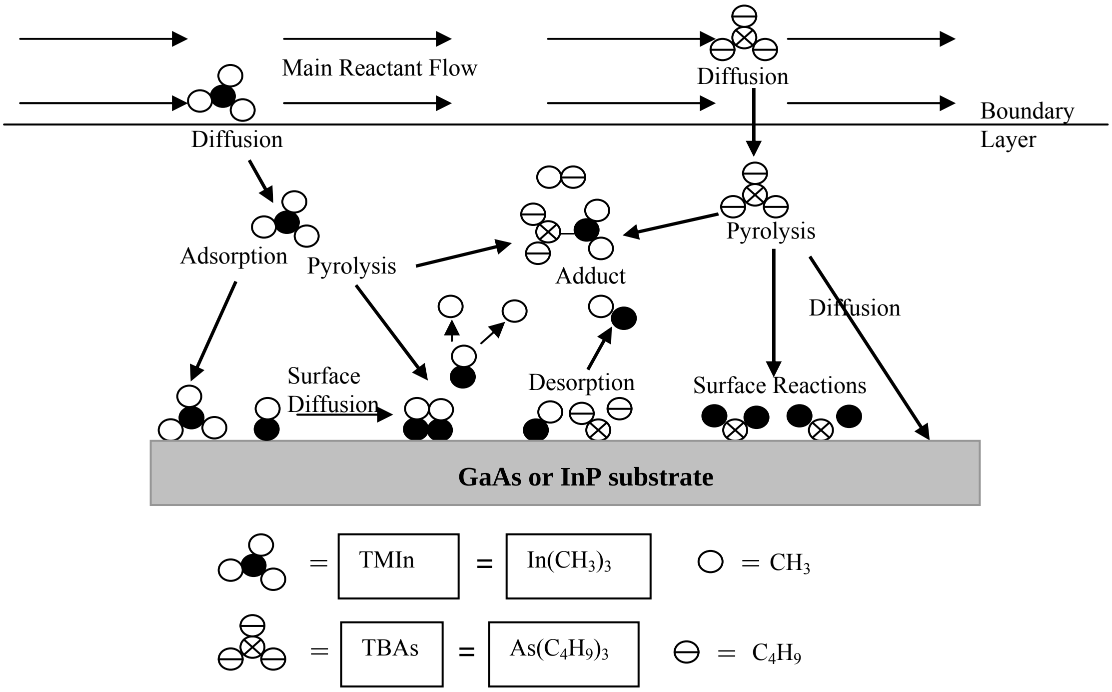

Figure 3.3 Schematic diagram of the growth process in the MOCVD reactor.

rate is limited by surface kinetics or mass-transport (applicable to the growth temperature < 800 ^{o}C). At conventional growth temperatures of 600 - 800 °C the MOVPE process is mass-transport limited, so that, to first order, growth rate and group III composition control is dependent mainly on the input partial pressure of the group III MO reactants in the reactor. In this regime the surface reactions are relatively fast, and the limiting step is the arrival flux of reagents by diffusion through a mass transport boundary layer above the heated susceptor. In contrast, for certain applications it is necessary to slow down the kinetics by lowering growth temperature (< 600 °C) as in growths of highly strained QDs. However, low reactor temperature induces the surface-kinetics controlled growth regime. This weakens the dependence of layer growth rate on the input srouce flux, and sometimes comes with unwanted complications related to the incomplete source pyrolysis and by-product desorption. For example, the growth rate of InAs is temperature dependent over a large temperature interval in the mass transport temperature regime. But, at low temperatures (< 500 °C), the growth rate of the InAs layer is mainly dependant on the surface reaction rate but not on the input source flux. In this case, an effective way to increase the layer thickness is to prolong the growth time not to increase the input source flux. The surface reaction rate is affected by multiple factors, including the diffusion of the adsorbed species on substrate surface, the incorporation of the constituent elements into the crystal lattice, and the desorption of the reaction by-products, etc. For QD growth, diffusion length reduction of MO reactants at low temperature is advantageous to increase QD density. However, the crystal quality of the QD layers degrades due to the incomplete source pyrolysis and/or incomplete by-product desorption. To develop QDs for laser applications, the high performance, i.e. high crystal quality and high density, QDs are needed. So, the growth temperature cannot be too high or too low in order to receive high performance QDs. As a balance, the temperatures in MOCVD reactor for the growth of QDs layer in QD laser structures are generally set at around 500 - 550 °C as reported [130 - 132]. Also, this is main temperature range for InAs QDs growth in this work. On the other hand, MOCVD growth of the high crystal-quality GaAs or InP cap layer in QD structures needs $\geq$ 550 °C reactor temperature. However, direct reactor temperature ramping-up after QD layer growth will destroy the dots formed due to the evaporation. So, in order to protect the formed QDs and also improve the cap layer crystal quality, a very thin covering layer is generally deposited at the same temperature as that for QDs growth before increasing the temperature for the cap layer deposition.

In addition, we have studied the stability of our MOCVD system on QDs growths and found that the system is well stable in re-producing the QDs in terms of the dot morphology and crystal quality. This guarantees the validity in studying/comparing QD's morphologies throughout the MOCVD epitaxy development for forming higher quality QDs by optimizing the growth conditions.

3.3 Self-assembly growth of QDs

Totally, there are two approaches for QDs preparation. One is based on the patterning with electron beam lithography. The other is the self-assembly method. In the first method, the electron beam lithography is used to pattern the nanostructures [133, 134]. The advantage of the patterning method is to produce the QDs with uniform size. However, this method is difficult to produce high density QDs and is expensive to pattern so with a time consuming and low yield process. Self-assembly method of growing III-V semiconductor QDs is realized by depositing the lattice mismatched material on the host substrate. Driven by the lattice-mismatched strain between the deposited material and the substrate, the deposited material, after several monolayers (MLs) deposition, will nucleate, grow into islands and the final QDs. Compared with the patterning method, the self-assembly method has the following two obvious merits. First, self-assembly method has been successful in preparing QDs with high density of dislocation-free nanostructures [135, 136]. Secondly, self-assembly is also more economical. So far, the best semiconductor QD devices reported were received by using self-assembly QDs method instead of using electron bean lithography patterning method [137, 138]. However, the challenge of self-assembly method is to grow QDs with high crystal quality and uniform size, which is one of the main factors restricting the performance improvement of QD devices.

In this research project, self-assembly method is used to form the InAs QDs on GaAs or InP substrates. In the following, the self-assembly QDs growth mode will be introduced with thermodynamic treatment. In III-V semiconductor heteroepitaxy, to take InAs/GaAs as the example, the chemical potential at the InAs/GaAs interface is higher than that of the bulk crystal due to the lattice mismatch and chemical composition difference. The chemical potential of each subsequent monolayer $\mu(n)$ from the interface are mainly dependant on the desorption energy of deposited material, the misfit dislocations and/or the homogeneous strain arising from the lattice mismatch, which can be approximately described with the expression [139, 140]:

$$\mu(n) = \mu_\infty + [\varphi_a - \varphi'_a(n) + \varepsilon_d(n) + \varepsilon_e(n)] \tag{3.1}$$

where μ_∞ is the chemical potential of the infinitely thick crystal, i.e. bulk crystal, of the deposited material; φ_a is the desorption energy of the bulk crystal, and $\varphi'_a(n)$ is the desorption energy of the grown material after n-monolayer deposition; $\varepsilon_d(n)$ is the energy of misfit dislocations and $\varepsilon_e(n)$ is the energy of the homogeneous strain between the deposited material and the host-substrate. The major three growth modes

(Figure 3.4), which are mainly dependant on the lattice mismatch degree between the deposited material and host substrate, can be derived from the expression.

Frank-van der Merwe growth: The chemical potential of the deposited material $\mu(n)$ is dependent on the atomic distance between the deposited layer and the substrate. Considering the very small lattice mismatch between the deposited material and substrate, $\varepsilon_e(n) << \mu_\infty$ is received. If the first monolayer of the deposited material adheres better to the substrate than to itself, we receive $\varphi'_a(1) > \varphi_a$, and then $\mu(1) < \mu_\infty$ based on equation 3.1. Here, no misfit dislocation in the interface is assumed, so with $\varepsilon_d(n) = 0$. When the deposited layer thickness, i.e. the number n, increases, the desorption energy of the deposited material $\varphi'_a(n)$ approaches that of bulk crystal φ_a. As a result, the $\mu(n)$ approaches μ_∞. So, the chemical potential increases continually till reaches the bulk crystal level. This is the thermodynamic case of Frank-van der Merwe (FM) epitaxial growth. The chemical potential as function of the monolayer thickness of this growth mode is shown in Figure 3.5 after Sotyanov *et al.* [141]. In this growth mode, layer-by-layer growth occurs since the lower layer is energetically favored to complete before the subsequent layers above it [142]. Examples of FM

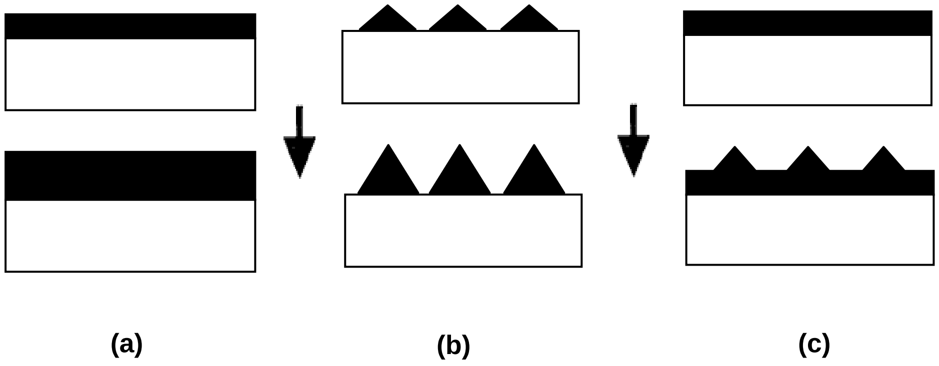

Figure 3.4 Schematic diagrams of three growth modes for heteroepitaxial systems: (a) Frank-van der Merwe layer-by-layer growth, (b) Volmer-Weber direct 3-D island growth and (c) Stranski-Krastaanow layer-by layer followed by 3-D island growth.

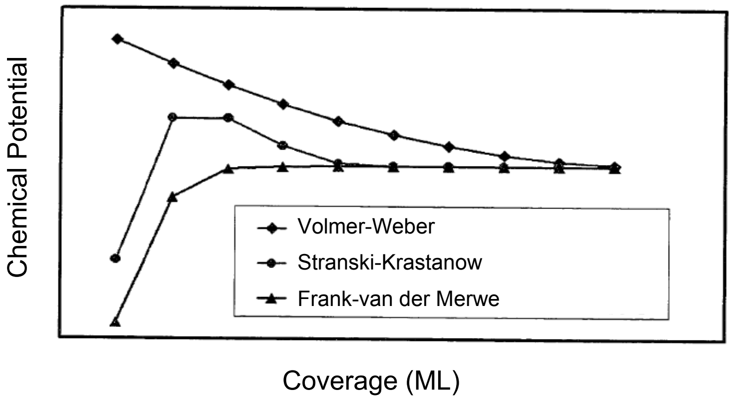

Figure 3.5 Chemical potentials for Frank-van der Merwe, Stranski-Krastanow and Volmer-Weber type growth as a function of monolayer thickness.

growth include the epitaxy of $Al_xGa_{1-x}As$ on GaAs, low Indium compositions of $In_xGa_{1-x}As$ on GaAs, low Arsenic compositions of $InAs_xP_{1-x}$ on InP, and $In_{\sim0.53}Ga_{\sim0.47}As$ on InP so on. So, this layer-by-layer growth mode is not applicable to the QDs growth.

Stranski-Krastanow growth: If the lattice mismatch induced homogeneous strain between the deposited material and substrate is substantial and significant as compared to μ_∞, so that 3-D islands formation occurs after a few monolayers layer-by-layer growth. In this case, $\varphi'_a(1) > \varphi_a$, and then $\mu(1) < \mu_\infty$ is received with assuming $\varepsilon_d(n) = 0$ and a small $\varepsilon_e(1)$ (see equation 3.1). When the deposited monolayer increases, the accumulated strain, $\varepsilon_e(n)$, increases quickly, and $\varphi'_a(n)$ approaches φ_a. Upon reaching a critical coverage ($n = n_{critical}$), $\varepsilon_e(n_{critical})$ increases to a maximum level, thus $\mu(n_{critical}) > \mu_\infty$. If the layer deposition continues, i.e. $n > n_{critical}$, $\varepsilon_e(n)$ starts to decrease with strain partial relaxation by coherent 3-D island formation. Correspondingly, the chemical potential increases initially with the deposited layer thickness as the FW growth mode (see Figure 3.5) till reaching the maximum level at the critical coverage, and then lowers down to μ_∞ with the deposited layer increase further. The critical coverage is the thickness at which the 2-D film to 3-D island growth transition occurs. This is called the Stranski-Krastanow (SK) self-assembly growth mode [143], where an initial layer-by-layer (2-D) growth is thermodynamically favorable before 3-D growth occurs. In this project, the InAs QDs formation on GaAs or InP substrate is just based this growth mode.

Volmer-Weber growth: If the misfit is large enough and the interfacial bonding between the deposited film and the substrate is weaker than the bonding in the deposited film itself, so that the very first layer cannot maintain a strained layer but instead immediately initiates a dislocation interface. In this case, $\varphi'_a(1) < \varphi_{a,}$ and $\varepsilon_d(1) >> 0$, then $\mu(1) > \mu_\infty$ with assuming the $\varepsilon_e(1) = 0$. So, the chemical potential as function of the monolayer coverage is with a negative slope, i.e. a decrease of $\mu(n)$ with increasing the monolayer number n (see Figure 3.5). The chemical potential of the subsequent layers only depends on the atom interaction distance from the dislocation layers. This leads to immediate island growth, i.e. the formation of the subsequent layers occurs before the completion of the preceding layers. This is a mode called Volmer-Weber (VW) mechanism [144].

Among the three growth modes, VM and SK modes could be applied for 3-D QDs growth. The specific growth mode depends on the mismatch magnitude between QDs material and substrate. If the mismatch is too large, > 10%, the strain is difficult to be accommodated elastically by 3-D islanding, and much of it is dissipated from the inclusion of misfit dislocations between island-substrate interfaces. These misfit dislocations are disruptions in the lattice created in order to accommodate the material mismatch. Such QDs are said to be incoherent just as the schematic diagram shown in Figure 3.6 (a). The VM mode of growing QDs belongs to this type. Till now, few researchers reported VM mode for semiconductor QDs growth, and the reported QDs were with low optical performance due to the dislocations contained in the dots [145].

When the mismatch strain between QDs and host substrate is proper, i.e. in the range between 2% and 10%, the strain induced SK self-assembly growth mode will dominate. Islands generated after critical thickness deposition of strained layer on host substrate. The thin grown layer on substrate self-assembled into defect-free 3-D islands to minimize the total energy of the layer with reducing the strain energy. However, the nucleation of islands also increases the surface area so as to increase the surface energy, thus providing an opposing force favoring a flat layer. As the thickness of the grown layer increases, these two forces exert varying degrees of influence on the deposited film. In the first stage, the strain energy is low because of the thin deposited layer. The driving force reducing surface energy dominates, and the layer remains flat. After a certain thickness, the strain energy dominates and the layer tends to 3-D island self-assembly growth. The transition from a quasi-stable thin film to self-assembly islands is often called the 2-D to 3-D transition. Within this second stage, the increase in thickness past the 2-D to 3-D transition corresponds to an increase in the density of the QDs. These QDs are defect-free and are called coherent

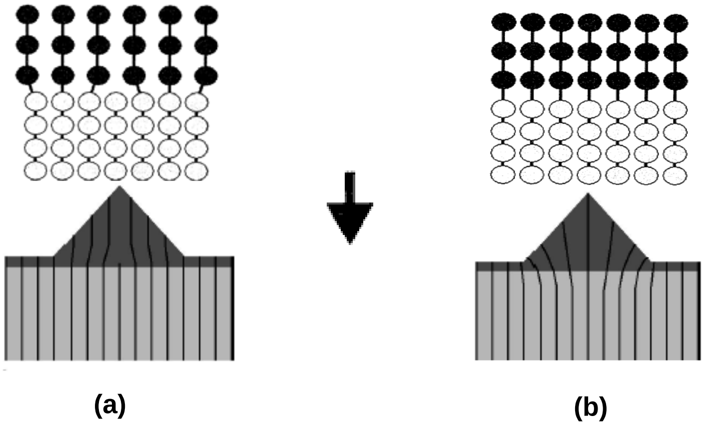
(a) (b)

Figure 3.6 (a) A relaxed island of larger lattice spacing with incorporated dislocations, and (b) A pseudomorphic coherently strained island of material with larger lattice spacing than substrate.

QDs as shown in Figure 3.6 (b). The SK growth of QDs, most intensively studied till now, belongs to this growth mode. However, if the inlet QD material is too much, the third stage begins. In this stage, self-assembly islanding can no longer accommodate the strain. Misfit dislocations begin to appear between island-substrate interfaces, and the QDs will become incoherent. These incoherent QDs have therefore much lower energy than their neighbor, quickly consume the surrounding QDs and become larger islands which is also called ripening process. So, control of QDs material inlet is also important for coherent QDs growth. But till now, it is still challenging to make the mid-IR QDs with uniform size/shape and with high density and crystal-quality by using this conventional SK self-assembly method as mentioned above. Much of the research work is needed further for better understanding and then renovating the conventional SK self-assembly method so that higher quality QDs can be formed.

3.4 Characterization technologies

In the following, AFM, PL, TEM and XRD four characterization technologies are introduced subsequently. When we use these technologies to characterize the studied samples in this work, we are always keeping making the received results reliable. For it, we keep on double-checking the results from one sample by doing the same measurement at least twice at two different locations on one sample, so to figure out the typical/average results as that presented in the thesis.

(i) *Atomic force microscopy (AFM)*

AFM is one of the surface probe microscopic techniques. It has many applications in analysis of the surface property. It can be used to analyze the morphology, size and density of nano-particles; it can also be used to obtain the surface depth of the scanned area. In addition, in terms of the sample preparation, AFM can image the conducting samples and also the insulators with no need to coat them with conductive films, thus with a very easy sample preparation. So, a wide variety of organic, biological and inorganic samples can be studied in a straightforward manner. Another important potential of AFM for surface chemistry is its capability to perform *in-situ* measurements under liquids and in air. However, it should be mentioned that one shortcoming of AFM is the fact that the chemical information or material specific properties cannot be obtained from AFM images directly [146]. In this study, the tapping-mode AFM, Nanoscope IIIa, is used to characterize the surface morphology, including dot-density, dot-size and size distribution, etc, of the InAs QDs grown on GaAs or InP substrates.

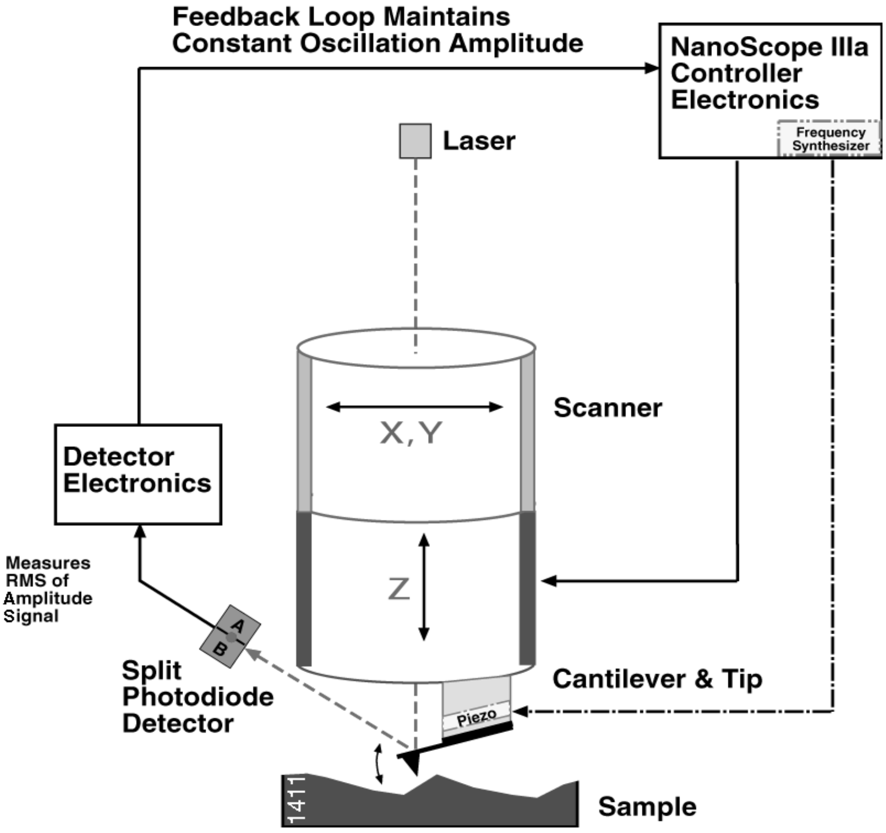

Figure 3.7 Schematic diagram of the tapping mode AFM .

The schematic diagram of the tapping-mode AFM is shown in Figure 3.7. Tapping-mode AFM operates by scanning a tip attached to the end of an oscillating cantilever across the sample surface, where the tip intermittently contacts (taps) sample surface during the measurement. The cantilever oscillates at or near its resonance frequency with an amplitude ranging typically from 20nm to 100nm. During the scanning, the probe-tip lightly taps the sample surface, contacting the surface at the bottom of its swing (See Figure 3.7); and the sample is kept constant in vertical position and is scanned in the lateral direction. A laser beam is reflected from the tip to the split photodiode detector for monitoring the cantilever deflection according to the shapes of the sample surface. The signal acquired by the detector will be received by a feedback loop. Based on the feedback information, the electronic controller adjusts the scanner accordingly in the vertical position, so that the constant oscillation amplitude and then the tip-sample interaction during imaging are maintained. The computer records the vertical position of the scanner at each (x,y) data point to form the topographic image of the sample surface. All the operations take place in ambient environments.

During the AFM measurement, the whole as-grown sample (near a quarter of 2 inch × 2 inch) can be put directly onto the holder for sample's surface morphology measurement. The surface image given by the AFM in this work consists of 512 × 512 measurement points and the measurement area is $1 \times 1\ \mu m^2$. The captured images can be analyzed by using the off-line image analysis software. For example, the surface depth, QD's height and lateral size can be measured by using the Cross-Section Analysis software. Figure 3.8-(b) is the Section Analysis results for a cross-sectional line across the image of Figure 3.8-(a). The vertical and lateral profiles along the line display. Based on the profiles, we can figure out the surface depth, QD's height and width along the line in the image. As shown in the Figure 3.8-(b), the right arrow points to one QD with large size. Its height is higher than 20 nm, and its width is around 123 nm. The left arrow in Figure 3.8-(b) shows a surface depth. Its depth is 13 nm with the width of 67 nm. Based on the measured surface profiles of the formed QDs, we can design the dots' growth mode/conditions for forming the target high quality QDs.

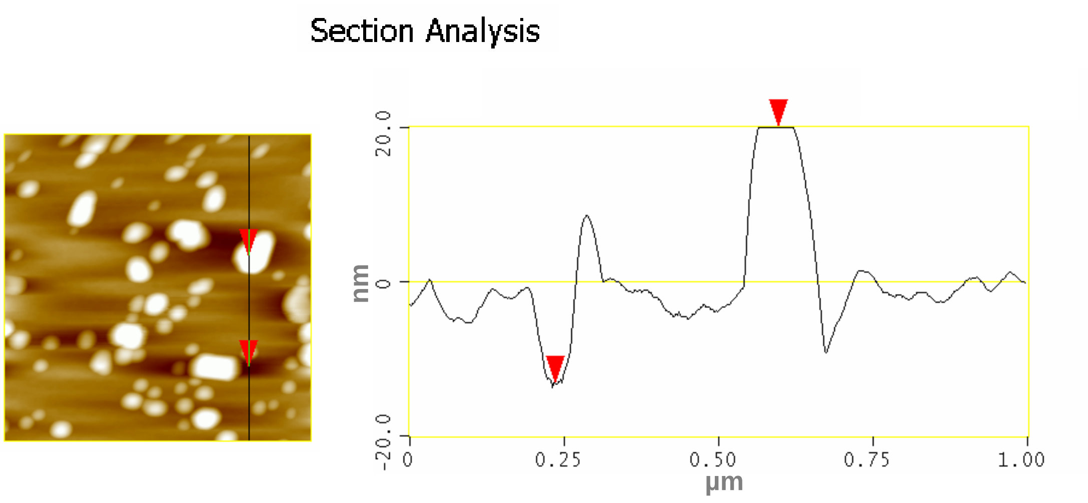

(a) (b)

Figure 3.8 (a) *A cross-sectional line across the1×1* μm^2 *top-view image for (b) AFM off-line Section Analysis.*

The advantages of tapping mode AFM is the high vertical resolution (< 1 nm) and lateral resolution (1 nm to 5 nm), and low scraping/damage to samples [147]. Also, the AFM measurement gives accurate information about the area density of the self-assembled QDs. The accuracy of the AFM apparatus is sufficient to resolve the morphology of the InAs QDs studied in this work with the height and diameter around 8 nm and 50 nm, respectively. If the QD samples are not measured at the same time, i.e. using the different tips or using the same tip but interrupted by others, the dot morphology received will be affected by the tip geometry convolution. In order to make a reliable comparison in dot morphology for a series of QD samples, we are always doing the AFM measurement in series with the same tip for all the samples under comparison.

(ii) *Photoluminescence (PL) spectroscopy*

The optical properties of the samples were studied mainly by PL spectroscopy. PL is a widely-used, non-destructive spectroscopic characterization method which gives information about energy states and different radiative recombination channels in semiconductors. When a piece of semiconductor is under a non-equilibrium condition, e.g. excited by the laser, radiative recombination will take place. A free electron and a free hole are created whenever a photon of energy greater than the energy gap is absorbed in the crystal. This electron and hole can then be bound together by an attractive coulomb interaction force to form an electron-hole pair, which is known as exciton. Excitons are unstable with respect to radiative recombination in which the electron combines with the hole in the VB, accompanied by the emission of a photon. The energy of the photon is equivalent to the crystal band gap of E_g as shown in Figure 3.9-(a) [148]. In case of QD structure, the dot's band gap is always blueshifted with respect to that of its bulk and the electron energy levels become discrete due to three dimensional quantum confinements in the dots. When the QDs are under a non-equilibrium condition, multi-wavelength emissions may occur due to a series of discrete electronic states in the dots [149] or due to the dissimilar dots' size. For the same QD material system, i.e. the same lattice-mismatch strain between QDs and host substrate, the PL emission wavelength from the QDs is mainly determined by the dot size, especially the dot height. However, the emission wavelength of the dots is also affected by the strain from the host substrate and the confinement barrier layers. Larger strain will increase the transition energy in the dots, thus blueshifting the emission wavelength. This can be used in designing the QD structures for different emission wavelength applications. Besides, QD's PL emission intensity is positively dependant on the dot density assuming the same crystal quality in the dots, and the PL linewidth will become narrower if the dot size is more uniform.

Low temperature PL measurement, as used in this work, is important since it produces a sharper and smoother profile. At lower temperature, the linewidth or the full-width at half-maximum (FWHM) of the profile is generally smaller. This is due to the lesser phonon vibration in the crystal at lower temperature, thus the less phonon scattering and the less sideband intensity. At RT, the large concentration of phonons and the exciton levels merge into the continuum absorption spectrum, thus broadening the emission linewidth. Also, at lower temperature, the charge carrier density decreases and reduces the sideband intensity, leading to the higher radiative

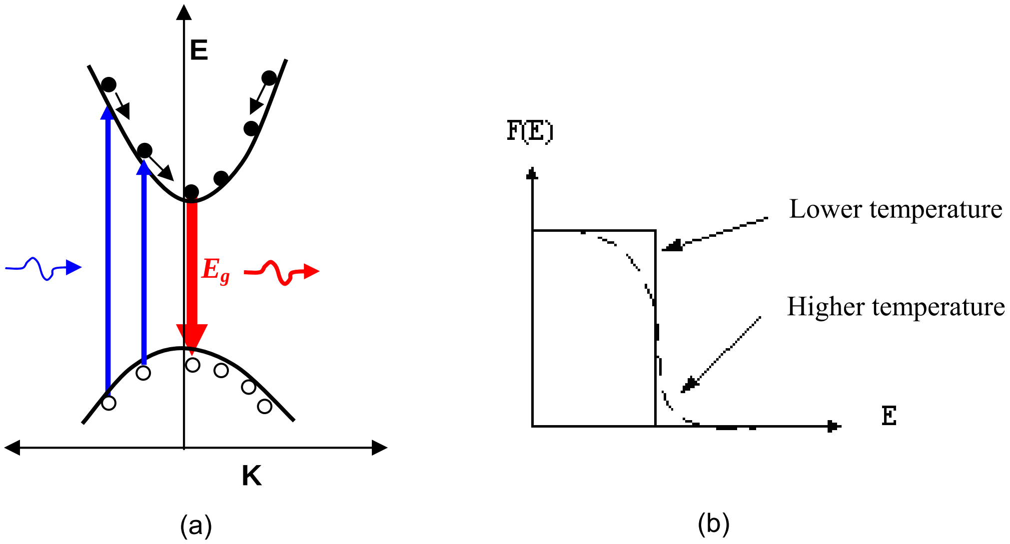

Figure 3.9 (a) Schematic diagram of laser-excitation-induced electron-hole interband transition in the direct-band semiconductors, and (b) Illustration of Fermi level distributions at different temperatures [150].

recombination efficiency and higher PL peak intensity. The decrease in the charge carrier density is due to the change of the Fermi level to a more abrupt profile at lower temperatures, as shown in Figure 3.9-(b). Besides, at lower temperature, the PL peak wavelength obtained is shifted to shorter wavelength. This can be explained by the increase in the bulk energy band gap at lower temperature, which is formulated as:

$$E_g = E_{go} - \frac{\alpha T^2}{(\beta + T)} \tag{3.2}$$

where E_g is the band gap energy at temperature T, E_{go} is band gap energy at 0 K, T is the temperature in Kelvin, and α and β are empirical constants [148]. From the equation $E = hc/\lambda$, where c is the velocity of light and λ is the wavelength, the PL peak wavelength attained would be shorter at lower temperature.

The homemade PL system setup is schematically shown in Figure 3.10. The excitation source is an Ar-ion laser with maximum power of 120 mW and peak wavelength at 514 nm. An optical chopper is used to modulate the laser beam so that signals can be processed by the lock-in amplifier. The laser beam is guided onto the

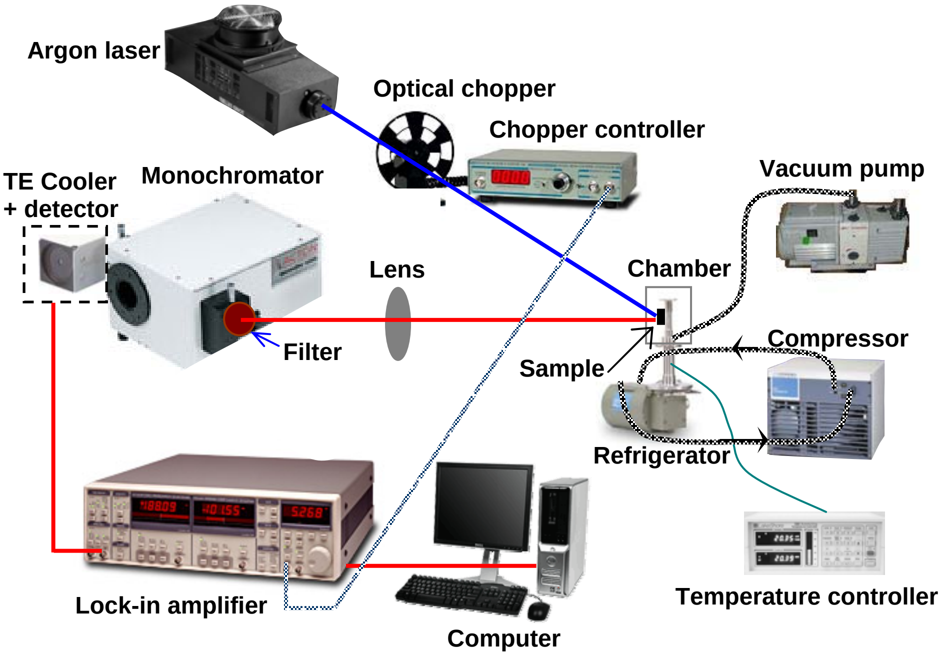

Figure 3.10 Schematic diagram of the photoluminescence measurement.

sample attached on the holder in the low-temperature chamber. To minimize the icing, the chamber is pumped to the vacuum state (~ 10^{-3} milli-torr) by a vacuum pump during the low-temperature measurement. The PL irradiation from the samples after laser-excitation is directed into the monochrometer. The PL spectrum is decomposed by optical grating (60 g/mm) in an Acton Research Corporation monochromator through a 0.5-mm-width slit and a 514-nm-wavelength filter, and then is detected by a thermo-electric (TE) cooled photodetector. The detector selection is based on samples' emission wavelengths: InGaAs detector is used for short wavelength (0.8-1.5 μm) measurement, while PbS detector is used for the long wavelength (1.5-3.0 μm) measurement. The output signals from the detectors are amplified by a SR-830 lock-in amplifier. Computer interface is used to control the PL measurement. The cryogenic temperature ambience (10 K and above), controlled by a temperature controller, in a CTI-cryogenics refrigerator is realized by using the cryostat through a compressor input with the continuous helium flow.

(iii) *Transmission Electron Microscope (TEM)*

TEM has become a very powerful technique in characterizing the micro-structure of materials, ranging from ceramic, metal, semiconductor, superconductor, and biological [151], due to the strong penetration of high energy electrons. The basic picture of TEM is shown in Figure 3.11. The electrons thermally emitted from tungsten are accelerated to high voltage (200kV for JEOL 2010F) to the anode by the electron gun. Various electron-optic lens and aperture are placed along the path of the electron to direct electron motion. The electron-optic lens formed by magnetic coil can be easily regulated by adjusting the current flowing through the coil, which makes TEM a very convenient instrument to access a large range of magnification and

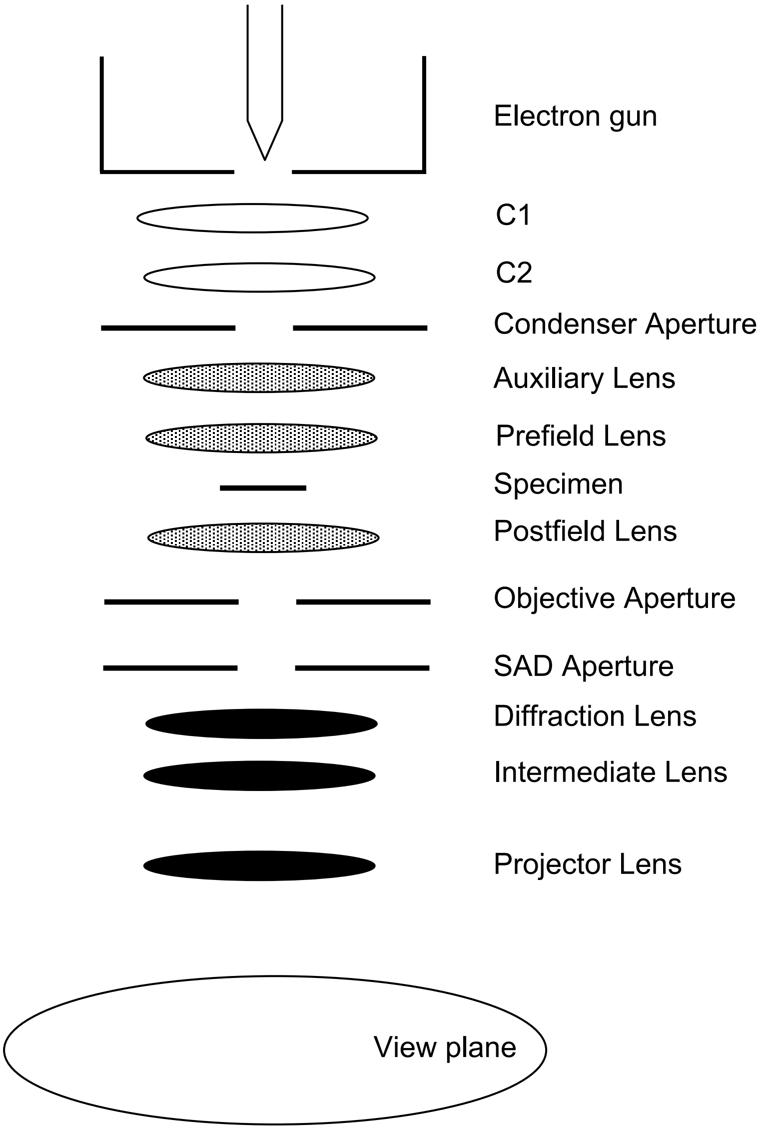

Figure 3.11 Schematic diagram of transmission electron microscope.

different illumination areas. An illumination system consisting of two condenser lens (C1 and C2) and a condenser aperture (CA) is used to focus the electron beam on the sample. The studied specimen is submerged in the objective lens system consisting of an auxiliary lens, a prefield lens and a postfield lens. This lens system collects the transmitted electrons scattered from the specimen and form a diffraction pattern on the objective back-focal plane and an image at the objective image plane. A diffraction lens, an intermediate lens and a projector lens are placed in-between the objective lens system and the view plane. By choosing suitable settings of these lenses, the images or the diffraction pattern can be projected to the view plane. An objective aperture (OA) is placed at the objective back focal plane for selecting different beam(s) to pass through for later imaging, acting as a spatial-frequency filter and enhancing the image contrast. A selective area diffraction aperture (SADA) is placed at the objective plane for selecting the diffraction only from the area covered by the aperture and thus allow a one-to-one correspondence between the image and diffraction to be recorded.

JEOL 2010F used in this work has a point-point resolution of 0.25 nm and a line-line resolution of 0.10 nm. All the lenses are controlled by a CPU and thus the operations can be made easy and reproducible. A Gatan YAG/fiber optic TV system is attached to the microscope. This can display an image with a magnification of ~ 10^6 allowing the image on an atomic scale to be visible on the video screen. This makes correction of astigmatism of the objective lenses involved in the high resolution lattice imaging considerably easier than via viewing on the normal screen.

The specimen to be examined by TEM must be thin enough (~ 1000Å for 200kV electrons) so as to allow the transmission of electrons, thus needing preparing the thin specimen. This leads to the disadvantage of destructive nature in TEM technique. Besides, the preparation procedures of thin specimens are always complicated and involve both physical and chemical processes. Skillful and cautious work is required to obtain a good specimen for electron transparency [152]. In this work, ion milling method is used to prepare the TEM thin specimens due to its ability to produce a relatively large thin, electron transparent area. The preparation of TEM thin films by ion milling mainly contains following steps:

Step 1: Cut two 1mm×3mm (x-y direction) rectangular wafers from the grown sample, and apply a high strength conductive epoxy to glue the two wafers together by facing the grown epilayers to each other, then sandwich them with another two similar sized dummy substrate wafers.

Step 2: Insert the sandwiched wafers into the clamp holder and put them on a 150 ^{o}C hot plate to cure the epoxy for 1 hour. Then, remove the sandwiched wafers from the hot plate and use high strength transparent wax to attach it onto the holder of the Gatan disc grinder.

Step 3: Thin the wafers to about 15 µm thick with 1200 grid silicon carbide sandpaper, and then use 1 µm, 0.3 µm, and 0.05 µm size alumina powders sequentially to polish the wafers to a mirror-like finish. The final thickness of the wafers is about 10 µm.

Step 4: Apply the conductive epoxy as described in step 1 to attach a 3mm diameter copper slot grid on the wafers and cure the epoxy at 150 ^{o}C for 1 hour. Then, dip and clean the wafers and stainless steel holder in acetone until the wax is fully dissolved. The wafer is ready for ion milling.

Step 5: Gatan-691 ion polishing system was used in this work. This machine is equipped with two ion guns, which can mill the specimen from both sides simultaneously. Pure argon was used as the ion source. Two ion guns are used simultaneously to mill the specimen through the entire process. The milling conditions were set at 5 kV accelerating voltage with an ion current of 0.04 µA at an incident angle of 15^{o}. The milling continues until the specimen is perforated. Then, the specimen is ready for TEM examination.

The TEM images are used to study single layer's thickness and QD's morphology based on the cross-sectional view in this study. Although TEM technique is destructive to the sample, it is an important method to study the thickness, interface uniformity and crystal quality of the epitaxial layers. Besides, the dot size, shape and aspect ratio can be affected by the capping process; the effect is dependant on the cap layer's growth conditions and the strain/composition gradient between the cap layer and the dots layer [153, 154]. So, it is necessary to rely on the TEM technique if for a more accurate characterization on dot morphology for the capped QD structures.

(iv) *X-ray diffraction (XRD)*

Nowadays， high resolution X-ray diffraction has been developed into a powerful tool for the nondestructive *ex-situ* investigation of epitaxial layers, hetero-structures and superlattice systems. The information obtained from diffraction patterns includes the composition and uniformity of epitaxial layers, their thicknesses, the built-in strain and strain relaxation, and the crystalline quality related to their dislocation density. The measurement of the diffraction is in principle determined by Bragg's Law with the following formula:

$$2d_{hkl}\sin\theta_B = n\lambda \tag{3.3}$$

where d_{hkl} is the spacing of lattice planes with Miller indices (*hkl*) and θ_B is the corresponding Bragg angle. When a monochromatic X-ray beam with wavelength λ is projected onto a crystalline material at an angle θ, diffraction occurs only when the distance traveled by the rays reflected from successive planes differs by a complete number n of wavelengths. By varying the angle θ_B, the Bragg's Law condition is satisfied by different spacing d in different materials. Plotting the angular positions and intensities of the resultant diffracted peaks of radiation produces a pattern which is characteristic of the sample and called rocking curve. The angular separation between the zero-order satellite peak of the epilayer and the Bragg peak of the substrate in X-ray rocking curve gives the average lattice mismatch information between the epilayer and the substrate along the growth axis.

In X-ray measurement, the rocking curve from a sample is numerically simulated using dynamical theory described by the Takagi-Taupin equations [155, 156]. This approach takes multiple scattering, reflection and absorption of x-rays into account and gives the correct reflectivity. Our measurement is implemented with a Philips X'Pert Material Research Diffractometer (X'Pert MRD). The system is configured with a hybrid monochromator or a high-resolution monochromator. Data collector software is to conduct and plot measured XRD profiles in X'Pert MRD systems. Figure.3.12 displays the typical schematic structure of Philips XRD system. Incident Beam Part consists of X-ray Tube and Incident Beam Optics. The X-ray tube emits a Cu $K_{\alpha 1}$ radiation with wavelength λ=1.54 Å. The incident beam optics is composed of beam attenuator, monochromator and filters. Diffracted beam part consists of diffracted beam optics and detectors. The diffracted beam optics consists

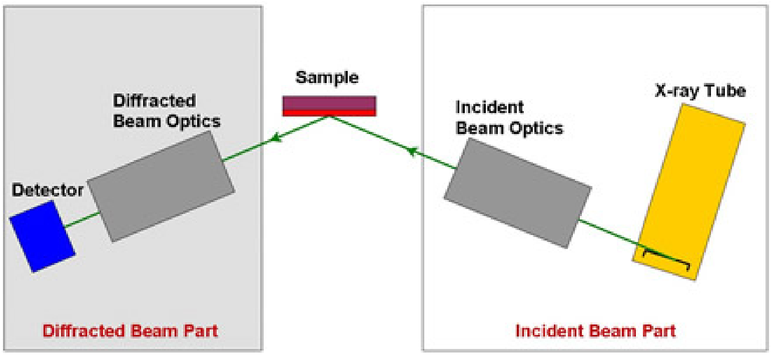

Figure 3.12 The typical schematic structure of Philips XRD system [156].

of Triple Axis Attachment for the reciprocal space mapping (RSM) or Rocking Curve Attachment for rocking curve measurements. X'Pert Epitaxy software provides functionality to analyze rocking curves, reciprocal space maps and wafer maps. In this project, the XRD is only used to study the InAs single layer grown on GaAs substrate. Due to the large lattice mismatch (~7%) between InAs and GaAs crystals, the InAs epilayer will relax with the misfit dislocation formation after the critical thickness. The dislocation in the epilayer will affect the lattice/composition homogeneity and then the intensity and linewidth of XRD curve of the epilayer. So, the XRD curve can be used to analyze the composition of the III-V semiconductor single layers and to qualitatively evaluate the crystal quality of the grown single layer.

3.5 Process technologies

(i) *Inductively coupled plasma (ICP) process*

The plasma system used in this work is Plasmalab System100 machine from Oxford Instruments Plasma Technology as shown in Figure 3.13 [157]. Plasma is an ionized gas with equal numbers of free negative and positive charges. The positive charge is mostly of singly ionized neutrals from which single electron has been stripped. The majority of negatively charged particles are usually free electrons. In this system, the plasma is created by electromagnetic induction when an alternating high frequency current in the radio frequency (RF) inductive coil causes a circulating current to flow in a low-pressure plasma. The plasma can be initiated by the induction coil or by the power applied to another system electrode, usually RF power to the substrate electrode. The 13.56 MHz radio frequency (RF) and ICP power supply can provide independent control on ion bombardment energy and ion current density with

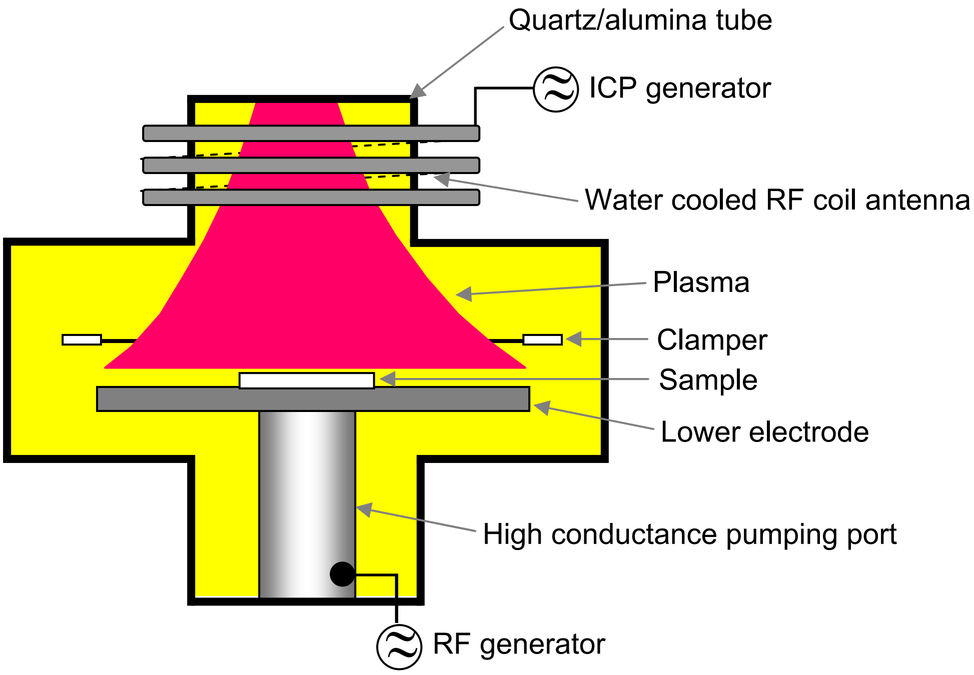

Figure 3.13 A schematic diagram of ICP reactor.

the operation power up to 500 W and 3000 W, respectively. To create a high current in the RF coil in this nonresonant design without high reflected power, an RF tuning network with automatic matching is mounted close to the coil. The ICP power is supplied via a coaxial N-type 50 Ω connector on the matching unit. The matching unit contains motor-driven vacuum capacitors and a directional detection unit, which acts to make the load impedance presented to the RF generator as close as possible to 50 Ω. During plasma exposure, the chamber base pressure is maintained at $5 \cdot 10^{-5}$ Torr. The ICP chamber is equipped with a water circulator to maintain the chuck (cathode) temperature at 60 ^{o}C. However, it should be noted that the actual sample surface temperature during plasma exposure is higher than the reading from the table temperature since the ions produced by plasma is very hot. Based on the ion energy (30 eV ~ 1 keV) in plasma chamber, an average energy of 500 eV is used to approximatively calculate the plasma temperature. The calculated plasma temperature is around 5.8 million of Kelvin. Such hot plasma induced thermal effect during the ICP process also affects the diffusion process in the QD structures. The ICP system is equipped with a back side He-cooled electrode with quartz as a wafer susceptor. The QD samples were placed on the silicon substrate to provide a fairly large (168 W/mK) heat conduction. Ar ion current density increases nearly linearly with the ICP power increase by fixing the RF power. The working pressure affect slightly the ion current density generated in chamber. High ion density in the order of 10^{16} m^{-3} can be generated in such ICP chamber. In the experiment of this work, the ICP and RF power was set at 500W and 480W, respectively, and the Ar gas flow rate was set at 100 sccm with the process pressure set at 60 mTorr. The point defects will be generated in the surface layers in the QD samples after ICP plasma exposure. These surface point defects diffuse down to the QD active region during high temperature annealing process, and subsequently promote intermixing between the dots and barriers, thus increasing the energy band gap of QDs.

(ii) *Annealing process in Rapid Thermal Processor (RTP)*

Rapid thermal annealing process, as a post-growth sample process, is a simple but effective method to adjust the energy band gaps of semiconductor low dimensional structures based on the material interdiffusion [158]. A schematic diagram of a typical RTP system using tungsten halogen lamps is shown in Figure 3.14. The RTP consists of four major components: energy source, process chamber, temperature measurement apparatus and temperature control part. The thermal process is carried out in the single-wafer reactor of the RTP system. The process chamber is usually made of quartz, silicon carbide or stainless steel, and has quartz windows for the optical radiation to illuminate the wafer. A measurement system is

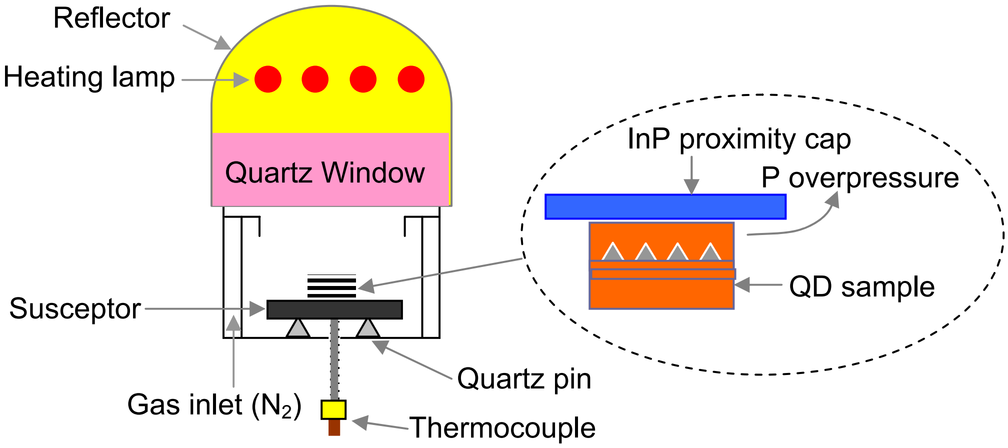

Figure 3.14 A schematic diagram of the RTP machine with the capping configuration for QDI process.

placed in a control loop to set wafer temperature. The wafer temperature in an RTP system can be measured with a noncontact optical pyrometer or a thermocouple. The as-grown and plasma-exposed InAs/InP QDs samples are annealed using a Jetstar rapid thermal processor (RTP) in N_2 atmosphere to prevent contamination. The temperature was controlled by a thermocouple with a high accuracy of ± 1 ^{o}C [157]. One fresh piece of InP proximity cap was used to provide P over-pressure environment and prevent the sample surface from P outdiffusion during the annealing process. The annealing temperature below 850 ^{o}C is chosen to avoid the thermal induced damage on QD samples. For the as-grown and plasma-exposed QD samples upon the thermal annealing, the increase rate of QD's energy band gap is different due to the extra surface point defects generated for the plasma-exposed QDs. This is useful in realizing multi-wavelengths regions across one wafer. In addition, the annealing process also removes the grown-in nonradiative centers in QD structures especially for the layers grown at low reactor temperature.

3.6 Summary

In this chapter, MOCVD epitaxy technology used for growing the QD structures in this work is introduced first. Then, self-assembly method for forming the 3-D QDs is presented. After that, the AFM measurement for characterizing the morphology/size of the uncapped QDs, the PL system for studying the transition energy of the uncapped/capped QDs, the TEM for characterizing the thickness of the grown single layer and the morphology/size of the capped QDs, and the XRD technique to study the single-layer's crystal quality are all introduced. Finally, ICP and RTA sample processes related to tune QD's energy band gap based on the QD intermixing is provided.

CHAPTER 4. MOCVD GROWTH OF QDs

4.1 Introduction

This chapter investigates the formation of high density & uniform InAs QDs on GaAs(001) substrate grown by MOCVD under the safer growth conditions, i.e. using TBA as group-V source to replace AsH_3, and N_2 as the carrier gas to replace H_2. Compared with AsH_3 source, TBA has lower decomposition temperature [159], which is helpful for suppressing the diffusion of dopants in device structures where an abrupt doping profile is critical to the device performance. Also, the high source decomposition efficiency of TBA allows the layer growths with lower V/III flux ratio, thus cutting down the source consumption. Using N_2 instead of H_2 advantages the layer growth with high composition uniformity [125, 160]. This is important to enhance the photoluminescence (PL) performance of QD structures thus for the development of higher performance QDs devices. Among the QDs based on group III-V semiconductor alloys, InAs/GaAs QD system has been investigated in experiment and theory since 1980's [161]. For InAs/GaAs QD system, due to the large lattice-mismatch (~7.2%) induced strain between InAs and GaAs bulks, the formation of InAs QDs on GaAs is strongly dependent on the deposition method and growth conditions. In order to grow high quality, high dot density and size uniformity of InAs/GaAs QDs, various growth conditions and methods on the QDs growth have been investigated in this chapter. Electron/hole transition energies of the QD structure were calculated by using an 8-band **k·p** theory.

In Section 4.2, the growth parameters including growth time, post-growth interruption, growth temperature and source flux were systematically investigated to study their effects on InAs QDs formation on the GaAs(001) substrate. In Section 4.3, a new two-step growth method was proposed to grow InAs/GaAs QDs with higher dot density and size uniformity. To better understand the two-step growth method and to obtain higher-density QDs, effects on the dot formation of the various two-step growth conditions, including the internal interruption time between step-1 and -2 and the TMIn source flux in step-2 growth have been investigated. Finally, in Section 4.4, 8 band **k·p** theory was introduced and applied to calculate the transition energies of InAs/GaAs QD structure. The theoretically calculated results were compared with the experimentally measured QDs' PL peak transition energies.

4.2 Growth-condition dependence of InAs QDs formation

To grow InAs QDs on GaAs or InP substrate, it is very important to determine the InAs growth rate, since the deposited material for QDs formation needs to be controlled in a few monolayers (MLs) thick. To determine the InAs growth rate, InAs bulk layer was grown on GaAs for 30 mins. The metal-organic (MO) sources used in the growths were TBA, TMGa, and TMIn. The carrier gas, nitrogen, was purified by a MonoTorr phase II Getter column with the dew point below –100 ^{o}C. Before starting the epitaxy growth, the GaAs substrate was annealed at 700 ^{o}C for 5 min inside the reactor, and then a 300 nm GaAs buffer layer was grown on the GaAs substrate at 680 ^{o}C. After that, the substrate temperature was lowered down to 500 ^{o}C for growing the InAs bulk layer. The TMIn flux was set at 30 sccm and grown for 30 min. Upon finishing the InAs layer growth, the heater was switched off and the system was cooled down. The Arsenic over pressure is provided by keeping TBA source flux open during the cooling down to protect the sample's surface until the reactor temperature was cooled down to 200 ^{o}C. In order to calibrate InAs growth rate, the *ex-situ* measurement of transmission electron microscope (TEM) was done for the grown sample. The accelerating voltage for electron beam in TEM is set at 200 kV, and the cross-sectional image is taken along the $[1\bar{1}0]$ direction. Based on the TEM

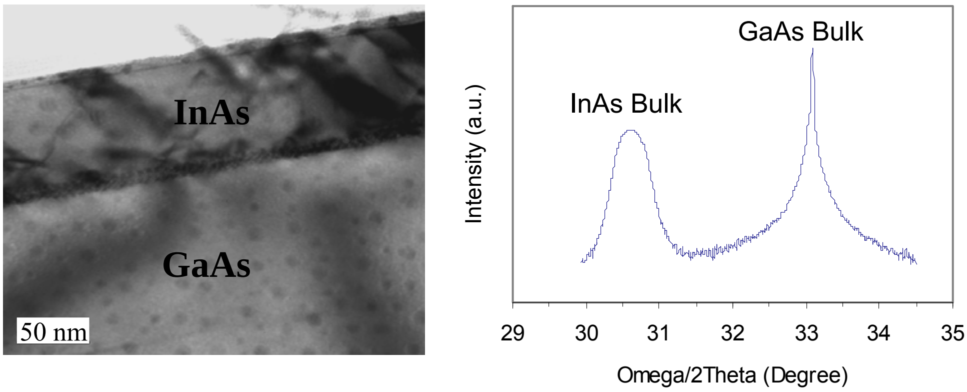

(a) (b)

Figure 4.1 (a) TEM cross-sectional image under g=002 and (b) XRD spectrum of InAs bulk grown on GaAs(001) substrate.

image shown in Figure 4.1-(a), InAs bulk thickness is around 80 nm. The InAs growth rate is calculated with 0.45 Å/s. Figure 4.1-(b) shows XRD rocking curve of the InAs/GaAs sample. The relatively narrow rocking curve of InAs layer indicates the good crystal quality. The XRD intensity ratio of InAs layer versus GaAs buffer is 74%, and the FWHM ratio of GaAs buffer versus InAs bulk reaches 65%. We think such InAs crystal is appropriate for calibrating InAs growth rate.

In the following, the SK self-assembly growth of InAs QDs on GaAs substrate was investigated. All InAs/GaAs QDs samples were grown with the reactor pressure set at 20 mbar, the V/III ratio was set at 24, and 10 for growing the GaAs buffer layer and InAs QDs, respectively. The total flow rate in the reactor was Q_{total} = 3.1 slm. GaAs epi-ready semi-insulating substrates oriented in (001) ±0.1^{o} direction were used for all the growths. Before growing InAs QDs, a 0.3 μm GaAs buffer layer was grown on GaAs substrate at 680 ^{o}C. Then, the reactor temperature was reduced to the target temperature for growing the InAs QDs. To grow the QDs, very thin InAs layer, few monolayers (MLs), was grown as normal; and then the TMIn source was closed for the post-growth interruption to let the QDs formed self-assembly. Surface morphology of all the samples was studied by using the AFM. The dot formation is affected by the growth conditions, including growth time, post-growth interruption, growth temperature and source flux, etc, which are discussed in detail below.

4.2.1 Effect of the growth time

To study the effect of the growth time (layer thickness) on the InAs QDs formation on GaAs substrate, five samples, samples (a) to (e), were grown by changing the InAs layer growth time. The substrate temperature and InAs growth rate was kept at 500 ^{o}C and 0.15 ML/s, respectively. All other growth conditions are the same for the five samples. Figure 4.2-(a) to -(e) compares the surface morphology of the five samples deposited with different InAs layer growth time. It is observed that when the growth time was equal to or less than 10 seconds, no QD was formed. When the InAs layer growth time increased to 12 seconds, QDs started to be formed as

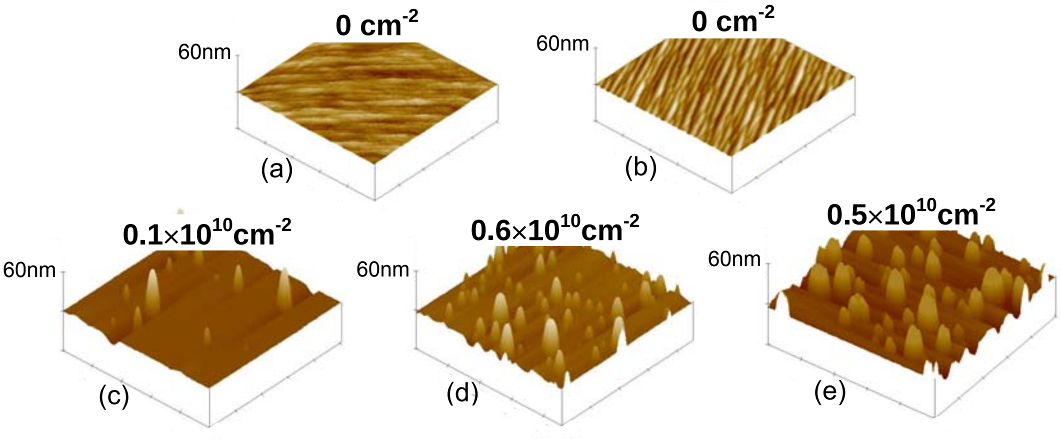

Figure 4.2 3-D 1×1 μm^2 AFM images with dot-density insets of samples (a), (b), (c), (d) and (e), grown by depositing InAs for 8 s (1.2 MLs), 10 s (1.5 MLs), 12 s (1.8 MLs), 15 s (2.25 MLs) and 18 s (2.7 MLs), respectively, after GaAs buffer growth.

shown in Figure 4.2-(c), but with very low density, ~1×10^9 cm^{-2}. Average dot height h_g of the samples was calculated by using the following formula [162].

$$\log_{10} h_g = \frac{\Sigma(n \log_{10} h_n)}{N} \tag{4.1}$$

where N is the total number of the dots counted on the sample, n is the number of the QDs with the same dot height of h_n. The average dot diameter was calculated using the similar equation. The calculated average dot height and diameter of sample (c) is 10.0 nm and 35.5 nm, respectively. Based on the dot size and number obtained, total volume of the QDs can be calculated by taking the dot with pyramid shape. The total volume of QDs of the sample was equivalent to a nominal thickness (assuming 1 ML = 0.3 nm) by dividing the QDs volume with the scanned area. In QDs self-assembly growth, a thin 2-D layer forms below before the 3-D nucleation starts, as mentioned in Section 2.3.2 of Chapter 2. The thin 2-D layer is called as the wetting layer. The thickness of InAs wetting layer was received by deducting the QDs nominal thickness

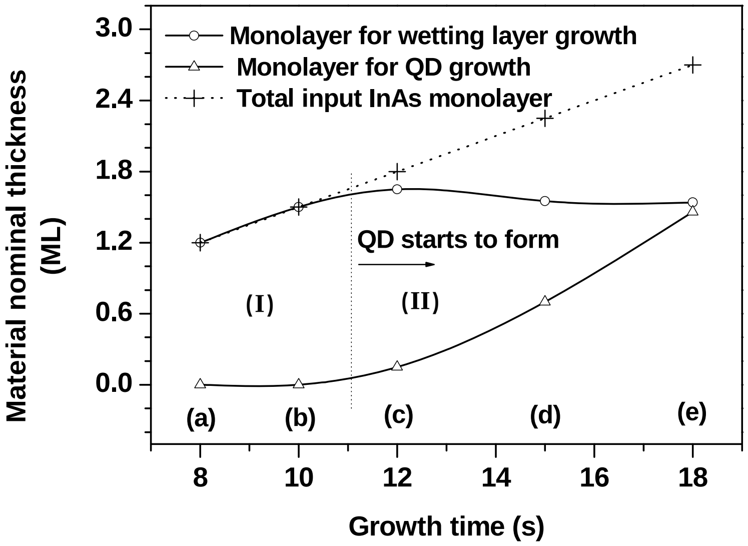

Figure 4.3 InAs material consumption during InAs wetting layer and QD growth under different InAs deposition time. The two solid curves show wetting layer and QDs, and dot-line with + symbol is related to the total input InAs monolayer.

from the total input InAs layer thickness. Figure 4.3 shows the evolution of the InAs material consumed for growing the wetting layer and the QDs with different InAs growth time. It shows that if the total deposited InAs layer thickness is less than 1.5 MLs, as in the cases of sample (a) and (b) in Figure 4.2, only the wetting layer is grown, no dot is formed. QDs formation started when the total deposited InAs layer is thicker than 1.8 MLs, as the shown samples (c), (d) and (e). For sample (d), the total input InAs material is 2.25 MLs, increased by 0.45 ML compared with that of sample (c). But, the QDs nominal thickness of sample (d) is 0.7 ML, 0.55 ML thicker than that of sample (c) with 0.15 ML QDs nominal thickness. The received wetting layer thickness of sample (c) and (d) is 1.65 MLs and 1.55 MLs, respectively, as shown in Figure 4.3. The reduced wetting layer thickness, or the more increase of QDs nominal thickness than that of the total input InAs material, from sample (c) to (d) shows that some InAs material was decomposed from the wetting layer and transferred to the dots during their formation. The similar decomposition of wetting layer was also observed in the InAs/GaAs QDs growth by using AsH_3/H_2 [163]. The reason for InAs material transformed from wetting layer to islands is because the strain energy in wetting layer is further relaxed into surface energy by forming more islands [164]. However, when the InAs growth time was increased to 18 seconds, the input InAs material is too much. At this time, the InAs islands no longer accommodate the strain, thus inducing misfit dislocations formation between island-substrate interfaces. This makes the QDs become incoherent and grow into larger islands by consuming the surrounding dots, i.e. the ripening process [165]. So, the dots of sample (e) are obviously larger in dot-size and lower in dot-density than those of sample (d). From this study, we can see that the growth time control is critical for forming coherent QDs. For the InAs/GaAs QDs grown under current conditions, the InAs growth time of 15-seconds, i.e. the input InAs material of 2.25 MLs, is the optimized growth condition, which will be used in the following QD study based on the different post-growth interruptions and growth temperatures.

4.2.2 Effect of the post-growth interruption

To study the effects of the post-growth interruption time on the QDs formation, four samples, samples (f), (g), (h) and (i), were grown at 500 ^{o}C with the same InAs layer thickness of 2.25 MLs. All other growth conditions of the four samples were the same, only the post-growth interruption time was varied from 0 to 20 seconds. During the post-growth interruption, the reactor temperature was kept the same, i.e. 500 ^{o}C, as that for growing the dots; the TMIn source was switched off but the TBA source was kept open. For the four samples studied, after post-growth interruption, the heater of the reactor was switched off to ramp-down the reactor temperature by the rate of 6 ^{o}C/min. The TBA source was still kept open until the reactor temperature reached 200 ^{o}C. For sample (f), when the InAs growth reached the target thickness, the reactor heater was switched off immediately, i.e. with post-growth interruption for zero second. While for growing sample (g) to sample (i), the post-growth interruption was kept for 5 seconds, 10 seconds and 20 seconds, respectively, before switching off the heater after the InAs growth. The AFM measurement results of the four samples are shown in Figure 4.4. Based on the AFM images, AFM Section Analysis results and the received dot's size distribution, the dot density, dot's size standard deviation and surface depth were also summarized in Table 4.1. It is found that there is not much difference in the dot density of the samples when the interruption time was changed from 0 to 20 seconds. However, the dot size distribution is sensitive to the post-growth interruption time. When the post-growth time is zero second, the dot's height standard deviation is 6.2 nm. When the interruption time is prolonged to 5 seconds, the dot's height standard deviation reduces to 5.2 nm. However, when the post-growth interruption time is increased to 20 seconds, the dot's height standard deviation increases again to 7.8 nm. So, the post-growth interruption time of 5 seconds gives

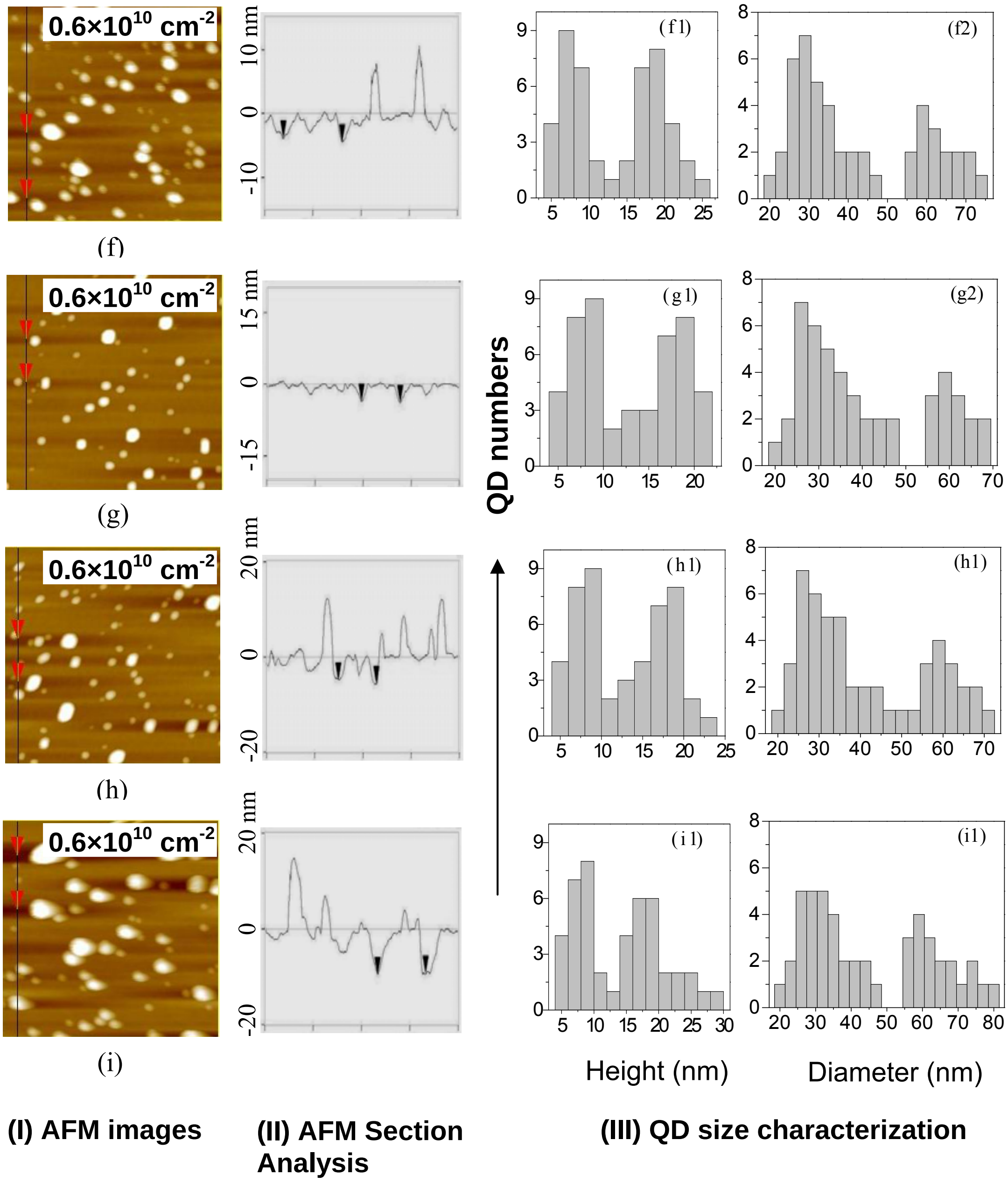

Figure 4.4 (I) Top-view 1×1 μm² AFM images with dot-density insets, (II) AFM in-situ Section Analysis with surface depth along a cross-sectional line across the image, and (III) Dot's diameter/height characterization are shown for samples (f), (g), (h) and (i) with post-growth interruption time set at 0 s, 5 s, 10 s and 20 s, respectively.

minimum height standard-deviation, i.e. the narrowest height distribution, of the dots. The similar change trend of dot's diameter standard deviation with the post-growth interruption time is also observed. The results show there is a window (5 seconds) in the post-growth interruption time for forming the dots with the narrowest dot-size distribution. Besides, as shown in table 4.1, the surface depth of the four samples changes with the similar trend. The depth from sample (i) is very large, about 9 nm, obviously larger than that from the other three samples grown with less than 10-second post-interruption. The possible reasons are discussed in the following paragraph.

Around a 3-D nucleation center, which acts as a sink for the surrounding adatoms during the dot formation, adatoms are collected by the nucleation center to make it grow bigger and no any other nucleation developed [166]. Besides, QD structures with large aspect ratio relax the strain energy caused by the lattice mismatch between the QDs and buffer/substrate easier [167]. For sample (f), the post-growth interruption is zero second, where the surface adatoms have no time to diffuse across the surface and hence could not be efficiently absorbed by the 3-D nucleation centers. As a result, some small islands have no time to grow larger by absorbing the residual surface adatoms. For sample (g), the 5-second post-growth interruption

Table 4.1 Comparison of QDs density, QDs' height & diameter standard deviations and wetting layer surface depth for the samples (f), (g), (h) and (i).

Compared parameters	**Sample (f)**	**Sample (g)**	**Sample (h)**	**Sample (i)**
QD density ($\times 10^{10}/cm^2$)	0.6	0.6	0.6	0.6
QD's height standard deviation (nm)	6.2	5.2	6.0	7.8
QD's diameter standard deviation (nm)	15.2	14.3	15.1	16.9
Surface depth (nm)	3.7	3.5	4.8	8.7

favors the small islands growing further by absorbing the remaining surface adatoms. This advantages narrowing the dot size distribution. So, the dot's size distribution of sample (g) is narrower than that of (f). For the sample (i) with the long post-growth interruption, when the surface adatoms are used out, some islands grow further into large clusters to relax the strain energy by consuming the material of the wetting layer. This results in the formation of the obvious deep surface depth in the wetting layer and a very broad dot size distribution. Large clusters may contain dislocations which act as nonradiative recombination centers in them [168], and degrade the QDs' PL performance. In the four samples (f) to (i), sample (g) has relatively narrower dot size dispersion and smoother wetting layer surface, but the dot density of the four samples is low and the size dispersion of the dots still has improvement space. Such QDs are not proper for the QDs device applications. In order to improve dot density and dot-size uniformity, the effects of the growth temperature, inlet source flux and growth mode are further investigated. In the following growth temperature study, the post-growth interruption of 5-seconds is used because it brings with the more uniform dot size and wetting layer surface.

4.2.3 Effect of the growth temperature

In order to study the effects of growth temperature on the QDs formation, we grew six QDs samples, sample (j) to (o), with different temperature in the range from 420 ^{o}C to 520 ^{o}C. For the six samples, the input InAs material was kept 2.25 MLs and the post-growth interruption time was 5 seconds. All other growth conditions were identical. Figure 4.5 shows the top-view AFM images of the six samples. High QD density of around 1.3×10^{10} cm^{-2} is obtained from the samples grown at the temperature range from 440 ^{o}C to 460 ^{o}C. Out of this temperature range, when the

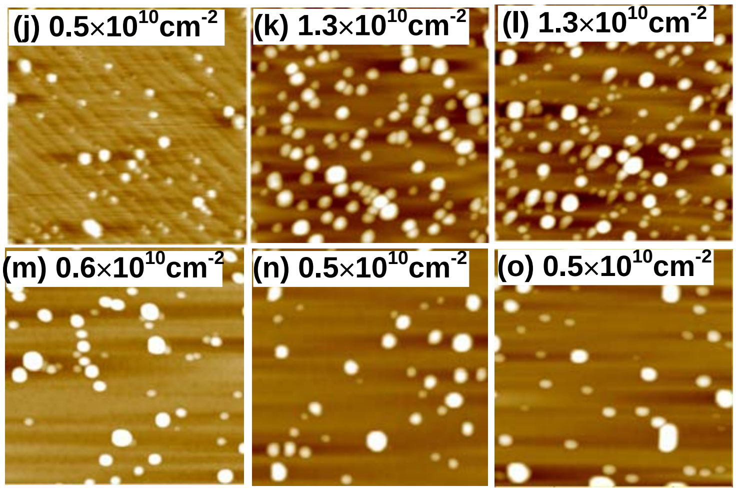

Figure 4.5 Top-view $1\times1 \mu m^2$ AFM images with dot-density insets of the InAs QD samples (j), (k), (l), (m), (n) and (o), respectively, grown at 420 °C, 440 °C, 460 °C, 480 °C, 500 °C and 520 °C.

sample was grown at the temperature either higher or lower by 20 °C, the QD density reduces dramatically to around 0.5×10^{10} cm^{-2}. When the growth temperature was above 480 °C, large InAs islands with lower density are obtained. This is due to the longer diffusion length of the adatoms at high temperature [169]. During the post growth interruption, larger islands grow further by consuming small islands in the island-coarsening process [168]. This can be seen from the AFM images of samples (m), (n) and (o) where some large dots are surrounded with sparse distribution of very small dots. QDs with low density are formed at low growth temperature, ≤ 420 °C. This is because: (i), the critical thickness of wetting layer for the onset of the dot formation increases with decreasing the growth temperature due to atoms' diffusion length reduced [170]; (ii), the diffusion coefficients of the source adatoms are smaller at lower temperature, which leads to lower growth efficiency [123]. Therefore, the material available for growing the InAs were reduced when the growth temperature

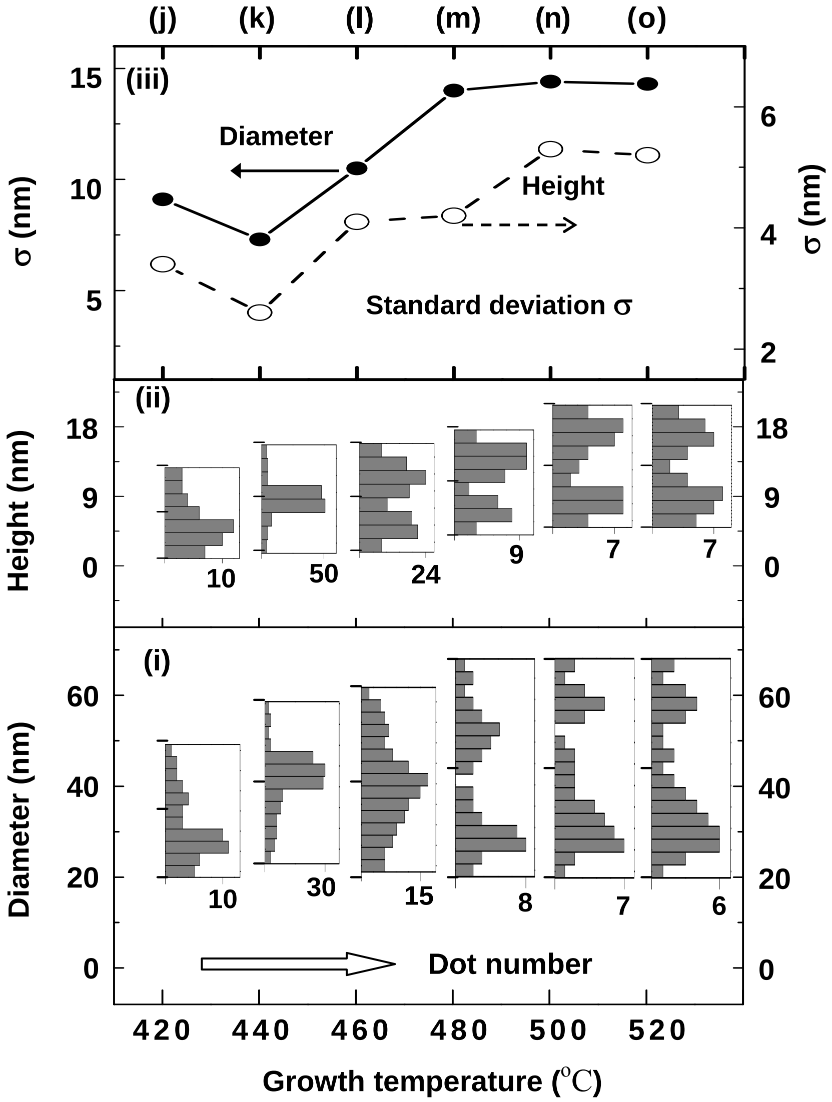

Figure 4.6 InAs QD's size distribution and standard deviation of samples (j), (k), (l), (m), (n) and (o) grown at different temperatures: (i) Histograms of QD's diameter distribution, (ii) histograms of QD's height distribution and (iii) standard deviation of QD's diameter & height as a function of deposition temperature.

was below 420 °C, which resulted in the low density of InAs dots formed.

The distribution and standard deviation of the QDs' diameter and height versus the growth temperature are plotted in Figure 4.6. Figure 4.6-(iii) shows that, when the growth temperature is increased, the standard deviation of dot size becomes larger, which is because of the occurrence of more and more islands' ripening. This results in larger dot size fluctuation and even bimodal distributions of the dot's diameter and height. Sample (k), which was grown at 440 ^{o}C, has the smallest standard deviation of dot's diameter and height, thus the narrowest dot's size distribution. But, too low reactor temperature will degrade dot's cap layer crystal-quality and then its PL performance in growing the QD structure where the dots will be capped by a layer. Generally, the temperature used in MOCVD for growing QDs' cap layer, e.g. GaAs or InP, is above 500 ^{o}C to receive high crystal quality layers as mentioned previously. So, to grow high density and uniform InAs/GaAs QDs at 500 ^{o}C or above is important. In the following QDs formation optimization based on source flux and growth method, the reactor temperature used for growing the InAs QDs layer is kept at 500 ^{o}C.

4.2.4 Effect of the source flux

In MOCVD growths of the layers of QD structures, the molar ratio of the total group-V sources versus the total group-III sources, so-called V/III ratio, is generally larger than 1, thus with rich group-V source ambient. The V/III ratio was set at 10 when growing the studied InAs QDs. The source flux effects on InAs QDs formation were investigated by changing the group-III (TMIn) and -V (TBA) source fluxes together to keep the V/III ratio during the InAs QDs growth. First, two samples of (p) and (q) were grown by setting the input TMIn flux at 30 sccm and 75 sccm, respectively. The substrate temperature was set at 500 ^{o}C and the post-growth interruption was kept for 5 seconds for the two samples. To keep the same deposited InAs layer thickness, the InAs growth time was changed accordingly when the input TMIn source flux changed. The received top-view AFM images of the two samples are listed in Table 4.2. It is observed higher density InAs QDs are formed in sample (q)

Table 4.2 Top-view 1×1μm^2 AFM images with dot-density insets of InAs QDs grown with different TMIn input flux & inflow time at 440 °C and 500 °C, respectively.

<table>
<tr><td></td><td></td><th colspan="2">Growth methods</th></tr>
<tr><td></td><td></td><th>Slow growth</th><th>Fast growth</th></tr>
<tr><th colspan="2">TMIn flux & inflow time</th><th>30 sccm & 15 s</th><th>75 sccm & 6 s</th></tr>
<tr><th rowspan="2">Growth temperature (°C)</th><th>500</th><td>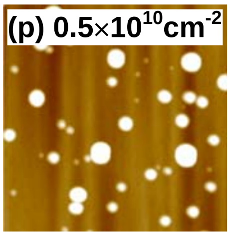 </td><td>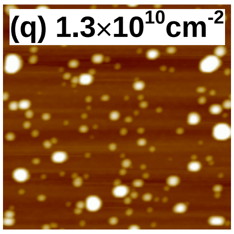 </td></tr>
<tr><th>440</th><td>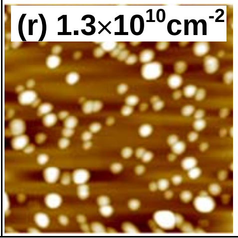 </td><td>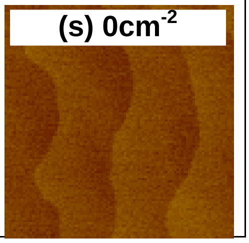 </td></tr>
</table>

than that of sample (p). This is because at the growth temperature of 500 °C, surface reaction dominates the growth. The MOCVD growth was in mass flow control, where the growth rate was proportional to the inlet TMIn flux flow. When the TMIn flow flux was increased in growing sample (q), the growth rate was higher and more nuclei were formed, thus leading to more dots formed.

To verify the temperature-dependant MOCVD growth mechanism when growing the QDs, other two samples, sample (r) and sample (s), were grown at lower temperature of 440 °C, while the TMIn flux was still set at 30 sccm and 75 sccm, respectively. It is observed that (see Table 4.2) no InAs QD was formed on sample (s) which was grown with higher TMIn input flux but shorter growth time. High density of QDs was formed on sample (r) which was grown with lower TMIn flux but longer growth time. At low substrate temperature, as for growing sample (r) and (s), the epitaxy growth was in surface reaction limited growth. The InAs growth rate did not increase accordingly when the TMIn input flux was increased. The InAs layer deposited in sample (h) was too thin to form the QDs when the growth time was reduced to 6 s.

From the above study, the dot density of InAs QDs grown at 500 ^{o}C by the optimized SK self-assembly is improved by increasing source flux, but still limited to 1.3×10^{10} cm^{-2}. At the same time, the dot size dispersion is large. Based on the optimized InAs monolayer input, growth temperature and source flux, further optimization on QDs formation has been carried out in the following by proposing a new QDs growth method.

4.3 A new two-step growth method for QDs

4.3.1 Two-step growth of QDs

In SK growth mode, the dot density is mainly determined by the nucleation density after the wetting layer growth. The dot growth from the nucleus formed is induced by the gradual relaxation of the accumulated strain in wetting layer. Too fast growth will make the large strain energy being dissipated with insufficient time, which easily results in non-crystalline disruption in QD structures, leading to large coalesced cluster formation and thus degrading dot’s size uniformity [169]. To grow high crystal quality QDs with high dot density and good size uniformity, a two-step growth of InAs QDs method is proposed. In this method, InAs growth is divided into two steps as shown in Figure 4.7. In step-1 growth, a thin InAs layer is deposited with high TMIn source flux, and then the growth is stopped for an internal interruption by closing the TMIn source. High density InAs nuclei are formed during the internal interruption. After the internal interruption, the TMIn source is opened again for the

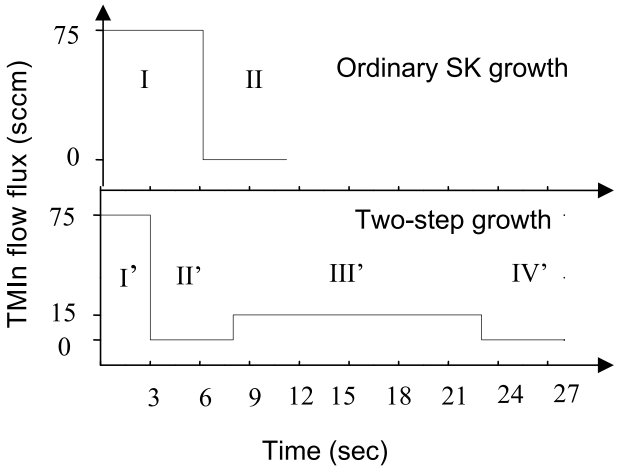

Figure 4.7 Schematic diagram of TMIn source flow settings during the InAs QDs growth. In ordinary SK growth: I, InAs deposition; II, Post-growth interruption; in two-step growth: I', step-1 InAs deposition; II', internal interruption; III', step-2 InAs growth; IV', post-growth interruption.

step-2 growth. In the step-2 growth, the InAs layer is grown with lower growth rate. When the constant target layer thickness is reached, the TMIn source is closed for post-growth interruption and the InAs QDs are finally formed self-assembly. This two-step growth mode is similar to the reported punctuated island growth [171], which studied the effect of later QD evolution stages on dot formation. It was found the punctuated island growth with input ~ 2.5 MLs InAs material received the best PL emission but still with bimodal QDs formed. In this two-step growth of QDs, we keep the step-1 fast nucleation unchanged and optimize the internal interruption time and step-2 source flux for forming high quality InAs QDs.

Sample (t) and (u) was grown at 500 ^{o}C and 440 ^{o}C, respectively, by the two-step growth. The measured AFM images of the two samples are shown in Table 4.3. For comparison, AFM images of samples (q) and (s) grown by the conventional SK self-assembly mentioned above are also shown in Table 4.3. The dot density of sample (u) is 0.2×10^{10} cm^{-2}. It is higher than that of the sample (s) grown at the same temperature by normal one step growth. For samples grown at 500 ^{o}C, the QDs density of sample (t) grown by two-step growth is about 30% higher than that of sample (q) which was grown by normal one step growth. The dot's diameter and

Table 4.3 Top-view 1×1μm^2 AFM images with dot-density insets of InAs QDs grown with fast growth and two-step growth at 440 ^{o}C and 500 ^{o}C, respectively.

		Growth methods	
		Fast growth	**Two-step growth**
TMIn flux & inflow time		**75 sccm & 6 s**	**75+15 sccm & 3+15 s**
Growth temperature (^{o}C)	**500**	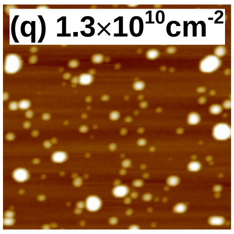 **(q) 1.3×10^{10}cm^{-2}**	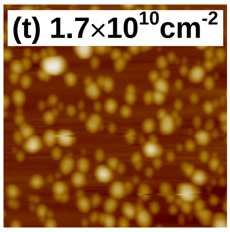 **(t) 1.7×10^{10}cm^{-2}**
	440	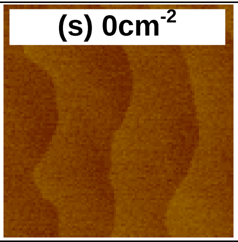 **(s) 0cm^{-2}**	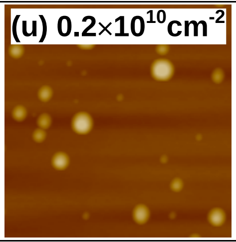 **(u) 0.2×10^{10}cm^{-2}**

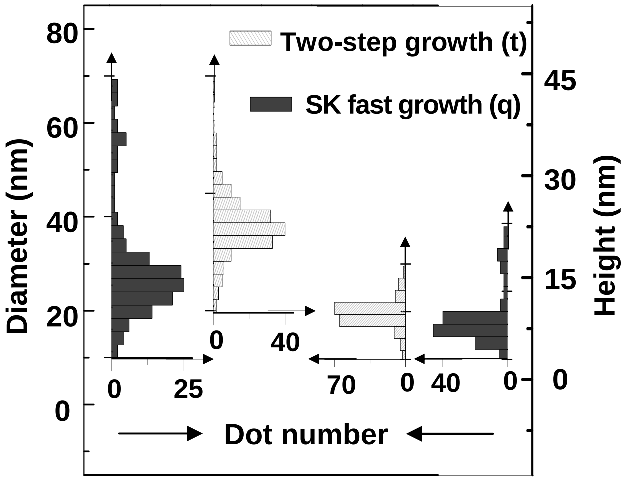

Figure 4.8 QDs' diameter (left) & height (right) histograms for the sample (q) grown by normal SK fast growth, and sample (t) by two-step growth both at 500 ^{o}C.

height distributions of samples (q) and (t) are shown in Figure 4.8. We can see the dot size dispersion of sample (t) is much narrower than that of sample (q). The standard deviation of the dot's diameter and height of sample (q) is 12.9 nm and 7.6 nm, respectively, while that of sample (t) is 4.2 nm and 2.3 nm, respectively. These results show that the dot uniformity of the sample has been improved by using the two-step growth.

A schematic diagram in Figure 4.9 shows the QDs formation mechanisms in two-step growth method. In two-step growth, nonuniform nucleus islands are formed after the first step fast growth; during the internal interruption, the islands continue growing by absorbing the surface atoms. At the same time, some of the atoms will self-nucleate between the relatively large islands, which increases the dot density. This is because atoms are difficult to reach the large islands since they have high edge energy barrier [172, 173]. All the formed islands continue growing during the step-2 growth. In step-2 growth, the TMIn source is with low source flux so that the islands could grow slowly into QDs, and at the same time, new nuclei are also formed in

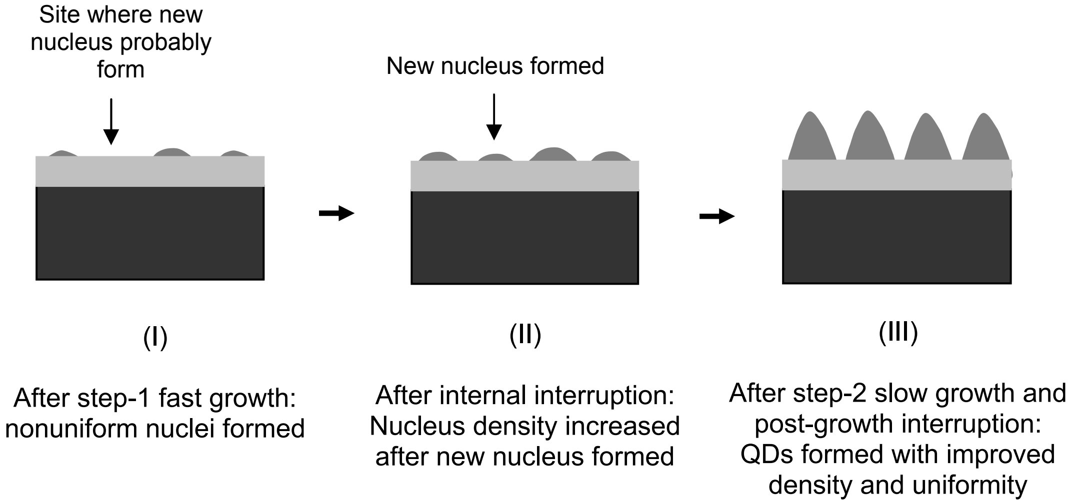

Figure 4.9 Schematic diagrams of proposed two-step growth mechanisms for InAs QD formation by MOCVD.

between the formed large dots. These new nuclei adsorb the coming Indium atoms during the growth stage and adsorb the residual substrate surface Indium atoms during the post-growth interruption stage. As a result, the dot density is increased. In the two-step growth, larger islands/dots grow much slower than the small islands/dots [173]. So, size uniformity of the QDs is improved. By employing the two-step growth of QDs, the dot density and size uniformity are both improved. In the following, the internal interruption time and step-2 source flux will be further investigated on the dot formation trend under the two-step growth mode.

4.3.2 Effect of the internal interruption time

As discussed above, the nucleation during the internal interruption between step-1 and -2 will affect the density of the QDs formed. In order to optimize the interruption time, different internal interruption time between step-1 and -2 growth on the InAs/GaAs QD formation have been carried out. For this study the total inlet InAs nominal thickness was still kept constant as 2.25 MLs and the growth temperature was set at 500 ^{o}C. The TMIn source flow flux settings and the growth time for each growth step in MOCVD deposition of the InAs QDs are listed in Table 4.4. Figure 4.10 shows 1×1 μm^2 AFM surface images of the InAs QDs samples grown by the

Table 4.4 The TMIn source flow flux settings and the growth time for each growth step in MOCVD growth of the InAs QD samples.

Compared samples	Two-step growth			
	Step 1	**Internal interruption**	Step 2	Post-growth interruption
(v)	75 sccm & 3 s	**0.5 s**	15 sccm & 15 s	5 s
(w)		**2 s**		
(x)		**5 s**		
(y)		**60 s**		

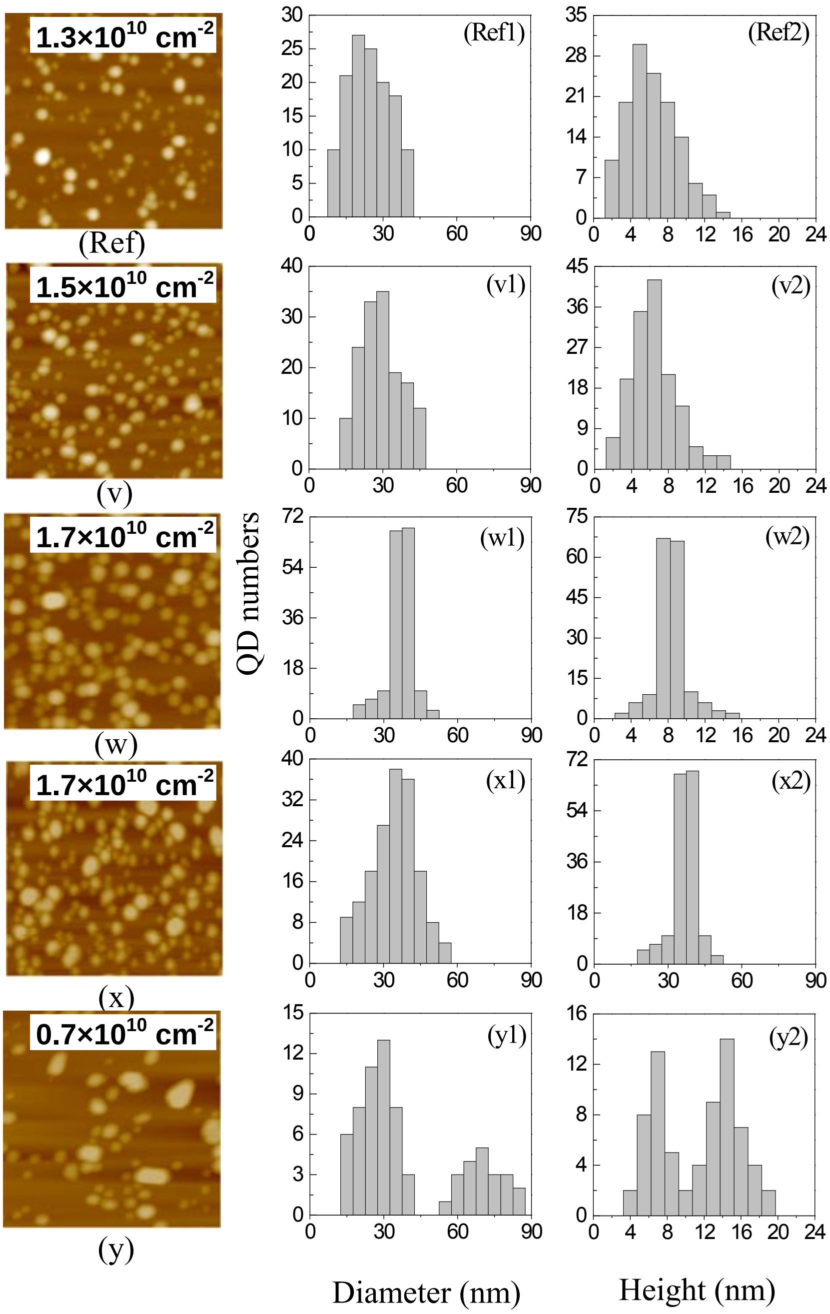

Figure 4.10 Top-view 1×1 μm^2 AFM images with dot-density insets of the Ref. SK grown InAs QDs sample and the two-step grown QDs samples (v), (w), (x) and (y) with the internal interruption time (t_{int}) set, respectively, at 0.5 s, 2 s, 5 s and 60 s. The dot diameter and height histograms related to each image are also shown.

two-step growth under different internal interruption time. For comparison, a Ref. sample was grown using normal SK one-step growth. It has been reported that in ordinary SK growth of QDs, higher QD density can be achieved if the InAs is grown with a faster growth rate [169,174]. The Ref. sample was grown with the fast growth rate of InAs. But, samples grown by using the two-step growth method, from sample (v) to sample (x), have higher dot density than that of the Ref. sample. The TMIn flow flux was reduced from 75 sccm for growing the Ref. sample in ordinary SK growth to 15 sccm for the step-2 growth in the two-step growth. As shown in the histograms in Figure 4.10, the average diameter of the InAs QDs grown by two-step growth is ~ 36 nm, while for the QDs grown by the ordinary SK method, the average diameter is ~ 25 nm. The diameter dispersion of the QDs grown by the two-step method is much narrower than that of the QDs grown by the ordinary SK method when the interruption time in two-step growth was set at t_{int} = 2 s. This shows that the QDs grown by two-step growth are more uniform in dot size. As shown in Figure 4.10, the interruption time, t_{int}, strongly affects the formed QD size uniformity and the dot density in two-step growth. When t_{int} is too short, as for sample (v), there is not enough time to form the new nuclei during the interruption. In this case, the growth is similar to that of ordinary SK growth. If t_{int} is too long, as in the case of sample (y), some very large dots or clusters are formed during the interruption by consuming the material from the wetting layer or adjacent smaller dots. These large dots are ripened further by merging with neighbor small dots in the step-2 growth, resulting in nonuniform dots with very large dot diameter distribution and very low dot density [175]. So, internal interruption time of 2-seconds is an optimized growth condition in the two-step growth of InAs QDs on GaAs in terms of dot density and dot-size dispersion. In the following step-2 growth source flux study, the internal interruption time is kept at 2 seconds.

4.3.3 Effect of the source flux in step-2 growth

The effects of the InAs growth rate in the step-2 growth on the formation of QDs in the two-step growth have also been investigated. Samples (w)–(w′′′) were grown with different TMIn source flow fluxes in the step-2 growth of InAs in the two-step growth of InAs QDs, while the conditions for step-1 growth and interruption were unchanged. As shown in Table 4.5, the TMIn flux in the step-2 growth increases with the duration time decrease so to keep the InAs thickness in the step-2 growth the same. Figure 4.11 shows the $1\times1\mu m^2$ AFM surface images of these four samples. When the TMIn flux in step 2 was increased from 15 sccm for growing sample (w) to 112.5 sccm for growing sample (w′′′), the dot density increased by 47%, reaching 2.5 $\times10^{10}$cm^{-2} in sample (w′′′). The average dot diameter increased from 36 to 43 nm, but the average height of the QDs decreased from 8.4 nm for sample (w) to 5.6 nm for sample (w′′′). The dot diameter dispersion was also observed to be increased when the growth rate in the step-2 growth was increased. With the faster growth rate, the growth time for the step-2 growth is shorter; the dots formed in the step-2 growth do not have enough time to release all their strain energy by increasing the aspect ratio. Dots formed under such conditions are large in diameter but with low height [167].

Table 4.5 The TMIn source flow flux settings and the growth time for each growth step in MOCVD growth of the InAs QD samples.

Compared samples	Two-step growth			
	Step 1	Internal interruption	**Step 2**	Post-growth interruption
(w)	75 sccm & 3 s	2 s	**15 sccm & 15 s**	5 s
(w’)			**30 sccm & 7.5 s**	
(w’’)			**56.3 sccm & 4 s**	
(w’’’)			**112.5 sccm & 2 s**	

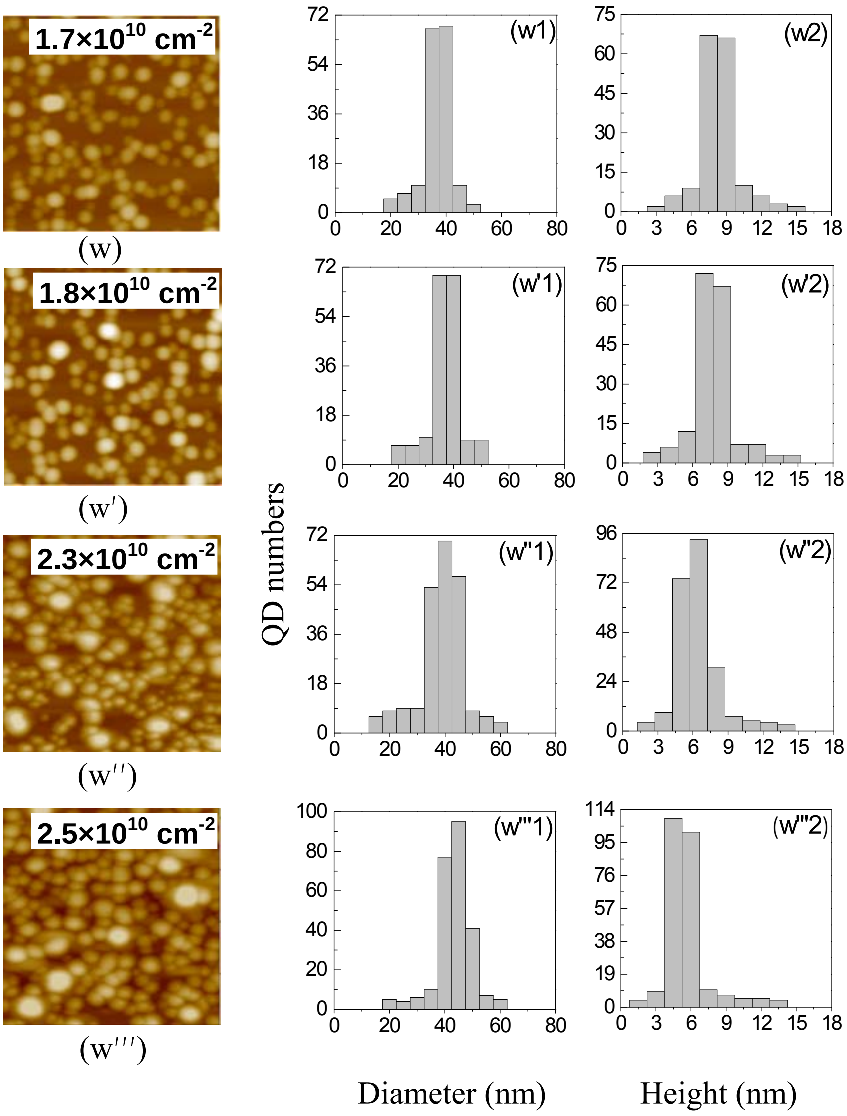

Figure 4.11 Top-view 1×1 μm^2 AFM images with dot-density insets of two-step grown InAs QD samples (w), (w'), (w'') and (w''') with TMIn source flux in step-2 growth set, respectively, at TMIn=15 sccm @ 15 s, 30 sccm @ 7.5 s, 56.3 sccm @ 4 s, 112.5 sccm @ 2 s. The total InAs layer thickness is kept the same. The dot diameter and height histograms related to each image are also shown.

Till now, it has been noticed that the average diameter & height of the dots formed in this work is around 40 nm & 7 nm, respectively, which is much larger than that of the QDs grown by using TBA/H_2 [176]. The dots grown under TBA/H_2 as reported in Ref. 176 have the average diameter & height of 20 nm & 5 nm, respectively, where the deposited InAs material of 2.6 MLs was even thicker than that used in this study. The reason for larger dots formed under TBA/N_2 than those formed under TBA/H_2 may be because of the lower thermal conductivity and larger viscosity of N_2 than that of H_2 as mentioned previously [177]. The atoms remained around the formed islands for longer time which increases the probability for them to be absorbed by the islands before they are desorbed or driven away to the exhaust. As a result, the total efficiency of the material consumed in forming the QDs in N_2 ambient was increased and hence the larger QDs were formed. On the other hand, InAs QDs grown by AsH_3/H_2 have been studied intensively for a long time [174, 178, 179, 180, 181]. The previous studies on InAs/GaAs QDs include: InAs QD formation on a strained InGaAs/GaAs matrix based on GaAs substrate [174], the InAs dots formed on the misorientated GaAs substrate [180] and the SiO_2 mask based area-controlled InAs QDs growth, etc. [181]. The dot morphology is strongly dependant on the matrix for the dots to form on top. However, the InAs QDs grown on GaAs(001) by using AsH_3/H_2 by other research groups can be compared reasonably with the InAs/GaAs QDs grown by using TBA/N_2 in this work. The reported highest InAs/GaAs QD density, to our best knowledge, was $1.5\times10^{11}cm^{-2}$ by using AsH_3/H_2 [178], much higher than the received dot density of $2.5\times10^{10}cm^{-2}$ in this work by using TBA/N_2. However, the QD surface coverage is only 12% as reported in Ref. 178, which is much lower than that, >40%, of this work. The relatively low dot density but with high surface coverage is because of the larger size of the dots formed under TBA/N_2 compared with the dots formed under AsH_3/H_2. The direct comparison of QDs formation by using the different carrier gases and/or arsenic sources in the same MOCVD reactor deserves the further research in future.

4.4 Transition energy of the QD structure

In this section, 8 band **k·p** theory is used to calculate the transition energies of the QD structure. The calculated transition energies of the QD structure are compared with the experimental results.

4.4.1 Introduction to the 8 band k·p theory model

For the theoretical analysis of the states in conduction-band and valence-band in low-dimensional structures (QWs, QWRs or QDs), the simple one-band effective-mass was initially used in this field [36, 182]. This method is of great value in the study of conduction-band states, but breaks down essentially in the valence-band study as well as the conduction band in the semiconductors with narrow band-gaps due to not considering the band coupling. The band coupling has an un-negligible effect on the valence-subband profile in QW [183], QWR and QD [184] structures. Moreover, a strong coupling between the conduction and valence bands also exists in the InAs/GaAs QD system due to the abrupt change in energy band profile from bulk to QD structure induced by the lattice mismatch strain [185 - 187]. The compressive strain is exerted on the InAs QDs from the surrounding GaAs confinement layers because the strained InAs QDs still has larger lattice constant than the GaAs layers after partially recovering their lattice constant to the InAs bulk lattice parameter during QDs self-assembly growth [143, 188]. One obvious energy band structure change can be seen from the change of the ground-state transition energy, E_g, in QD structure. The reported E_g at 2 K from the InAs/GaAs QDs is ~ 1.0 eV, which is much larger than that of InAs bulk crystal ~ 0.4 eV at 2 K [189, 190]. So, in this work, an 8-band **k·p** theory model, which will be presented in detail below, is used to theoretically calculate the transition-energy of the self-assembled InAs QD structures. In the 8-band **k·p** theory, the electron, heavy hole, light hole, spin-orbit splitting bands, the coupling between conduction and valence bands, and the coupling between the valence sub-bands are all taken into consideration.

The QD structure was prepared by capping a 50 nm GaAs cap layer after the post-growth interruption of InAs QDs growth. The TEM image, for which 200 kV accelerating voltage is set for the electron beam, of the QD structure is shown in Figure 4.12-(a). It shows the diameter (~ 35 nm) of the InAs QDs sandwiched between GaAs confinement layers is much larger than the QD's height (~8 nm),

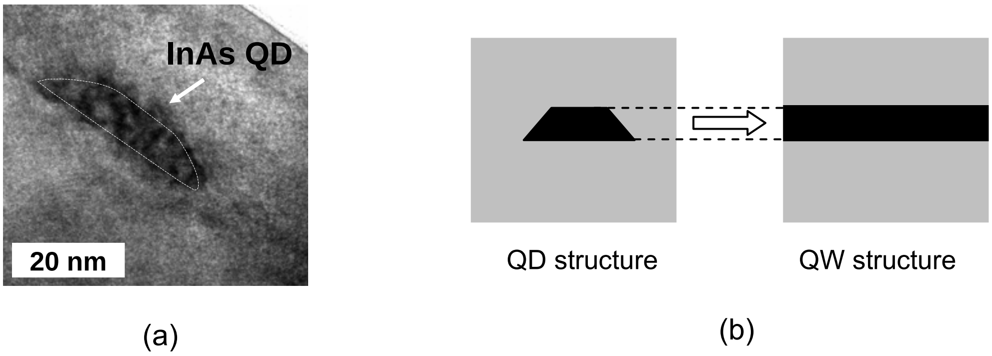

(a) (b)

Figure 4.12 (a) TEM cross-section image at $[\bar{1}10]$ *direction for the typical InAs dot capped with GaAs, and (b) approximation of QD structure into QW structure.*

We only took into account of the quantum confinement in the growth direction in the calculation, and the 3-D confinement QD structure was approximated into a 1-D confinement QW structure with the well width equal to the average height of the dots as shown in Figure 4.12-(b). The feasibility of such 1-D QW approximation for QD structure lies in the low aspect ratio, i.e. much smaller scale in dot height than that in dot lateral size, in the InAs/GaAs QD structures. In this case, the lateral quantum confinement on carriers is very weak compared with the vertical confinement in the QDs. Therefore, the dot size effect on the transition energy in QD structures is mainly determined by the height of the dots [107, 113, 191]. On the other hand, the QW approximation loses the other two quantum confinements in the dots. So, this approximation cannot give the accurate energy band structure of QDs and the calculated transition energy in the dots is expected to be slightly smaller than the actual value due to the omission in the lateral confinement consideration [107, 192].

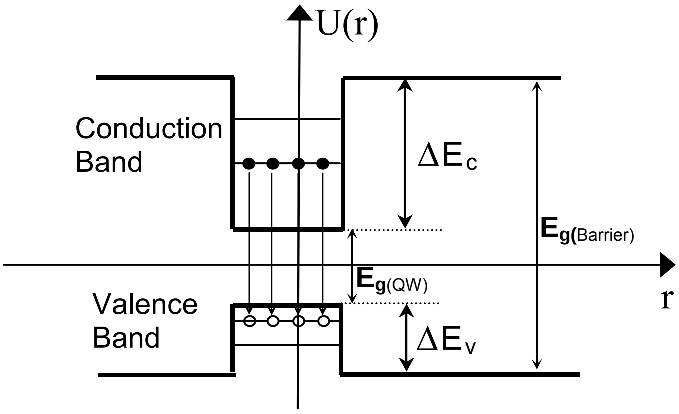

Figure 4.13 Schematic diagram of energy band line-up in the approximated QW structure.

Figure 4.13 shows the energy band structure of the QD structure with QW approximation. ΔE_c and ΔE_v are the band-edge discontinuities of conduction band and valence band, respectively. E_g is the material band gap. Y-axis U(r) represents the potential, and X-axis r donates the growth direction of the structure.

From the Effective Mass Theory for degenerate bands, the Schrödinger Equation with a perturbation $U(r)$ for a QW potential is:

$$[H + U(r)]\Psi(r) = E\Psi(r) \tag{4.2}$$

where the QW potential $U(r)$ is

$$U(r) = \begin{cases} \Delta E_c & |r| \geq L_w/2 \\ 0 & |r| < L_w/2 \end{cases} \tag{4.3}$$

for the conduction band and

$$U(r) = \begin{cases} -\Delta E_v & |r| \geq L_w/2 \\ 0 & |r| < L_w/2 \end{cases} \tag{4.4}$$

for the valance band. L_W is equivalent to the well width, i.e. dot's average height .

In the 8-band scheme, the total wave function in each layer of the QW structure can be written as

$$\Psi(r) = \sum_{j=1}^{8} F_j(r) u_j(r) = \sum_{j=1}^{8} \exp\left(ik_{//} \cdot \rho\right) \varphi_j(z) u_j(r), \quad j = 1,2,...,8 \tag{4.5}$$

where $F_j(r)$ is the envelope function, $k_{//} = (k_x, k_y)$ is a two dimensional in-plane wave vector which is a good quantum number, $\rho = (x, y)$ is a two dimensional in-plane space vector, and $r = (\rho, z)$. φ_j is slowly varying envelope function, and u_j is the periodic part of Bloch basis functions at zone center which are chosen to be eigenfunctions of the total angular momentum operators J and J_z. These basic functions $u_j = \left|J, J_z\right\rangle$ are linear combinations of the band-edge Bloch functions $\left|S\right\rangle$, $\left|X\right\rangle$, $\left|Y\right\rangle$, $\left|Z\right\rangle$, which have the same symmetry properties as the atomic s, x, y and z functions.

The 8×8 **k·p** Hamiltonian $\mathrm{H_k}$ including the electron, heavy hole, light hole and spin-orbit splitting bands is used. It is given by [186]

$$\mathrm{H_k} = \begin{bmatrix}
E_g + \frac{\hbar^2 k^2}{2m_c^{'}} & 0 & -pk_+ & \sqrt{\frac{2}{3}} pk_z & \frac{1}{\sqrt{3}} pk_- & 0 & \frac{1}{\sqrt{3}} pk_z & \sqrt{\frac{2}{3}} pk_- \\
0 & E_g + \frac{\hbar^2 k^2}{2m_c^{'}} & 0 & \frac{-1}{\sqrt{3}} pk_+ & \sqrt{\frac{2}{3}} pk_z & pk_- & \sqrt{\frac{2}{3}} pk_+ & \frac{-1}{\sqrt{3}} pk_z \\
-pk_- & 0 & F & H & I & 0 & \frac{H}{\sqrt{2}} & \sqrt{2} I \\
\sqrt{\frac{2}{3}} pk_z & -\frac{1}{\sqrt{3}} pk_- & H^* & G & 0 & I & \frac{1}{\sqrt{2}}(G-F) & -\sqrt{\frac{3}{2}} H \\
\frac{1}{\sqrt{3}} pk_+ & \sqrt{\frac{2}{3}} pk_z & I^* & 0 & G & -H & -\sqrt{\frac{3}{2}} H^* & \frac{-1}{\sqrt{2}}(G-F) \\
0 & pk_+ & 0 & I^* & -H^* & F & -\sqrt{2} I^* & \frac{H^*}{\sqrt{2}} \\
\frac{1}{\sqrt{3}} pk_z & \sqrt{\frac{2}{3}} pk_- & \frac{H^*}{\sqrt{2}} & \frac{1}{\sqrt{2}}(G-F) & -\sqrt{\frac{3}{2}} H & \sqrt{2} I & \Delta + \frac{F+G}{2} & 0 \\
\sqrt{\frac{2}{3}} pk_+ & \frac{-1}{\sqrt{3}} pk_z & \sqrt{2} I^* & -\sqrt{\frac{3}{2}} H^* & \frac{-1}{\sqrt{2}}(G-F) & \frac{H}{\sqrt{2}} & 0 & \Delta + \frac{F+G}{2}
\end{bmatrix}$$

(4.6)

where

$$k_+ = (k_x + ik_y)/\sqrt{2}\,, \tag{4.7}$$

$$k_- = (k_x - ik_y)/\sqrt{2}\,, \tag{4.8}$$

$$F = Ak^2 + \frac{B}{2}(k^2 - 3k_z^2)\,, \tag{4.9}$$

$$G = Ak^2 - \frac{B}{2}(k^2 - 3k_z^2)\,, \tag{4.10}$$

$$H = -Dk_z(k_x - ik_y)\,, \tag{4.11}$$

$$I = -\frac{\sqrt{3}}{2}B(k_x^2 - k_y^2) + iDk_xk_y\,, \tag{4.12}$$

$$A = \frac{\hbar^2\gamma_1}{2m_0}\,, \tag{4.13}$$

$$B = \frac{\hbar^2\gamma_2}{m_0}\,, \tag{4.14}$$

$$D = -\sqrt{3}\frac{\hbar^2\gamma_3}{m_0}\,, \tag{4.15}$$

and $p = (\hbar/m_0)\langle s|p_v|v\rangle = (\hbar/m_0)\cdot P_0$ (4.16)

where P_0 is the momentum matrix element for the conduction band. Δ is the spin-orbit splitting energy. γ_i (i=1, 2, 3) are modified Luttinger parameters defined in terms of the usual Luttinger parameters, γ_i^L, by

$$\gamma_1 = \gamma_1^L - \frac{E_P}{3E_g}\,, \tag{4.17}$$

$$\gamma_2 = \gamma_2^L - \frac{1}{2}\frac{E_P}{3E_g}\,, \tag{4.18}$$

$$\gamma_3 = \gamma_3^L - \frac{1}{2}\frac{E_P}{3E_g}\,. \tag{4.19}$$

E_P is the optical matrix parameter that is expressed as

$$E_P = 2m_0 p^2 / \hbar^2 \tag{4.20}$$

The strain part H$_s$ can be obtained by the following substitution because of the same underlying symmetry: $A \to -a_v$, $B \to -b$, $D \to d$, $k_x k_y \to \varepsilon_{xy}$, and $\hbar^2 k^2 / 2m_c^{'} \leftrightarrow a_c$, etc, for conduction band, where ε_{xy} is the strain tensor, b and d are the shear deformation potentials, a_v is the hydrostatic valence-band deformation potential, and a_c is the conduction-band deformation potential.

According to the Effective Mass Theory, we get

$$\left[H + U(z)\overset{=}{\mathrm{I}}\right] \cdot \begin{bmatrix} F_1 \\ \vdots \\ F_8 \end{bmatrix} = E \cdot \begin{bmatrix} F_1 \\ \vdots \\ F_8 \end{bmatrix} \tag{4.21}$$

where $H = H_k + H_s$, H_k is the 8-band **k·p** Hamiltonian, H_s is the strain Hamiltonian of the QW structure, $U(z)$ is the electron potential energy, $F_j(r)\,(j = 1,2,...8)$ are envelope functions and E is the eigen-energy of the QWs.

The envelope-function Fourier expansion method has been proven to be an effective method for calculating subband dispersions and wave functions in one-dimensional confinement structures [193, 194, 195]. So, to solve Eq. (4.21) for the QW structure we expand the envelope functions $F_j(r)$ to a discrete Fourier series, and then convert (4.21) to giant algebraic set of coupled equations for the Fourier coefficients. [195]. The expansion takes the form of

$$F_j(r) \cong \sum_{m=1}^{M} a_{j,m} \phi_m(z) \qquad j = 1,2,...,J \tag{4.22}$$

where $\phi_m(z) = \exp[i(k_x x + k_y y)] \frac{1}{\sqrt{L}} \exp\left[i\left(k_z + m \cdot \frac{2\pi}{L}\right) \cdot z \right]$, (4.23)

L is overall thickness of the QW structure, and $L = L_W + L_B$, where L_W is the well thickness equal to QD's average height in the approximation, and L_B is the total barrier layer thickness, m is an integer denoting the order of related expansion term, k_z is the wave vector at the growth direction, It is assumed $k_z = 0$ for the bound states in the calculations. Inserting (4.22) and (4.23) into (4.21), then multiplying by $\phi_m^*(z)$ and integrating over one QW period L, we get

$$\sum_{j',m'} H_{jj'}(m,m')a_{j',m'} = Ea_{j,m} \tag{4.24}$$

where the matrix elements $H_{jj'}(m',m)$ are given by

$$H_{jj'}(m,m') = \int_{-L/2}^{L/2} \phi_m^*(z)\left[H_{jj'} + \delta_{jj'}U(z)\right]\phi_{m'}(z)dz = \langle m|H_{jj'} + \delta_{jj'}U(z)|m'\rangle \tag{4.25}$$

when calculation direction is along z (the growth direction). For the approximated QW structure studied, the electronic potential function $U(z)$ that was included in Eq. (4.25) consists of two parts:

$$U(z) = V_0 + V_s, \tag{4.26}$$

where V_0 is the quantum confinement potential from the band discontinuity between barrier/dot and V_s is the potential change induced by strains. The subband energy eigen-values and the coefficients $a_{j',m'}$ can then be obtained by solving Eq. (4.24).

For the square barrier potential as in the case of the InAs/GaAs QD structure studied now, the integration of the barrier potential in the growth direction $U(z)$ with the expansion terms by approximating QD into QW structure takes the form of

$$\langle \phi_m|U(z)|\phi_m\rangle = V_1 \cdot L_B/L \tag{4.27}$$

$$\langle \phi_m|U(z)|\phi_{m'}\rangle = -V_1 \cdot \frac{\sin(\pi L_W f)}{\pi f L} \tag{4.28}$$

where $f = (m - m')/L$ and $L_B = L - L_W$ as mentioned previously.

In the following section, we'll use the 8-band **k·p** theory to calculate the transition energies of the InAs/GaAs QD structure under the QW approximation.

4.4.2 Theoretical calculation with experiment results comparison

By using the approximated 8-band **k·p** model as described in last section, the energy band structure for InAs/GaAs QD structure is calculated. In the calculation, the conduction band offset ratio of the InAs/GaAs system is assumed to be 85% [185]. The lattice mismatch induced strain between InAs material and GaAs substrate used is 7.2%. The other material parameters for InAs and GaAs at low temperature [196] used in the calculation are listed in Table 4.6. Based on the calculated subband structure, we have obtained one bound electron state ($E1$) with energy level of 1074.3 meV in conduction band, and three bound heavy and light hole states ($HH1$, $LH1$ and $HH2$) with energy levels of 72.5 meV, -42.8 meV and –145.4 meV, respectively, in valence band of the QDs at the zone centre (wave vector $k = 0$ at the dot line) in the momentum space. The edge of bulk valence band of the InAs material without strain is taken as the reference of zero energy for all the calculations. Based on the calculated $E1$, $HH1$, $LH1$ and $HH2$ energy levels, the received theoretical possible transition energy of $E1$-$HH1$, $E1$-$LH1$, and $E1$-$HH2$ is 1001.8 meV, 1117.1 meV and 1219.7 meV, respectively.

Table 4.6 Parameters used in calculations.

Parameters	GaAs	InAs
a_c (eV)	-7.17	-5.08
a_v (eV)	1.16	1.0
b (eV)	-2.0	-1.8
c_{11} (10 Gpa)	12.21	8.329
c_{12} (10 Gpa)	5.66	4.526
Lattice constant a (Å)	5.6533	6.0584
Luttinger parameter γ_1^L	6.98	20.0
Luttinger parameter γ_2^L	2.06	8.5
Luttinger parameter γ_3^L	2.93	9.2
Spin-orbit splitting energy Δ (eV)	0.341	0.390
Optical matrix parameter $E_P = 2P_0^2 / m_0$ (eV)	28.8	21.5

The experimental PL spectrum, measured at 10 K, of the InAs/GaAs QD structure is shown in Figure 4.14. Four emission peaks for the QD structure were observed. The first two emission peaks with higher photon energy are from GaAs bulk and the InAs wetting layer of the samples, respectively. The two peaks marked with n = 1 and 2 come from the InAs QDs. For better comparison, the calculated transition energies and the measured PL peak positions were both listed in Table 4.7.

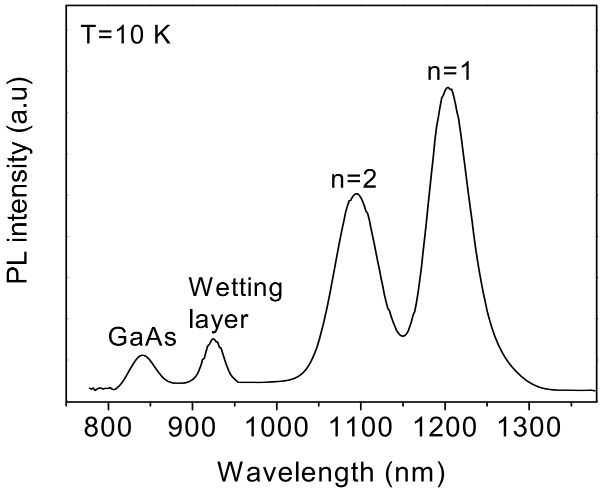

Figure 4.14 Low-temperature PL spectrum of the InAs/GaAs QD structure.

Table 4.7 List of the calculated E1, HH1, LH1 and HH2 energy levels relative to the valence band edge of InAs material without strain in InAs/GaAs QD structure by using 8-band ***k·p*** *theory, and the transition energy comparison for the QDs between theoretical calculated E1-HH1 & E1-LH1 and experimental measured results.*

Compared parameters		**Results**
Theoretical calculated	*E*1 (meV)	1074.3
	*HH*1 (meV)	72.5
	*LH*1 (meV)	-42.8
	*HH*2 (meV)	-145.
Theoretical calculated $E_{E1\text{-}HH1}$, $E_{E1\text{-}LH1}$ (meV)		1001.8, 1117.1
Experimental measured PL peak position (meV)		1030.8, 1133.5

It is deduced that the observed two PL peaks at 1.203 μm (1030.8 meV) and 1.094 μm (1133.5 meV) are attributed to *E*1-*HH*1 and *E*1-*LH*1 transitions in the QDs, respectively. The similar transition behavior in InAs/GaAs QD system was also reported in Ref. 189 and 197. Our calculated transition energies are consistent well with the PL experimental results, which shows the approximated 8 band **k·p** theory model can effectively direct our study on the QD electronic structure. Besides, the measured transition energies are systematically slightly larger than the calculated results. This is due to the neglected consideration of dot's lateral confinement, which will blueshift the transition energy although with small extent [107, 192].

4.5 Summary

In this chapter, MOCVD growth of InAs QDs on GaAs substrate, using TBA/N_2 to replace AsH_3/H_2, under different growth conditions has been investigated. It was found the dot formation was very sensitive to the growth condition. But the density and size uniformity of the QDs grown by the conventional one-step SK growth method were still low after the growth-conditions optimization.

In order to form higher quality dots, a new growth method of two-step growth, i.e. fast growth plus slow growth, was proposed. After optimizing the internal interruption time and the step-2 growth rate, the narrow dot size dispersion with several nanometers and high dot density of 2.5×10^{10}cm^{-2} were achieved.

8 band **k·p** theory with approximation was used to calculate the transition energies of the InAs/GaAs QDs. It was found that the calculated results match the experimental ones well. This shows that the approximated 8 band **k·p** model can effectively direct our studying and designing the target QD structures.

CHAPTER 5. MOCVD GROWTH OF MID-IR EMISSIVE InAs/InP QDs

5.1 Introduction

Large compressive strain in InAs/GaAs QDs induces a great increase in InAs band gap energy. The longest RT emission wavelength from InAs/GaAs QD system reported so far is only 1.52 μm [198]. It is impossible to realize mid-IR emission from InAs/GaAs QD structure. However, the lattice mismatch between InAs and InP is around 3.2%, which is much smaller than that of InAs/GaAs system. Growing InAs QDs on InP has advantage to reduce the band gap energy of the InAs QDs. Researches on InAs/InP QD systems for long wavelength emission have attracted much interest in the past years. Researchers have developed the QD structures for 1.55 μm wavelength emission, which has important applications in the ultra-low-loss optical fiber communications [199-201]. Extending the emission wavelength of InAs/InP QDs to mid-IR range has recently also attracted more and more research attention, because mid-IR optoelectronic devices are very important in variety of military, biomedical, environmental and industrial applications, including range-finding, laser surgery and remote trace-gas sensing, etc [2, 3, 81, 202]. An effective way to extend the emission wavelength of InAs/InP QDs into mid-IR region (2 ~ 5 μm) is by inserting In(Al)GaAs confinement layers in InAs/InP QD structures [12, 13, 203, 204]. However, InAs QDs formed self-assembly on InGaAs/InP matrix are generally with large size dispersion, which is caused by the anisotropic surface diffusion of In adatoms on InGaAs/InP matrix during InAs QDs' SK self-assembly growths [119,120]. Besides, the longest emission wavelength from the InAs/InP QD system reported so far is only 2.1 μm by embedding InAs QDs in InAlGaAs confinement layers [12]. Further improvement in the QDs' size uniformity and larger extension in the QDs' emission wavelength are both important in order to make them suitable for mid-IR optoelectronic device applications.

In this chapter, we first design the mid-IR emissive QD structures based on InAs/InP QD system by using the 8 band **k·p** theory model. Then, the investigation on growing the uniform-sized and high-density mid-IR QDs is carried out based on the two-step QDs growth method we proposed in Chapter 4. After that, the MOCVD growth, experiment investigation and analyzing for the designed mid-IR QD structures are carried out.

5.2 Design of mid-IR emissive InAs/InP QD structures

To extend the emission wavelength of InAs/InP QD structures, three factors are considered in the design: QD's size, QD's barrier height and lattice mismatch strain between QD and matrix layers. First, the size of the InAs QDs grown on InP matrix using our MOCVD system is varied from around 7 to 9 nm based on different QDs' growth conditions. In the design, the dot's size is assumed to be 9 nm. In order to tune the emission wavelength of InAs/InP QDs to the longer emission wavelength, InGaAs instead of InP layers are used as the barrier layers of InAs QDs. This is because InGaAs barrier height is lower than InP and can be reduced further by increasing Indium or decreasing Gallium compositions. At the same time, the lattice mismatch strain between InAs and InGaAs layer is decreased since the lattice constant of InGaAs layer increases with increasing the Indium content of InGaAs. This results in more strain relaxation in the strained InAs dots, thus lowering the electron/hole transition energy levels of the dots. So, using the composition-adjustable InGaAs as

InAs QDs' barrier layers is advantageous to extend the emission wavelength of the QD structure. In this section, the mid-IR emissive InAs/InP QD structures are designed based on the InGaAs barrier/strain engineering by using 8 band **k·p** theory to calculate the transition energies in the QD structures. Indium content of InGaAs can be tuned by two modes: directly or gradedly, thus forming the square or graded confinement barrier for the dots. Emission wavelength redshift degree by using two different, square and graded, InGaAs barriers in the InAs/InGaAs/InP QD structures has been studied, respectively, in the design.

5.2.1 Square-barrier mid-IR QD structures

Schematic diagram of the square barrier QD structures and the conduction band profiles of the structures are shown in Figure 5.1. The Indium content x of the $In_xGa_{1-x}As$ barriers of the $InAs/In_xGa_{1-x}As/InP$ QD structure (a), (b) and (c) is set at 0.53, 0.63 and 0.72, respectively. The thickness of the $In_xGa_{1-x}As$ barrier layer is assumed be equal to 35 nm.

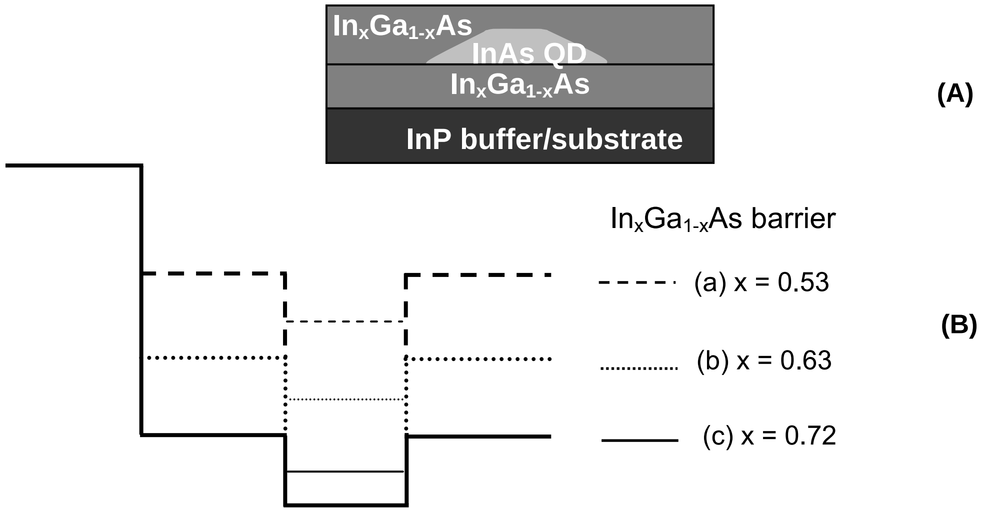

Figure 5.1 (A) Schematic diagram of the designed $InAs/In_xGa_{1-x}As/InP$ mid-IR QDs structures of (a), (b) and (c), and (B) the conduction band diagrams of the structures with different $In_xGa_{1-x}As$ square barriers.

The transition energies of the InAs/InGaAs/InP QD structures are also calculated under the QW approximation as described in Chapter 4. But for the InAs/$In_xGa_{1-x}As$/InP QD structure, the $In_xGa_{1-x}As$ confinement layers are compressively strained to the substrate InP when the barrier composition x is larger than 0.53. The strain between the InAs QDs and the upper InGaAs cap layer is reduced compared with that between InAs dots and InP layer, which is taken into consideration in the calculation. All the transition energies are calculated at the temperature of 77 K, so it can be compared with the measured 77-K PL emission wavelengths to be investigated in the experiment part of Section 5.4.

In the calculation, for the square barrier potential of the QD structure as shown in Figure 5.2, the integration of the InAs QDs potential energy in the growth direction $U(z)$ (refer to the $U(z)$ in Equation 4.21) with the expansion terms still takes the form of

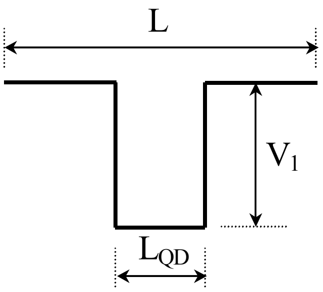

Figure 5.2 Schematic diagram of the potential in the growth direction of the QDs structure with InGaAs square barrier.

$$\langle \phi_m | U(z) | \phi_m \rangle = V_1 \cdot L_B / L \tag{5.1}$$

$$\langle \phi_m | U(z) | \phi_{m'} \rangle = -V_1 \cdot \frac{\sin(\pi L_{QD} f)}{\pi f L} \tag{5.2}$$

where $f = (m - m')/L$ and $L_B = L - L_{QD}$ (m is an integral denoting the order of related expansion term), V_1 is the InGaAs barrier potential height, L is overall thickness of the QD structure, and $L = L_{QD} + L_B$, where L_{QD} is the InAs QD's mean height and L_B is the InGaAs barrier layer thickness. It is assumed $k_z = 0$ for the bound states in the calculations.

The conduction band offset ratio of the InAs/In$_x$Ga$_{1-x}$As system is assumed to be 95% [205]. Except the band gap energy and electron effective mass, most parameters for the ternary compounds are obtained using a linear interpolation between the parameters of the relevant binary semiconductors. The material parameters for binary semiconductors used in the calculation are listed in Table 4.6 of Section 4.4.2.

Figure 5.3 shows the ground state electron energy level ($E1$) in conduction band and the ground state heavy hole energy level ($HH1$) in valence band of the QDs. The transition energy, $E1$-$HH1$, of the InAs QD structure at wave vector k = 0 in the

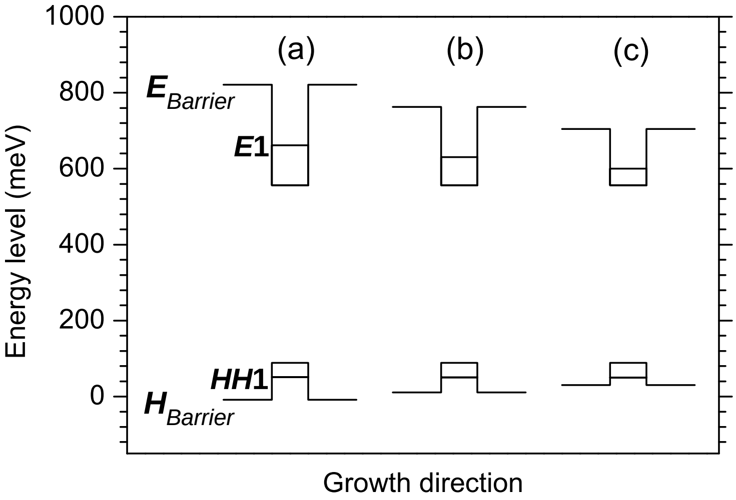

Figure 5.3 Energy band profiles as a function of the structure layer along the growth direction are plotted for the InGaAs/InAs(QDs)/InGaAs QD structures (a), (b) and (c) with different InGaAs square barriers based on 8-band $\mathbf{k{\cdot}p}$ *theoretical calculation. The thickness of structure's layers along x-axis is not the exact value.*

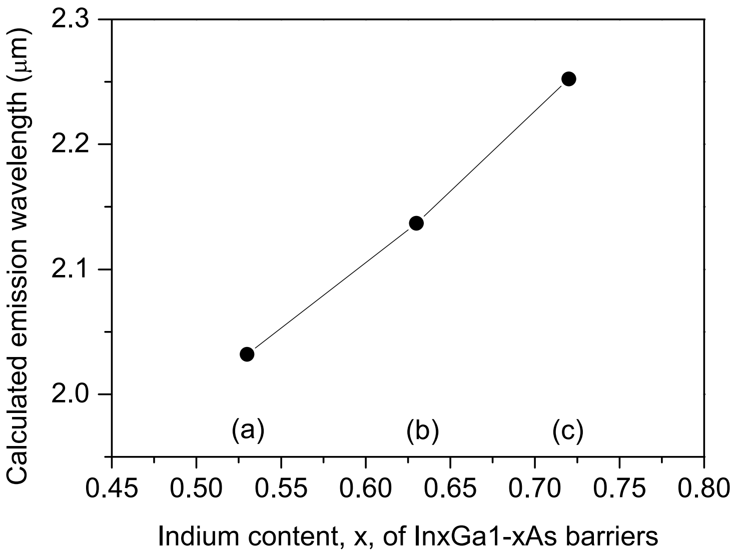

Figure 5.4 Emission wavelength of the designed (a)-(c) InAs/InGaAs/InP QDs structures as the function of the Indium content of $In_xGa_{1-x}As$ *barrier layers.*

momentum space can be obtained. The barrier energy levels of the QD structures were also calculated after taking account of the strain effect. For all the calculation, valance band edge of InAs bulk material was taken as the reference zero point. Based on the calculated band profiles, transition energies of the QD structures and thus the emission wavelengths of the QD structures (a) to (c) as the function of $In_xGa_{1-x}As$ barriers' Indium content, x, has been plotted in Figure 5.4. It shows that when the indium content of $In_xGa_{1-x}As$ barriers is increased from 0.53 to 0.72, the emission wavelength of $InAs/In_xGa_{1-x}As/InP$ QD structure is redshift by 220 nm and reaches 2.25 µm at the temperature of 77 K.

5.2.2 Graded-barrier mid-IR QD structures

To further extend the InAs QD structure's emission wavelength, graded InGaAs barrier InAs QD structures are proposed. The gradation, y, of the graded $In_{0.53\rightarrow(0.53+y)}Ga_{0.47\rightarrow(0.47-y)}As$ barriers is changed from 0.12 to 0.37. Figure 5.5 shows the schematic structures of the graded barrier InAs QD structures. The compositions of the cap and bottom graded InGaAs barriers are symmetric in all the graded barrier QD structures.

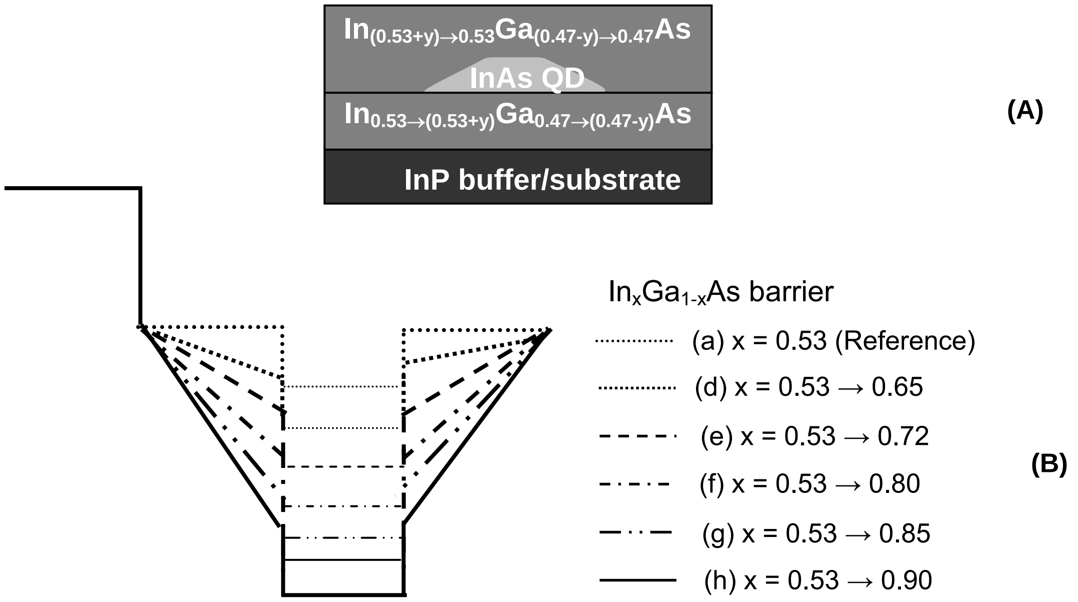

Figure 5.5 (A) Schematic diagram of the designed InAs/In_xGa_{1-x}As/InP mid-IR QDs structure of (d) - (h) and (B) the conduction band diagrams of the structures with different In_xGa_{1-x}As barriers. (a) is the Ref. QD structure.

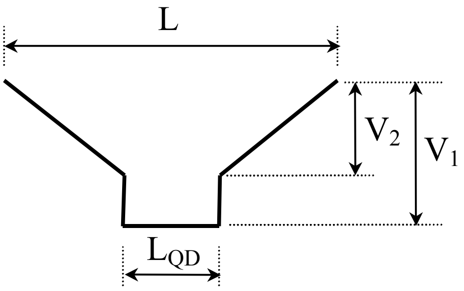

Figure 5.6 Schematic diagram of the potential in the growth direction of the QDs structure with graded InGaAs barriers.

The transition energy of graded barrier QD structure has been calculated using 8 band **k·p** theory. As shown in Figure 5.6, the integration of the QDs potential energy in the growth direction $U(z)$ with the expansion terms takes the form of

$$\left\langle \phi_m \middle| U(z) \middle| \phi_m \right\rangle = \left(V_1 \cdot L_B - V_2 \cdot \frac{L^2}{2L_B} + V_2 \cdot L_{QD} + V_2 \cdot \frac{L_{QD}^2}{2L_B} \right) \Big/ L \tag{5.3}$$

$$\left\langle \phi_m \middle| U(z) \middle| \phi_{m'} \right\rangle = \left(-V_2 \cdot \frac{2L}{L_B} \cdot \frac{\sin^2(0.5\pi L f)}{\pi^2 L f^2} - (V_1 - V_2) \cdot \frac{\sin(\pi L_{QD} f)}{\pi f} + V_2 \cdot \frac{2L_{QD}}{L_B} \cdot \frac{\sin^2(0.5\pi L_{QD} f)}{\pi^2 L_{QD} f^2} \right) \Big/ L \tag{5.4}$$

Where the items *f, L,* L_{QD} *and* L_B are defined the same as those used in the Equations of (5.1) and (5.2). The k_z is still assumed to be equal to zero for the bound states in the calculations.

The calculated typical subband profiles for the graded-barrier QD structure is shown in Figure 5.7. The ground electron energy level (*E*1) in conduction band and

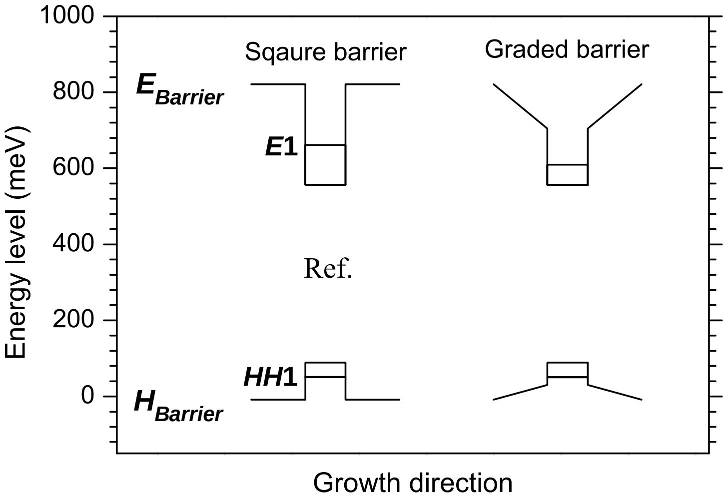

Figure 5.7 The calculated energy band profiles for the InGaAs/InAs(QDs)/InGaAs QD structures of (e) in Figure 5.5 with graded InGaAs barriers. The square-barrier based structure of (a) is for the reference.

the ground heavy hole energy level (*HH*1) in valence band, so the transition energy, *E*1-*HH*1, in the InAs QDs at wave vector k = 0 in the momentum space are obtained. The band profiles of the $In_{0.53}Ga_{0.47}As$ square-barrier based QD structure is also shown in Figure 5.7 for the reference.

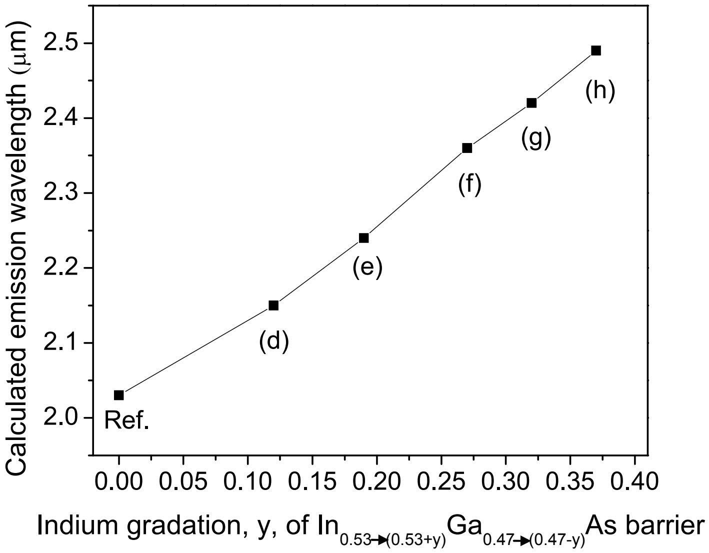

Figure 5.8 Emission peak position of the theoretical designed (d)-(h) InAs/InGaAs/InP QD structures as the function of the gradation of the different $In_xGa_{1-x}As$ *barrier layers.*

Figure 5.8 shows the calculated emission wavelength of InGaAs graded barrier InAs QD structure as the function of the Indium gradation, y, of $In_{0.53\rightarrow(0.53+y)}Ga_{0.47\rightarrow(0.47-y)}As$ barriers. It shows that when the gradation reaches 0.37, i.e. with $In_{0.53\rightarrow0.90}Ga_{0.47\rightarrow0.10}As$ barriers for the InAs dots, the longest emission wavelength reaches around 2.5 μm.

5.3 Form high quality InAs QDs on the InGaAs/InP matrix

In Chapter 4, a two-step growth of QD method has been proposed to grow high density and uniform InAs/GaAs QDs. In this section, this two-step growth method is used in the growth of InAs/InGaAs/InP QDs. InAs/InGaAs/InP QDs is a different QD system with smaller lattice-mismatch strain (3.2%) than that (7.2%) of InAs/GaAs QD system. Besides, the designed InAs QD structures for mid-IR emission employ the compressively strained InGaAs layers on InP substrate. That is, the InAs QDs will be grown on a strained InGaAs/InP matrix. Deposition conditions of two-step growing the high-quality InAs/InGaAs/InP QDs will be explored in this section. For comparison, four different QDs growth methods with different growth conditions are investigated on the formation of InAs QDs on the two different $In_{0.53}Ga_{0.47}As/InP$ and $In_{0.53-0.72}Ga_{0.47-0.28}As/InP$ matrixes. The unstrained $In_{0.53}Ga_{0.47}As/InP$ matrix is used for the comparison with the typical graded strained $In_{0.53-0.72}Ga_{0.47-0.28}As/InP$ matrix. The four growth methods include the ordinary SK growth, two-step of fast-growth + slow-growth (FG+SG for short), atomic layer epitaxy (ALE) and two-step of fast-growth + ALE (FG+ALE). The growth conditions studied include growth temperature, growth rate and V/III flux ratio.

5.3.1 Different InAs QDs growth methods

The growth conditions for growing the QDs layer of four different growth methods are summarized in Table 5.1. The growth temperature for all the samples was set at 550 ^{o}C, which advantages growing higher crystal quality top cap layers for the dots to be capped. In samples (a) - (d), InAs QDs are grown on the $In_{0.53}Ga_{0.47}As/InP$ matrix using the four growth methods, and for samples (a’) - (d’), the QDs are grown on the graded $In_{0.53-0.72}Ga_{0.47-0.28}As/InP$ matrix. The reactor pressure was set at 20 mbar for growing the InAs QDs, and it was set at 100 mbar for growing all other layers. A 200 nm InP buffer followed by a ~ 35 nm InGaAs matrix layer was grown on InP (001) substrate at 600 ~ 630 ^{o}C before growing the InAs QDs. Nominal InAs layer thickness for all the samples was targeted at 6.7 MLs.

In ordinary SK method self-assembly growth of InAs QDs, (a)/(a’), the InAs QD layer was grown in one-step growth with fast growth rate. The InAs growth rate

Table 5.1 Comparison of four different growth methods for growing InAs QDs on the two different matrixes: $In_{0.53}Ga_{0.47}As/InP$ matrix for samples (a)-(d) and $In_{0.53-0.72}Ga_{0.47-0.28}As/InP$ matrix for samples (a')-(d'), where the group-III TMIn source flux and the growth time for growing the InAs QDs layer were listed.

Growth mode (Samples)	**TMIn source flux and duration time during growth**				
Ordinary SK	**One-step fast growth**				
(a)/(a')	200 sccm, 8 s				
Two-step (FG+SG)	**Step 1**	**Internal interruption**	**Step 2**	**Post-growth interruption**	
(b)/(b')	200 sccm, 4 s	2 s	50 sccm, 16 s	5 s	
ALE in each cycle	**On_TMIn**	**Off**	**On_TBA**	**Off**	
(c)/(c')	50 sccm, 2 s	1 s	40 sccm, 3 s	1 s	(8 cycles)
Two-step (FG+ALE)	**Step 1**	**Internal interruption**	**Step 2**		
(d)/(d')	200 sccm, 4 s	2 s	ALE (4 cycles)		

was 0.83 ML/s with the TMIn flux setting at 200 sccm and grew for 8 seconds. Samples (b)/(b') were grown by two steps: after fast growing a thin InAs layer, the growth was interrupted for few seconds by closing the TMIn source flux and then continued growing the InAs by using the slow growth rate of 0.2 ML/s. In the step-1 growth of such two-step growth method, the growth conditions were identical as that used in the ordinary SK growth method for growing samples (a)/(a'), but only grew for 4 seconds. For the ALE growth of InAs QDs, (c)/(c'), the group-III TMIn source and group-V TBA source were switched on and off alternatively, so to make the

growth in atomic layers in each cycle. Between on and off the MO sources, a short interruption, few seconds, was introduced in. Multi-repeat of such growth procedures is used to realize multiple-cycle growth of InAs QDs layer. The TMIn and TBA flux used in each atomic layer growth cycle was set at 50 sccm and 40 sccm, respectively. After 2-second opening of the TMIn source, there was a 1-second interruption, and then TBA source was opened for 3 seconds followed by another 1-second interruption. The fourth growth method is a different two-step method for growing samples (d)/(d'). In this two-step method, the step-1 fast growth is identical as that used for growing samples (b)/(b'). But, after the few-second interruption following step-1 growth, the ALE growth method is used in step-2 growth to grow the continued InAs layer, replacing the slow growth used for samples (b)/(b'). Growth conditions in this step-2 ALE growth of InAs are the same as that used in the ALE method for growing samples (c)/(c'), but only grew for 4 cycles. So that the total InAs layer thickness was kept the same for all the samples (a)/(a') to (d)/(d').

The top-view AFM morphology and the corresponding low temperature PL spectrum of these uncapped QDs samples are shown in Figure 5.9. In order to receive low temperature PL spectrum, the QD samples are cut into small pieces with 3mm×5mm size and put into the cooling chamber with the chamber temperature controlled at 20 K during the measurement. Dot's size standard deviation, dot density, the PL peak intensity and linewidth are summarized in Figure 5.10. The standard deviation σ of dot's height and diameter has been calculated. Equation (4.1) is used for calculating the mean dot height h_g and the corresponding standard deviation was calculated by using following formula [162],

$$\log_{10}\sigma = \left(\frac{\sum \left[n \left(\log_{10} h_n - \log_{10} h_g \right)^2 \right]}{N} \right)^{1/2}, \qquad (5.5)$$

where N is the total number of the dots counted on the sample for the calculation, n is the number of the QDs counted with the same dot height of h_n. Mean dot diameter and the corresponding standard deviation was calculated using similar equations.

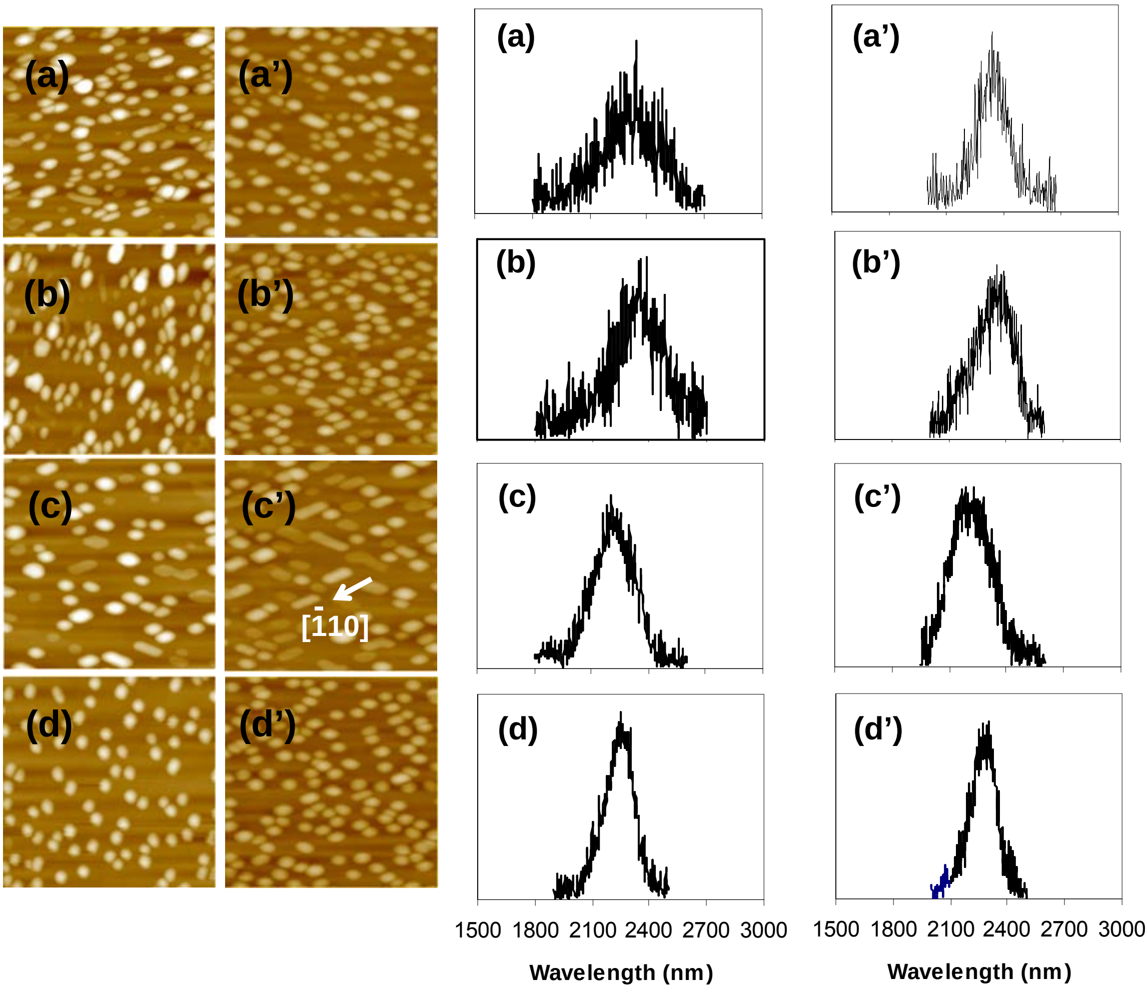

Figure 5.9 AFM (1×1 μm^2) top-view images and 20-K PL spectra for samples (a) – (d) with InAs QDs grown on In$_{0.53}$Ga$_{0.47}$As/InP matrix and samples (a')-(d') with InAs QDs grown on In$_{0.53\text{-}0.72}$Ga$_{0.47\text{-}0.28}$As/InP.

As shown in Figure 5.10, compared with samples (a)/(a') which were grown by using conventional SK method, samples (b)/(b') do not show an obvious improvement in QD density and dot-size dispersion, so without obvious improvement in PL peak intensity and linewidth. Samples (c)/(c') grown by using ALE growth method have low QD density and broad size dispersion, and show a broad PL spectrum and low PL intensity. However, samples (d)/(d') which were grown by the two-step of FG+ALE growth method have the smallest dot-size dispersion; and their

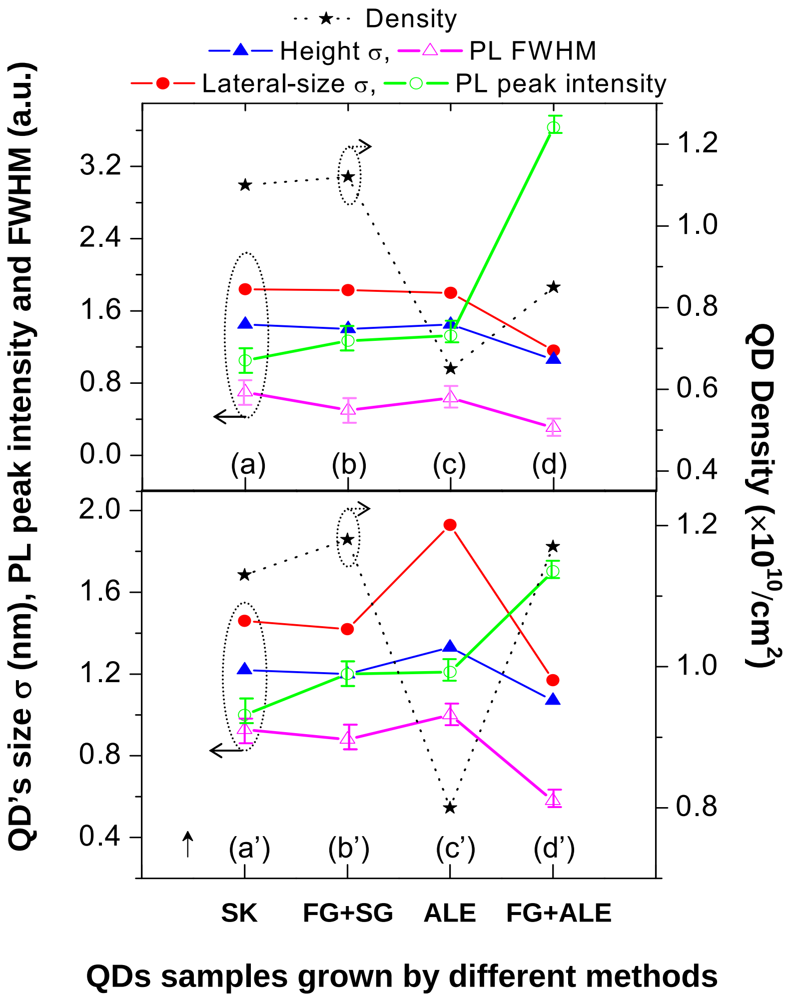

Figure 5.10 Comparison of the InAs QDs parameters including: dot-density, dot-size standard deviation (σ), PL peak intensity and linewidth for samples (a)/(a') - (d)/(d') based on the AFM images and PL spectra in Figure 5.9.

PL peak intensity and linewidth are improved greatly compared with other samples, although the dot-density of (d)/(d') is not higher than that of samples (a)/(a') or (b)/(b') as shown in Figure 5.9 and 5.10. The observed QDs formation trend and PL results under different growth methods are discussed in the following.

AFM images of SK fast grown InAs QDs of samples (a) and (a') with different InGaAs/InP matrixes (see Figure 5.9) show the similar QDs morphology: the dots are with high dot density but broad size dispersion. This also could be seen from the large standard deviation σ of the dot diameter and height of the two samples as shown in Figure 5.10. This indicates that using fast SK growth mode is difficult to grow uniform sized InAs/InGaAs/InP QDs. It has been reported that the elongated InAs QDs (dash) was formed on InGaAs/InP because of the anisotropic surface diffusion of adatoms induced by As dimer surface reconstruction under As-terminated growth [206, 207]. For sample (a) and sample (a'), randomly distributed in-homogeneous QDs were formed. No dash is observed in these two samples. This is because in ordinary SK growth of QDs, the QDs are formed self-assembly when the strain energy in InAs wetting layer was released; and under the fast growth rate, the nucleation rate of QDs is high because the Indium atoms are forced to coalesce due to the short surface diffusion time/length, which suppresses the formation of dashes [120]. But, at the same time, the nonuniform strained surface layer leads to form the nuclei or dots in high density with nonuniform size [208]. So, dots grown by ordinary SK growth is not uniform in size distribution, and as expected, their PL curve linewidth is wide with low PL peak intensity.

For the ALE grown samples (c)/(c'), it is observed that some InAs dashes, especially for sample (c'), were also formed besides the dots. More dash structures formed in sample (c') than that in (c) is attributed to the strained roughened surface of $In_{0.53-0.72}Ga_{0.47-0.28}As$ matrix layer due to its lattice mismatch to InP buffer/substrate. There are three types of nanostructures formed (see AFM image of (c')). The first type is anisotropic quantum dashes (QDHs) aligned along $[\bar{1}10]$ direction. The second type is also in dash form but these QDHs are not aligned along $[\bar{1}10]$ direction.

Formation of the two types of QDHs was because the anisotropic surface diffusion of adatoms during the InAs QD layer growth on InGaAs matrix [206, 207, 209], and the strain induced roughening of $In_{0.53-0.72}Ga_{0.47-0.28}As$ matrix layer enforces adatoms' anisotropic diffusion. However, the reason for the two types of dashes is still not clear. The third type is QDs. These QDs are formed between the dashes. About half of the total dots formed on sample (c') are the QDs. The energy barrier at the edge of the formed dashes is higher when the lateral size of the dashes increases. This energy barrier prevents the Indium atoms approaching the dashes, which limits the dashes growing further [173]. These Indium atoms then self-nucleate between the dashes and new dots are formed. As shown in the AFM images of sample (c'), the dashes are with lower height but longer size: the aspect ratio of the dashes is about 0.05, while for the QDs the aspect ratio is around 0.15. Large variation of the dot size distribution in sample (c') is because there are both dashes and dots formed during the ALE growth. So it shows QDs grown by ALE-method have low density, $0.6 \sim 0.8\times10^{10}$ cm^{-2}, and broad dot-size dispersion. This could also be seen from the dot's diameter standard deviation, over 1.8 nm. Correspondingly, the PL peak intensity is not high and PL linewidth is not narrow.

Samples (b)/(b') were grown by using the FG+SG two-step growth method. Their dots' size uniformity and PL performance are much lower than that of samples (d)/(d'), which were grown by FG+ALE two-step method. In the two-step growth, the advantages of using fast growth rate in step-1 growth are: suppressing the formation of dash-like structures [120] and forming high-density nuclei for further QDs growth. During the internal growth interruption and the step-2 growth, the meta-stable adatoms on the surface redistributed because of the concentration gradient [210]; some of these adatoms could self-nucleate to form new nuclei between large islands as mentioned previously, which is advantageous to density increase of the dots formed. The difference between FG+SG and FG+ALE growth methods lies in the step-2 growth, where the formed high density nuclei further developed into the final QDs. Compared with the slow growth (SG), in the ALE growth, there is an interruption between alternatively opening TMIn and TBA sources. These interruptions give longer time for atoms to be selectively incorporated onto the smaller islands for growth under kinetically self-limiting growth as discussed in Chapter 4. As a result, the size uniformity is improved (see dots' size standard deviation σ in Figure 5.10) when the dots are grown by the FG+ALE two-step growth instead of the FG+SG two-step method. Although, the dot-density of FG+ALE grown QDs is not higher than that of FG+SG grown dots, but their PL intensity and linewidth is much better than that of FG+SG grown QDs. This shows the crystal quality of the FG+ALE grown QDs is improved, which is attributed to the longer interruption in the ALE growth than that in slow growth used in step-2 growth. The longer interruption advantages breaking the weak atom-bonding of the grown-defects formed in the QDs [174], thus increasing the dots' crystal quality.

Besides, the dot density of sample (d') is 1.17×10^{10} cm^{-2}, which increased by around 38% from 0.85×10^{10} cm^{-2}, the density of (d), as the AFM images shown in Figure 5.9. Also, the dots of sample (d') are larger than those of (d) in the size. This is because: first, the strain-induced rough surface of $In_{0.53-0.72}Ga_{0.47-0.28}As$, compared with $In_{0.53}Ga_{0.47}As$, layer provides more sites for forming the InAs nuclei which results in higher dot density; Secondly, rough matrix layer surface enhances the probability for adatoms to be adsorbed and then increases the consumption efficiency of the Indium source during the InAs layer deposition. Therefore, InAs QDs formed on strained $In_xGa_{1-x}As/InP$ matrix have higher density and larger size than those grown on unstrained $In_{0.53}Ga_{0.47}As/InP$ matrix. It has been estimated that the nominal thickness of the formed InAs QDs of sample (d') is about 2.8 MLs which is about 1 ML thicker than that of sample (d). The QD's forming efficiency, defined as the ratio of the total volume of the formed InAs QDs versus the total input InAs material during the MOCVD growth, of (d') is about 56% higher than that of sample (d). These results show that under using the FG+ALE two-step method for InAs QDs growth, the dot density could be increased further with the slight increase in dot size if InGaAs/InP matrix is strained. This is significant to develop such QD systems for mid-IR applications. In conclusion, the FG+ALE two-step method improves the dot size uniformity, and further increases the dot density if growing the dots on the strained $In_{0.53-0.72}Ga_{0.47-0.28}As/InP$, instead of the matched $In_{0.53}Ga_{0.47}As/InP$, matrix. In the following, the growth conditions of the FG+ALE two-step method will be optimized further to improve the dot density and crystal quality of the dots grown on the strained $In_{0.53-0.72}Ga_{0.47-0.28}As/InP$ matrix.

5.3.2 Step-1 nucleation growth dependence

In the two-step QDs growth, 3-D island nucleation starts in step-1 growth and then followed by the kinetic self-limiting growth of uniform QDs in step-2 ALE growth. In previous studies, optimization of the step-2 growth has been investigated. However, the first step nucleation has important impact on the morphology and crystal-quality of the QDs finally formed in the two-step growths.

In this section, the effects of growth rate, substrate temperature and input sources V/III ratio for the first step InAs QDs nucleation growth on InAs/InGaAs/InP QDs formation are investigated. The optimized ALE growth is used in the second step growth for all the QDs growths. And the InAs QDs are grown on the strained $In_{0.53-}$

$_{0.72}$Ga$_{0.47\text{-}0.28}$As/InP matrix. The detailed growth conditions for InAs QDs layer growths were listed in Table 5.2.

Table 5.2 Comparison of growth rate (samples (e)-(h)), growth temperature (samples (i)-(m)) and V/III flux ratio (samples (n)-(u)) for growing InAs QDs on In$_{0.53\text{-}0.72}$Ga$_{0.47\text{-}0.28}$As/InP matrix. The other common growth conditions are also listed.

Two-step growth QDs samples	Step 1	Internal interruption	Step 2 (ALE)	Post-growth interruption
(e) – (h)	**0.42~1.68 ML/s** (550 °C & V/III = 6.5)	2 s	4-cycle monolayer growth:⎍⎍	5 s
(i) - (m)	**Temp: 460 ~ 600 °C** (0.84 ML/s & V/III = 6.5)			
(n) – (u)	**V/III ratio = 0 ~ 11** (0.84 ML/s & 550 °C)			

(i) *Effect of the growth rate*

First, for the growth-rate study, four samples (e), (f), (g) and (h) were grown by setting the growth rate in step-1 at 0.42, 0.84, 1.26 and 1.68 ML/s, respectively, when growing the QDs layer. Top-view AFM images and the corresponding low temperature PL spectra of these samples are shown in Figure 5.11. Dot's size standard deviation, dot density, PL peak intensity and linewidth are summarized in Figure 5.12.

The results show that when the growth rate is around 0.84 ML/s in step-1 growth, the sample (sample (f)) has the highest dot density, strongest PL emission intensity and narrowest PL spectrum, which indicates the narrowest dot size dispersion and high crystal-quality of the QDs of sample (f). The kinetic theory of stress driving QD growth shows that the 3-D island surface density rises with increasing the growth rate, V, approximately as $V^{3/2}$ [211]. In the two-step growth, QDs growth is divided into two steps. In step-1 growth, high-density nuclei are formed. Then the formed nuclei will further develop into the QDs in step-2 ALE

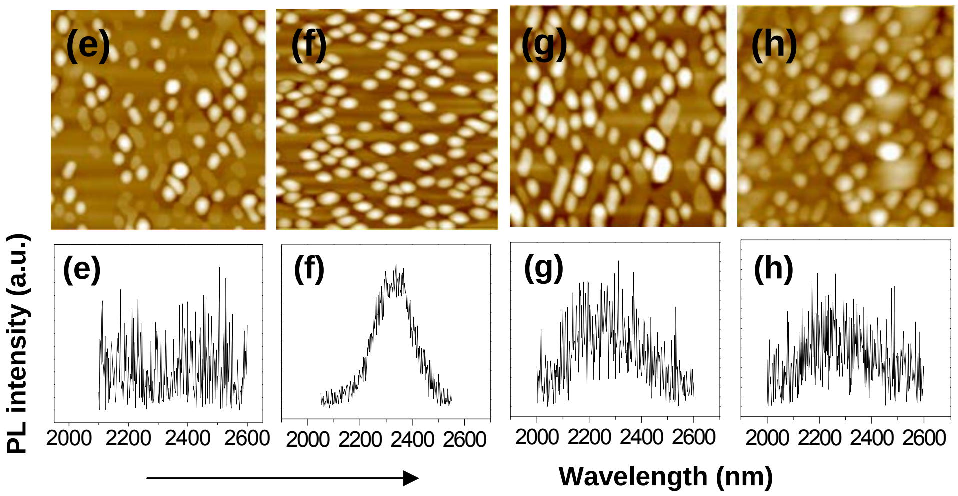

Figure 5.11 AFM ($1\times1\mu m^2$) top-view images and 20-K PL spectra for samples (e) – (h) with different growth rates in step-1 growth during growing InAs QDs on $In_{0.53-0.72}Ga_{0.47-0.28}As/InP$ matrix.

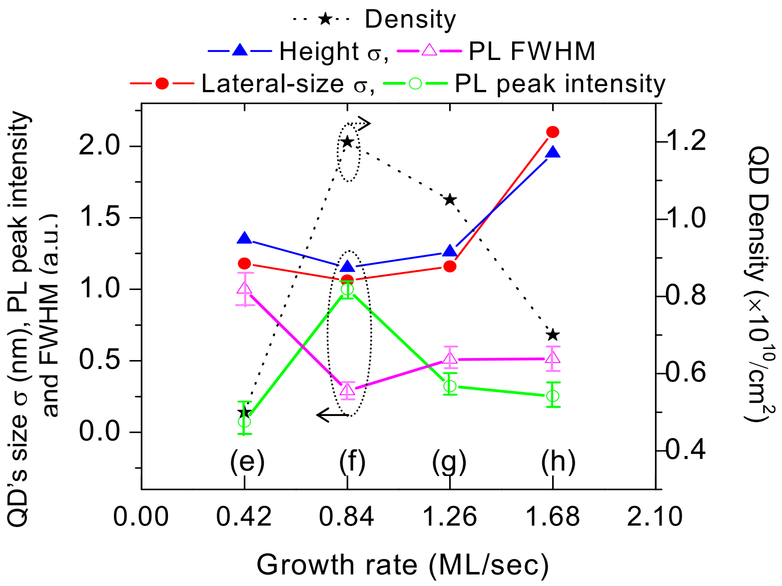

Figure 5.12 Comparison of the InAs QDs parameters including: dot-density, dot-size standard deviation (σ), PL peak intensity and linewidth for samples (e) – (h) based on the AFM images and PL spectra in Figure 5.11.

growth. As predicted in Ref. 211, the characteristic time of the nucleation during the QD formation is much shorter than the time for the nuclei being developed into the

QDs. In two-step growth of QDs, if the growth rate, thus the nucleation rate, in step-1 growth is too fast, ≥ 1.26 MLs/s, a large amount of strain energy must be dissipated with the insufficient time for single-crystalline material formation. This causes the formation of non-crystalline defects in the QDs. These defects are with lower energy barrier and grow faster than the crystallographically-selective slow-growing single-crystals [169]. These defects will become the seeds for forming the incoherent islands or even the large clusters. As a result, the crystal quality, dot density and size uniformity of the QDs will be affected if the growth rate is too high in step-1 growth. This is shown from the measured results of samples (e), (f), (g) and (h) in Figure 5.11 and Figure 5.12: when the growth rate in step1 growth is increased properly from 0.42 ML/s to 0.84 ML/s, the dot density, size uniformity and PL emission of the sample has been improved much. But when the growth rate is increased to 1.26 MLs/s and above with less than 2.7-second duration in step-1 growth, the dot density decreases due to the small QDs being consumed for the ripening growth from the incoherent islands into the large clusters. This obviously degrades the dot size-uniformity and PL emission intensity of the samples. So, the growth rate of 0.84 ML/s in step-1 QD growth is selected for the further study since which brings with the best dot morphology and crystal quality, and then the best PL emission performance.

(ii) *Effect of the growth temperature*

To investigate the effects of the substrate temperature on the InAs/InGaAs/InP QDs formation, five samples, samples (i), (j), (k), (l) (= (f)) and (m), were grown at the temperature of 460, 500, 520, 550 and 600 ^{o}C, respectively, while the growth rate in step 1 was set at the optimized growth rate of 0.84 ML/s and other growth conditions were kept the same during the growths. Figure 5.13 shows the AFM images and the low temperature PL spectra of the five samples. The dot size standard deviation, dot density, PL peak intensity and PL spectrum linewidth of the samples are summarized in Figure 5.14.

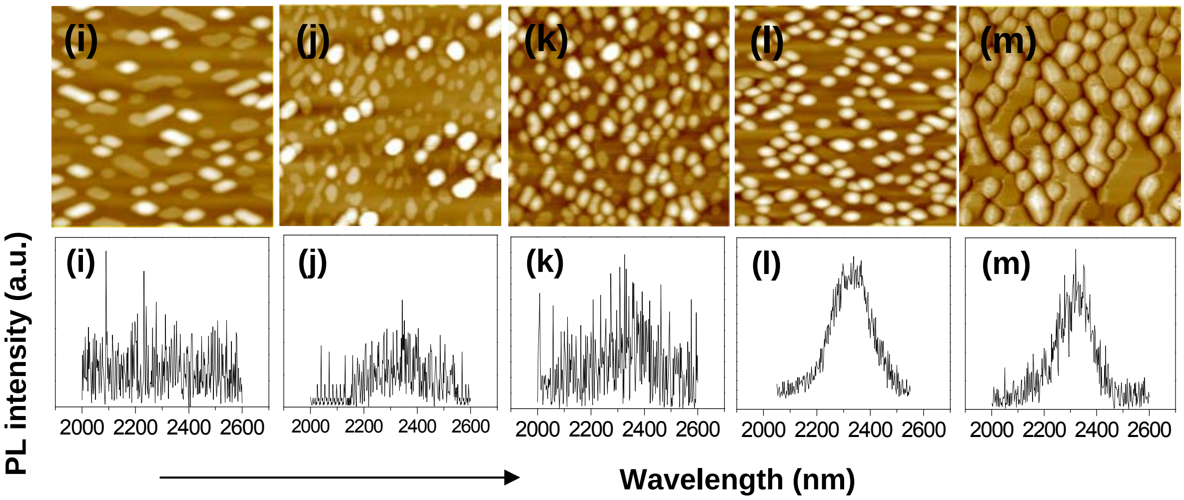

Figure 5.13 AFM (1×1μm²) top-view images and 20-K PL spectra for samples (i) – (m) with different growth temperatures for growing InAs QDs on In$_{0.53\text{-}0.72}$Ga$_{0.47\text{-}0.28}$As/InP matrix.

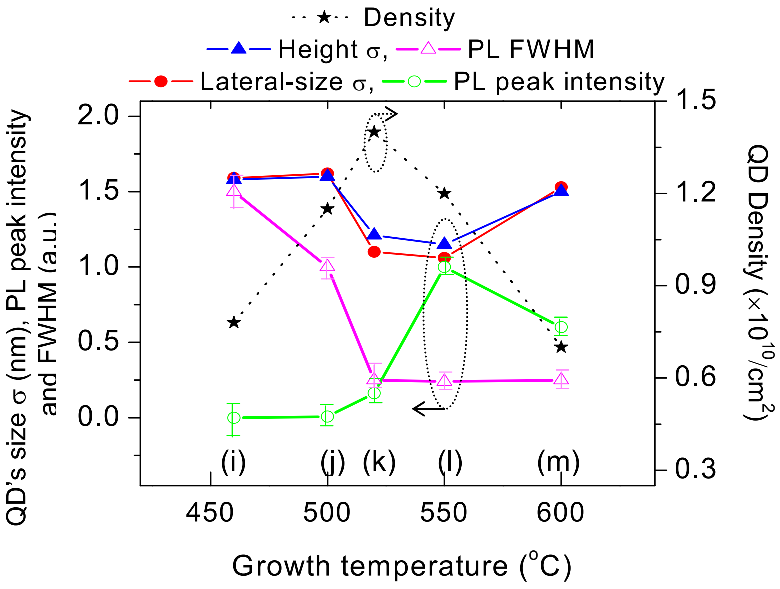

Figure 5.14 Comparison of the InAs QDs parameters including: dot-density, dot-size standard deviation (σ), PL peak intensity and linewidth for samples (i) - (m) based on the AFM images and PL spectra in Figure 5.13.

It has been observed: (I) when grown at low temperature, 460 °C, bi-modal sized QDs were formed; when the temperature was increased to 550 °C, the dot size dispersion becomes narrower, but it becomes broader again when the temperature was further increased to 600 °C; (II) The highest dot density of the sample (sample (k)) was grown at the temperature of ~520 °C; (III) The sample with the best PL performance was grown at 550 °C, not the sample (sample (k)) which was grown at 520 °C with the highest dot density.

At low growth temperature, ≤ 500 °C, incorporation of adatoms for the epitaxy growth is low. There was not enough time to grow enough material for forming QD nuclei in the step-1 growth, and only wetting layer was grown. The QDs were mainly grown in step-2 ALE growth. Therefore, the AFM image of the QDs of sample (i) which was grown at 460 °C looks similar to that of the QDs grown using normal ALE growth mode as that of (c') in Figure 5.9 of this chapter. When the temperature was increased to 520 °C, the nuclei formed in step-1 are all developed into the QDs during step-2 growth, high density QDs of $1.4\times10^{10}/\text{cm}^2$ have been received in sample (k). However, the dot density of the samples decreases when the growth temperature was increased above 520 °C and the dot size becomes bigger, which is caused by the increased diffusion length of adatoms at higher temperature [169]. The better PL performance of sample (l) which was grown at 550 °C, rather than that of sample (k) with higher dot density, is because crystal quality of the formed QDs is better when grown at higher temperature. Material grown at higher temperature normally has better crystal quality due to the reduced grown-in defects, such as non-/poly-crystalline structures. Non-crystallines are generated at the QDs/matrix interface due to the large lattice mismatch strain between the InAs dots and the InGaAs/InP matrix [239]. At higher growth temperature these non-crystalline structures are broken [174], and hence the crystal quality of the QDs has been improved. But, if the growth temperature is too high, ≥ 600 ^{o}C, in the case of sample (m), the sample's dot-density is reduced because the larger size dots are formed at higher temperature. So that, sample (m)'s PL intensity is lower than that from sample (l). The results show that an optimized growth temperature of 550 ^{o}C, which brings with high dot density, uniform dot size and best PL performance of the QDs, has been received under the current conditions. This temperature with the optimized step-1 growth rate (0.84 ML/s) in QD growth will be applied for the following V/III flux ratio study.

(iii) *Effect of the V/III flux ratio*

In the above investigations, dot density of the samples under the optimized growth conditions reaches around $1.2\times10^{10}/\text{cm}^2$. It can be calculated with the dot density the corresponding QDs' surface coverage of the dots is only ~23%. In order to enhance the sample's PL performance further, it is very important to grow the sample with higher dot density. In this investigation, we have tried to increase the dot density by optimizing the inlet source flux of group-V source TBA flux in step-1 growth.

In this study, the TMIn group-III source flux and all other growth conditions were kept unchanged for growing the samples. Only group-V source flux of TBA for step-1 growth was changed from 0 to 4.52×10^{-4} mol/min, with the V/III ratio correspondingly changed from 0 to 11, in the two-step growths of QDs. Samples (n), (o), (p), (q), (r), (s), (t) and (u) were grown by two step growth with the input source flux V/III ratio in step-1 growth set at 0, 0.2, 0.5, 1.1, 2, 4, 6.5 and 11, respectively, by adjusting the TBA flux. Figure 5.15 shows the QDs' AFM images and low-temperature PL spectra of these samples. The dot density of the samples with different input V/III ratio in step-1 growth is summarized in Figure 5.16.

Very high dot density, ~2.5×10^{10} cm^{-2}, has been achieved and it slightly changes with the input V/III source flow ratio in step-1 growth when the V/III ratio changed from 0 to 1. When the V/III ratio is >1, the formed QD density drops sharply with increasing the V/III ratio. This observation is different from what has been reported where the dot density increased with the V/III source flow ratio [212, 213]. In the range of V/III >1, the surface-diffusion length of Indium adatom is increased when the group V atom concentration on the epitaxy growth surface is reduced by lowering the V/III ratio [214,215], so that the effective coverage of the Indium adatoms on the growth surface is enlarged. The formed nuclei density is thus

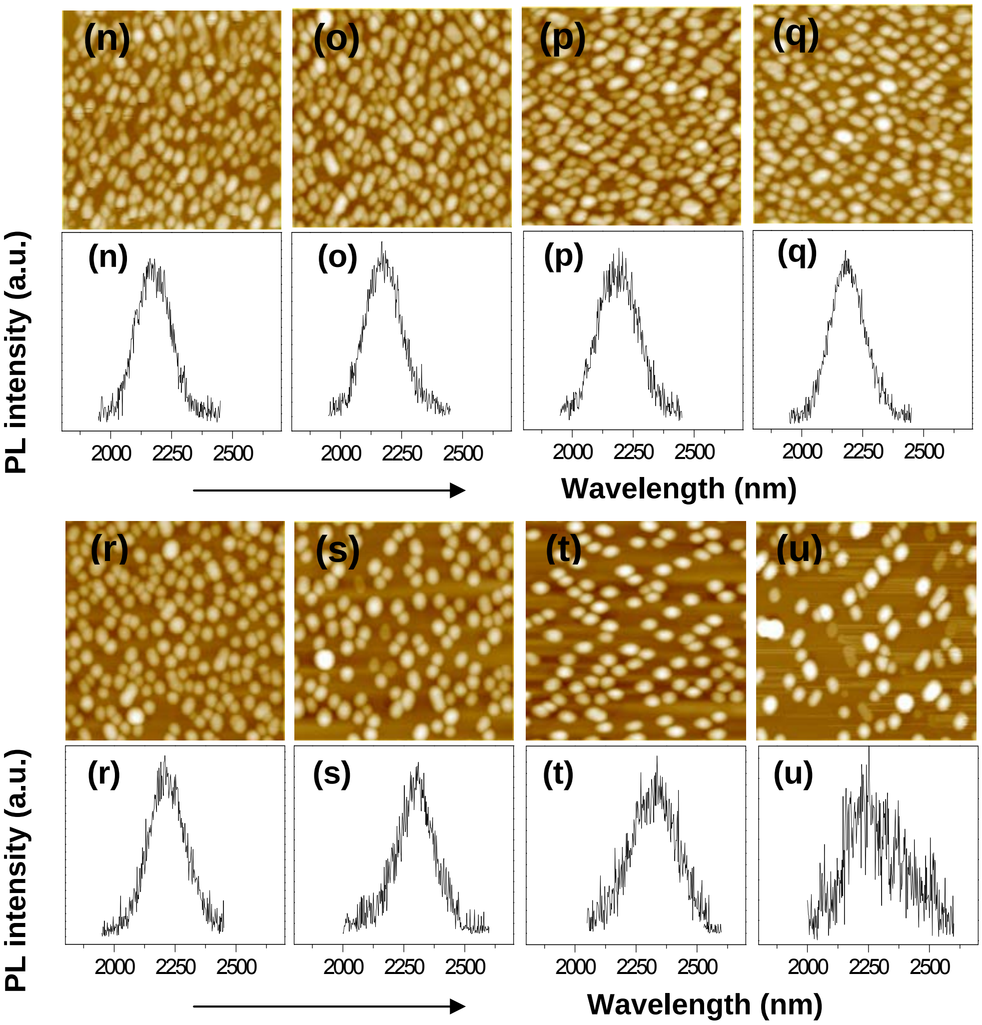

Figure 5.15 1×1μm² AFM top-view images and low temperature PL spectra of samples (n), (o), (p), (q), (r), (s), (t) and (u).

increased with the reduction of V/III ratio during the step-1 growth in two-step growth of InAs QDs, which results in higher dot density. Besides, it has also been shown that a smaller critical thickness is obtained when the group V source, TBAs, inlet flux is decreased in SK growth of QDs [216]. Or in other wards, the low group V source flow can accelerate the onset of the 3-D islands formation in SK QDs growths, thus resulting in higher density nuclei/QDs with lower inlet V/III ratio.

When the input V/III ratio during the step-1 growth is very low, V/III<1, input Indium adatoms are more than the arsenic adatoms on the reaction surface. The extra Indium adatoms act as surface surfactant to enforce roughening the growth surface

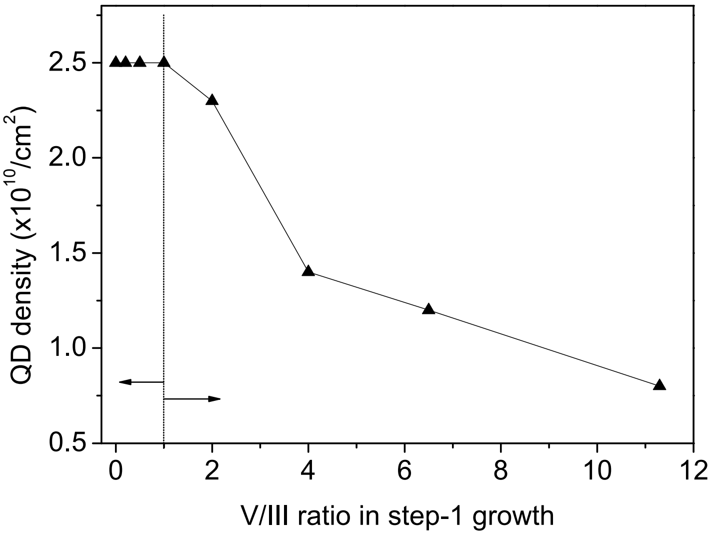

Figure 5.16 QDs density as the function of V/III ratio used in step-1 growth for growing QDs of samples (n), (o), (p), (q), (r), (s), (t) and (u).

[217]. A roughened growth surface has much lower energy sites for 3-D growth and at the same time reduces the critical thickness for the onset of 2-D to 3-D growth transformation [218]. As a result, the formed QDs' dot-density in the two-step growth becomes higher when the input V/III ratio in step-1 growth reduces to less than 1. On the other hand, the reduced arriving arsenic atoms under the lower V/III ratio enable

the arriving indium atoms to mainly bond with the dangling arsenic atoms on the matrix InGaAs surface instead of forming large InAs islands through free atoms congregating together. This also contributes to the dot density increase as discussed in Ref. [219]. It is calculated that the surface coverage of the QDs of sample (q) with setting the V/III input flow ratio in step-1 growth at V/III = 1.1 is ~ 60 %, which is very high. There are not many rooms to further increase the dot density of the sample by further reducing the input flow V/III ratio in step-1 growth. So, the dot-density of samples (n), (o) and (p) did not increase much when the V/III ratio in step-1 growth was reduced from 1 to zero.

Optical and crystal properties of the InAs QDs samples grown with different input V/III ratio in step-1 growths have been studied using PL measurement, and the measured PL spectra are also shown in Figure 5.15. Figure 5.17 plots the PL peak position, peak emission intensity, integrated emission intensity and PL linewidth of the samples grown with different input V/III ratios in step-1 growth.

It is observed that the PL peak position of the QD samples slightly blueshifts

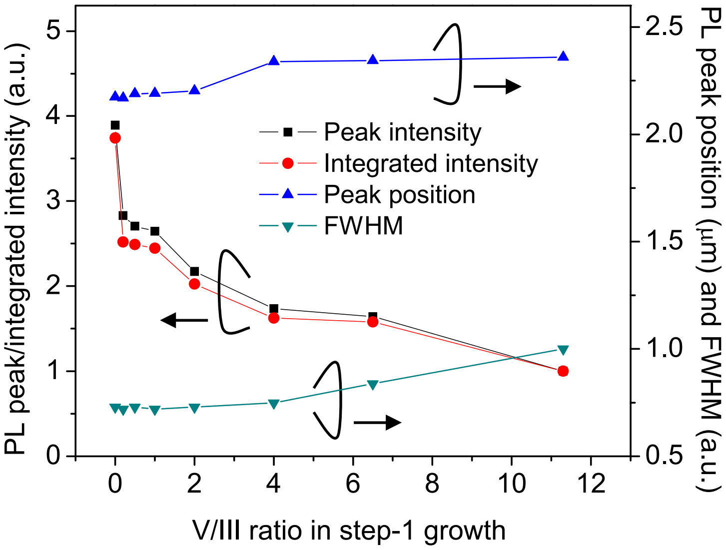

Figure 5.17 PL results, including PL peak position, peak intensity, integrated intensity and FWHM, as the function of V/III ratio used for samples (n)- (u).

with the reduction of input flow V/III ratio in step-1 growth. This is because the dot's height grown with lower input V/III ratio is lower when the sample's dot-density is higher. It shows that both the peak emission intensity and the integrated emission intensity of the samples increase with reducing the input flow V/III ratio in step-1 growth. The PL emission changes follow the changes of the samples' dot-density with the input V/III ratio, which shows that the crystal quality of the QDs grown with the input V/III ratio in step-1 growth being reduced does not degrade. The increase in the PL emission intensity of the sample grown with lower input V/III ratio in step-1 growth is because of the higher dot density of the sample. The PL linewidths of the samples growth with the input V/III ratio ≤ 4 are similar, which shows the uniformity of dot size and crystal quality of the QDs formed of the samples are similar, even though the input V/III ratio was reduced. It is noticeable that for sample (n) with the input V/III ratio in step-1 growth was V/III = 0, the PL intensity is much higher than that of the other samples. The real mechanism of this sharp increase in the PL emission intensity of the QDs grown with zero input V/III ratio in step-1 growth of the two-step growth InAs QDs needs to be further analyzed. So, for the InAs QDs grown on $In_{0.53-0.72}Ga_{0.47-0.28}As/InP$ matrix under the optimized growth temperature (550 ^{o}C) and step-1 growth rate (0.84 ML/s), lowering the V/III ratio in step-1 growth enhances dot density and then dots' PL performance.

Till now, high quality mid-IR emissive InAs QDs have been grown on the InGaAs/InP matrix after optimizing the dots' growth method and growth conditions. The highest dot density obtained is $2.5\times10^{10}/cm^{2}$, and the standard deviation, for characterizing dots' size uniformity, of the dots formed is smaller than 2 nm. The received high quality InAs/InGaAs/InP QDs in this work are comparable with the reported InAs/In(Al)GaAs/InP QDs grown by AsH_3/H_2 with dot-density&standard-

deviation of $2.5\times10^{10}/cm^2$&1.4nm in Ref. 12 and $3.0\times10^{10}/cm^2$&5.2nm in Ref. 13. This makes it promising to develop the QDs for practical application by growing QD structures with the safer process conditions, i.e. using TBA/N_2 in MOCVD. For a QD structure, the dots will be capped by a cap layer with the composition similar to that of dots' matrix layer. This cap layer will enforce the strain on the dots below as mentioned previously, thus affecting dots' PL emission spectrum. In the sub-section below, a comparison study of the PL emission spectra for the capped QDs with different QD densities&sizes have been carried out; the PL results are also compared with that of the corresponding uncapped QDs.

5.3.3 PL spectrum of the capped QD structure

To study the PL performance of the capped QDs, two capped QD structures were grown based on the uncapped InAs/$In_{0.53\text{-}0.72}Ga_{0.47\text{-}0.28}As$/InP QDs (q) and (t) mentioned in Figure 5.15. As shown in Figure 5.18, a cap layer of ~ 50 nm $In_{0.72\text{-}0.53}Ga_{0.28\text{-}0.47}As$ layer was deposited on the free-standing QDs to form the two corresponding capped QDs samples (q+) and (t+). The dot density of samples (q)/(q+) and (t)/(t+) is $2.5\times10^{10}/cm^2$ and $1.2\times10^{10}/cm^2$, respectively, based on the AFM images measured. And the QD's height is 9 nm and 7 nm, respectively. The similarly small dot size standard deviation of 1.1 nm and 1.4 nm, respectively, for sample (q)/(q+) and (t)/(t+) shows the dots are uniform in size. The reason for choosing the two samples is because the dots of the two samples have different dot density and size but both with uniform dot size distribution. This is good for the study of dot density/size effects on the PL properties. Besides, sample (t) has the same dot height as used/assumbed in the theoretical design for mid-IR QD structures (Refer to paragraph 1 in Section 5.2). During growing the InGaAs cap layer immediately after InAs QDs growth, the temperature was gradually increased from 550 °C to 580 °C to improve the layer's crystal quality as mentioned previously. The temperature increase rate is ~ 0.1 °C/s. We observe no effect on dot's energy band gap when the reactor temperature is increased by 30 °C for growing the cap layer. However, when the growth temperature increases by 50 °C or above for cap layer growth, the dot's PL wavelength blueshifts due to dot's size decrease induced by indium evaporation and/or *in-situ* intermixing between InAs QDs and InGaAs top barrier layer. The PL spectra of the samples were shown in Figure 5.18. In Figure 5.19, the PL peak/integrated emission intensity and PL linewidth are summarized; and the dot height of the uncapped QDs and the PL peak positions of the uncapped and capped QDs are shown in Figure 5.20.

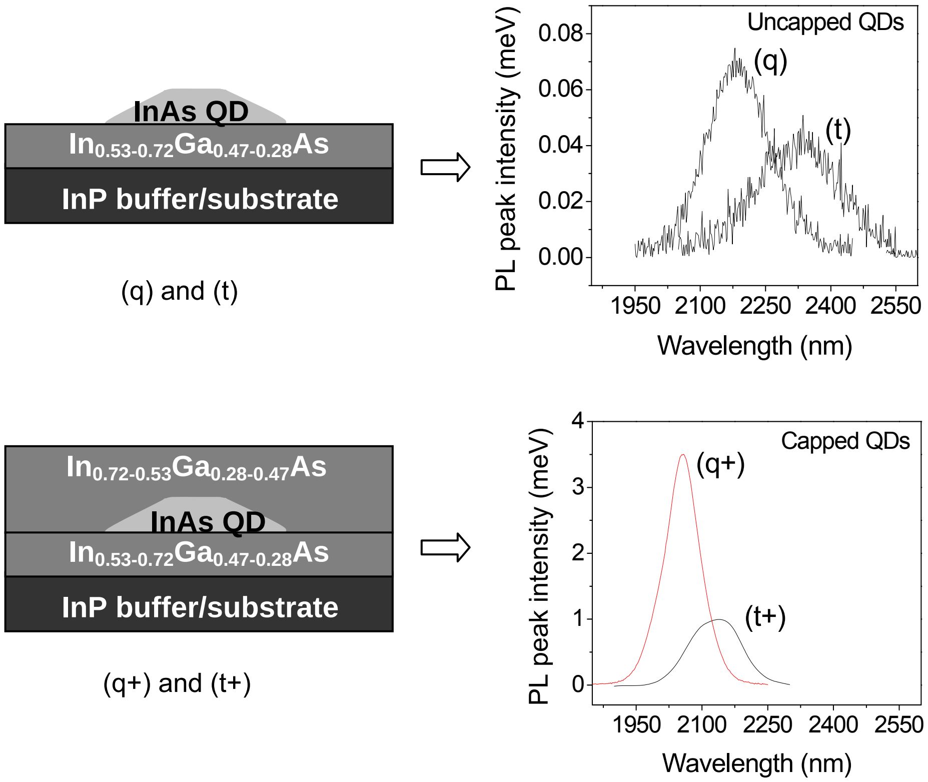

Figure 5.18 Schematic uncapped & capped QD structures with different dot density of samples (q)/(q+) and (t)/(t+); the corresponding PL spectra for the two groups of samples are measured at 20 K.

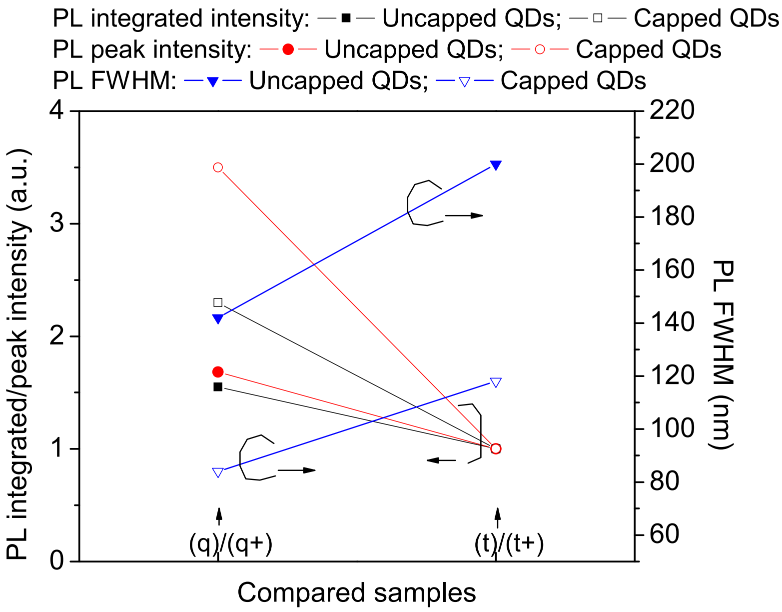

Figure 5.19 Comparison of PL peak/integrated intensity and PL linewidth between the uncapped/capped samples (q)/(q+) and (t)/(t+).

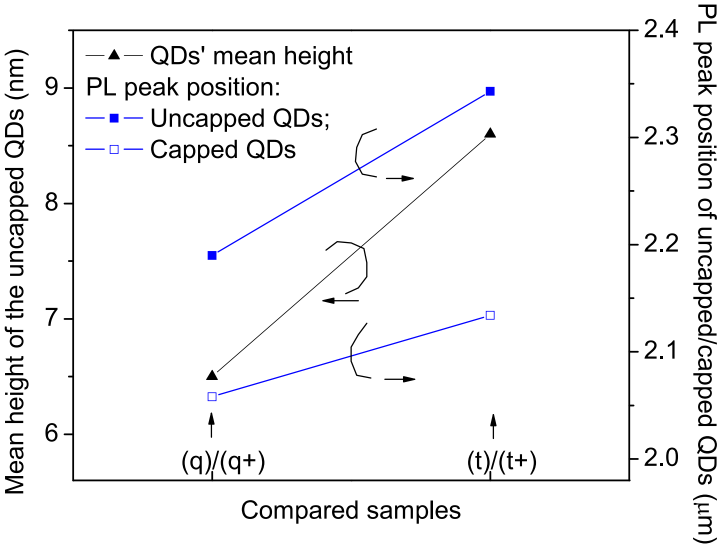

Figure 5.20 Comparison of QDs' mean height and PL peak-positions between the uncapped/capped samples (q)/(q+) and (t)/(t+).

As expected the dots' PL emission intensity is increased greatly because of the better barrier confinement on the carriers in the dots layer after capping the dots with the top barrier layer. As shown in Figure 5.19, when the dot-density increases, the peak/integrated intensities of the uncapped and capped samples both increase, but the integrated intensity increases faster than the peak intensity with the dot-density increase. This further confirms increasing the dot density by lowering the input V/III flux ratio does not degrade the crystal-quality of the dots formed. Besides, the PL linewidth of low-density QDs (samples (t)/(t+)) is larger than that of high-density dots (samples (q)/(q+)) for both the uncapped and capped dots, while the dot size dispersion of low-density QDs is narrower than that of high-density dots. This shows QDs' PL linewidth is not determined by the dot's size distribution only. This is probably related to the $In_{0.72-0.53}Ga_{0.28-0.47}As$ cap layer. When growing the cap layer, the initial several monolayers are grown on the free-standing dots with a rough growth surface. The larger the QD's size, the rougher the growth surface to the InGaAs cap layer. So, the rougher growth surface during growing the InGaAs cap layer of sample (t+) results in the lower uniformity in the composition of the InGaAs layer, thus resulting in the larger fluctuated confinement barrier and then broadening the PL linewidth. As shown in Figure 5.20, the PL emission peaks of the uncapped and capped QDs are both in a positive relation to the dots' mean height. But obviously, the emission peak blueshifts from the uncapped to the capped QDs. This further demonstrates the compressive strain of the cap layer enforced on the below QDs increases the transition energy in the dots layer. So, the redshift technologies in our designing the mid-IR QD structures include the use of the strain engineering between the QDs and the top cap layer. In addition, when the dots' mean-height increases from 7 to 9 nm, the PL emission peak position redshifts by 76 nm, i.e. from 2.058 μm to 2.134 μm. This indicates adjusting dots' height is another effective method to tune the emission wavelength of the QDs.

Figure 5.21 shows the PL spectra of the two samples under different excitation power. The excitation power is changed from 20 mW to 120 mW. It is noted that when the excitation power increased, the integrated PL intensity of the samples increased with the linewidth broadening. When the excitation power increases from 20 mW to 120 mW, a higher energy emission peak of sample (t+) becomes stronger as labeled with the arrow in Figure 5.21. This is not observed for sample (q+). For sample (t+), the larger dot size induced nonuniform confinement potential of the top cap layer widens the nonequilibrium carrier distributions in QDs. Carrier occupancy states at the ground energy level related to the radiative emission become more dispersed. When the excitation power increases, the dominated photongenerated transitions gradually transfer from low-energy to high-energy due to the saturation of lower-energy transitions. So, the high energy sub-peak appears under the higher excitation power in sample (t+). One of the reasons for the stronger emission intensity of high energy peak compared with that of low energy peak maybe is because there are less number of states in the ground state as compared to the higher excited states, which needs the further study and confirmation.

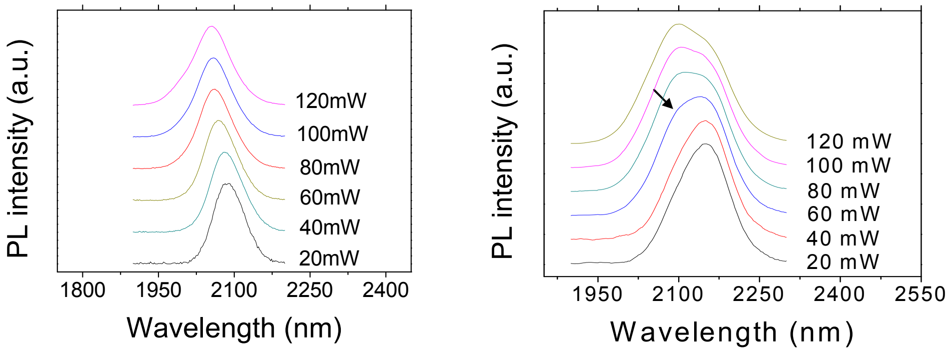

(q+) **(t+)**

Figure 5.21 Excitation-power-PL spectra for samples (q+) and (t+) with different QDs morphology.

5.4 Extend the emission wavelength of QDs

To extend the emission wavelength of InAs/InGaAs/InP QD structure, square and graded InGaAs barriers as designed are used when growing the QD structures. The mean height of the InAs dots grown is controlled at around ~ 9 nm with the dot density of ~ $1.2\times10^{10}/\mathrm{cm}^2$. First, the PL emission performance has been compared for the QD structures with square and graded InGaAs barriers. After that, the PL emission of the InAs/InGaAs/InP QD structures with different graded InGaAs barriers is investigated. The experimental PL emission wavelengths have also been compared with the designed transition energies.

5.4.1 Graded barrier InAs QDs

Three different barriers, i.e. square high-barrier $\mathrm{In_{0.53}Ga_{0.47}As}$, graded barrier $\mathrm{In_{0.53\text{-}0.72}Ga_{0.47\text{-}0.28}As}$ and square low-barrier $\mathrm{In_{0.72}Ga_{0.28}As}$, were used to confine InAs QDs in the InAs/InGaAs/InP QD structures for PL study. The top and bottom InGaAs barriers are symmetric in composition. The specific QD structures studied are

Table 5.3 Summary of the InAs QD structures of samples (a), (b) and (c). The 3-D AFM images, dots' height and dot density of the InAs QDs are also listed for each of the samples.

QD structure		Sample (a)	Sample (b)	Sample (c)
Top barrier		$\mathrm{In_{0.53}Ga_{0.47}As}$	$\mathrm{In_{0.72\text{-}0.53}Ga_{0.28\text{-}0.47}As}$	$\mathrm{In_{0.72}Ga_{0.28}As}$
QDs layer	3-D AFM images		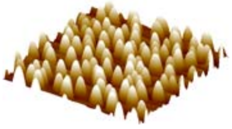	
	Average height (nm) & density ($\times10^{10}/\mathrm{cm}^2$)	9.0&1.00	8.9&1.25	8.9&1.32
Bottom barrier		$\mathrm{In_{0.53}Ga_{0.47}As}$	$\mathrm{In_{0.53\text{-}0.72}Ga_{0.47\text{-}0.28}As}$	$\mathrm{In_{0.72}Ga_{0.28}As}$
Buffer/substrate			InP(001)	

compared in Table 5.3. The InAs QDs' top-view 3-D AFM images of the three uncapped QD samples were also shown in Table 5.3. The thickness of all the InGaAs barrier layers is around 35 nm. The InAs QDs were grown by the optimized FG+ALE two-step method. For all the samples, a 200 nm InP buffer layer was grown on InP (001) substrate with the temperature increased from 600 °C to 630 °C before growing the QD structure on top. The QD structure consists of an un-relaxed $In_xGa_{1-x}As$ bottom barrier layer, InAs QDs grown on top and then $In_xGa_{1-x}As$ upper barrier layer to cover the QDs. The bottom $In_xGa_{1-x}As$ layers were grown at 600 °C with different Indium composition, x. After growing InAs dots at 550 °C, the growth temperature was gradually increased to 580 °C for growing high quality InGaAs layer and also to minimize the material re-evaporation from the formed dots. After the whole QD structure growth, the reactor temperature was immediately cooled down to RT.

Figure 5.22 shows the 77-K PL spectra of samples (a), (b) and (c). In sample (a), InAs QDs are embedded in lattice-matched $In_{0.53}Ga_{0.47}As$ barriers; while in sample (b), the InAs QDs are embedded in symmetric $In_{0.72-0.53}Ga_{0.28-0.47}As$ graded barrier layers; and for sample (c), the InAs QDs are embedded in highly strained

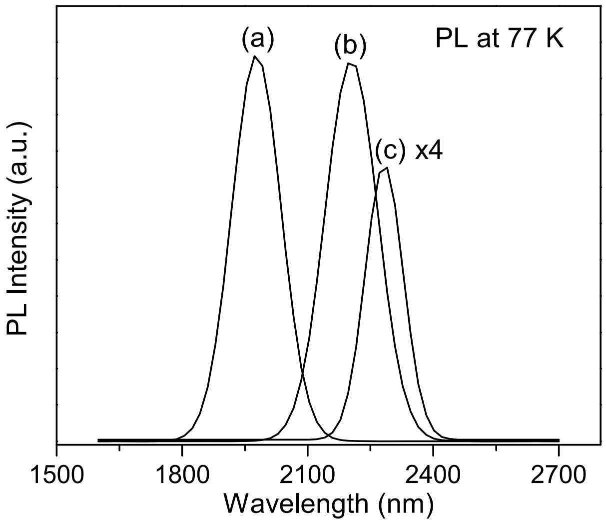

Figure 5.22 PL spectra of samples (a), (b) and (c) measured at 77 K.

$In_{0.72}Ga_{0.28}As$ barrier layers. The measured emission wavelength of sample (a), (b) and (c) at 77 K is 1.98 μm, 2.20 μm and 2.28 μm, respectively.

Emission wavelength of a QD structure is affected by the dot's size, mainly its height [107, 191], energy band gap of the barriers [114, 118], and the lattice-mismatch induced strain from dot's upper barrier layer [115, 117] and the substrate, etc. All these factors have been put into consideration in designing the mid-IR QD structures. The theoretically predicted emission wavelength for the three QD structures of (a), (b) and (c) is 2.03 μm, 2.21 μm and 2.25 μm, respectively. These results match to the observed experimental PL emission peaks well. This further confirms the validity of employing the 8 band **k·p** theory for predicting the QDs' transition energies. Besides, the mean dot heights of the three samples as indicated in Table 5.3 are almost the same, about 9 nm. This will not contribute to the large redshift of the emission wavelength, ≥ 220 nm, of sample (b) and (c) when compared with that of sample (a). So, as proposed in the design, the redshift is induced by two factors: barrier band gap and top barrier's strain. The barrier's energy band gap of the QD structures in sample (b) and (c) are both lower than that of (a). And the strain between InAs QDs and the $In_xGa_{1-x}As$ upper barrier layers is smaller of (b) and (c) when compared with that of (a). Moreover, sample (c) has the lowest barrier height, and the lattice mismatch between the $In_{0.72}Ga_{0.28}As$ upper barrier layer and InAs QDs is the smallest. So, sample (c) has the longest emission wavelength among the three samples. In sample (b), the InAs QDs are embedded in $In_{0.53-0.72}Ga_{0.47-0.28}As$ symmetric graded barriers. Its emission peak is greatly redshifted from that of sample (a), only slightly shorter than that of sample (c).

The PL emission intensity and FWHM of the three QD structures are compared in Figure 5.23. Sample (a) and sample (b) have high PL emission intensity and the narrow FWHM. Sample (c) has the narrowest FWHM PL spectrum, but its emission intensity is the lowest among the three samples. The narrower PL spectrum of sample (c) is attributed to its more uniform dot size. However, the lower barrier height of sample (c) reduces the carrier's confinement, resulting in lower PL emission intensity. The dot density of sample (a) and (b) is slightly lower than that of sample (c). So, the higher PL peak emission intensity of sample (a) and (b) is because they have higher barrier heights, thus better carrier confinement. Sample (c) has lower barrier height leading to the lowest PL peak intensity. The results show sample (b), with the graded barrier for QDs, has long emission wavelength and at the same time has strong PL emission intensity. This indicates that InAs QD structure with $In_xGa_{1-x}As$ graded barrier grown on InP substrate is more suitable for mid-IR optoelectronic device applications. In the following mid-IR QD structures growths, the graded InGaAs barriers are employed.

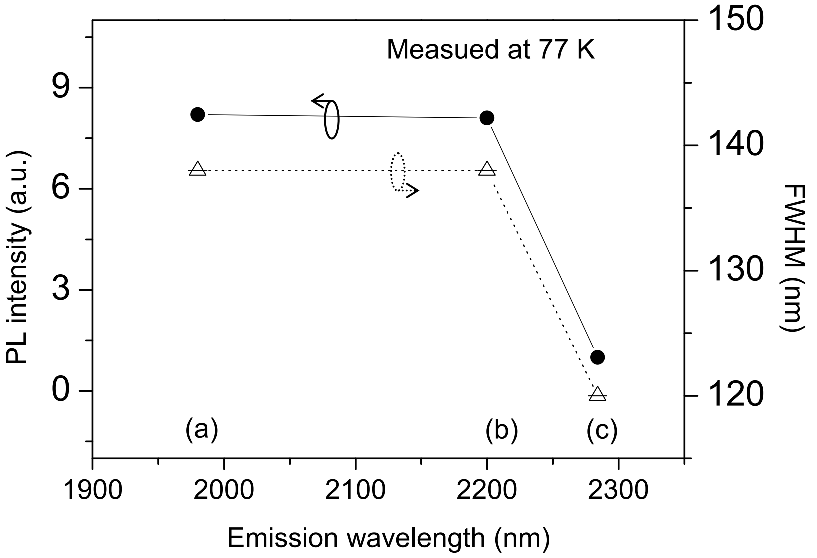

Figure 5.23 The measured PL peak intensity and FWHM of the PL spectrum versus the peak emission wavelength of samples (a), (b) and (c).

5.4.2 Barrier's gradation dependence of QDs' PL emission

As the designed QD structures in Section 5.1.2, five graded-barrier based QDs samples (d'), (e'), (f'), (g') and (h') with symmetric graded barriers of $In_{0.53-0.65}Ga_{0.47-0.35}As$, $In_{0.53-0.72}Ga_{0.47-0.28}As$, $In_{0.53-0.8}Ga_{0.47-0.2}As$, $In_{0.53-0.85}Ga_{0.47-0.15}As$ and $In_{0.53-0.9}Ga_{0.47-0.1}As$, respectively, as the InAs QDs have been grown on InP(100) substrate. Reference sample (a') with $In_{0.53}Ga_{0.47}As$ as the barriers was also grown for comparison. In the growth of these QD structures, layers growths are the same as described in last section except the bottom barrier layers of samples (g') and (h'). For the two samples, the gradation, y, of $In_{0.53\rightarrow(0.53+y)}Ga_{0.47\rightarrow(0.47-y)}As$ is wider and then its lattice mismatch to InP buffer/substrate is larger. This results in the reduction of the critical thickness before the relaxation of $In_{0.53\rightarrow(0.53+y)}Ga_{0.47\rightarrow(0.47-y)}As$ layer when grown on InP buffer/substrate. So, the thickness of the bottom $In_{0.53\rightarrow(0.53+y)}Ga_{0.47\rightarrow(0.47-y)}As$ layer for samples (h) and (i) is only 20 nm. But the corresponding top InGaAs layer thickness is still 35 nm as the other samples. The barrier effects on dots' PL properties were investigated based on the PL emission wavelength, PL intensity and

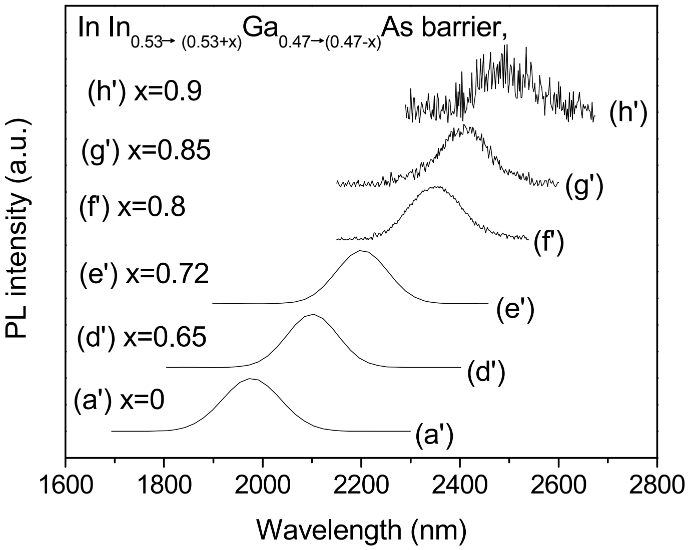

Figure 5.24 77-K PL spectra for the QD structures with different graded InGaAs barriers of samples (a'), (d'), (e'), (f'), (g') and (h').

PL linewidth of the QD structures.

The low-temperature normalized PL spectra for samples (d') - (h') were shown in Figure 5.24 and the PL peak intensities and the linewidths of the corresponding PL spectra as the function of the emission wavelengths are plotted in Figure 5.25. The dot's size, size standard deviation, and dot density of the uncapped QDs corresponding to the QD samples of (d') - (h') were compared in Table 5.4. It's noted that the dot density, which affect the PL intensity, of samples (d') - (h') is

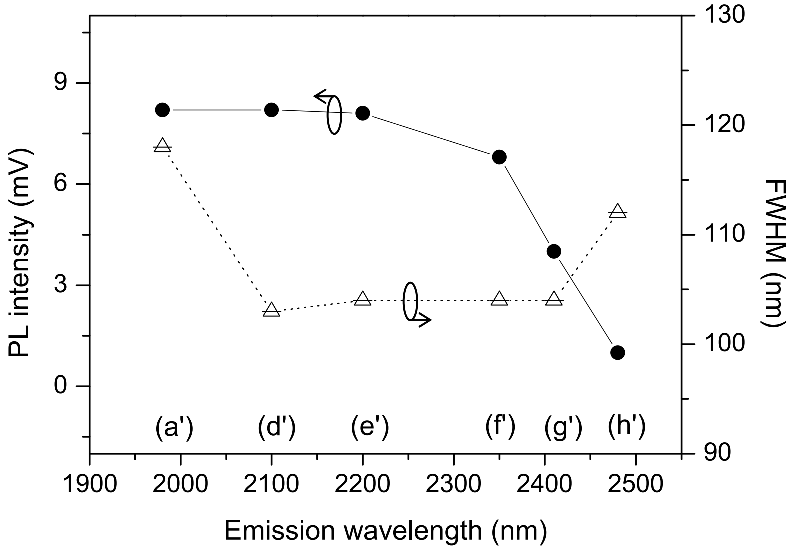

Figure 5.25 PL intensity and PL-spectrum linewidth as the function of the emission wavelength of samples (a'), (d'), (e'), (f'), (g') and (h').

Table 5.4 Summary of dot size (height/diameter), height/diameter standard deviation, dot density and $In_xGa_{1-x}As$ barrier layers of the grown QDs samples (a'), (d'), (e'), (f'), (g') and (h').

QD samples	(a')	(d')	(e')	(f')	(g')	(h')
h & d (nm)	9.0 & 48	8.9 & 54	8.9 & 54	9.1 & 54	9.1 & 55	9.1 & 55
σ_h & σ_d (nm)	1.17 & 1.09	1.17 & 1.08	1.17 & 1.07	1.17 & 1.08	1.18 & 1.09	1.18 & 1.09
Density (10^{10}/cm^2)	1.0	1.24	1.26	1.25	1.24	1.23
x of $In_xGa_{1-x}As$ layer	0.53	0.53→0.65	0.53→0.72	0.53→0.8	0.53→0.85	0.53→0.9

similar, around $1.2\times10^{10}/cm^2$, but for the reference sample (a') with square barrier , its dot density is lower. With increasing the gradation, y, of $In_{0.53\rightarrow(0.53+y)}Ga_{0.47\rightarrow(0.47-y)}As$ barriers, the barrier height between InAs QDs and $In_{0.53\rightarrow(0.53+y)}Ga_{0.47\rightarrow(0.47-y)}As$ barriers decreases gradually. The high PL peak intensity of samples (a'), (d') and (e'), as shown in Figure 5.25, is attributed to the InAs QDs being embedded in relatively high barriers of $In_{0.53}Ga_{0.47}As$, $In_{0.53-0.65}Ga_{0.47-0.35}As$ and $In_{0.53-0.72}Ga_{0.47-0.28}As$ barriers. However, when the gradation rises to 0.27 for sample (g'), the PL peak intensity begins to decrease evidently until very low magnitude at the gradation of 0.37 for sample (h'). For all the dots, the size dispersion is narrow since the standard deviation of the dot's height and diameter is small as around 1.2 nm and 1.1 nm, respectively. Correspondingly, the linewidth of all the samples is < 120 nm as indicated in Figure 5.25. It is noted that samples (d'), (e'), (f') and (g') have comparable narrower linewidth, while samples (a') and (h') have relatively larger width. In case of (h'), its largest gradation, y, of $In_{0.53\rightarrow(0.53+y)}Ga_{0.47\rightarrow(0.47-y)}As$ barrier requires the fastest Indium/Gallium source flux, i.e. Indium/Gallium content, change during the layer growth by MOCVD. So, the content uniformity of the layer is not kept well, thus resulting in the nonuniform confinement on the dots and thus broadening the PL spectrum linewidth. On the other hand, compared with the samples (d') - (g'), sample (a') has the relatively broader linewidth in spite of its higher barrier. The reasons for it lie in: (i) less strain of the QDs because of the higher Indium content of the upper InGaAs barrier layer and (ii) the larger dot size of samples (d') - (g'). With the higher Indium content, lattice constant of the InGaAs cap layer matches better to that of InAs QD layer, which suppresses the Indium mixing or segregation between the InAs QDs and the InGaAs cap layer [113]. So, the InAs QDs of the samples keep their dot height uniformity when they are covered by the graded InGaAs cap layer, thus they have narrower emission spectra. As listed in Table 5.4, the dot's lateral size of (a') is smaller than other samples. Optical transition energies from the larger QDs will be less affected by the dot size fluctuation [220, 221], which also contributes the narrower PL linewidth of (d') - (g').

As shown in Figure 5.24, with the Indium content of the graded $In_{0.53\rightarrow(0.53+y)}Ga_{0.47\rightarrow(0.47-y)}As$ layer increased linearly from 0.53 ~ 0.65 to 0.53 ~ 0.9, the emission wavelength of the QD structure increased as designed. All the emission peaks of the InAs QDs embedded in $In_{0.53\rightarrow(0.53+y)}Ga_{0.47\rightarrow(0.47-y)}As$ graded barriers red-shift from that of InAs QDs embedded in lattice matched $In_{0.53}Ga_{0.47}As$ barriers of sample (a'). Increasing the gradation, y, of the $In_{0.53\rightarrow(0.53+y)}Ga_{0.47\rightarrow(0.47-y)}As$ graded barriers of sample (d') - (h') from 0.12 to 0.37, the InAs QD structure's emission wavelength shifts by 120 nm, 220 nm, 370 nm, 430 nm and 500 nm, respectively. When the gradation of the $In_{0.53\rightarrow(0.53+y)}Ga_{0.47\rightarrow(0.47-y)}As$ graded barrier layer, y, increases by every 0.01, the emission wavelength of the InAs QD structure red shifts about 13.5 nm. When the gradation, y, increases to > 0.27, the 77-K emission wavelength of the InAs QDs embedded in $In_{0.53\rightarrow0.8}Ga_{0.47\rightarrow0.2}As$ barriers reaches > 2.35 μm. The longest wavelength reaches around 2.5 μm for sample (h'). This is, to our best knowledge, the longest inter-band transition emission wavelength from InAs QDs reported so far. However, the PL intensity degrades with the emission wavelength increase due to the dot's barrier height decrease. The study on how to enhance the PL performance for these QD structures is required before developing them for the QD device applications.

Emission wavelength of the InAs QDs embedded in strained $In_xGa_{1-x}As$ barriers are affected in three ways: **(i)** Height of the QDs formed. Since the aspect ratio, which is defined as the QD height versus its diameter, of the InAs QDs formed in the six samples is very small, ~ 0.18, quantum effect of the QDs is mainly determined by their QD height [191, 107]. Table 5.4 shows that the aspect ratio of the corresponding uncapped QDs of the samples (a') - (h'), is almost same, 0.17~0.19. The mean dot height of these six samples is also similar, 8.9 nm ~ 9.1 nm. Therefore, the measured obvious red-shift of PL peak of samples (d') – (h') versus that of sample (a') is not because of the sample's QD height variation. **(ii)** The second factor causes the sample's emission peak's red-shift is its InGaAs barrier layer, as considered in the theoretical design. As the conduction band profiles of the six samples shown in Figure 5.5, confinement potential of carriers in the InAs QD structure is reduced with increasing the Indium content of the $In_xGa_{1-x}As$ graded barriers, which lowers the transition energy in QDs and decreases cap-layer's stress on the QDs, thus redshifting the dots' emission wavelength. **(iii)** The third is partial decomposition of the $In_xGa_{1-x}As$ cap layer during the MOVPE growth, which effectively increases height of the underneath InAs QDs [222,223], thus redshifting the QDs' PL emission peaks. This Indium decomposition from the $In_xGa_{1-x}As$ cap layer growth depends on its Indium composition. The higher the Indium content of the $In_xGa_{1-x}As$ cap layer, the larger the indium decomposition effect, hence resulting in the larger red-shift of QDs' emission wavelength [223].

Figure 5.26 shows the calculated emission wavelength as the function of the gradation of the InGaAs barrier in the InAs/InGaAs QD structures and the measured PL peak position. The theoretical and experimental results match well. It has been noted that the calculated peak emission wavelength of the samples systematically slightly longer than the experimental results, and the difference between the calculated and experimental results becomes smaller when the Indium composition of the InGaAs barriers of the QD structure is increased. This systematically longer calculated emission wavelengths are because of the neglected consideration of QD's lateral confinement, which will increase the transition energy and then blueshift the emission peak position as mentioned in Chapter 3. Besides, partially decomposition of the $In_xGa_{1-x}As$ cap layer during the MOVPE growth effectively increases height of the underneath InAs QDs [222, 223]. So, the actual capped-QD height is expected to be increased compared with the un-capped InAs QDs of the corresponding samples. The increased dot's height will redshift its PL emission wavelength. As a result, QD's emission peak redshift in the calculation would be counteracted when the actual capped dot's height increased due to the decomposition effect. This explains the reduction of the difference between the calculated and measured peak positions of the sample when the Indium content of the $In_xGa_{1-x}As$ cap layer is increased as shown in Figure 5.26.

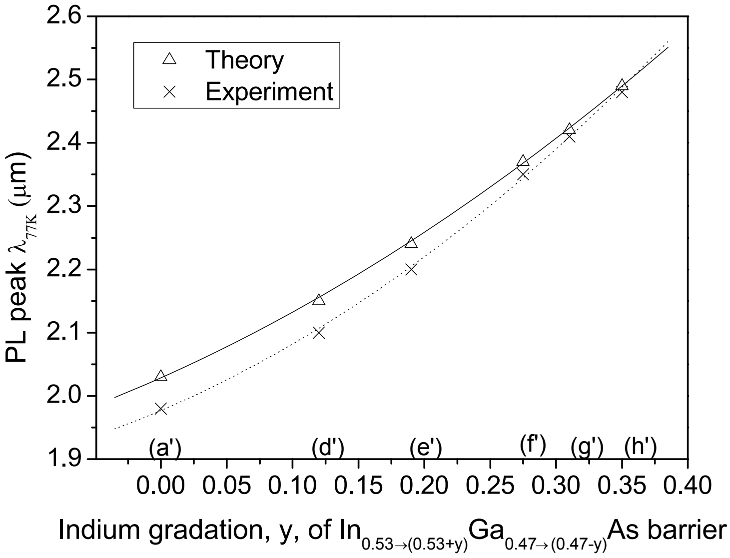

Figure 5.26 Comparison between the experimental measured (samples (d')-(h')) and the theoretical designed PL peak positions for the InAs QDs embedded in different $In_xGa_{1-x}As/InP$ matrixes.

5.5 Summary

In this chapter, 8 band **k·p** theory model was used to design the mid-IR InAs/InP QD structures based on the barrier/strain technology by using the InGaAs as the confinement barrier layer for the InAs QDs. The emission wavelength of the designed mid-IR QD structures redshifts with increasing the Indium content of InGaAs barrier layers, and can reach > 2.2 μm when the Indium content of InGaAs is >0.72 for the square barrier case or the gradation, y, of $In_{0.53-(0.53+y)}Ga_{0.47-(0.47-y)}As$ is >0.19 in case of the graded barrier.

To grow high quality InAs QDs on InGaAs/InP matrix, the QDs two-step growth method was optimized, i.e. to replace the slow growth in step-2 growth by the atomic layer epitaxy. Growth conditions, including growth rate, temperature and the input V/III flux ratio, in step-1 nucleation growth was investigated and optimized in QDs formation. After the growth optimization, InAs/InGaAs/InP QDs with very high dot density of ~ $2.5\times10^{10}cm^{-2}$ and uniform dot size of ~ 1 nm size-dispersion were achieved.

Based on the designed mid-IR QDs, we grow the mid-IR InAs/InGaAs/InP QD structures by MOCVD. The results show the measured PL emission wavelengths of the grown QD structures match well to the theoretically predicted emission peaks. The longest emission wavelength of >2.35 μm was achieved from the InGaAs graded barrier based QD structures by setting the gradation, y, of $In_{0.53-(0.53+y)}Ga_{0.47-(0.47-y)}As$ barrier >0.27. The study on how to enhance the PL performance for these QD structures is required before developing them for the QD device applications.

CHAPTER 6. INTERMIXING OF InAs/InGaAs/InP QD STRUCTURES

6.1 Introduction

Integration of different optoelectronic devices like semiconductor lasers, high-speed modulators, amplifiers, low-loss waveguides, photodetectors, etc. onto one chip is very important in developing high performance optical communication. To develop monolithic photonic integrated circuits (MPICs), controllable large range tailoring of material energy band gap is important. Post-growth band gap tuning based on the material intermixing offers simplicity and flexibility as compared to the epitaxial regrowth technique [224] and the selective area epitaxy technique [225]. On the other hand, after the research on extending the emission wavelength of QD structures in last chapter, it is also significant to carry out the study on the emission wavelength shortening of QD structures in this chapter.

Quantum dot intermixing (QDI), which can enlarge the energy band gap of the QDs material by the QDs/barrier material interdiffusion, has attracted a lot of researches for post-growth tuning the energy band gap of the QD structures [226,227,228,229,230,231]. The reported QDI techniques so far include *in-situ* annealing during QDs growth [226], post-growth rapid thermal annealing (RTA) of QDs [227], impurity-free vacancy disordering [228], laser-induced intermixing [229], and heavy/light ion implantation for intermixing [230,231]. Among these techniques, ion implantation and laser-induced intermixing have sufficient lateral resolution. But, the thick cap layer of a QD laser structure limits the effectiveness of laser-induced intermixing due to the small light penetration depth [232]. On the other hand, ion-implantation intermixing can be used for much thicker layer structures by using higher energy ions. However, intermixing effect from heavy ion implantation is limited due to the low-density point defects formed [232]; while for light ion implantation, implantation energy of ~ 100 keV is required to obtain sufficient intermixing effect [231,232,233].

Plasma-induced QDI is attractive since i) the low-energy (with hundreds eV) ions generated in a plasma chamber minimize the degradation of QD optical quality with comparable band gap tuning; ii) short processing time (typically from several minutes to 10 minutes); iii) relatively simple and low-cost plasma etch facilities; iv) temperature independent of plasma process. Initial plasma-induced intermixing in quantum well (QW) structure was done using H_2-plasma generated by reactive ion etcher (RIE) [234], but this technique was limited in the intermixing. Intermixing in QW structures induced by Ar plasma generated in an inductively coupled plasma (ICP) RIE system has shown large energy band gap tuning capacity [235,236].

In this chapter, Argon (Ar) plasma exposure induced intermixing in the QD structures was studied. Based on the Ar-plasma exposure, the selective intermixing of QD structures across the wafer was investigated. Besides, rapid thermal annealing (RTA) is the simplest among the post-growth intermixing techniques, so the thermal annealing induced intermixing on the band gap shift of InAs/InGaAs/InP QDs was investigated also.

6.2 Thermal annealing induced QD intermixing

The interdiffusion for InAs/InGaAs QD systems under thermal annealing occurs between the group III Indium and Gallium atoms due to the presence of the concentration/strain gradient across the interface, as shown in Figure 6.1. After the material interdiffusion between InAs QDs and InGaAs barriers in InAs/InGaAs/InP

QD structures, the decreased/increased Indium/Gallium content in InAs dots increases the transition energy in the QDs layer, thus blushifting the QD's energy band gap as the dot-line curve in Figure 6.1. The interdiffusion thus the energy band gap shift

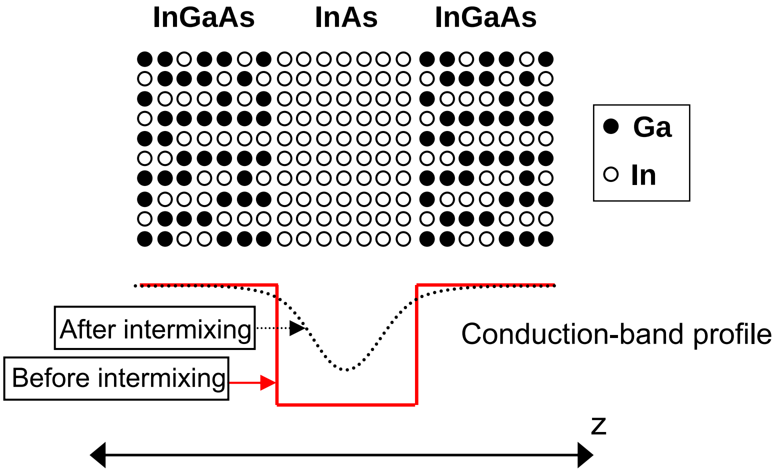

Figure 6.1 Schematic diagram for the intermixing upon thermal annealing.

extent is related to the lattice mismatch strain between InAs(QDs) and InGaAs(barrier), composition of InGaAs barrier and the annealing temperature, etc. In this section, the effects of the graded InGaAs barriers on the energy band gap tuning of InAs/InGaAs/InP QD structures upon the thermal annealing are investigated first. Then the effects of the top cap thickness and dot-density of the QD structures on the thermal-annealing induced band gap shift are also studied.

To study the QD's barrier effects on the intermixing, three QDs samples with different barrier layers are annealed in the RTP system, which was introduced in Chapter 3, at the same time from 500 ^{o}C to 800 ^{o}C for 60 seconds. The QD structures of the QDs samples are schematically shown in Figure 6.2-(a). The dots for the three samples were all grown on the $In_{0.53-0.72}Ga_{0.47-0.28}As$/InP matrix. So the QD's density and size-distribution of the three samples are the same. The upper barrier InGaAs layer thickness is kept at ~ 35 nm for the three samples. The only difference between the three samples lies in the composition of upper InGaAs barrier layers, i.e. $In_{0.72-0.53}Ga_{0.28-0.47}As$, $In_{0.8-0.53}Ga_{0.2-0.47}As$ and $In_{0.85-0.53}Ga_{0.15-0.47}As$ for sample (i), (ii) and (iii), respectively, as shown in Figure 6.2. In Figure 6.2-(b), the peak shift and PL peak intensity as to as-grown samples as the function of the annealing temperature are summarized. Compared with the as-grown samples, the energy band gaps of the three

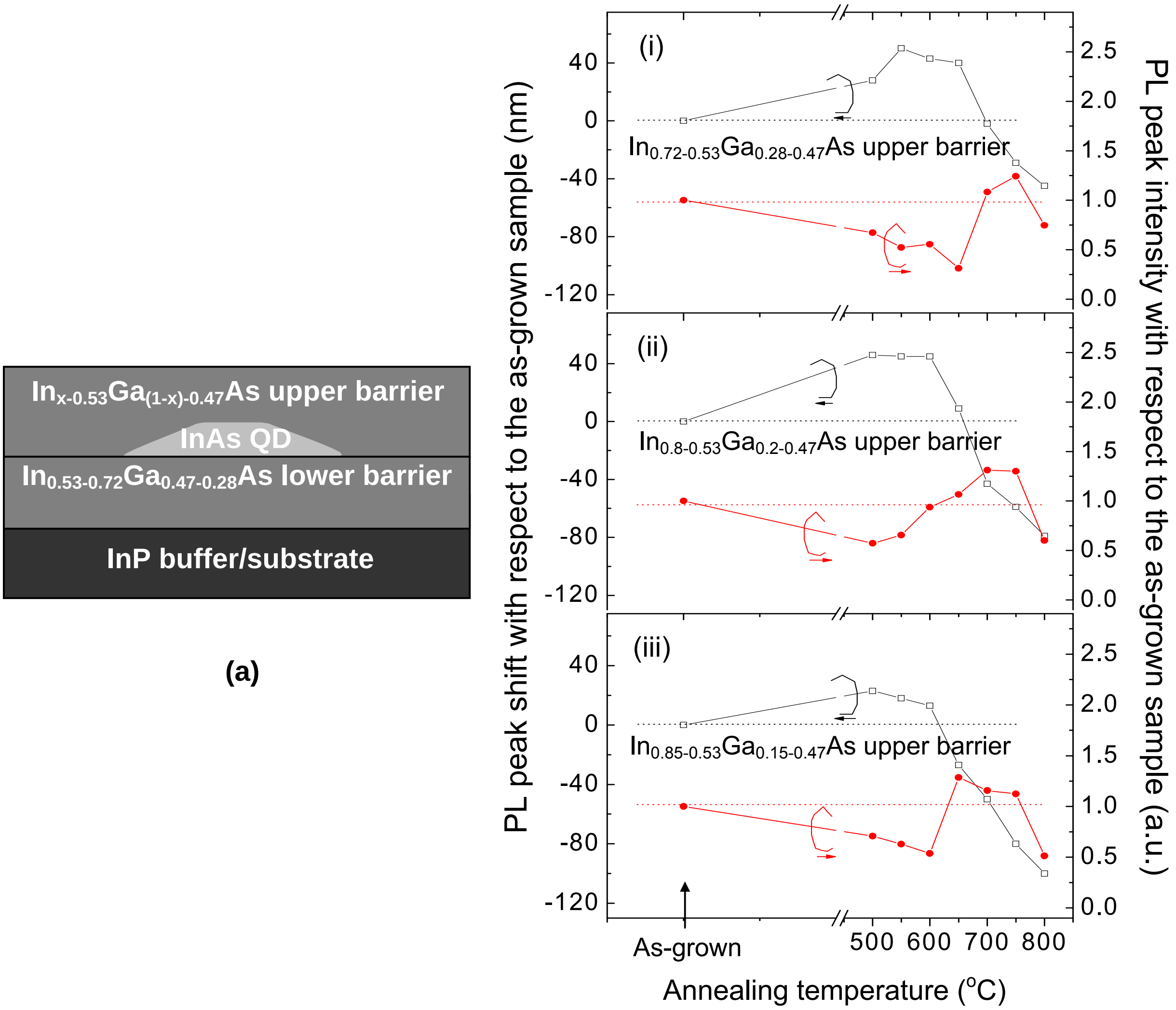

(a)

(b)

Figure 6.2 (a) Schematic diagram of QD structure for the three QDs samples to be thermally annealed at the same time; (b) The PL peak shift and PL intensity change with respect, respectively, to that of the as-grown sample have been plotted as the function of the annealing temperature for the three QDs samples.

samples after the annealing similarly redshift with PL intensity decrease first and then start to blueshift with PL intensity increase when the annealing temperature is increased to a certain point. This temperature is called as the threshold temperature for triggering the blueshift. It is observed that the threshold temperature and the blueshift extent are different between the three samples.

The literatures also reported red-shift at relatively low annealing temperature in the GaAs/InGaP multiple QW [237] and InGaAsP/InP single QW structures [238]. However, the redshift was attributed to the dominance of group-III sublattice intermixing at low annealing temperature. This mechanism based on the sublattice intermixing cannot explain our observed results since the InAs QDs are sandwiched between $In_xGa_{1-x}As$ barrier layers. No matter what extent intermixing existing between the group-III species, the InAs QDs will blueshift since the Indium atom of InAs QDs will be replaced by the Gallium atom from InGaAs barriers after the material interdiffusion. So, we believe there is a different mechanism behind for the observed band gap redshift in the QD system after annealed at relatively low temperature. A plausible explanation is based on the dots' size micro-increment after the interdiffusion between QDs/barriers. In growing the QD structure, it is unavoidable to bring with the grown-in defects in the dot/barrier interface region due to the large lattice mismatch between the dots and their barriers [239]. For InGaAs/InAs/InGaAs/InP QD structures studied here, the strain-induced grown-in defects are mainly In or As atom vacancies near surface region of the dots [240, 241]. Under thermal annealing, the diffusion of each type atom species (group-V or -III) is self-diffused through its own sublattice; and the activation energy for atom diffusion follows the sequence of In < Ga < As atoms [238, 242]. When the annealing temperature is low, some In, Ga and As atoms from QDs' barrier InGaAs will diffuse into the vacancy positions of the dots' surface region. However, in group III atoms, Ga atom has higher activation energy than In atom, so some In vacancies near dots' surface region will be filled by In atom of InGaAs barrier under the limitation of the self-diffusion mechanism. Correspondingly, the As vacancy will be filled by As atom of InGaAs barrier. As a result, the effective height of dots will increase, thus redshifting the PL emission. After calculation, for the studied QDs emitting around 2 μm, one nanometer increase in dots' height could generate around 96 nm QD' redshift. So, the received 40 nm and 20 nm redshift for Figure 6.2-(b)-(i)/-(ii) and -(iii) QD samples, respectively, corresponds to 0.4 nm and 0.2 nm increment of the QD's height. Besides, the faster vacancy diffusion at low temperature than at high temperature annealing may also contribute to the redshift. When the annealing temperature increases, the high thermal energy weakens the activation energy difference of the atom diffusion between Indium and Gallium atoms. This recovers the normal In-Ga interdiffusion between the InAs QDs and InGaAs barriers, thus triggering the dots' band gap normal blueshift. PL intensity becomes low in emission's redshift region and increases as normal in the blueshift region. This is because under low annealing temperature the vacancy fillings of In and As atoms, which are from the InGaAs barriers, leave the new vacancies in the InGaAs barriers. These vacancies act as the nonradiative centers and degrade the PL emission. After increasing annealing temperature, the normal material interdiffusion reduces all kinds of nonradiative recombination centers in the QD structure, thus increasing the PL intensity.

The observed different band gap shift between the three samples after annealing is that the blueshift extent increases with the gradation, y, of dots' upper $In_{(0.53+y)-0.53}Ga_{(0.47-y)-0.47}As$ barrier. This is probably attributed to the more defects formed in the wider-graded InGaAs barrier layers. For the $In_{0.85-0.53}Ga_{0.15-0.47}As$ barrier layer in sample (iii), the Indium composition is changed from 0.85 to 0.53. The larger gradation InGaAs need faster source flux adjustment during growing the InGaAs layer. More defects are generated in the graded InGaAs layer. These defects enhance the intermixing upon the thermal annealing, resulting in larger blueshift. As expected, the enhanced intermixing also reduces the threshold temperature for the blueshift. The threshold temperature decreases from 700 ^{o}C to 620 ^{o}C when the gradation, y, of the upper $In_{(0.53+y)-0.53}Ga_{(0.47-y)-0.47}As$ barrier increases from 0.19 to 0.32. Too high annealing temperature, $\geq$ 800 ^{o}C, degrades QDs structural quality and hence weakens the PL intensity of QDs samples [243].

Effects of the top-cap layer thickness and dot-density on the QD intermixing have been studied. Two groups of QDs samples have been prepared. Samples (i) and (ii) is capped by the InP layer with the thickness of 700 nm and 20 nm, respectively; and all other structures are the same. Samples (ii) and (iii) are with different dot density; the dot density of the two samples is $1.2\times10^{10}/cm^2$ and $2.5\times10^{10}/cm^2$, respectively. The dot mean height of sample (ii) is 9 nm, larger than that of sample (iii) with 7 nm. All other layers in QD structures for the two samples are the same. The detailed QD structures for these samples are described in Figure 6.3-(a) and -(b). All the samples are annealed at the same time for 60 seconds at the temperature of 500 ^{o}C ~ 800 ^{o}C. The PL peak shift and PL peak intensity change trend of the annealed samples with respect to the as-grown samples are summarized and plotted as the function of annealing temperature in Figure 6.3-(c).

Figure 6.3-(c) shows the threshold annealing temperature for the blueshift of sample (i) is lower by 70 ^{o}C compared with that of the sample (ii). Besides, the blueshift of (i) is ~ 90 nm, which is two times of that of (ii) with only 45 nm blueshift,

when the two samples are annealed at 800 °C. The thick-InP-capped QDs show stronger intermixing upon annealing. For samples (i) and (ii), the dot density is the same and the top InP cap thickness is different. During growing the InAs/InGaAs/InP

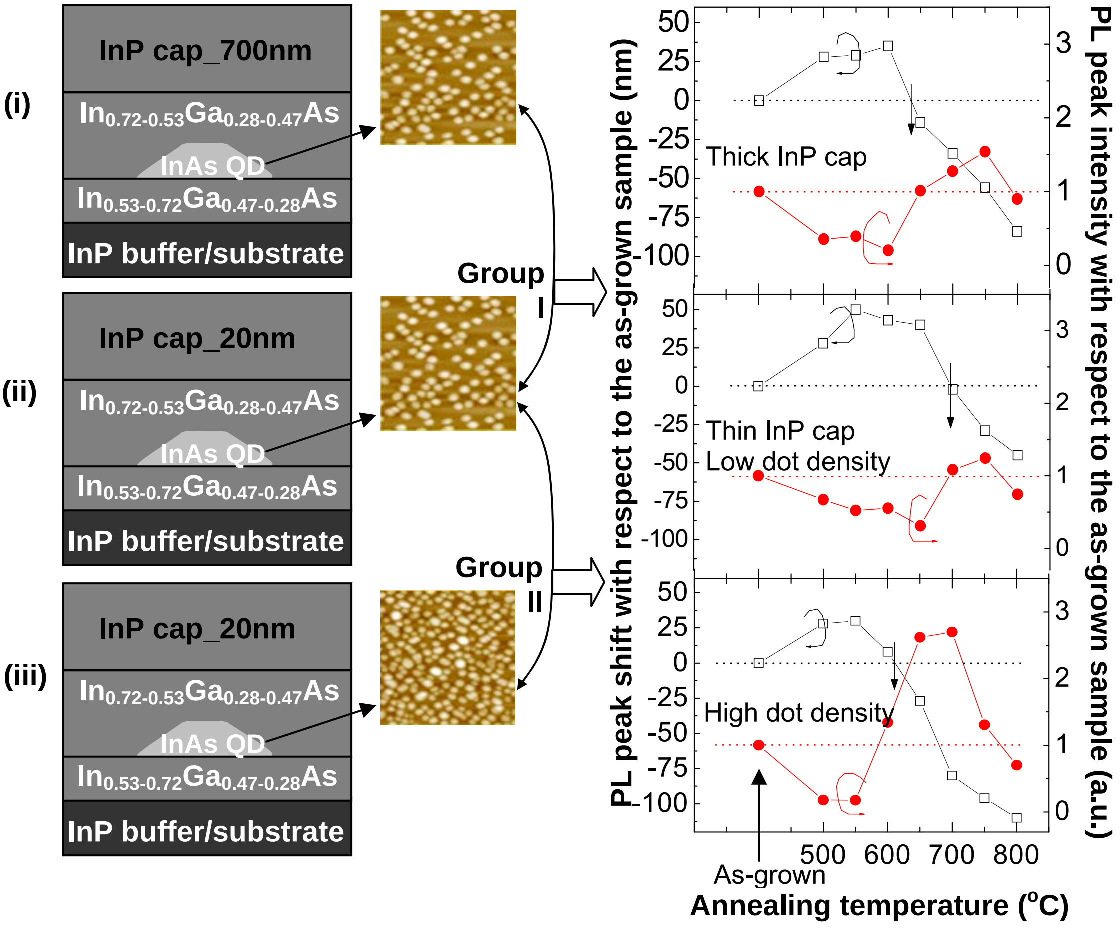

(a) (b) (c)

Figure 6.3 (a) Schematic QD structures, (b) top-view 1μm×1μm AFM images of the corresponding uncapped dots, and (c) PL peak shift and intensity change trend as regard to the as-grown samples.

QD structures, the reactor temperature was kept at 550 °C for growing the InAs QDs layer, top InGaAs barrier and top InP cap. Low reactor temperature for InP cap growth will introduce more grown-in defects in the thicker InP cap layer. These grown-in defects will engage in the material diffusing upon the thermal annealing, thus enhancing the diffusion extent in the QDs of sample (i) with thicker top InP cap. Besides, the thermal expansion coefficient of InP (α_{InP}) is 4.6×10^{-6} $^{o}C^{-1}$, and that of $In_{0.72-0.53}Ga_{0.28-0.47}As$ (α_{InGaAs}) is around 5.0×10^{-6} $^{o}C^{-1}$ after a linear interpolation based on the 4.52×10^{-6} $^{o}C^{-1}$ and 5.73×10^{-6} $^{o}C^{-1}$ of InAs and GaAs material, respectively. α_{InGaAs} is 38% larger than $\alpha_{InP,}$ which generates the compressive strain on InGaAs during the thermal annealing. Such strain enhances the grown-in defects diffusion across the QDs region, thus also promoting the QD intermixing of sample (i).

Figure 6.3-(c) shows the threshold annealing temperatures for the blueshift of sample (iii) is lowered by 90 ^{o}C compared with that of the sample (ii). After annealed at 800 ^{o}C, the band gap shift of sample (iii) reaches 130 nm, which is three times of that of sample (ii) with the blueshift of only 45 nm after annealing. However, as in the previous reports, larger dots have stronger blueshift effect under the same thermal annealing conditions [229, 232]. The received blueshift trend in this study is opposite: the smaller sized dots (higher density) have larger blueshift. The possible reason may be related to the defect density in the dot/barrier interface and strain distribution in the dots for the QDs with different dot density. Further detailed study on this is planned in the future research.

6.3 Argon plasma enhanced QD intermixing

6.3.1 Plasma-exposure effect

In this section, Ar-plasma enhanced intermixing of InAs/InGaAs/InP QDs has been investigated. We studied the effects of Ar-plasma exposure time and annealing conditions on the QDs' energy band gap tuning.

In order to investigate Ar-plasma exposure effects on the QD intermixing, InP/In$_{0.53}$Ga$_{0.47}$As/InAs/In$_{0.53}$Ga$_{0.47}$As/InP QDs sample was prepared with growing a thick, ~ 700 nm, InP top layer for Ar-plasma exposure. The AFM image of the uncapped QDs of the sample is shown in Figure 6.4. The standard deviation of dot's diameter/height is around 1 nm, so the dots formed are with good size uniformity. Dot

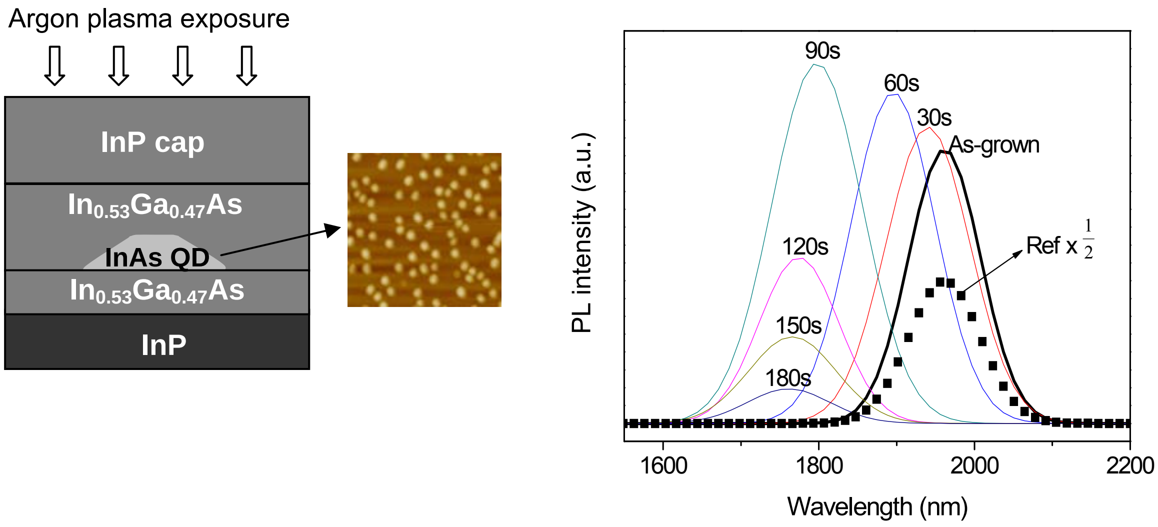

Figure 6.4 77-K PL spectra for InP/In$_{0.53}$Ga$_{0.47}$As/InAs/In$_{0.53}$Ga$_{0.47}$As/InP QDs samples after Ar-plasma exposure for 30 s ~ 180 s. The schematic QD structure and the corresponding top-view 1×1 μm^2 AFM images are also shown.

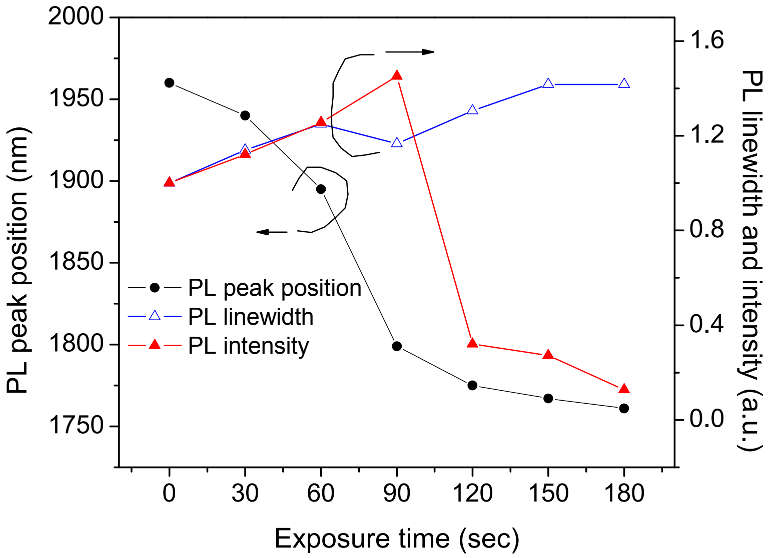

Figure 6.5 Summarized PL peak position, linewidth and intensity for the samples with different Ar-plasma exposure time based on the PL results in Figure 6.4.

density of the samples are around 1.0×10^{10} cm^{-2}. The plasma system used in this work has been introduced in Chapter 3. The point defects, which affect QD intermixing, will be generated in the surface InP layer in QDs samples after plasma exposure. Effects of the intermixing were evaluated by studying the changes in the samples' PL peak position, intensity and linewidth before and after the ICP treatment.

The QDs sample was exposed to ICP Ar plasma with different time but without the RTA treatment. A reference InP/$In_{0.53}Ga_{0.47}As$/InAs/$In_{0.53}Ga_{0.47}As$/InP QD sample was deposited with 200 nm SiO_2 cover layer before the 90-second-ICP plasma exposure, so that the sample's epilayer would not be exposed to the plasma during the ICP process. All low-temperature PL spectra were shown in Figure 6.4, and the PL property change trend as the function of exposure time is summarized in Figure 6.5. It is observed that after the ICP Ar-plasma exposure, PL peak of the reference QD sample (The black dot line curve in Figure 6.4) is the same as that of the as-grown QD sample. This shows the 200 nm SiO_2 mask can effectively prevent the epilayer from plasma bombardment. The interesting phenomenon observed is that, for samples without the SiO_2 mask layer, the PL spectrum exhibits a blueshift right after the Ar-plasma exposure. This is different from that of QW structure, where the PL emission blueshift occurs only after the subsequent thermal annealing. For the QD samples studied in this work, the blueshift of the dots' PL emission increases with the Ar plasma exposure time up to 90 seconds and then saturates. At the same time, the PL intensity of the QDs increases with the exposure time up to 90 seconds, and it decreases when exposed to Ar plasma longer. This is attributed to the material sputtering of the samples during the Ar plasma exposure. Based on the top-view AFM images in Figure 6.6, the sample surfaces become rough after exposure to ICP plasma, a result of surface sputtering during the ICP process. The sputtering rate can be

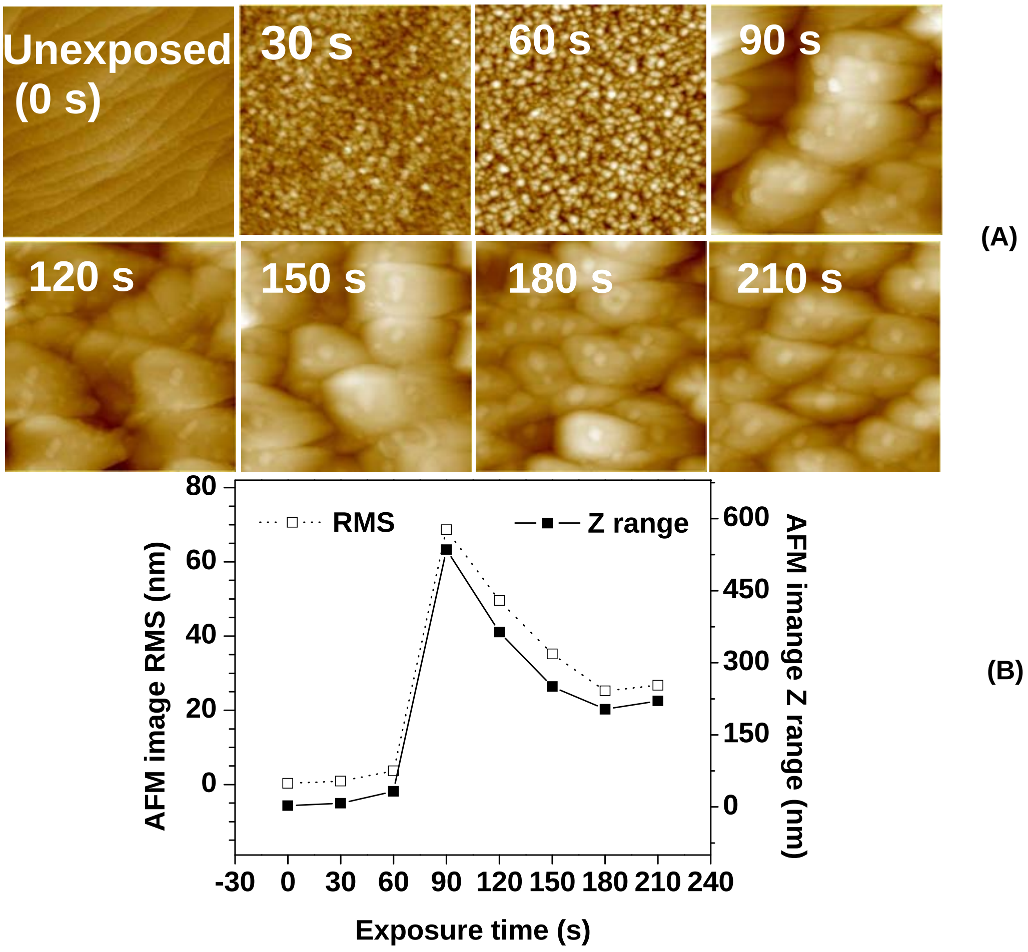

Figure 6.6 (A) Top-view 1×1 μm^2 AFM images of as-grown (unexposed) and exposed InP/$In_{0.53}Ga_{0.47}As$/InAs/$In_{0.53}Ga_{0.47}As$/InP QD samples, and (B) the surface RMS roughness and Z-range (based on 5×5 μm^2 AFM images) as a function of the exposure time. The exposure time changes from 30 s to 210 s.

deduced from the surface roughness and the Z-range measured by AFM after different ICP exposure time. The surface RMS (Root-mean-square) roughness and the Z-range versus the exposure time are also shown in Figure 6.6. Z-range of the sample increases to a maximum of 535 nm with the ICP exposure time increased to 90 seconds and then decreases when further exposed to plasma. The decrease in the sputtering with longer plasma exposure is because the plasma sputtering tends to remove the surface hills faster, thus reducing the RMS and Z-range of the surface.

The results show that PL emission of the QD sample blueshifts after sample's exposure to plasma. From our previous study, we have measured the sputtering rate of InP material with the same experimental conditions. It is about 100 nm/min, which is significantly slower for InGaAs or InGaAsP material. The surface roughness measured by AFM in Figure 6.6 indicates the roughening rate (proportional to the sputtering rate) of sample's InP cap layer is around 300-400 nm/min which is higher than the sputtering rate received before. This is because the top InP layer of the studied QD sample was grown at the relatively low temperature. Therefore, the cap layer was removed during ICP process at a higher etching rate. The removal of the cap layer explains the increase of the sample's PL intensity. At the same time, because of the removal of the cap layer, the plasma-generated defects at the surface are close to the QDs. After sufficient plasma exposure time, some of the defects can diffuse into the QDs, thereby inducing the QD/barrier material intermixing under the high cation concentration gradient between the QD material (InAs) and its surrounding material (InGaAs). These effects contribute to a blueshift of the QDs' PL emission after ICP Ar-plasma exposure. After long time exposure to plasma, the whole InP cap layer is removed. The etch rate of InGaAs barrier layer of the sputtering is slower. At the same time, the number of defects generated is saturated [236]. Therefore, the sample's PL blueshift saturates after 120 second plasma exposure. The reduction of PL intensity after long time plasma exposure shows that the thin upper InGaAs barrier layer is insufficient to confine the carriers in the QD, and at the same time, some of the QDs may even be removed by the sputtering.

6.3.2 Large band gap tuning

To study the plasma-exposure effect on the band gap shift extent upon thermal annealing, we annealed InP/$In_{0.53}Ga_{0.47}As$/InAs/$In_{0.53}Ga_{0.47}As$/InP QDs sample at 580 - 620 °C for 60 seconds after their exposure to plasma with different time. The 77-K PL curves for the samples annealed at 620 °C are shown in Figure 6.7. Changes in the sample's (i) PL peak shift, (ii) FWHM of the PL spectra, and (iii) PL peak emission intensity, as a function of the plasma exposure time for the three groups of samples annealed at different temperatures are plotted in Figure 6.8. Thermal annealing effects of the as-grown samples, i.e. with plasma exposure for zero second, are also plotted in Figure 6.8. As the reference, the PL peak shift, PL linewidth and peak intensity as the function of exposure time of the samples after their only plasma exposure are also shown in Figure 6.8 based on the PL curves in Figure 6.4. It shows with plasma exposure of less than 90 seconds, the sample's PL blueshift and intensity increase further after RTA treatment while the FWHM of their PL spectra reduces. The longer the plasma exposure time, the greater these changes received. When the plasma

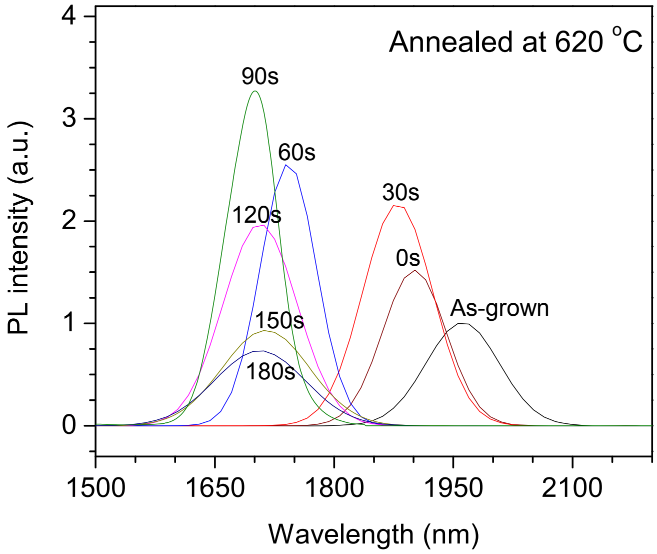

Figure 6.7 77-K PL spectra for the QDs samples after Ar-plasma exposure for 30 s ~ 180 s followed by the RTA at 620 °C for 60 s, i.e. an RTA process is added based on the plasma-exposed QDs samples as mentioned in Figure 6.4.

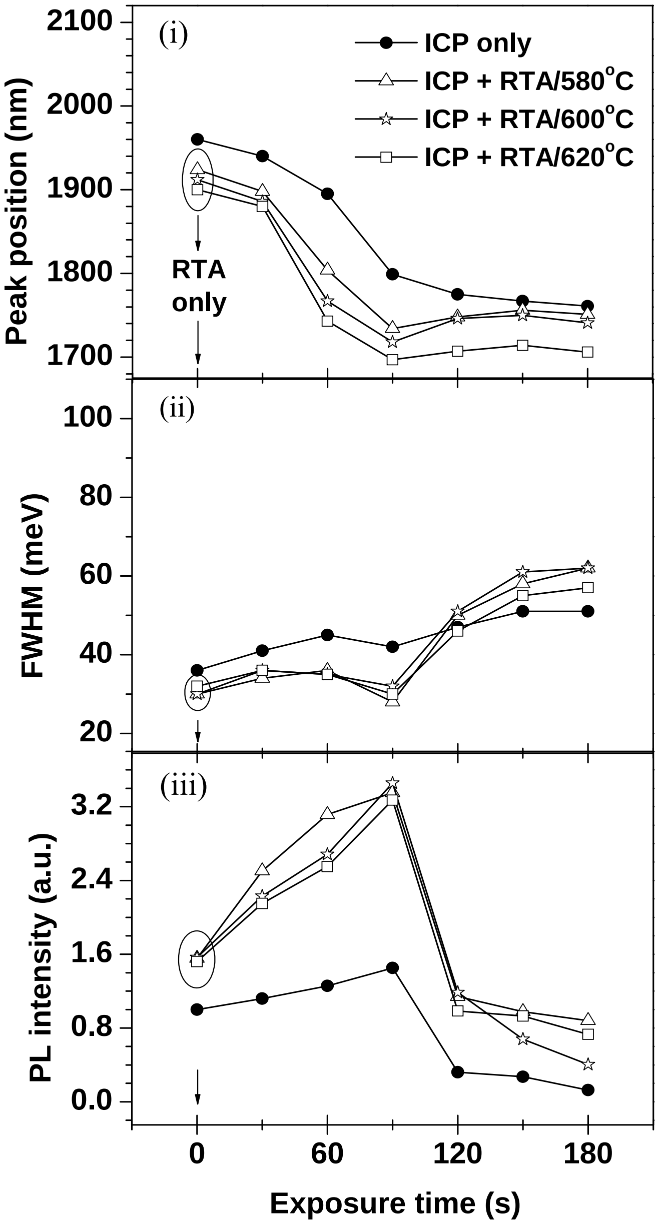

Figure 6.8 (i) The PL peak wavelength, (ii) the FWHM linewidth, and (iii) the relative PL peak intensity of InAs(QD)/$In_{0.53}Ga_{0.47}As$*/InP QDs samples after their ICP plasma exposure with different time followed by RTA for 60 s at different temperatures are plotted as a function of the Ar-plasma exposure time. Data points for the as-grown samples after only RTA treatment are circled for notice.*

exposure time exceeds 90 seconds, the samples' emission blueshift saturates and PL intensity drops dramatically, while their linewidth becomes broader. For the as-grown samples, i.e. without plasma exposure, RTA treatment makes their PL blueshifts and emission intensities changes in small range.

The RTA-treatment enhanced PL blueshift of the samples after Ar-plasma exposure less than 90 seconds is due to the larger plasma-generated defect density in the interdiffusion between the QDs and their barrier layer during the RTA annealing. The increase in the samples' PL intensity and the narrowing of their PL linewidth is because (i) thermal annealing increases the defects' mobility and homogenizes their distribution in the QD structure, thereby homogenizing the intermixing between the QDs and their barrier material; (ii) thermal-annealing induced QD/barrier interdiffusion enhances the mobility of the atoms in QD structure, hence averaging the local compositional/strain fluctuation in the dots [244]. However, if the Ar plasma exposure time is too long, over 120 seconds, the plasma sputtering partially removes the InGaAs upper barrier layer, which reduces the uniformity of InGaAs upper barrier. This causes the nonuniform emission from the QDs and broadens the emission linewidth. The reduced barrier confinement from upper InGaAs barrier layer would also weaken the PL emission intensity. Similar degradation of the PL emission after too long plasma exposure has also been observed in bulk material [245] and QW structure [236].

To investigate the high temperature annealing effect on the QD's emission shift range, we annealed the as-grown InP/$In_{0.53}Ga_{0.47}As$/InAs/$In_{0.53}Ga_{0.47}As$/InP QDs sample and the sample after ICP Ar-plasma exposure for 90 seconds together at 720 ^{o}C for 60 seconds. To check the maximum band gap tunability of this technology, we also annealed the sample at 780 ^{o}C after 90-second-ICP plasma exposure. Figure 6.9 shows the PL curves of these samples. Very large PL emission blueshift of 394 nm when compared with that of the as-grown QDs is obtained from the QD sample RTA

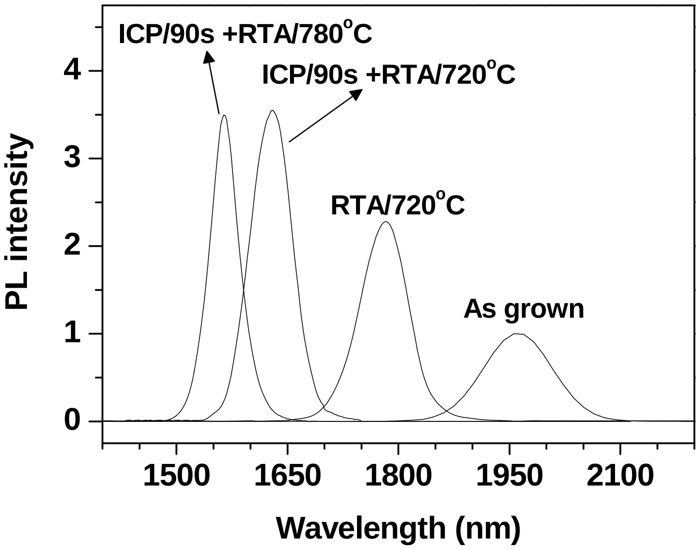

Figure 6.9 77-K PL spectra for the samples of as-grown, RTA at 720 °C for 60 s, and ICP for 90 s followed by RTA at 720 °C/780 °C for 60 s.

annealed at 780 °C after 90-second plasma exposure. The corresponding energy band gap increase of the QD sample after ICP+RTA treatment in this study is $\Delta E_g = 159$ meV. Such band gap tuning range based on low energy Ar-plasma exposure is much larger than the reported maximum band gap tuning range of 126 meV [246] and 120 meV [231], respectively, based on using high energy P-ion and H-ion implantation both for the $In_{\sim 0.55}Ga_{\sim 0.45}As/GaAs$ QD structures. This comparison on QD's band gap tuning capacity between the different intermixing technologies is sound since the reported $In_{\sim 0.55}Ga_{\sim 0.45}As/GaAs$ QD structures have a comparable group-III atom concentration gradient, which mainly determines the intermixing degree in terms of QD structures, with the $InAs/In_{0.53}Ga_{0.47}As$ QD structure studied in this work. In addition, it is observed in this study that the PL peak blueshift after Ar-plasma exposure followed by thermal annealing at 720 °C is 330 nm larger than that of the sample only going through the thermal annealing. This further confirms the Ar-plasma-exposure generated mobile point defects in the sample play a great role in further widening the QD's energy band gap during the thermal process afterwards. Compared with that of the as-grown sample, the PL intensity and linewidth of the QD sample after 90-second-ICP followed by RTA at 720 ^{o}C ~ 780 ^{o}C increases by ~ 2.5 times and narrows by ~ 46%, respectively.

6.4 Selective intermixing

A post-growth multi-band gap tuning technique for QD structures is important for monolithic photonic integration of passive and active QD based multifunctional optoelectronic devices. Different band engineering technologies of spatial selective intermixing for the QD structures across a wafer, including titanium-dioxide (TiO_2) interdiffusion-suppression [228], laser radiation [229], neutral ion-implantation [246] and silica-sputtering [247], etc, have been investigated. In this part, based on the Ar-plasma enhanced intermixing in tuning the QDs' energy band gap, spatial selectivity of the intermixing by employing a SiO_2 mask on the wafers during the intermixing has been investigated in detail for the InAs/InGaAs/InP QD structures.

The InP/$In_{0.53}Ga_{0.47}As$/InAs/$In_{0.53}Ga_{0.47}As$/InP QD structures were used for this study. The InAs QDs were covered by a 50 nm $In_{0.53}Ga_{0.47}As$ upper barrier layer and finally capped with a 700 nm InP cap layer. The intermixing of the QDs samples was carried out by exposing them to Ar plasma and followed by thermal annealing. To investigate the spatial selectivity of the intermixing, as shown in Figure 6.10, portion of the sample was deposited with a 200-nm SiO_2 mask layer by plasma enhanced chemical vapor deposition (PECVD). Then, the samples were exposed to ICP Ar plasma in an ICP chamber. The ICP/RF power, Ar gas flow rate inside the chamber and the process pressure settings in this experiment are the same as before. After the Ar plasma exposure, the samples were annealed in a RTA chamber with

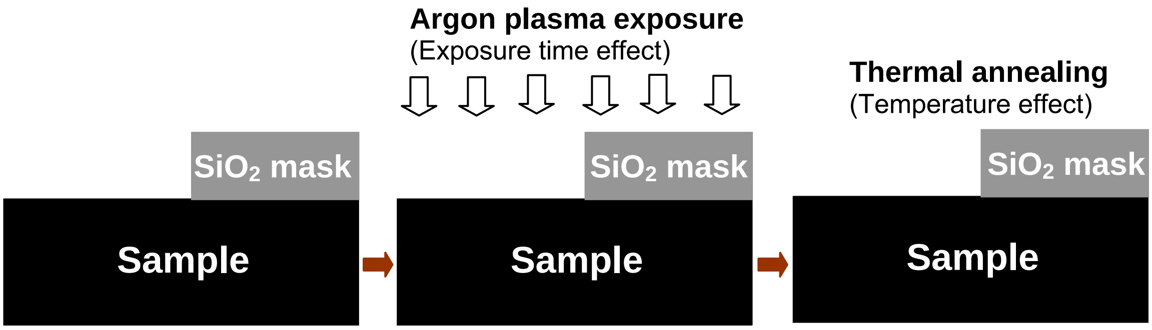

Figure 6.10 Process flow in the selective intermixing study for InAs/InGaAs/InP QDs structure.

atmospheric pressure of nitrogen ambient. Samples were covered with InP wafers to prevent the surface evaporation during the RTA process. The energy band gap tuning of the QD samples after the intermixing was investigated by using PL measurement.

First, we studied the PL results between two groups of samples after exposed to the ICP Ar-plasma for different time and followed by RTA anneal at 620 ^{o}C for 60 seconds. Samples (i) are not masked by the SiO_2 layer during the plasma exposure and (ii) are covered with the SiO_2-mask layer. The 77-K PL spectra of group (i) samples have been shown in Figure 6.7, and that of group (ii) are not shown since there is almost no change in the PL curves of the samples in this group. The (i)/(ii)-samples' peak emission blue shift and linewidth as a function of the Ar plasma exposure time during the intermixing are summarized in Figure 6.11-(a) and Figure 6.11-(b), respectively. Large blue shift of the peak emission has been observed from the samples without the SiO_2 mask after the intermixing, while that for the samples covered by the SiO_2 mask during the plasma exposure is very limited. Moreover, the blue shift does not change with the plasma exposure time after the RTA annealing; and the blue shift is the same as that of the sample only going through the RTA annealing without the plasma exposure. This further confirms that the 200-nm SiO_2

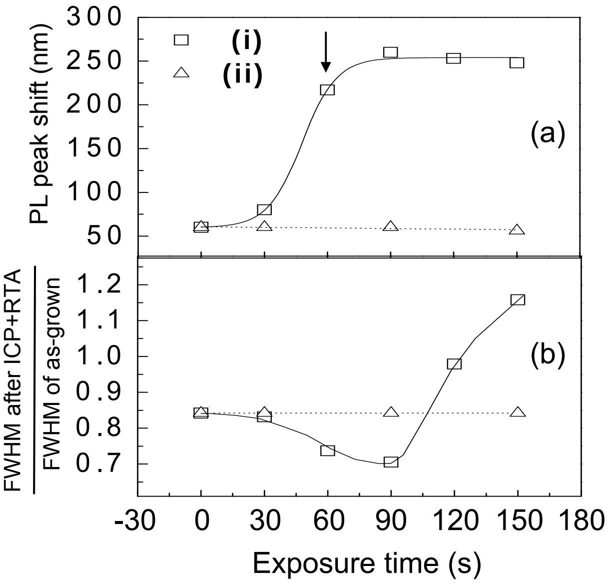

Figure 6.11 (a) PL peak blue shifts and (b) ratio of PL spectra FWHM of the (i) un-masked sample and (ii) masked sample as a function of the Ar plasma exposure time during the intermixing for samples. All the samples were annealed at 620 °C for 60 s after the plasma exposure.

mask layer effectively blocks off the Ar plasma exposure to the sample. So, the PL blue shift of the SiO_2 masked sample after intermixing is only because of the RTA thermal anneal. The difference of blue shift (or spatial selectivity of the intermixing) between the un-masked and masked samples' emission peaks can be continuously tuned from 0 to 200 nm through the intermixing by increasing the plasma-exposure time from 0 to 90 seconds followed by thermal annealing at 620 °C.

To study the temperature dependence of the selective intermixing, samples (SiO_2 masked and un-masked) were annealed at different temperatures ranging from 580 ~ 780 °C after exposed to the ICP Ar plasma for 90 seconds. Figure 6.12 shows the PL spectra of (iii) un-masked samples, (iv) SiO_2 masked samples annealed at different temperatures in the intermixing. For reference, we removed one sample's (sample (v)) SiO_2 mask after the ICP plasma exposure and RTA annealed it together with sample (iii) and (iv). Figure 6.12-(v) shows the PL spectra of the sample (v) annealed at different temperatures. Figure 6.13 shows the blue shifts of the PL emission peaks and the linewidths of the three samples after going through the intermixing with different annealing temperatures. The results show that for sample (iii), large blue shifts have been received after the intermixing, while its PL peak intensity increases and the linewidth decreases with the ICP Ar plasma exposure up to 90 seconds, which shows that the ICP plasma dose not damage the InAs QDs' crystal quality up to 90 seconds plasma exposure.

It is noticed that for the un-masked sample (iii), the sample's PL peak blue shift increases with the annealing temperature during the intermixing almost linearly. However, for the SiO_2 masked sample (iv), the PL peak blue shift increases slowly

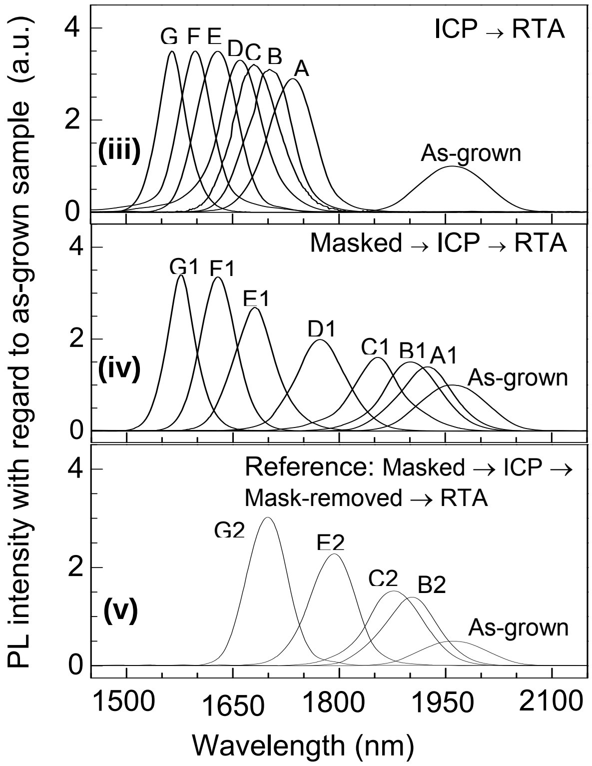

Figure 6.12 77-K PL spectra of the (iii) un-masked, (iv) masked and (v) mask removed samples after the intermixing. The samples were exposed to ICP Ar plasma for 90 s followed by RTA for 60 s and annealed at different temperatures: A: 580 °C, B: 620 °C, C: 650 °C, D: 680 °C, E: 720 °C, F: 750 °C and G: 780 °C.

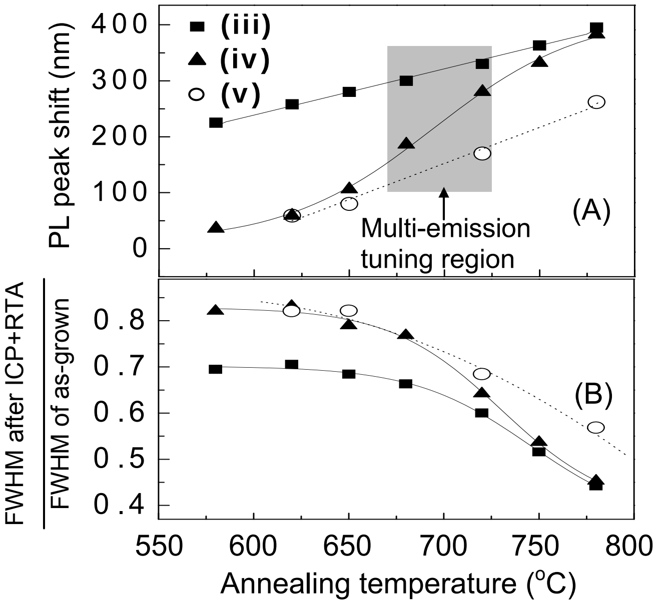

Figure 6.13 (A) PL peak blue shifts and (B) ratio of PL spectra FWHM of the (iii) un-masked sample, (iv) masked sample and (v) mask removed sample as a function of the RTA annealing temperature. All the samples were exposed to the ICP Ar plasma for 90 s for the intermixing.

with the RTA annealing temperature in the intermixing when the annealing temperature is below 650 °C. When the annealing temperature increases from 650 °C to 750 °C, the blue shift of the SiO_2 masked sample increases much faster after the intermixing. At low RTA annealing temperature, < 650 °C, the difference of the blueshift between the SiO_2 masked and unmasked samples after the intermixing is very large, ~200 nm. When the RTA annealing temperature is above 650 °C, the difference of the blue shift between the masked and un-masked samples after the intermixing becomes smaller when annealed the samples at higher temperature. The blue shift difference between the samples is only 10 nm when annealed the samples at 780 °C during the intermixing. These show that the selectivity of intermixing between the SiO_2 masked and un-masked samples is dependant on the annealing temperature. It shows that the lower annealing temperature, the wider intermixing selectivity, which is good for device fabrications. Too high annealing temperature, > 800 ^{o}C, will degrades the 3-dimentional carriers' confinement of the QD structures and even destroy the highly-strained QDs [247, 248].

As shown in Figure 6.13, for the reference sample (v) with SiO_2 mask layer removed from the top, its PL peak blue shift after the annealing induced intermixing increases almost linearly with the annealing temperature, while for sample (iv) with the SiO_2 on top during the RTA annealing, the blue shift increases much faster when annealed at the temperature above 650 ^{o}C. This is attributed to the strain generated between the SiO_2 mask and the InP cap layer of the sample during the thermal annealing. Since the thermal expansion coefficient of InP ($\sim 4.6\times10^{-6}$ $^{o}C^{-1}$) is more than 8 times larger than that for SiO_2 ($\sim 0.52\times10^{-6}$ $^{o}C^{-1}$), large strain is generated in the InP cap layer during the thermal anneal. This thermal strain leads to the generation of the group III vacancies in the sublattices of InP [249]. At the same time, the diffusion of the defects into the InAs QDs is enhanced by the strain, which promotes the QD intermixing of the sample as the annealing temperature is increased [228].

Figure 6.13-(A) shows when the samples are annealed in the temperature range from 675 ^{o}C to 725 ^{o}C during the intermixing, three different band gap tunings across a wafer can be obtained by adding the SiO_2-mask removal between plasma exposure and thermal annealing steps in the intermixing. The different blue shift between un-masked (iii) and masked (iv) and mask removed (v) samples reaches as wide as around 50 nm (~20 meV) at annealing temperature of 700 ^{o}C in the intermixing. The difference in the intermixing between the un-masked sample (iii) and masked sample (iv) or between the masked sample (iv) and masked removed sample (v) can be modulated by changing the annealing temperature, which achieves the multiple band gap changes across a wafer through the intermixing. This is

important in realizing multi-functional monolithic integration circuits, which generally requires different energy band gaps across a wafer for different function devices, e.g. the emitter, modulator and detectors, etc. Besides, in the multi-emission tuning region, the PL linewidths for the samples (iii), (iv) and (v) are all smaller than that of their as-grown samples. This shows the uniformity of composition/strain in the dots is improved, which advantages improving the spatial resolution across sample's adjacent regions under different intermixing treatments. Moreover, the spatial resolution in the intermixed QDs is also dependent on the lateral diffusion distance/uniformity of the point defects induced by the plasma conditions (plasma energy, density and time), annealing conditions (annealing temperature and time), and mask conditions (SiO_2 film thickness and uniformity), etc. This needs further systematic study in future.

6.5 Summary

In this chapter, thermal annealing on QDs' energy band gap tuning was studied. It was observed that annealing at low temperature induces the redshift which is attributed to the dots size micro-increase. The grown-in defects in the upper barrier or top cap, and the high dot-density both enhance the intermixing in the QD structures upon thermal annealing.

The Ar-plasma exposure on QDs' energy band gap tuning was investigated. It was found that the dots' band gap could be tuned in an obviously larger range by exposing the sample to Ar-plasma before the thermal annealing compared with by using the thermal annealing only. The enhanced QD intermixing is attributed to the point defects generated near sample's surface region after its exposure to the plasma.

By combining the plasma exposure and SiO_2 mask techniques, the spatial selective intermixing has been obtained through controlling the plasma exposure time or the annealing temperature. Based on the selective intermixing, multi-wavelengths across one wafer with 50-nm wavelength separation were achieved.

CHAPTER 7. CONCLUSIONS

7.1 Conclusions

In conclusion, MOCVD growth of mid-IR QDs has been studied in detail in this project. Improvement of QDs formation under the safer growth conditions have been made. We have designed, grown and characterized mid-IR QD structures, and investigated the post-growth QDs' band gap tuning based on Ar-plasma exposure. The major conclusions are listed below.

(i) Improved QDs' dot-density and size-uniformity of InAs/GaAs and InAs/InGaAs/InP QDs grown by safety-improved MOCVD were demonstrated by using the proposed and optimized two-step QDs growth method. Compared with the dots grown by conventional SK growth method, two-step grown QDs have much higher dot-density (~$2.5\times10^{10}\text{cm}^{-2}$) and narrower dot size dispersion (~1 nm).

(ii) 8 band **k·p** theory was used to design mid-IR emissive InAs/InP QD structures based on the strain/barrier technologies by using InGaAs as the QDs' confinement layers. Based on the transition energy calculation, the emission wavelength of InAs/InGaAs/InP QD structures can reach >2.2 μm by adjusting the Indium content of InGaAs barriers.

(iii) Mid-IR InAs/InGaAs/InP QD structures have been grown by MOCVD. The measured emission wavelengths from the grown QDs match well to the theoretical results. Long emission wavelength received from the QD structures reaches > 2.35 μm at 77 K, which is the longest inter-band transition emission wavelength from InAs QDs reported so far. This shows it promising to develop InAs QDs for mid-IR device applications.

(iv) Ar-plasma enhanced QD intermixing for wider energy band gap tuning for QD structures has been investigated. The QD intermixing is enhanced greatly after employing the plasma exposure before thermal annealing. By combining plasma exposure and SiO_2 mask techniques, the selective intermixing with 50-nm separation multi-wavelengths across one wafer has been achieved. This paves a new way to realize multi-functional monolithic integration circuits which needs different energy band gaps across a wafer for different function active/passive devices.

7.2 Recommendations

The recommendations for future research are summarized as the following:

(i) The two-step growth we proposed involves the atomic-level layer deposition. How to control accurately the atomic-layer deposition for reducing the grown-in defects, such as the Indium droplets, in the QDs is crucial for improving the dots' crystal quality and then their PL performance. PL performance enhancement also relies on the improvement in the composition-uniformity and crystal quality of dot's cap layer growths. Besides, understanding of PL emission characteristics of the QD structures with different dots' morphologies are also important before developing the dots for practical devices applications. All these leave much research space further.

(ii) For mid-IR QDs' application in optoelectronic devices, it's important to select the barrier material which well confines the carriers of QDs layer and also exerts smaller lattice mismatch stress on the dots for keeping the long wavelength emission. In this point, for InAs/InP QD system, AlGaAsSb with high energy band gap and large lattice constant is promising if used as the

InAs QDs' top-barrier layers. However, it is a challenge to grow high crystal quality of AlGaAsSb material so far. On the other hand, to narrow the band gap of QD material, such as replacing InAs with InAsN or InAsBi or even InAsNBi, is also promising for realizing the mid-IR emissive QDs. The similar challenge till now is also to grow high quality QDs using these new semiconductor alloys. So, material growth with high quality for these alloys leaves the research space in future. Besides, research on the stacking technique for increasing the dots' PL emission performance is significant for developing the QDs for high performance device applications.

(iii) To realize multifunctional integrated circuits based on the QDs, it is promising and also challenging to develop Ar-plasma exposure post-growth intermixing technology for QDs band gap tuning across a wafer. Two research topics are expected to become more and more interesting in future researches: controllable large-range multi-bandgap tuning technique across a wafer based on the plasma exposure, and development of multifunctional integrated circuits based on QDs active/passive components.

(iv) Finally, for better understanding QDs' electronic structures, further study on theoretical calculation of QDs' energy band structure with considering the accurate dots' shape/size and the strain distribution in QDs and dots' barrier-layers by 8 band **k·p** theory is significant. This is because the dots reported so far are different in the shapes/sizes, which affects the stain distribution in QDs and dots' barrier-layers, thus affecting the dots' electronic structures.

AUTHOR'S PUBLICATIONS

Journal papers

1. **Z. Y. Yin**, X. H. Tang, J. X. Zhang, J. H. Zhao, S. Deny, J. H. Teng, A. Y. Du and M. K. Chin, "Photoluminescence properties of InAs/InGaAs/InP quantum dots under thermal annealing from low to high temperatures", submitted to ***Journal of Applied Physics,*** 2008.
2. **Z. Y. Yin**, X. H. Tang, J. X. Zhang, S. Deny, J. H. Teng, A. Y. Du and M. K. Chin, "Step-1 nucleation growth dependence of InAs/InGaAs/InP quantum dots formation in two-step growth", ***Nanotechnology,*** *2008, v. 19, p. 085603-1-6.*
3. **Z. Y. Yin**, X. H. Tang, "A review of energy band gap engineering in III-V semiconductor alloys for mid-infrared laser applications", ***Solid-State Electronics,*** *2007, v. 51, p. 6.*
4. **Z. Y. Yin**, X. H. Tang, S. Deny and J. H. Zhao, "Study of InAs/GaAs quantum dots grown by MOVPE under the safer growth conditions", ***Journal of Nanoparticle Research*** *2007, v. 9, p. 877.*
5. **Z. Y. Yin**, X. H. Tang, C. W. Lee, J. H. Zhao, S. Deny and M. K. Chin, "Argon-plasma-induced InAs/InGaAs/InP quantum dot intermixing", ***Nanotechnology,*** *2006, v. 17, p. 4664.*
6. **Z. Y. Yin**, X. H. Tang, S. Deny and J. H. Zhao, "Formation of mid-infrared emissive InAs quantum dots on a graded InxGa1-xAs/InP matrix with a more uniform size and higher density under safer growth conditions", ***Nanotechnology,*** *2006, v. 17, p. 1646.*

7. **Z. Y. Yin**, X. H. Tang, W. Liu and D. H. Zhang, "Effects of $In_xGa_{1-x}As$ matrix layer on InAs quantum dot formation and their emission wavelength", ***Journal of Applied Physics*** *2006, v. 100, p. 033109.*
8. **Z. Y. Yin**, X. H. Tang, J. H. Zhao and S. Deny, "Effects of growth conditions on InAs quantum dot formation by metalorganic chemical vapor deposition using tertiarybutylarsine in pure N_2 ambient", ***Journal of Applied Physics*** *2006, v. 99, p. 124306.*
9. X. H. Tang, **Z. Y. Yin,** J. H. Teng, A. Y. Du and M. K. Chin, "Effects of SiO_2 mask on plasma enhanced selective intermixing of InAs/InGaAs/InP quantum dots", accepted to be published in ***IEEE Transactions on Nanotechnology*** *2008.*
10. X. H. Tang, **Z. Y. Yin,** J. H. Zhao and S. Deny, "A new method of two-step growth of InAs/GaAs quantum dots with higher density and more size uniformity", ***Nanotechnology****, 2006, v. 17, p. 295.*
11. X. H. Tang, **Z. Y. Yin**, W. Liu and D. H. Zhang, "Mid-Infrared emission from InAs quantum dots grown by metal-organic vapor phase epitaxy", ***IEEE Transactions on Nanotechnology*** *2006, v. 5, p. 683.*
12. X. H. Tang, **Z. Y. Yin,** A. Y. Du, J. H. Zhao and S. Deny, "MOVPE growth of InAs quantum dots for mid-IR applications", ***Trans. Nonferrous Met. Soc. China*** *2006, v. 16, p. s25.*
13. J. H. Zhao, X. H. Tang, **Z. Y. Yin** and S. Deny, "MOVPE growth of AlxIn1-xP using tertiarybutylphosphine in pure N2 ambient", ***Thin Solid Films****, 2007, v. 515, p. 4454.*
14. S. Deny, X. H. Tang, **Z. Y. Yin** and S. J. Chua**,** "Thermal annealing effect on GaNAs epilayers with different nitrogen compositions grown by MOCVD", ***Journal of Crystal Growth,*** *2007, v. 307, p. 229.*

15. S. Deny, X. H. Tang, S. J. Chua and **Z. Y. Yin**, "Below bandgap emission with intensity higher than band-to-band transition in GaAsN", ***Physica Status Solidi (C),*** *2008, v. 5, p. 464.*
16. X. H. Tang, J. H. Zhao, M. K. Chin, T. Mei, **Z. Y. Yin**, S. Deny and A. Y. Du, "Effect of rapid thermal annealing on the ordering of AlInP grown by metal-organic vapor-phase epitaxy", ***Applied Physics Letters****, 2005, v. 87, p. 181906.*

Conference papers

1. **Z. Y. Yin**, X. H. Tang, J. X. Zhang, S. Deny, J. H. Teng, A. Y. Du and M. K. Chin, "Morphology and crystal quality of InAs QDs grown by MOVPE using different growth modes", ***International Conference on Materials for Advanced Technologies (ICMAT07)***, *Singapore, 1 July - 6 July, 2007.*
2. **Z. Y. Yin**, X. H. Tang, J. H. Zhao and S. Deny, "LP-MOCVD growth of InAs quantum dot on $In_xGa_{1-x}As/InP$ material system for extending emission wavelength", ***The Materials Research Society Fall Conference (MRS05)***, *Boston, 28 November - 2 December, 2005.*
3. **Z. Y. Yin**, X. H. Tang, S. Deny and J. H. Zhao, "Effect of growth conditions on InAs/GaAs quantum dots formation by LP-MOCVD using TBAs in pure N_2 ambient", ***International Conference on Materials for Advanced Technologies (ICMAT05)***, *Singapore, 3 July - 8 July, 2005.*
4. **Z. Y. Yin**, X. H. Tang, J. H. Zhao and S. Deny, "Raman scattering investigation of *in-situ* and *ex-situ* thermally annealed GaAs", ***International Conference on Materials for Advanced Technologies (ICMAT05),*** *Singapore, 3 July – 8 July, 2005.*
5. X. H. Tang, J. H. Zhao, **Z. Y. Yin** and S. Deny, "MOCVD growth of AlInP by

using TBP in N_2 ambient", ***International Conference on Materials for Advanced Technologies (ICMAT05)***, *Singapore, 3 July – 8 July, 2005.*

6. S. Deny, X. H. Tang, **Z. Y. Yin,** J. H. Zhao and S. J. Chua, "Thermal annealing effect on GaNAs grown by MOCVD with different nitrogen compositions", ***International Conference on Materials for Advanced Technologies (ICMAT05)***, *Singapore, 3 July – 8 July, 2005.*
7. S. Deny, X. H. Tang, **Z. Y. Yin,** J. H. Zhao and S. J. Chua, "Photoluminescence of GaNAs epilayers on GaAs grown by MOCVD", ***International Conference on Materials for Advanced Technologies (ICMAT05)***, *Singapore, 3 July – 8 July, 2005.*
8. X. H. Tang, S. Deny, J. H. Zhao, **Z. Y. Yin** and S. J. Chua, "MOCVD growth of GaNAs using UDMHy and TBAs as nitrogen and arsine sources and N_2 as carrier gas", ***International Conference on Materials for Advanced Technologies (ICMAT05)***, *Singapore, 3 July – 8 July, 2005.*

BIBLIOGRAPPHY

---

[1] J. T. Olesberg, "Design and characterization of the electronic and optical properties of materials for mid-infrared laser diode active regions", The *Dissertation for the Ph. D degree*, Chapter 1, pp. 1-2, 1999.

[2] Y. H. Zhang, "Continuous wave operation of InAs/InAsxSb1-x midinfrared lasers", *Appl. Phys.* Lett., vol. 66, pp.118-120, 1995.

[3] V. V. Sherstnev, A. M. Monahov, A. Krier and G. Hill, "Superluminescence in InAsSb circular-ring-mode light-emitting diodes for CO gas detection", *Appl. Phys. Lett*., vol. 77, pp.3908-3910, 2000.

[4] H. H. Zenzie and P. F. Moulton, Lasers and Electro-Optics Society Annual Meeting, "Medical Applications of Solid-state Mid-infrared Lasers 1992". *LEOS '92, Conference Proceedings*, pp. 651- 651, 16-19 Nov. 1992.

[5] C. Sirtori and J. Nagle, "Quantum Cascade Lasers: the quantum technology for semiconductor lasers in the mid-far-infrared", *C. R. Physique, Semiconductor lasers/Lasers semiconductors*, vol. 4, pp. 639-648, 2003.

[6] T. H. Chiu, W. T. Tsang, J. A. Ditzenberger and J. P. van der Ziel, "Room-temperature operation of InGaAsSb/AlGaSb double heterostructure lasers near 2.2 μm prepared by molecular beam epitaxy", *Appl. Phys. Lett*., vol. 49(17), pp. 1051-1052, 1986.

[7] C. Mermelstein, S. Simanowski, M. Mayer, R. Kiefer, J. Schmitz, M. Walther and J. Wagner, "Room-temperature low-threshold low-loss continuous-wave operation of 2.26 μm GaInAsSb/AlGaAsSb quantum-well laser diodes", *Appl. Phys. Lett*., vol. 77, pp. 1581-1583, 2000.

[8] D. H. Chow, R. H. Miles, T. C. Hasenberg, A. R. Kost, Y. H. Yang, H. L. Dunlap and L. West, "Mid-wave infrared diode lasers based on GaInSb/InAs and InAs/AlSb superlattices", *Appl. Phys. Lett.*, vol. 67, pp. 3700-3702, 1995.

[9] J. Faist, F. Capasso, C. Sirtori, D. L. Sivco, J. N. Baillargeon and A. Y. Cho, "High power mid infrared (λ~ 5 μm) quantum cascade lasers operating above room temperature", *Appl. Phys. Lett.*, vol. 68, pp. 3680-3682, 1996.

[10] C. Caneau, A. K. Srivastava, A. G. Dentai, J. L. Zyskind and M. A. Pollack, "Room-temperature GaInAsSb/AlGaAsSb DH injection lasers at 2.2 μm", *Electron. Lett.*, vol. 21, pp. 815-817, 1985.

[11] B. H. Koo, T. Hanada, H. Makino and T. Yao, "Effect of lattice mismatch on surface morphology of InAs quantum dots on (100) In1-xAlxAs/InP," *Appl. Phys. Lett.*, vol. 79, pp. 4331-4333, 2001.

[12] M. Borgstrom, M. P. Pires, T.Bryllert, S. Landi, W. Seifert and P. L. Souza, "InAs quantum dots grown on InAlGaAs lattice matched to InP", *J. Cryst. Growth*, vol. 252, pp. 481-485 2003.

[13] Y. M. Qiu, and D. Uhl, "Effect of thin GaAs interface layer on InAs quantum dots grown on InGaAs/InP using metalorganic vapor phase epitaxy," *J. Cryst. Growth,* vol. 257, pp. 225-230 2003.

[14] Z. Feit, D. Kostyk, R. Woods and P. Mak, "Single-mode molecular beam epitaxy grown PbEuSeTe/PbTe buried-heterostructure diode lasers for CO2 high-resolution spectroscopy", *Appl. Phys. Lett.*, vol. 58, pp. 343-345, 1991.

[15] Z. Shi, M. Tacke, A. Lambrecht and H. Bottner, "Midinfrared lead salt multi-quantum-well diode lasers with 282 K operation" *Appl. Phys. Lett.*, vol. 66, pp. 2537-2539, 1995.

[16] J. M. Arias, M. Zandian, R. Zucca and J. Singh, "HgCdTe infrared diode lasers grown by MBE", *Semicond. Sci. Tech.*, vol. 8, pp. S255-260, 1993.

[17] D. Wu, "MOCVD growth and characterization of InAsSb/InAs(SbP) on InAs substrate for the mid-infrared laser applications", The Dissertation for the Ph. D degree, Chapter 2, pp. 5-6, 1999.

[18] M. R. Gokhale, F. Wei, H. S. Wang and S. R. Forrest, "Growth and characterization of small band gap (~0.6 eV) InGaAsN layers on InP," *Appl. Phys. Lett.*, vol. 74 pp. 1287-1289, 1999.

[19] D. K. Shih and H. H. Lin, "Strained InAsN/InGaAs/InP multiple quantum well structures grown by RF-plasma assisted GSMBE for mid-infrared laser applications," *IEE Proceedings, Optoelectronics,* vol. 150 pp. 253-258, 2003.

[20] H. Lee, P. K. York, R. J. Menna, R. U. Martinelli, D. Z. Garbuzov, S. Y. Narayan and J. C. Connolly, "Room-temperature 2.78 μm AlGaAsSb/InGaAsSb quantum-well lasers," *Appl. Phys. Lett.*, vol. 66 pp. 1942-1944 1995.

[21] T. Newell, X. Wu, A. L. Gray, S. Dorato, H. Lee and L. F. Lester, "The effect of increased valence band offset on the operation of 2 μm GaInAsSb-AlGaAsSb lasers," *IEEE, Photon. Tech. Lett.*, vol. 11 pp. 30-32, 1999.

[22] A. N. Baranov, N. Bertru, Y. Cuminal, G. Boissier, C. Alibert and A. Joullie, "Observation of room-temperature laser emission from type III InAs/GaSb multiple quantum well structures," *Appl. Phys. Lett.*, vol. 71 pp. 735-737, 1997.

[23] J. Faist, F. Capasso, D. L. Sivco, C. Sirtori, A. L. Hutchinson and A. Y. Cho, "Quantum cascade laser," *Science,* vol. 264 pp. 553-556, 1994.

[24] M. Beck, D. Hofstetter, T. Aellen, J. Faist, U. Oesterle, M. Ilegems, E. Gini and H. Melchior, "Continuous wave operation of a mid-infrared semiconductor laser at room temperature," *Science,* vol. 295 pp. 301-305, 2002.

[25] M. Higashiwaki, S. Shimomura, S. Hiyamizu and S. Ikawa S, "Self-organized GaAs quantum-wire lasers grown on (775)B-oriented GaAs substrates by molecular beam epitaxy," *Appl. Phys. Lett.*, vol. 74 pp. 780-782, 1999.

[26] T. J. Rotter, A. Stintz and K. J. Malloy, "InP based quantum dash lasers with 2 µm wavelength," *IEE Proc. –Optoelectron,* vol. 150 pp. 318-321, 2003.

[27] N. Kirstaedter, N. N. Ledentsov, M. Grundamann, D. Bimberg, V. M. Ustinov, S. S. Ruvimov, M. V. Maximov, P. S. Kop'ev, Z. I. Alferov, U. Richter, P. Werner, U. Gosele and J. Heydenreich, "Low threshold, large To injection laser emission from (InGa)As quantum dots," *Electron. Lett.*, vol. 30 pp. 1416-1417, 1994.

[28] J. C. DeWinter, M. A. Pollack, A. K. Srivastava and J. L. Zyskind, "Liquid phase epitaxial Ga1-xInxAsySb1-y lattice-matched to (100) GaSb over the 1.71 to 2.33 µm wavelength range", *J.Electron. Mater.*, vol. 14, pp. 729-747, 1985.

[29] G. B. Stringfellow, "Miscibility gaps in quaternary III/V alloys", *J. Cryst. Growth*, vol. 58, pp. 194-202 (1982).

[30] A. N. Baranov, A. N. Imenkov, V. V. Sherstner and Yu.P. Yakovlev, "2.7–3.9 µm InAsSb(P)/InAsSbP low threshold diode lasers", *Appl. Phys. Lett.*, vol. 64, pp. 2480-2482 1994.

[31] G. B. Stringfellow, "Organomettalic vapor phase epitaxy reaction kinetics", *In Hurle. D. T. J., editor, Handbook of Crystal Growth*, 3b, chapter 12., Elsevier Science, Netherlands 1989.

[32] T. F. Kuech, "Recent advances in metal-organic vapor phase epitaxy", *Proceedings of the IEEE*, vol. 80, pp. 1609-1624 1992.

[33] H. K. Choi and S. J. Eglash, "Room-temperature CW operation at 2.2 µm of GaInAsSb/AlGaAsSb diode lasers grown by molecular beam epitaxy", *Appl. Phys. Lett.*, vol. 59, pp. 1165-1166 1991.

[34] Z. I. Alferov "The Double Heterostructure: The Concept and its Applications in Physics, Electronics, and Technology (Nobel Lecture)", *CHEMPHYSCHEM*, vol. 2, pp. 500-513 2001.

[35] B. Zhao, T. R. Chen and A. Yariv, "Comparison of differential gain in single quantum well and bulk double heterostructure lasers", *Electron. Lett.*, vol. 27, pp. 2343 -2345 1991.

[36] Y. Arakawa, K. Vahala and A. Yariv, "Quantum noise and dynamics in quantum well and quantum wire lasers", *Appl. Phys. Lett.*, vol. 45, pp. 950-952 1984.

[37] W. T. Tsang, "Extremely low threshold (AlGa)As graded-index waveguide separate-confinement heterostructure lasers grown by molecular beam epitaxy", *Appl. Phys. Lett.,* vol. 40, pp. 217-219 1982.

[38] D. Z. Garbuzov, R. U. Martinelli, H. Lee, P. K. York, R. J. Menna, J. C. Connolly, S. Y. Narayan, "Ultralow-loss broadened-waveguide high-power 2 μm AlGaAsSb/InGaAsSb/GaSb separate-confinement quantum-well lasers," *Appl. Phys. Lett*., vol. 69 2006-2008 1996.

[39] E. P. O'Reilly and A. R. Adams, "Band-structure engineering in strained semiconductor lasers," *IEEE J. Quantum Electron,* vol. 30 pp. 366-379 1994.

[40] A. Joullié and P. Christol, "GaSb-based mid-infrared 2–5 μm laser diodes", *C. R. Physique,* vol. 4 pp. 621–637 2003.

[41] L. Shterengas, G. Belenky, M. V. Kisin and D. Donetsky, "High power 2.4 μm heavily strained type-I quantum well GaSb-based diode lasers with more than 1 W of continuous wave output power and a maximum power-conversion efficiency of 17.5%", *Appl. Phys. Lett*., vol. 90 pp. 011119-1-3 2007.

[42] J. L. Lazzari, E. Tournié, F. Pitard, A. Joullié, B. Lambert, "Growth limitations by the miscibility gap in liquid phase epitaxy of $Ga_{1-x}In_xAs_ySb_{1-y}$ on GaSb,"*Mater. Sci. Eng*. B, vol. B9 pp. 125-128 1991.

[43] J. B. Heroux, C. W. Pei and W. I. Wang, "Epitaxial growth of InGaAsSb/AlGaAsSb heterostructures for mid-infrared lasers based on strain engineering", *J. Vac. Sci. Technol. B*, vol. 22(4) pp. 240-2243 2004.

[44] H. K. Choi, G. W. Turner, M. J. Manfra and M. K. Connors, "175 K continuous wave operation of InAsSb/InAlAsSb quantum-well diode lasers emitting at 3.5 µm,"*Appl. Phys. Lett*., vol. 68 pp. 2936-2938 1996.

[45] H. K. Choi, G. W. Turner and H. Q. Le, "InAsSb/InAlAs strained quantum-well lasers emitting at 4.5 µm,"*Appl. Phys. Lett*., vol. 66 pp. 3543-3545 1995.

[46] J. R. Meyer, C. A. Hoffman, F. J. Bartoli and L. R. Ram-Mohan, "Type-II quantum-well lasers for the mid-wavelength infrared,"*Appl. Phys. Lett*., vol. 67, pp.757-759 1995.

[47] L. Bellaiche, "Band gaps of lattice-matched (Ga,In)(As,N) alloys,"*Appl. Phys. Lett*., vol. 75 pp. 2578-2580 1999.

[48] I. Vurgaftman, J. R. Meyer and L. R. Ram-Mohan, "Band parameters for III–V compound semiconductors and their alloys", *J. Appl. Phys*., vol. 89, pp. 5836-5837 2001.

[49] J. W, W. Walukiewicz, K. M. Yu, J. W. Ager III, E. E. Haller, H. Lu, W. J. Schaff, Y. Saito and Y. Naishi. "Unusual properties of the fundamental band gap of InN", *Appl. Phys. Lett*., vol. 80, pp. 3967-3969 2002.

[50] T. Kitatani, M. Kondow, K. Shinoda, Y. Yazawa and M. Okai, "Characterization of the Refractive Index of Strained GaInNAs Layers by Spectroscopic Ellipsometry", *Jpn. J. Appl. Phys.,* vol. 37 pp. 753-757 1998.

[51] M. Maier, D. Serries, T. Geppert, K. Kohler, H. Gullich, N. Herres, "SIMS depth profiling of InGaAs/InAlAs quantum wells on InP", *Appl. Surf. Sci.*, vol. 203-204, pp. 486-489 2003.

[52] I. Vurgaftman, J. R. Meyer, N. Tansu and L. J. Mawst, "InP-based dilute-nitride mid-infrared type-II "W" quantum well lasers", *J. Appl. Phys.*, vol. 96, pp. 4653-4655 2004.

[53] P. Christol, P. Bigenwald, A. Joullié, Y. Cuminal, A. N. Baranov, N. Bertru, Y. Rouillard, "Improvement of Sb-based multiquantum well lasers by Coulomb enhancement", *IEE Proc.-Optoelectron,* vol. 146 pp. 3-8 1999.

[54] A. N. Baranov, Y. Cuminal, N. Bertru, C. Alibert, A. Joullié, "Strained multiple quantum well lasers grown on GaSb emitting between 2 and 2.4 µm", *SPIE* 2997, 2–13 1997.

[55] R. H. Miles, D. H. Chow, Y. H. Zhang, P. D. Brewer and R. G. Wilson, "Midwave infrared stimulated emission from a GaInSb/InAs superlattice", *Appl. Phys. Lett.*, vol. 66, pp. 1921-1923 1995.

[56] W. W. Bewley, H. Lee, I. Vurgaftman, R. J. Menna, C. L. Felix, R. U. Martinelli, D. W. Stokes, D. Z. Garbuzov, J. R. Meyer, M. Maiorov, J. C. Connolly, A. R. Sugg, and G. H. Olsen, "Continuous-wave operation of λ = 3.25 µm broadened-waveguide W quantum-well diode lasers up to T = 195K", *Appl. Phys. Lett.*, vol. 76, pp. 256-258 2000.

[57] W.W. Bewley, I. Vurgaftman, C.L. Felix, J.R. Meyer, C.H. Lin, D. Zhang, S.J. Murry, S.S. Pei, L.R. Ram-Mohan, "Role of internal loss in limiting type-II mid-IR laser performance", *J. Appl. Phys.*, vol. 83 pp. 2384–2391 1998.

[58] G. Dumitras and H. Riechert, "Determination of band offsets in semiconductor quantum well structures using surface photovoltage", *J. Appl. Phys.*, vol. 94, pp.

3955-3959 2003.

[59] S. Suchalkin, L. Shterengas, M. Kisin, S. Luryi, G. Belenky, R. Kaspi, A. Ongstad, J. G. Kim and R. U. Martinelli, "Mechanism of the temperature sensitivity of mid-infrared GaSb-based semiconductor lasers", *Appl. Phys. Lett.*, vol. 87, pp. 041102-1-3 2005.

[60] J. S. Yu, S. Slivken, A. Evans, L Doris and M. Razeghi, "High-power continuous-wave operation of a 6 µm quantum-cascade laser at room temperature", *Appl. Phys. Lett.*, vol. 83, pp. 2503-2505 2003.

[61] J. Ulrich, J. Kreuter, W. Schrenk, G. Strasser and K. Unterrainer "Long wavelength (15 and 23 µm) GaAs/AlGaAs quantum cascade lasers", *Appl. Phys. Lett.*, vol. 80, pp. 3691-3693 2002.

[62] B. S. Williams, S. Kumar, O. Hu and J. L. Reno, "High-power terahertz quantum-cascade", *Electron. Lett.*, vol. 42, pp. 89-91 2006.

[63] B. S. Williams, S. Kumar, O. Hu and J. L. Reno, "Resonant-phonon terahertz quantum-cascade laser operating at 2.1 THz (λ ~141 µm)", *Electron. Lett.*, vol. 40, pp. 431-433 2004.

[64] R. Q. Yang and S. S. Pei, "Novel type-II quantum cascade lasers", *J. Appl. Phys.*, vol. 79, pp. 8197- 8203 1996.

[65] C. Sirtori, J. Faist, F. Capasso and A. Y. Cho, "The quantum cascade laser. A device based on two-dimensional electronic subbands", *Pure and Applied Optics*, vol. 7, pp. 373-381 1998.

[66] D. Barate, R. Teissier, Y. Wang and A. N. Baranov, "Short wavelength intersubband emission from InAs/AlSb quantum cascade structures", *Appl. Phys. Lett.*, vol. 87, pp. 051103-1-3 2005.

[67] D. G. Revin, J. W. Cockburn, M. J. Steer, R. J. Airey, M. Hopkinson, A. B. Krysa, L. R. Wilson and S. Menzel, "InGaAs/AlAsSb/InP quantum cascade lasers operating at wavelengths close to 3 μm", *Appl. Phys. Lett.*, vol. 90, pp. 021108-1-3 2007.

[68] J. Faist, F. Capasso, D. L. Sivco, A. L. Hutchinson, G. Chu Sung-Nee, A. Y. Cho, "Short wavelength (λ = 3.4 μm) quantum cascade laser based on strain-compensated InGaAs/AlInAs," *Appl. Phys. Lett.*, vol. 72 pp. 680–682 1998.

[69] M. P. Semtsiv, S. Dressler and W. T. Masselink, "Short-wavelength (λ ~ 3.6 μm) InGaAs-AlAs-InP quantum-cascade laser", *IEEE J. Quantum Electron.*, vol. 43 pp. 42-46 2007.

[70] J. S. Yu, S. R. Darvish, A. Evans, J. Nguyen, S. Slivken and M. Razeghi, "Room-temperature continuous-wave operation of quantum-cascade lasers at $\lambda \sim 4$ μm ", *Appl. Phys. Lett.*, vol. 88 pp. 041111-1-3 2006.

[71] J. S. Yu, A. Evans, S. Slivken, S. R. Darvish and M. Razeghi, "Short wavelength (λ ~ 4.3 μm) high-performance continuous-wave quantum-cascade lasers ", *IEEE Photon. Tech. Lett.*, vol. 17, pp. 1154-1156 2005.

[72] J. S. Yu, S. Slivken, S. R. Darvish, A. Evans, B. Gokden and M. Razeghi, "High-power, room-temperature, and continuous-wave operation of distributed-feedback quantum-cascade lasers at λ ~ 4.8 μm", *Appl. Phys. Lett.,* vol. 87 pp. 041104-1-3 2005.

[73] M. S. Vitiello, G. Scamarcio, V. Spagnolo, A. Lops, Q. Yang, C. Manz and J. Wagner, "Experimental investigation of the lattice and electronic temperatures in Ga0.47In0.53As/Al0.62Ga0.38As1$-x$Sbx quantum-cascade lasers", *Appl. Phys. Lett.,* vol. 90 pp. 121109-1-3 2007.

[74] Q. K. Yang, C. Mann, F. Fuchs, R. Kiefer, K. Kohler, N. Rollbuhler, H. Schneider and J. Wagner, "Improvement of λ ~ 5 μm quantum cascade lasers by blocking barriers in the active regions", *Appl. Phys. Lett.,* vol. 80 pp. 2048-2050 2002.

[75] J. L. Bradshaw, R. Q. Yang, J. D. Bruno, J. T. Pham, D. E. Wortman, "High efficiency interband cascade lasers with peak power exceeding 4W⁄facet," *Appl. Phys. Lett.,* vol. 75 pp. 2362–2364 1999.

[76] C. J. Hill and R. Q. Yang, "MBE growth optimization of Sb-based interband cascade lasers", *J. Cryst. Growth,* vol. 278, pp. 167-172 2005.

[77] J. D. Bruno, J. L. Bradshaw, R. Q. Yang, J. T. Pham and D. E. Wortman, "Low-threshold interband cascade lasers with power efficiency exceeding 9%", *Appl. Phys. Lett.,* vol. 76 pp. 3167-3169 2000.

[78] W. W. Bewley, C. L. Canedy, M. Kim, C. S. Kim, J. A. Nolde, J. R. Lindle, I. Vurgaftman and J. R. Meyer, "Interband cascade laser operating to 269 K at λ = 4.05 μm", *Electron. Lett.*, vol. 43, pp. 283-284 2007.

[79] R. Q. Yang, C. J. Hill, B. Yang and J. K. Liu, "Room-temperature type-II interband cascade lasers near 4.1 μm", *Appl. Phys. Lett.,* vol. 83 pp. 2109-2111 2003.

[80] R. Q. Yang, C. J. Hill, B. Yang and C. M. Wong, "Type-II interband cascade lasers in the 4.3-4.7 μm wavelength region", *IEEE Photon. Tech. Lett.*, vol. 16, pp. 987-989 2004.

[81] R. Q. Yang, J. L. Bradshaw, J. D. Bruno, J. T. Pham, D. E. Wortman, R. L. Tober, "Room temperature type-II interband cascade laser," *Appl. Phys. Lett.,* vol. 81 pp. 397–399 2002.

[82] C. S. Kim, C. L. Canedy, E. H. Aifer, M. Kim, W. W. Bewley, J. G. Tischler, D. C. Larrabee, J. A. Nolde, J. H. Warner, I. Vurgaftman, E. M. Jackson and J. R. Meyer, "Molecular beam epitaxy growth of antimonide type-II "W" high-power interband cascade lasers and long-wavelength infrared photodiodes", *J. Vac. Sci. Technol. B*, vol. 25(3) pp. 991-994 2007.

[83] O. Reentila, M. Mattila, L. Knuuttila, T. Hakkarainen, M. Sopanen, H. Lipsanen, "Comparision of H2 and N2 as carrier gas in MOVPE growth of InGaAsN quantum wells", *J. Cryst. Growth,* vol. 298, pp. 536-539 2007.

[84] C. Weisbuch and B. Vinter, "Quantum semiconductor structures", Academic Press, San Diego, pp. 19-21 1991.

[85] M. Henini, "Quantum dot Nanostructure," *Materialstoday*, pp. 48-53 2002.

[86] Y. Arakawa and H. Sakaki, "Multidimensional quantum well laser and temperature dependence of its threshold current", *Appl. Phys. Lett.*, vol. 40, pp. 939-941 1982.

[87] M. Asada, Y. Miyamoto and Y. Suematsu, "Gain and the threshold of three-dimensional quantum-box lasers", *IEEE J. Quantum Electron.*, vol. QE-22, No.9, pp. 1915-1921 1986.

[88] H. Sakaki, "Quantum wires, quantum boxes and related structures: physics, device potentials and structural requirements", *Surf. Science*, vol. 267, pp. 623-629 1992.

[89] C. R. Martin, "Nanomaterials: A membrane-based synthetic approach," *Science,* vol. 266 pp. 1961-1966 1994.

[90] P. M. Penner, "Mesoscopic metal particles and wires by electrodeposition," *J. Phys. Chem. B*, vol. 106 pp. 3339-3353 2002.

[91] L. H. Pfeiffer, L. Störmer, K. W. Baldwin, K. W. West, A. R. Goñi, A. Pinczuk, R. C. Ashoori, M. M. Dignam and W. Wegscheider, "Cleaved edge overgrowth for quantum wire fabrication," *J. Cryst. Growth,* vol. 127, pp. 849-857 1993.

[92] Y. Ohno, S. Shimomura, S. Hiyamizu, Y. Takasuka, M. Ogura and K. Komori, "Polarization control of vertical cavity surface emitting laser structure by using self-organized quantum wires grown on (775)B-oriented GaAs substrate by molecular beam epitaxy," *J. Vac. Sci. Technol. B*, vol. 22 pp. 1526-1528 2004.

[93] T. Yamauchi, T. Takahashi and Y. Arakawa, "Tight binding analysis for quantum-wire lasers and quantum-wire infrared detectors," *IEEE J. Quantum Electron.*, vol. 27 pp. 1817-1823 1991.

[94] H. Dery, E. Benisty, A. Epstein, R. Alizon, V. Mikhelashvili, G. Eisenstein, R. Schwertberger, D. Gold, J. P. Reithmaier and A. Forchel, "On the nature of quantum dash structures", *J. Appl. Phys.*, vol. 95, pp. 6103-6111 2004.

[95] I. Hayashi, M. B. Panish, P. W. Foy and S. Sumski, "Junction lasers which operate continuously at room temperature", *Appl. Phys. Lett.*, vol. 17, pp. 109-111 1970.

[96] R. D. Dupuis, P. D. Dapkus, N. Holonyak, Jr., E. A. Rezek and R. Chin, "Room Temperature operation of quantum-well Ga1-xAlxAs-GaAs laser diodes grown by metalorganic chemical vapor deposition", *Appl. Phys. Lett.*, vol. 32, pp. 295-297 1978.

[97] K. Y. Lau and A. Yariv, "Ultrahigh Speed Semiconductor Lasers", *IEEE, J. Quantum Electron.*, vol. 21, pp. 121-138 1985.

[98] A, Yariv, "Scaling laws and minimum threshold currents for quantum-confined semiconductor lasers," *Appl. Phys. Lett.*, vol. 53 pp. 1033-1035 1988.

[99] S. Chakravarty, P. Bhattacharya and Z. Mi, "Electrically Injected Quantum-Dot Photonic Crystal Microcavity Light-Emitting Arrays With Air-Bridge Contacts", *IEEE Photon. Tech. Lett.*, vol. 18, pp. 2665-2667 2006.

[100] C. Emary and L. J. Sham, "Optically controlled single-qubit rotations in self-assembled InAs quantum dots", *J. Phys.: Condens. Matter,* vol. 19**, pp.** 056203-1-10 2007.

[101] N. Ozaki, Y. Takata, S. Ohkouchi, Y. Sugimoto, Y. Nakamura, N. Ikeda and K. Asakawa, "Selective area growth of InAs quantum dots with a metal mask towards optical integrated circuit devices", *J. Cryst.Growth*, vol. 301-301, pp. 771-775 2007.

[102] Y. M. Qiu, D. Uhl and S. Keo, "Room-temperature continuous-wave operation of InAsSb quantum-dot lasers near 2 μm based on (001) InP substrate", *Appl. Phys. Lett.*, vol. 84, pp. 263-265 2004.

[103] X. D. Huang, A. Stintz, C. P. Hains, G. T. Liu and J. L. Cheng, "Very Low Threshold Current Density Room Temperature Continuous-Wave Lasing from a Single-Layer InAs Quantum-Dot Laser", *IEEE Photon. Tech. Lett.*, vol. 12, pp. 227-229 2000.

[104] Saulius Marcinkevièius, Yueming Qiu, Rosa Leon, Jordi Ibáñez, Ramon Cuscó and Lluís Artús, "Time-resolved photoluminescence and Raman scattering of InAsSb/InP quantum dots", *Appl. Phys. Lett.*, vol. 86, pp. 181110-1-3 2005.

[105] J. F. Chen, R. S. Hsiao, W. D. Huang, Y. H. Wu, L. Chang, J. S. Wang and J. Y. Chi, "Strain relaxation and induced defects in InAsSb self-assembled quantum dots", *Appl. Phys. Lett.*, vol. 88, pp. 233113-1-3 2006.

[106] Z. Z. Sun, F. Q. Liu, D. Ding, B. Xu and Z. G. Wang, "Self-assembled InAs and

In0.9Al0.1As quantum dots on (0 0 1)InP substrates grown by molecular beam epitaxy (MBE)", *J. Cryst.Growth*, vol. 204, pp. 24-28 1999.

[107] F.Q. Liu, Zh.G. Wang, J. Wu, B. Xu, Q. Gong and J. Liang, "Structure and photoluminescence of InGaAs self-assembled quantum dots grown on InP(001)", *J. Appl. Phys*., vol. 85, pp. 619-621 1999.

[108] F. Faradiev, "Extremely narrow photoluminescence from the ensemble of InAsP/InP quantum dots", *Materials Science and Engineering B*, vol. 95, pp. 279-282 2002.

[109] Y. M. Qiu and D. Uhl, "Self-assembled InAsSb quantum dots on (001) InP substrates", *Appl. Phys. Lett*., vol. 84, pp. 1510-1512 2004.

[110] J. C. Ferrer, F. Peiro, A. Cornet, J. R. Morante, T. Uztmeier, G. Armelles and F. Briones, "Self-assembled quantum dots of InSb grown on InP by atomic layer molecular beam epitaxy: morphology and strain relaxation", *Appl. Phys. Lett*., vol. 69, pp. 3887-3889 1996.

[111] X. Z. Liao, Y. T. Zhu, Y. M. Qiu, D. Uhl and H. F. Xu "Quantum dot/substrate interaction in InAs/In0.53Ga0.47As/InP(001)", *Appl. Phys. Lett*., vol. 84, pp. 511-533, 2004.

[112] S. Zaitsev, N. Y. Gordeev, V. I. Kopchatov, V. M. Ustinov, A. E. Zhukov, A. Y. Egorov, A. R. Kovsh and P. S. Kopev, "Multi-stacked InAs/InGaAs/InP quantum dot laser (Jth = 11 A/cm2, λ =1.9 μm (77 K))", *Jpn. J. Appl. Phys*., Part 1, vol. 38, pp. 601-604 1999.

[113] K. Nishi, H. Saito, S. Sugou and J. S. Lee, "A narrow photoluminescence linewidth of 21 meV at 1.35 μm from strain-reduced InAs quantum dots covered by In0.2Ga0.8As grown on GaAs substrates," *Appl. Phys. Lett*., vol. 74, pp. 1111-1113 1999.

[114] A. Stintz, G. T. Liu, A. L. Gray, R. Spillers, S. M. Delgado and K. J. Malloy, "Characterization of InAs quantum dots in strained InxG1-xAs quantum wells," *J. Vac. Sci. Technol. B,* vol. 18, pp. 1496-1501 2000.

[115] F. Guffarth, R. Heitz, A. Schliwa, O. Stier, N. N. Ledentsov, A. R. Kovsh, V. M. Ustinov and D. Bimberg, "Strain engineering of self-organized InAs quantum dots," *Phys. Rev. B,* vol. 64, pp. 085305-1-7 2001.

[116] J. He, B. Xu, Z. G. Wang, S. C. Qu, F. Q. Liu, T. W. Zhu, X. L. Ye, F. A. Zhao and X. Q. Meng, "Structure and optical properties of self-assembled InAs/GaAs quantum dots with In0.15Ga0.85As underlying layer," *J. Cryst. Growth,* vol. 240, pp. 395-400 2002.

[117] F. Y. Chang, C. C. Wu, and H. H. Lin, "Effect of InGaAs capping layer on the properties of InAs/InGaAs quatum dots and lasers,"*Appl. Phys. Lett*., vol. 82, pp. 4477-4479 2003.

[118] O. Schumann, S. Birner, M. Baudach, L. Geelhaar, H. Eisele, L. Ivanova, R. Timm, A. Lenz, S. K. Becker, M. Povolotskyi, M. Dahne, G. Abstreiter, and H. Riechert, "Effects of strain and confinement on the emission wavelength of InAs quantum dots due to a GaAs1-xNx capping layer," *Phys. Rev. B,* vol. 71, pp. 245316-1-10 2005.

[119] H. X. Li, T. Daniels-Race, and M. A. Hasan, "Effects of the matrix on self-organization of InAs quantum nanostructures grown on InP substrates," *Appl. Phys. Lett.,* vol. 80, pp. 1367-1369 2002.

[120] Z. H. Zhang, G. W. Pickrell, K. L. Chang, H. C. Lin, K. C. Hsieh, and K. Y. Cheng, "Surface morphology control of InAs nanostructures grown on InGaAs/InP," *Appl. Phys. Lett*., vol. 82, pp. 4555-4557 2003.

[121] H. M. Manasevit and W. I. Simpson, "The Use of Metal-Organics in the Preparation of Semiconductor Materials, I. Epitaxial Gallium-V Compounds", *J. Electrochem. Soc.*, vol. 116, pp. 1725-1732 1969.

[122] A. Ougazzaden, E. Rao, B. Sermage, L. Leprince and M. Gauneau, "High-quality InGaAsN growth by metalorganic vapor-pahse epitaxy using nitrogen carrier gas and dimethylhydrazine, tertiarybutylarsine as group V precursors", *Jpn. J. Appl. Phys.*, vol. 38, 1019-1021, 1999.

[123] C. C. Hsu, Y. F. Yang, H. J. Ou, E. S. Yang, and H. B. Lo, "Carbon-doped GaInP/GaAs heterojunction bipolar transistors grown by metalorganic chemical vapor deposition using nitrogen as the carrier gas," *Appl. Phys. Lett.*, vol. 71, pp. 3248-3250 1997.

[124] R. Schmidt, T. Korst, M. v.d. Ahe, D. Schmitz, H. Hardtdegen and H. Luth, "LP-MOVPE of (Al)GaInP with N2 or H2 as the carrier gas", *Proceedings of 7th European Workshop on Metal-Organic Vapour Phase Epitaxy,* Berlin, Germany, 8-11 June, 1997.

[125] M. Dauelsberg, H. Hardtdegen, L. Kadinski, A. Kaluza and P. Kaufmann, "Modeling and experimental verification of deposition behavior during AlGaAs growth: a comparison for the carrier gases N2 and H2", *J. Cryst. Growth*, vol. 223, pp.21-28 2001.

[126] H. Tanaka, T. Kikkawa, K. Kasai and J. Komeno, "MOVPE growth of selectively doped AlGaAs/GaAs heterostructures with tertiarybutylarsine", *Jpn. J. Appl. Phys.*, part 2, vol. 28, pp. L901-L903 1989.

[127] M. Horita, M. Suzuki and Y. Matsushima, "Electrical and optical properties of InP grown by metalorganic vapor phase epitaxy with extremely low V/III ratios using tertiarybutylphosphine", *Appl. Phys. Lett.*, vol. 62, pp. 882-884 1993.

[128] H. B. Serreze, J. A. Baumann, L. Bunz, R. Schachter and R. D. Esman, “GaAs p-i-n photodiodes made by metalorganic chemical vapor deposition using tertiarybutylarsine and arsine”, *Appl. Phys. Lett.*, vol. 55, pp. 2532-2534 1989.

[129] G.B. Stringfellow, “Organometallic Vapor-Phase Epitaxy: Theory and Practice”, *2nd Edition, Academic Press*, San Diego, 1999.

[130] J. Tatebayashi, N. Hatori, H. Kakuma, H. Ebe, H. Sudo, A. Kuramata, *Y.* Nakata, M. Sugawara and *Y.* Arakawa, “Low threshold current operation of self-assembled InAs/GaAs quantum dot lasers by metal organic chemical vapour deposition”, *Electron. Lett.,* vol. 39, pp. 1130-1131 2003.

[131] K. Sears, M. Buda, H. H. Tan and C. Jagadish, “Modeling and characterization of InAs/GaAs quantum dot lasers grown using metal organic chemical vapor deposition”, *J. Appl. Phys*. vol. 101, pp. 013112-1-9, 2007.

[132] D. Guimard, Y. Arakawa, M. Ishida, S. Tsukamoto, M. Nishioka, Y. Nakata, H. Sudo, T. Yamamoto and M. Sugawara, “Ground state lasing at 1.34 μm from InAs/GaAs quantum dots grown by antimony-mediated metal organic chemical vapor deposition”, *Appl. Phys. Lett*., vol. 90, pp. 241110-1-3 2007.

[133] R. C. Flagan, H. A. Atwater and K. J. Vahala, “Fabricaiton of semiconductor quantum dots”, *J. Aerosol Sci.*, vol. 22, pp. S31-S33 1991.

[134] T. Fukui, S. Ando, T. Honda and T. Toriyama, “GaAs tetrahedral quantum dot structures fabricated using selective area MOCVD”, *Surf. Science*, vol. 267, pp. 236-240 1992.

[135] T. S. Yeoh, C. P. Liu, Y. W. Kim and J. J. Coleman, “Evolution of Coherent InAs Quantum Dots Above the Coherent Critical Thickness Window by MOCVD”, *Mat. Res. Soc. Symp., Proc*, vol. 672, pp. O8.7.1-O8.7.5 2001.

[136] T. S. Yeoh, C. P. Liu, R. B. Swint, A. E. Huber, S. D. Roh, C. Y. Woo, K. E.

Lee and J. J. Coleman, “Epiaxy of InAs QDs on self-organized two-dimensional InAs islands by atmosphere pressure MOCVD”, *Appl. Phys. Lett.*, vol. 79, pp. 221-223 2001.

[137] R. L. Sellin, C. Ribbat, M. Grundmann, N. N. Ledentsov and D. Bimberg, “Close-to-ideal device characteristics of high-power InGaAs/GaAs quantum dot lasers”, *Appl. Phys. Lett.*, vol. 78, pp. 1207-1209 2001.

[138] A. Stintz, G. T. Liu, H. Li, L. F. Lester and K. J. Malloy, “Low-threshold current density 1.3-µm InAs quantum-dot lasers with the dots-in-a-well (DWELL) structure”, *IEEE Photon. Tech. Lett.*, vol. 12, pp. 591-593 2000.

[139] I. V. Markov, “Crystal Growth for Beginners”, *1st Editioned.* Singapore, World Scientific, 1995.

[140] T. S. Yeoh, “Epitaxy of self-assembled nanostructures by metalorganic chemical vapor deposition”, *The Dissertation for the Ph. D degree*, Chapter 1, pp. 1-4, 1998.

[141] S. Stoyanov, “On the theory of epitaxial growth”, *Surf. Science*, vol. 172, pp. 198-210 1986.

[142] F. C. Frank, and J. H. van der Merwe, “One-dimensional dislocations”, *I. Static theory, Proc. R. Soc.* London A vol. 198, pp. 205-216 1949.

[143] D. J. Eaglesham and M. Cerullo. “Dislocation-free Stranski-Krastanow growth of Ge on Si(100)”, *Phys. Rev. Lett.*, vol. 64, pp. 1943-1946 1990.

[144] M. Volmer and A. Weber, “Keimbildung in ubersattigten Gebilden”, *Z. Phys. Chem.*, vol. 119, pp. 277-301 1926.

[145] R. Leon, C. Lobo, T. P. Chin, J. M. Woodall, S. Fafard, S. Ruvimov, Z. Liliental-Weber and M. A. Stevens Kalceff, “Self-forming InAs/GaP quantum dots by direct island growth,” *Appl. Phys. Lett.,* vol. 72, pp. 1356-1358, 1998.

[146] H. Bubert and H. Jenett, “Surface and thin film analysis: principles, instrumentation, applications,” Wiley-VCH Verlag GmbH, pp. 276-284, 2002.

[147] V. A. Shchukin, and D. Bimberg, “Spontaneous ordering of nanostructures on cryst surfaces,” *Rev. Mod. Phys*., vol. 71, pp. 1152-1154, 1999.

[148] V. Swaminathan, and A. T. Macrander, “Materials aspects of GaAs and InP based structures,” *Prentice Hall,* New Jersey, 1991.

[149] J. Hongtao, and S. Jasprit, “Strain distribution and electronic spectra of InAs/GaAs self-assembled dots: An eight-band study,” *Phys. Rev. B,* vol. 56, pp. 4696-4707, 1997.

[150] Klaus D. Mielenz, *Measurement of photoluminescence*. New York: Academic Press, 1982.

[151] H. D. Bauer, J. Thomas and K. Wetaiq, “Analytical transmission electron microscopy in materials research”, *Physica Status Solidi A*, vol. 150, pp. 141-152, 1995.

[152] G. S. Chen, “Transmission electron microscope characterization of III/V alloys grown by organometallic vapor phase epitaxy ”, *The Dissertation for the Ph. D degree*, Chapter 1, pp. 42-47, 1991.

[153] A. Passaseo, V. Tasco, M. De Giorgi, M. T. Todaro, M. De Vittorio, and R. Cingolani, “Long wavelength emission in InxGa1-xAs quantum dot structures grown in a GaAs barrier by metalorganic chemical vapor deposition”, *Appl. Phys. Lett.*, vol. 84, pp. 1868-1870, 2004.

[154] B. J. Riel, K. Hinzer, S. Moisa, J. Fraser, P. Finnie, P. Piercy, S. Farard, Z. R. Wasilewski, “InAs/GaAs(100) self-assembled quantum dots: arsenic pressure and capping effects”, *J. Cryst. Growth,* vol. 236, pp. 145-154, 2002.

[155] J. H. Li, Z.H. Mai and S.F.Cui, “X-ray analysis of strain relaxation in strained-layer superlattices”, *J. Appl. Phys.*, vol. 76, pp. 810-814 1994.

[156] http://glam.stanford.edu/xlab/XPert/XPert.htm.

[157] H. S. Djie, “Plasma Induced Quantum Well Intermixing for Photonic Integration”, The *Dissertation for the Ph. D degree*, Chapter 1, pp. 25-30, 2005.

[158] S. J. Pearton and A. Katz, “High temperature rapid thermal annealing of InP and related materials”, *Mat. Sci. Eng. B*, vol. B18, pp. 153-168, 1993.

[159] C. A. Larsen, N. I. Buchan, S. H. Li and G. B. Stringfellow, “Decomposition mechanisms of tertiarybutylarsine,” *J. Cryst. Growth,* vol. 94, pp. 663-672, 1989.

[160] G. S. Huang, X. H. Tang, B. L. Zhang and S. C. Tjin, “Arsenic incorporation into InGaAsP grown by low-pressure metalorganic vapor phase epitaxy using tertiarybutylarsine and tertiarybutylphosphine in N2 ambient,” *J. Appl. Phys*. vol. 94, pp. 4890-4895, 2003.

[161] L. Goldstein, F. Glas, J. Y. Marzin, M. N. Charasse, and G. Le Roux, “Growth by molecular beam epitaxy and characterization of InAs/GaAs strained-layer superlattices,” *Appl. Phys. Lett.*, vol. 47, pp. 1099-1101, 1985.

[162] Y. Maeda, “Visible photoluminescence from nanocrystallite Ge embedded in a glassy SiO2 matrix: Evidence in support of the quantum-confinement mechanism,” *Phys. Rev. B,* vol. 51, pp. 1658-1670, 1995.

[163] J. Johansson, and W. Seifert, “Kinetics of self-assembled island formation. I. Island density,” *J. Cryst. Growth,* vol. 234, pp. 132-138, 2002.

[164] V. A. Shchukin, and D. Bimberg, “Spontaneous ordering of nanostructures on crystal surfaces,” *Rev. Mod. Phys.,* vol. 71, pp. 1125-1171, 1999.

[165] F. K. LeGoues, M. C. Reuter, J. Tersoff, M. Hammar, and R. M. Tromp, "Cyclic growth of strain-relaxed islands," *Phys. Rev. Lett.*, vol. 73, pp. 300-303 1994.

[166] T. T. Ngo, P. M. Petroff, H. Sakaki, and J. L. Merz, "Simulation model for self-ordering of strained islands in molecular-beam epitaxy," *Phys. Rev. B,* vol. 53, pp. 9618-9621, 1996.

[167] F. M. Ross, J. Tersoff, and R. M. Tromp, "Coarsening of self-assembled Ge quantum dots on Si(001)," *Phys. Rev. Lett.,* vol. 80, pp. 984-987, 1998.

[168] J. G. Cederberg, F. H. Kaats, and R. M. Biefeld, "The impact of growth parameters on the formation of InAs quantum dots on GaAs(1 0 0) by MOCVD," *J. Cryst. Growth,* vol. 261, pp. 197-203, 2004.

[169] A. A. El-Emawy, S. Birudavolu, P. S. Wong, Y.-B. Jiang, H. Xu, S. Huang, and D. L. Huffaker, "Formation trends in quantum dot growth using metalorganic chemical vapor deposition," *J. Appl. Phys.,* vol. 93, pp. 3529-3534, 2003.

[170] C. W. Snyder, J. F. Mansfield, and B. G. Orr, "Kinetically controlled critical thickness for coherent islanding and thick highly strained pseudomorphic films of InxGa1-xAs on GaAs(100)," *Phys. Rev. B,* vol. 46, pp. 9551-9554 1992.

[171] I. Mukhametzhanov, Z. Wei, R. Heitz and A. Madhukar, "Punctuated island growth: An approach to examination and control of quantum dot density, size, and shape evolution", *Appl. Phys. Lett.,* vol. 75, pp. 85-87 1999.

[172] M. Kastner, and G. Voigtlander, "Kinetically self-limiting growth of Ge islands on Si(001)," *Phys. Rev. Lett.*, vol. 82, pp. 2745-2748 1999.

[173] Y. Chen, and J. Washburn, "Structure transition in large-lattice-mismatch heteroepitaxy," *Phys. Rev. Lett.*, vol. 77, pp. 4046-4049 1996.

[174] A. A. El-Emawy, S. Birudavolu, S. Huang, H. Xu, and D. L. Huffakera. "Selective surface migration for defect-free quantum dot ensembles using metal organic chemical vapor deposition," *J. Cryst. Growth*, vol. 255, pp. 213-219 2003.

[175] A. V. Osipov, F. Schmitt, S. A. Kukushkin, and P. Hess, "Stress-driven nucleation of coherent islands: theory and experiment, " *Appl. Surf. Sci.*, vol. 188, pp. 156-162 2002.

[176] J. Tatebayashi, M. Nishioka, and Y. Arakawa, "Over 1.5 μm light emission from InAs quantum dots embedded in InGaAs strain-reducing layer grown by metalorganic chemical vapor deposition," *Appl. Phys. Lett.,* vol. 78, pp. 3469-3471 2001.

[177] S. C. Saxena, and V. K. Saxena, "Thermal conductivity data for hydrogen and deuterium in the range 100-1100 oC," *J. Phys. A: Gen. Phys.,* vol. 3, pp. 309-320 1970.

[178] F. Heinrichsdorff, A. krost, D. Bimberg, A.O. Kosogov, P. Werner, "Self organized defect free InAs/GaAs and InAs/InGaAs/GaAs quantum dots with high lateral density grown by MOCVD," *Appl. Surf. Sci*., vol. 123/124, pp. 725-728 1998.

[179] F. Heinrichsdorff, M. H. Mao, N. Kirstaedter, A. Krost, D. Bimberg, A.O. Kosogov, P. Werner, "Room-temperature continuous-wave lasing from stacked InAs/GaAs quantum dots grown by metalorganic chemical vapor deposition," *Appl. Phys. Lett*., vol. 71(1), pp. 22-24 1997.

[180] G. Walter, T. Chung and N. Holonyak, Jr., "High-gain coupled InGaAs quantum well InAs quantum dot AlGaAs–GaAs–InGaAs–InAs heterostructure diode laser operation," *Appl. Phys. Lett*., vol. 80, pp. 1126-1128 2002.

[181] T. Jun, N. Masao, S. Takao and A. Yasuhiko, "Area-controlled growth of InAs quantum dots and improvement of density and size distribution," *Appl. Phys. Lett.*, vol. 77, pp. 3382-3384 2000.

[182] T. Kodama, Y. Osaka, and M. Yamanishi, "Binding energies of Wannier excitons in Ga1-xAlxAs quantum-well wires," *Jpn. J. Appl. Phys.*, vol. 24, pp. 1370-1371 1985.

[183] A. Fasolino and M. Altarelli, *Two-Dimensional Systems, Heterostructures, and Superlattices,* Springer-Verlag, New York, 1984.

[184] P. C. Sercel and K. J. Vahala, "Analytical formalism for determining quantum-wire and quantum-dot band structure in the multiband envelop-function approximation," *Phys. Rev. B*, vol. 42, pp. 3690-3710 1990.

[185] M. Grundmann, O. Stier, and D. Bimberg, "InAs/GaAs pyramidal quantum dots: strain distribution, optical phonons, and electronic structure," *Phys. Rev. B,* vol. 52, pp. 11969-11981 1995.

[186] H. T. Jiang and J. Singh, "Strain distribution and electronic spectra of InAs/GaAs self-assembled dots: An eight-band study," *Phys. Rev. B,* vol. 56, pp. 4696-4701 1997.

[187] A. L. Efros and M. Rosen, "Quantum size level structure of narrow-gap semiconductor nanocrystals: Effect of band coupling," *Phys. Rev. B*, vol. 58, pp. 7120-7135 1998.

[188] T. U. Schulli, M. Sztucki, V. Chamard, T. H. Metzger and D. Schuh, "Anomalous x-ray diffraction on InAs/GaAs quantum dot systems", *Appl. Phys. Lett.*, vol. 81, pp. 448-450 2002.

[189] F. Adler, M. Geiger, A. Bauknecht, F. Scholz, H. Schweizer, M. H. Pilkuhn, B. Ohnesorge and A. Forchel, "Optical transitions and carrier relaxation in self-

assembled InAs/GaAs quantum dots," *J. Appl. Phys.,* vol. 80, pp. 4019-4026 1996.

[190] Z. Y. Yin, X. H. Tang, J. H. Zhao and S. Deny, "Effects of growth conditions on InAs quantum dot formation by metal-organic chemical vapor deposition using tertiarybutyl rsine in pure N2 ambient," *J. Appl. Phys.,* vol. 99, pp. 124306-1-4 2006.

[191] K. H. Schmidt, G. Medeiros-Ribeiro, J. Garcia, and P. M. Petroff, "Size quantization effects in InAs self-assembled quantum dots," *Appl. Phys. Lett*., vol. 70, pp. 1727-1729 1997.

[192] M. Illing, G. Bacher, T. Kummell, A. Forchel, T. G. Andersson, D. Hommel, B. Jobst and G. Landwehr, "Lateral quantization effects in lithographically defined CdZnSe/ZnSe quantum dots and quantum wires," *Appl. Phys. Lett.,* vol. 67, pp. 124-126 1995.

[193] J. B. Xia, and W. J. Fan, "Electronic structures of superlattices under in-plane magnetic field," *Phys. Rev. B,* vol. 40**,** pp. 8508-8515 1989.

[194] W. J. Fan, M. F. Li, and T. C. Chong, "Valence hole subbands and optical gain spectra of GaN/Ga1xAlxN strained quantum wells," *J. Appl. Phys*., vol. 80, pp. 3471-3478 1996.

[195] D. Gershoni, C. H. Henry and G. A. Baraff, "Calculating the optical properties of Multidimensional heterostructures: application to the modeling of quaternary quantum well lasers," *IEEE, J. Quant. Electron*., vol. 29, pp. 2433-2450 1993.

[196] I. Vurgaftman, J. R. Meyer, and L. R. Ram-Mohan, "Band parameters for III-V compound semiconductors and their alloys," *J. Appl. Phys*., vol. 89, pp. 5815-5875 2001.

[197] J. Y. Marzin, J. M. Gerard, A. Izrael, D. Barrier and G. Bastard, “Photoluminescence of single InAs quantum dots obtained by self-organized growth on GaAs,” *Phys. Rev. Lett.,* vol. 73, pp. 716-719 1994.

[198] J. Tatebayashi, M. Nishioka, and Y. Arakawa, “Over 1.5 µm light emission from InAs quantum dots embedded in InGaAs strain-reducing layer grown by metalorganic chemical vapor deposition,” *Appl. Phys. Lett.*, vol. 78, pp. 3469-3471 2001.

[199] P. Miska, C. Paranthoen, J. Even, O. Dehaese, H. Folliot, N. Bertru, S. Loualiche, M. Senes, and X Marie, “Optical spectroscopy and modelling of double-cap grown InAs/InP quantum dots with long wavelength emission,” *Semicond. Sci. Technol.,* vol. 17, pp. L63-L67 2002.

[200] Q. Gong, R. Notzel, P. J. van Veldhoven, T. J. Eijkemans, and J. H. Wolter, “InAs/InP quantum dots emitting in the 1.55 µm wavelength region by inserting submonolayer GaP interlayers,” *Appl. Phys. Lett.*, vol. 85, pp. 1404-1406 2004.

[201] F. Lelarge, B. Rousseau, B. Dagens, F. Poingt, F. Pommereau, and A. Accard, “Room temperature continuous-wave operation of buried ridge stripe lasers using InAs-InP (100) quantum dots as active core,” *IEEE Photonics Technol. Lett.*, vol. 17, pp. 1369-1371 2005.

[202] C. Becker, I. Prevot, X. Marcadet, B. Vinter, and C. Sirtori, “InAs/AlSb quantum-cascade light-emitting devices in the 3–5 µm wavelength region,” *Appl. Phys. Lett.*, vol. 78, pp. 1029-1031 2001.

[203] Z. Z. Sun, J. Wu, F. Q. Liu, H. Z. Xu, Y. H. Chen, X. L. Ye, W. H. Jiang, B. Xu, and Z. G. Wang, “Structural and photoluminescence properties of In0.9(Ga/Al)0.1As self-assembled quantum dots on InP substrate,” *J. Appl. Phys.*, vol. 88, pp. 533-536 2000.

[204] S. M. Landi, M. P. Pires, C. V. -B Tribuzy, P. L. Souza, E. Marega Jr., A. G. Silva, and P. S. S. Guimaraes, "InAs/InGaAs/InP structures for quantum dot infrared photodetectors," *Phys. Stat. Sol.*(c), vol. 2, pp. 3171-3174 2005.

[205] S. H. Wei, and A. Zunger, "Calculated natural band offsets of all II–VI and III–V semiconductors: Chemical trends and the role of cation *d* orbitals," *Appl. Phys. Lett.,* vol. 72, pp. 2011-2013 1998.

[206] M. A. Cotta, R. A. Hann, T. W. Staley, S. N. Chu, L. R. Harriott, M. B. Panish, and H. Tempkin, "Kinetic surface roughening in molecular beam epitaxy of InP," *Phys. Rev. Lett*., vol. 70, pp. 4106-4109 1993.

[207] T. Hashizume, Q. K. Xue, A. Ichimiya, and T. Sakurai, "Determination of the surface structures of the GaAs(001)-(2×4) As-rich phase," *Phys. Rev. B,* vol. 51, pp. 4200-4212 1995.

[208] J. E. Guyer, and P. W. Voorhees, "Morphological stability of alloy thin films," *Phys. Rev. Lett*., vol. 74, pp. 4031-4034 1995.

[209] Z. H. Zhang, and K. Y. Cheng, "Growth of uniform InAs quantum dots on InGaAs surface structure modified superlattices on InP," *Appl. Phys. Lett.*, vol. 83, pp. 3183-3185 2003.

[210] Z. Sobiesierski, D. I. Westwood, C. C. Matthai, E. Steimetz, T. Zettler and W. Richter, "Processes of quantum dot formation in the InAs on GaAs(001) system: A reflectance anisotropy spectroscopy study," *J. Vac. Sci. Technol. B,* vol. 16, pp. 2358-2366 1998.

[211] V. G. Dubrovskii, G. E. Cirlin, and V. M. Ustinov, "Kinetics of the initial stage of coherent island formation in heteroepitaxial systems", *Phys. Rev. B.* vol. 68, pp. 75409-1-9 2003.

[212] M. C. Chen, H. H. Lin and C. W. Shie, "Self-organized InAs/GaAs quantum dots grown by gas source molecular beam epitaxy," *J. Appl. Phys.,* vol. 83, pp. 3061-3064 1998.

[213] R. Leon, C. Lobo, A. Clark, R. Bozek, A. Wysmolek, A. Kurpiewski and M. Kaminska, "Different paths to tunabiltiy in III-V quantum dots," *J. Appl. Phys.,* vol. 84, pp. 248-254 1998.

[214] Y. Horikoshi, M. Kawashima, and Hiroshi Yamaguchi, "Low-temperature growth of GaAs and AlAs-GaAs quantum-well layers by modified molecular beam epitaxy," *Jpn. J. Appl. Phys*., vol. 25, L868-870, 1986.

[215] G. S. Solomon, J. A. Trezza and J. S. Harrris, Jr., "Effects of monolayer coverage, flux ratio, and growth rate on the island density of InAs islands on GaAs,", *Appl. Phys. Lett.,* vol. 66, pp. 3161-3163 1995.

[216] R. Leon, C. Lobo, J. Zou, T. Romeo, and D. J. H. Cockayne, "Stable and Metastable InGaAsyGaAs Island Shapes and Surfactantlike Suppression of the Wetting Transformation," *Phys. Rev. Lett*., vol. 81, pp. 2486-2489 1998.

[217] C. S. Peng, Q. Huang, W. Q. Cheng, J. M. Zhou, Y. H. Zhang, T. T. Sheng and C. H. Tung, "Improvement of Ge self-organized quantum dots by use of Sb surfactant," *Appl. Phys. Lett.,* vol. 72, pp. 2541-2543 1998.

[218] D. J. Eaglesham, F. C. Unterwald and D. C. Jacobson, "Growth morphology and the equilibrium shape: The role of "surfactants" in Ge/Si island formaiton," *Phys. Rev. Lett*., vol. 70, pp. 966-969 1993.

[219] T. Chung, G. Walter and N. Holonyak, Jr., "Growth mechanism of InAs quantum dots on GaAs by metal-organic chemical-vapor deposition", *J. Appl. Phys*., vol. 97, pp. 053510-1-4, 2005.

[220] A E Zhukov, V M Ustinov, A R Kovsh, A Yu Egorov, N N Ledentsov, N A Maleev, A F Tsatsul'ikov, M V Maximov, Yu G Musikhin, N A Bert, P S Kop'v, D Bimberg, and Zh I Alferov, "Control of the emission wavelength of self-organized InGaAs quantum dots: main achievements and present status," *Semicond. Sci. Technol.*, vol. 14, pp. 575-581, 1999.

[221] R. Heitz, I. Mukhametzhanov, J. Zeng, P. Chen, A. Madhukar, and D. Bimberg, "Excitation transfer in novel self-organized quantum dot structures," *Superlattices Microstruct.*, vol. 25, pp. 97-104, 1999.

[222] M. V. Maximov, A. F. Tsatsul'nikov, B. V. Volovik, D. S. Sizov, Yu. M. Shernyakov, I. N. Kaiander, A. E. Zhukov, A. R. Kovsh, S. S. Mikhrin, V. M. Ustinov, Zh. I. Alferov, R. Heitz, V. A. Shchukin, N. N. Ledentsov, D. Bimberg, Yu. G. Musikhin, and W. Neumann, "Tuning quantum dot properties by activated phase separation of an InGa(Al)As alloy grown on InAs stressors," *Phys. Rev. B*, vol. 62, pp. 16 671-16 680, 2000.

[223] W. H. Chang, H. Y. Chen, H. S. Chang, W. Y. Chen, T. M. Hsu, T. P. Hsieh, J. I. Chyi, and N. T. Yeh, " Electroreflectance studies of InAs quantum dots with In xGa1-xAs capping layer grown by metalorganic chemical vapor deposition," *Appl. Phys. Lett.*, vol. 86, pp. 131917-1-3, 2005.

[224] T. Nishikawa, M. Kubo, and Y. Sasai, “Surface migration of ZnSe regrowth using compound source molecular beam epitaxy,” *Appl. Phys. Lett.,* vol. 68**,** pp. 3428-3430, 1996.

[225] T. Tanbun-ek, P. F. Sciortino, Jr., A. M. Sergent, K. W. Wecht, P. Wisk, Y. K. Chen, C. G. Bethea, and S. K. Sputz, “DFB lasers integrated with Mach-Zehnder optical modulator fabricated by selective area growth MOVPE technuqie,” *IEEE Photon. Technol. Lett.,* vol. 7, pp. 1019-1021, 1995.

[226] S. Fafard, Z. R. Wasilewski, C. N. Allen, D. Picard, M. Spanner, J. P. McCaffrey and P. G. Piva "Manipulating the energy levels of semiconductor quantum dots," *Phys. Rev. B,* vol. 59, pp. 15368-15373 1999.

[227] J. F. Girard, C. Dion, P. Desjardins, C. N. Allen, P. J. Poole and S. Raymond "Tuning of the electronic properties of self-assembled InAs/InP(001) quantum dots by rapid thermal annealing," *Appl. Phys. Lett.,* vol. 84, pp. 3382-3384 2004.

[228] L. Fu, P. Lever, H. H. Tan, C. Jagadish, P. Reece and M. Gal "Suppression of interdiffusion in InGaAs/GaAs quantum dots using dielectric layer of titanium dioxide," *Appl. Phys. Lett.,* vol. 82, pp. 2613-2615 2003.

[229] J. J. Dubowski, C. N. Allen and S. Fafard "Laser-induced InAs/GaAs quantum dot intermixing," *Appl. Phys. Lett.,* vol. 77, pp. 3583-3585 2000.

[230] T. Surkova, A. Patane, L. Eaves, P. C. Main, M. Henini, A. Polimeni, A. P. Knights and C. Jeynes "Indium interdiffusion in annealed and implanted InAs/(AlGa)As self-assembled quantum dots," *J. Appl. Phys.,* vol. 89, pp. 6044-6047 2001.

[231] P. Lever, H. H. Tan, C. Jagadish, P. Reece and M. Gal "Proton-irradiation-induced intermixing of InGaAs quantum dots," *Appl. Phys. Lett.,* vol. 82, pp. 2053-2055 2003.

[232] Y. L. Ji,, W. Lu, G. B. Chen, X. S. Chen, and Q. Wang "InAs/GaAs quantum dot intermixing induced by proton implantation," *J. Appl. Phys.,* vol. 93, pp. 1208-1211 2003.

[233] V. Aimez,, J. Beauvais, J. Beerens, D. Morris, H. S. Lim, and B. S. Ooi, "Low-energy ion-implantation-induced quantum-well intermixing," *IEEE J. Select. Topics Quantum Electron.,* vol. 8, pp. 870-879 2002.

[234] B. S. Ooi, A. C. Bryce and J. H. Marsh “Integration process for photonic integrated circuits using plasma damage induced layer intermixing,” *Electron. Lett.,* vol. 31, pp. 449-451 1995.

[235] H. S. Djie, T. Mei and J. Arokiaraj “Photoluminescence enhancement by inductively coupled argon plasma exposure for quantum-well intermixing,” *Appl. Phys. Lett.,* vol. 83, 60-62 2003.

[236] H. S. Djie, T. Mei, J. Arokiaraj, C. Sookdhis, S. F. Yu, L. K. Ang and X. H. Tang “Experimental and theoretical analysis of argon plasma-enhanced quantum-well intermixing,” *IEEE J. Quantum Electron,* vol. 40, pp. 166-174 2004.

[237] C. Francis, M. A. Bradley, P. Boucaud, F. H. Julien, and M. Razeghi “Intermixing of GaInP/GaAs multiple quantum well,” *Appl. Phys. Lett.,* vol. 62, pp. 178-180 1993.

[238] D. Nie, T. Mei, X. H. Tang, M. K. Chin, H. S. Djie, and Y. X. Wang, “Argon plasma exposure enhanced intermixing in an undoped InGaAsP/InP quantum-well structure,” *J. Appl. Phys*., vol. 100, pp. 046103-1-3, 2006.

[239] C. Walther, J. Bollmann, H. Kissel, H. Kirmse, W. Neumann, and W. T. Masselink, “Characterization of electron trap states due to InAs quantum dots in GaAs,” *Appl. Phys. Lett.* , vol. 76, pp. 2916-2918 2000.

[240] C. J. Park, H. B. Kim, Y. H. Lee, D. Y. Kim, T. W. Kang, C. Y. Hong, H. Y. Cho and M. D. Kim, “Deep level defects of InAs quantum dots grown on GaAs by molecular beam epitaxy,” *J. Cryst. Growth*, vol. 227-228, pp. 1057-1061 2001.

[241] G. N. Semenova, Y. F. Venger, M. Y. Valakh, Y. G. Sadofyev, N. O. Korsunska, V. V. Strelchuk, L. V. Borkovska, V. P. Papusha and M. V. Vuychik, “Optical investigations of the influence of point defects on quantum dots in

CdSe/ZnSe heterostructures," *J. Phys.: Condens. Matter,* vol. 14, pp. 13375-13380 2002.

[242] B. Goldstein**, "**Diffusion in Compound Semiconductors," *Phys. Rev.,* vol. 121, pp. 1305-1311 1961.

[243] S. J. Xu, X. C. Wang, S. J. Chua, C. H. Wang, W. J. Fan, J. Jiang, and X. G. Xie, "Effects of rapid thermal annealing on structure and luminescence of self-assembled InAs/GaAs quantum dots," *Appl. Phys. Lett.,* vol. 72, pp. 3335-3337 1998.

[244] Q. Gao, H. H. Tan, L. Fu and C. Jagadish "Effects of thermal stress on interdiffusion in InGaAsN/GaAs quantum dots," *Appl. Phys. Lett.,* vol. 84, pp. 4950-4952 2004.

[245] D. Lootens, P. Van Daele, P. Demeester, and P. Clauws, "Study of electrical damage in GaAs induced by SiCl4 reactive ion etching," *J. Appl. Phys*., vol. 70, pp. 221-224 1991.

[246] H. S. Djie, B. S. Ooi, and V. Aimes, "Neutral ion-implantation-induced selective quantum-dot intermixing," *Appl. Phys. Lett*., vol. 87, pp. 261102-1-3 2005.

[247] D. Bhattacharyya, A. Saher helmy, A. C. Bryce, E. A. Avrutin, and J. H. Marsh, "Selective control of self-organized In0.5Ga0.5As/GaAs quantum dot properties: Quantum dot intermixing," *J. Appl. Phys*., vol. 88, pp. 4619-4622 2000.

[248] A. O. Kosogov, P. Werner, U. Gosele, N. N. Ledentsov, D. Bimberg, V. M. Ustinov, A. Yu. Egorov, A. E. Zhukov, P. S. Kop'v, N. A. Bert, and and Zh. I. Alferov, "Structural and optical properties of InAs-GaAs quantum dots subjected to high temperature annealing," *Appl. Phys. Lett*., vol. 69**,** pp. 3072-3074 1996.

[249] H. S. Kim, J. W. Park, D. K. Oh, K. R. Oh, S. J. K, and In-H. Choi, "Quantum well intermixing of In1.*x*Ga*x*As/InP and In1.*x*Ga*x*As/In1.*x*Ga*x*As1.*y*P*y* multiple-quantum-well structures by using the impurity-free vacancy diffusion technique," *Semicond. Sci. Technol.*, vol. 15**,** pp. 1005-1009 2000.